TOWARDS SPATIAL COMPUTING AND CHEMICAL INFORMATION STORAGE IN SOFT MATERIALS USING DNA PROGRAMMING

by
Phillip James Dorsey

A dissertation submitted to Johns Hopkins University in conformity with the requirements for the degree of Doctor of Philosophy

Baltimore, Maryland
January 2020

Abstract

Living organisms possess the ability to form and recover complex patterns in prescribed locations at length scales of hundreds of microns. During the past 15 years, experimentalists within the fields of DNA nanotechnology and synthetic biology have developed a variety of systems capable of self-assembly and reorganization at the nanoscale using synthetic oligonucleotide building blocks to mimic the functions of biological tissues and to provide new routes of manipulating materials with molecular programs. Programming 'smart and responsive' nano- and micromaterials using DNA circuits has the potential to impact numerous applications including molecular diagnostics, biodefense, drug delivery systems, and low-energy information storage. In this thesis, I present and develop computational and experimental systems that leverage oligonucleotide strand displacement reaction networks, digital maskless photolithographic technology, and microfluidic delivery methods to design DNA-functionalized micro-materials that process and store chemical information spatiotemporally. These systems couple reactions, transport, and feedback control to achieve specific temporal concentration profiles at specific points in hydrogel substrates. First, I developed a reaction-diffusion waveguide designed to coordinate spatiotemporal sensing and regulation of synthetic DNA-based materials using autocatalysis. I discuss the design requirements for this architecture and the results of in silico and experimental analyses of the components of this system. Based on the operational requirements of this system, I then designed a DNA-compatible hydrogel microfabrication method that accommodates UV photo-directed release of oligonucleotides from defined regions of a hydrogel, which can be used to initiate downstream reaction-diffusion processes in materials. Building on this platform, I constructed a reaction-diffusion system that enables shape programming of biomolecular attractor patterns in photopatterned poly(ethylene-

glycol) diacrylate microgels. These patterns were able to heal their structure in response to spatial perturbation. Finally, I develop and discuss a model of a reaction-diffusion associative memory, consisting of a distributed network of nodes that store and repair spatial chemical patterns.

Thesis Advisor:
Professor Rebecca Schulman, Department of Chemical & Biomolecular Engineering

Thesis Committee Members:
Professor Jeffrey Gray, Department of Chemical & Biomolecular Engineering
Professor Sung Hoon Kang, Department of Mechanical Engineering
Professor Luo Gu, Department of Materials Science & Engineering
Professor Efie Kokkoli, Department of Chemical & Biomolecular Engineering

To my parents

Acknowledgements

First and foremost, I thank my advisor, Professor Rebecca Schulman, for supporting me during my educational journey at Johns Hopkins. Conducting research as a member of the Adaptive and Biomolecular Materials lab has truly transformed the way I view the world around me and enabled me to appreciate the impact our research has on society. Secondly, I thank my parents: my mom for supporting me unwaveringly during my education and encouraging my dreams and ambitions; and my father, who passed away when I was 10, for helping me imagine a limitless future for myself as a child.

I am sincerely grateful to my thesis committee for providing direction and feedback during my studies. My lab mates were an incredible resource to have at my disposal and were a privilege to work with. I'd like to thank Dominic Scalise, John Zenk, and Abdul Mohammed for showing me the ropes when I began my doctoral studies. To Misha Rubanov, Joshua Cole, Rachel Shi, Wenlu Wang, Yi Li, Naresh, Sisi Jia, Katherine Miller, Samuel Schaffer, Charlie Chen, and Lei Zhang, thank you for providing advice during experimental troubleshooting and for being a source of fun and wacky debates about science.

Outside of the lab, I'd like to thank Professor Howard Stone for providing me with my first research experience as an undergraduate at Princeton, and my high school and middle school science and math teachers at Moorestown Friends School, Timothy Clarke, Dr. Barbara Kreider, Kathy Bernard, and Andrew Newman, you all helped demystify science and initially inspired me to pursue chemical engineering. To my family and friends, thank you for supporting me, I am a product of my environment and I could not have achieved my goals without your endless love and encouragement.

Table of Contents

Table of Contents

List of Tables

List of Figures

List of Supplementary Figures

Chapter 1

1.1 Introduction

Living organisms provide a diverse set of phenomena to study how physiological systems have evolved to efficiently detect, process, and communicate biochemical information spatiotemporally. Colonies of microorganisms use genetic regulatory networks in a process known a quorum sensing to regulate proliferation and growth phase. Multi-cellular organisms employ intricate feedback loops in reaction-diffusion networks to coordinate complex pattern formation programs across hundreds of cells during morphogenesis. As one of the building blocks for all terrestrial life, oligonucleotides, biology's information storage material, are inextricably linked to these processes. Within the past 10 years, the fields of DNA nanotechnology and synthetic biology have matured as researchers explored routes of designing and programming synthetic biological systems and materials using DNA and RNA. Importantly, the explosion of research regarding DNA nanotechnology has been coupled with decreasing synthesis costs and an increasing ability to understand how regulation of genetic material from a single base-pair all the way to the genomic scale impacts the function and dysfunction of living systems. Interest in DNA as a computing material grew during the 1980's and 1990's as nanotechnology and molecular computing.[1,2] During the second decade of the 21st century, having established the theoretical computing power provided by DNA-based systems, experimentalists have begun to explore the versatility of designing material systems using oligonucleotides, paving the way for the construction of new classes of nano- and micromaterials with physical & biological functions previously limited to silicon-based computing[3–5].

Importantly, a key step for the continued development and maturation of DNA and RNA-based computing materials for numerous applications including smart robotics[6–9] drug delivery[10–14], large-scale bottom-up assembly[15–19], molecular diagnostics and biodefense[20–26], is the ability to coordinate the exchange of chemical information spatiotemporally to regulate structure and function. In well-mixed solution, DNA strand displacement networks have been used as buffers to store chemical information[27], performed combinatorial logic operations[3], functioned as neural networks to enable molecular recognition[7], and have been incorporated into in-vitro transcriptional switches exhibiting bi-stability[28]. In order to develop DNA programmable material systems that function in spatial contexts at length scales ranging from nanometers to microns, DNA-based circuits and nanomaterials must be designed with the ability to integrate, propagate and store information spatiotemporally. Such functions are, for example, critical for developing stimuli responsive biomaterials[29], coordinating chemomechanical actuation of nano- and micro-robots[30], and templating of substrates to create molecular landmarks[31].

Fundamentally, designing such systems to operate in space introduces the problem of leveraging and or mitigating the energy provided by diffusion and convection within an aqueous environment. Nature is full of reaction-diffusion systems that fuel and sustain pattern formation processes. For example, morphogen gradients diffuse across the blastoderm of vertebrate and invertebrate organisms during embryogenesis to control dorsal-ventral axis patterning[32]. Inspired by how reaction-diffusion processes might direct the anatomical organization of an organism during its development, Alan Turing in 1952, proposed a mechanism for how transient fluctuations occurring within a homogenous state could form periodic chemical patterns.[33] This discovery combined with a burgeoning interest in synthetic chemical oscillators and nonlinear chemical dynamics in the 1970's and 1980's catalyzed the

study of reaction-diffusion systems as a means of achieving chemical and molecular computing.[34–36] Importantly, the use of DNA as a substrate in reaction-diffusion processes extends its combinatorial phase space for computing to spatial contexts. DNA reaction-diffusion systems have been used to compute the shortest distance within a maze[37], and to propagate signals cross populations of synthetic protocells[38]. Zenk et al. implemented a system of stable DNA reaction-diffusion patterns in molded agarose hydrogels[39]. Zadorin et al. and Gines et al. designed systems of traveling autocatalytic reaction-diffusion waves in capillary tubes using enzymatic machinery[40,41]. Cangialosi et al. demonstrated addressable chemomechanical actuation of specific domains within a DNA-crosslinked bis-acrylamide bilayer using a DNA hairpin insertion reaction[42]. Importantly, the process to design the bilayers leveraged microfabrication techniques, specifically photolithography, to precisely control where specific oligonucleotides with specific sequences were embedded within the hydrogel substrate.

As will be addressed in this thesis, several challenges remain regarding the design and integration of DNA reaction-diffusion circuits and soft materials to create systems capable of autonomously sensing and integrating spatial stimuli. Specifically, the development of DNA compatible microfabrication methods to enable stimuli responsive functions in DNA-based soft materials like hydrogels remains a critical area of ongoing research and development. Mechanisms enabling addressable sensing and signal propagation of biomolecules within DNA-functionalized substrates at biologically relevant length scales of tens to hundreds of microns remain undeveloped in part due to the difficulty of physically assembling a multicomponent system at that size and the challenges of designing DNA circuitry that ensures signal propagation at a rate faster than what is achievable with simple diffusion. Additionally, successful computation in physiological environments invariably entails resilience to noise or degradation,

which requires new classes of DNA reaction-diffusion systems that are capable of storing and retrieving spatially distributed information and are resilient to external perturbations and damage.

In this thesis, it was my goal to: 1) develop a mechanism of propagating DNA signals super-diffusively between specific locations within soft materials by embedding the circuitry necessary for such a function within the substrate itself; this capability, similar to the function of the vascular system in the human body, could enable directed transmission of signals between distal locations in a synthetic material and possibly provide a way of coordinating sensing across a material; 2) develop a DNA-compatible microfabrication method that enabled the construction of multicomponent hydrogels with addressable DNA domains at the microscale and accommodated UV photo-directed release of oligonucleotides to trigger downstream processes; 3) design a dissipative chemical system using DNA, capable of recovering and maintaining spatial patterns in response to perturbation; 4) develop distributed DNA-based networks capable of sensing and maintaining spatial patterns in the presence of degradation.

In Chapter 2, I discuss the function of a DNA reaction-diffusion waveguide enabling super-diffusive transport of stable traveling chemical waves and simulate its dynamics using known biophysical parameters for DNA diffusivity and DNA strand displacement reactions. I then review our experimental results for an autocatalytic amplification strand displacement circuit designed to transmit signals within the waveguide architecture. Overall, our analyses show that autocatalysis enables super-diffusive transport of biomolecular species and that thresholding reactions mitigate the effects of spurious leak reactions. Chapter 3 reviews a digital photolithographic hydrogel patterning method we developed that is compatible with oligonucleotides and incorporates a visible light absorbing photoinitiator to enable subsequent UV light directed photocleavage of nitrobenzyl-modified DNA from defined regions of a

substrate. In Chapter 4, I discuss a system of DNA reaction-diffusion attractors that we designed to repair spatial damage using negative feedback control. I discuss the implementation of reaction-diffusion system within a distributed spatial network of chemical computing nodes using a consensus algorithm in Chapter 5. Chapter 6 concludes the thesis and provides future directions for the research and applications covered within it.

Contributions

Chapter 3
A version of Chapter 3 was published:

Reproduced with permission from P. Dorsey, R. Rubanov, W. Wang, and R. Schulman. Digital Maskless Photolithographic Patterning of DNA-Functionalized Poly(Ethylene Glycol) Diacrylate Hydrogels with Visible Light Enabling Photodirected Release of Oligonucleotides. *ACS Macro Lett.* **2019**, *8* (9), 1133–1140.

Chapter 4
A version of Chapter 4 is in preparation for submission.

P. Dorsey, D. Scalise, and R. Schulman. DNA Reaction-Diffusion Attractor Patterns. *In preparation.*

PD and RS designed the experiments. PD conducted the experiments and simulations. DS provided conceptual & technical advice. PD performed the data analyses. PD and RS and wrote the paper.

Chapter 5
A version of Chapter 5 is in preparation for submission.
P. Dorsey & Rebecca Schulman. A DNA-based reaction-diffusion associative memory for storage & repair of spatial molecular patterns. *In preparation.*

Additional Contributions

Zenk, J.; Scalise, D.; Wang, K.; Dorsey, P.; Fern, J.; Cruz, A.; Schulman, R. Stable DNA-Based Reaction-Diffusion Patterns. *RSC Adv.* **2017**, *7* (29), 18032–18040.

Moshe Rubanov, Phillip J. Dorsey, Dominic Scalise, Wenlu Wang, and Rebecca Schulman. The Spatiotemporal Release of DNA for Soft Material Programming. *In preparation.*

Chapter 2 Enabling spatiotemporal regulation within biomaterials using DNA reaction-diffusion waveguides

Summary

In complex multicellular organisms, cells and tissues coordinate sensing and propagation of biochemical signals across multiple length scales spanning from single microns to meters. Cells signal to adjacent cells using surface receptors such as cadherins, and to nearby cells via paracrine signaling pathways involving growth factors and corresponding receptors. Importantly, the vascular system enables communication between cells in distal locations of an organism and serves as a conduit for endocrine signals that convect through the bloodstream from one tissue to another. This route of communication facilitates hierarchical structural organization and modularity as multiple sets of tissues and organs within an organism can respond dynamically to spatiotemporal cues and exchange such information in the form of biomolecules with other organs across length scales at a faster rate than what could be achieved through simple diffusion of such molecules. Additionally, the vascular system facilitates complex coordinated responses to environmental cues via chemomechanical actuation by providing oxygen to muscles moving limbs or coordinating metabolically intensive processes like wound-healing at sites of injury. Extending these capabilities to synthetic biological systems and materials is critical for the development of new classes of intelligent and adaptable soft materials and sensors capable of interfacing with biological systems and communicating spatiotemporal information. Specifically, a requirement for coordination between biomolecular devices is the reliable transmission of signals to and from other devices. While pneumatic and micro-electro-mechanical systems (MEMs) provide possible routes for designing a synthetic

vasculature, such systems face numerous challenges regarding miniaturization and integration within biomaterials and compatibility with aqueous environments. Here, we combine ideas from cell signaling with electronic circuit design to develop "biochemical reaction-diffusion waveguides" that transmit information in the form of a concentration of a biomolecule on a directed path. A wavefront produced by coupled biochemical reactions in a reaction-diffusion process can be used to drive spatial signal propagation. These waveguides, or wires, also offer the capability of seamless integration within a material such that there is virtually no difference in the chemical or physical properties of the wires or their insulators and the material they are embedded within. We propose the design of DNA-based circuitry to construct these systems and characterize the behavior of such circuitry. We then explore challenges for the spatial implementation of DNA-based reaction-diffusion waveguides.

2.1 Introduction

The biomolecular components residing within cells are powerful computational tools: they serve as exquisite detectors of signaling molecules[43], pathogens[44] and metabolites[45,46], orchestrate multistep chemical synthesis and catalysis, and self-assemble nanostructures[47] or materials with unique structural properties [48] and geometry[49]. Synthetic biomolecular sensors can detect concentrations of drugs in the blood in real time[50,51], approaching the sensitivity with which cells detect substances. Similarly, engineered enzyme cascades can orchestrate multistage chemical reactions[52], biomolecular assemblies can template electronic devices[53,54], and therapeutics can sense local conditions and dispense medication in at the right time[55–57]. Recently, engineers and nanotechnologists have sought to design synthetic materials capable of sensing, integrating, and transmitting spatial information in processes similar to the functions performed by vascularized tissues. Microfabricated systems composed of fluidic or pneumatic

vasculature have been designed to coordinate and direct delivery of fuel or nutrients to various locations in soft polymer substrates[58] to control actuation and growth and migration of cells in tissue scaffolds. However, fluidic control mechanisms present several challenges for designing triggerable sensing, communication, and computation in material systems. Such systems often require tethers to external power sources or fuel depots that are difficult to integrate within the structure of the material.

The approach we designed builds upon molecular programming concepts from synthetic biology and DNA nanotechnology and leverages the dynamics of non-linear chemical and biological reaction networks coupled to diffusive transport of biomolecular species to achieve super-diffusive transport of chemical signals through biomaterial medium. Reaction-diffusion waveguides or wires consist of a region of a hydrogel substrate that acts as an excitable medium, where an autocatalytic reaction propagates spatially in the form of a traveling wavefront. Multiple wires could be integrated within a substrate and insulated from one another using competitive reactions to restrict the autocatalytic reaction to the specific path defined by the waveguide. It is important to note that chemical reactions generally take seconds to hours to reach completion and can require nano- to micro-liter volumes to ensure deterministic behavior. As such, the system we describe and characterize is not intended to compete with electronic wires for speed or computational power. Instead, our biochemical waveguide serves as a stepping stone towards more robust chemical coordination of biomolecular sensors, polymer actuators, biomaterials, and soft robots in millimeter-scale architectures without the need for electronics.

The study of nonlinear chemical reaction networks, often inspired by biological phenomena, to enable chemical computation is not new. Alan Turing's seminal research

regarding the origins of pattern formation during morphogenesis described how periodic spatial patterns of chemical species could arise from transient fluctuations within an initially homogenous system.[33] Experimental implementations of the Belousov-Zhabotinsky reaction-diffusion system, and more specifically aerosol OT microemulsion and chlorite-iodide-malonic acid reaction systems respectively, have been demonstrated as mechanisms to propagate chemical species spatially.[59,60] Recently, the growing research field of DNA nanotechnology has provided new routes of material programming, enabling the design of experimental oscillators and amplifiers composed of biomolecular components capable of interfacing with biological systems.

A growing class of synthetic biomolecular devices can release or respond to nucleic acid (DNA or RNA) signals of 20-100 bases in length. These signals can start or stop molecular machines[61], or catalysis[62], and direct hydrogel[63,64] or nanostructure self-assembly[65,66]. Nucleic acid signals can also be released by aptamer or antibody sensors[67,68]. Molecular "circuits" operate on the concentrations of nucleic acids in well-mixed solution, analogous to the functions of electronic circuits, and have been used to perform complex computation by emulating the functions of Boolean logic gates to conduct mathematical operations[3] or act as chemical implementations of neural networks for pattern recognition[7]. These molecular circuits can execute logic operation on or classify multiple nucleic acid signals inputs, act as memory latches or direct oscillatory cycles of signal activity[3,69,70]. Zadorin et al. used a polymerase-exonuclease-nickase (PEN) enzyme reaction with a template DNA duplex to produce a traveling wavefront within a buffer-filled polystyrene channel.[71] Similarly, Zambrano et al. implemented an enzymatic Predator-Prey reaction network within a microfluidic network to compute the shortest distance within the network from entrance to exit[37].

In this work, we adapted an enzyme-free DNA-based autocatalytic amplifier[72] developed by Zhang and colleagues for incorporation within an insulated reaction-diffusion waveguide. Importantly, we asked whether it was possible to design a system that would enable super-diffusive transport of chemical signals over dimensions of hundreds of microns to millimeters. We first conducted in silico analyses to determine rates of spatial propagation achievable with autocatalytic waves using strand-displacement processes within a reaction-diffusion medium. We then designed a thresholding reaction and amplification quenching strategy to enable insulation of waveguides and to prevent spurious activation by undesired leak reactions between different DNA species. We characterized the effectiveness of these strategies for achieving controlled triggerable activation of the autocatalysis reaction in well-mixed experimental conditions and analyzed how these strategies impacted the in silico performance of spatial wavefront propagation speeds.

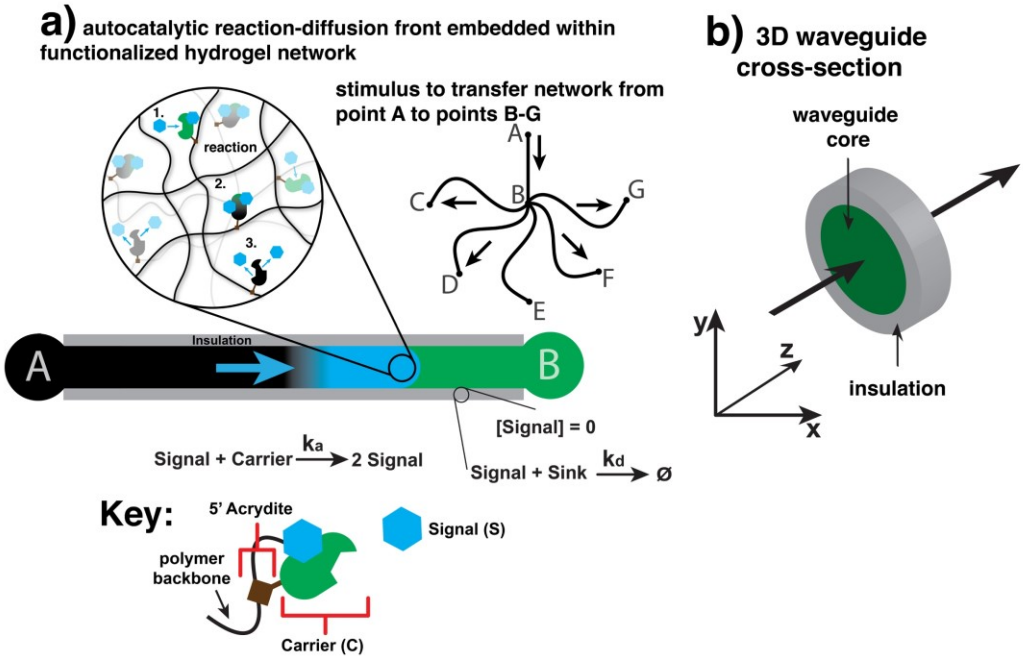

Figure 2.1. Schematic: Design and function of a reaction-diffusion waveguide in a hydrogel. a) A chemical wave of Signal is propagated between points A and B via an autocatalytic reaction that make copies of Signal from a Carrier species that is crosslinked to the hydrogel network. Such a system could be used to route chemical signals simultaneously between multiple points in space: 1) Signal reacts with patterned Carrier, 2) Carrier transitions into its release state, 3) Carrier releases 2 Signal

molecules. b) Schematic cross section of a 3-dimensional waveguide showing its core where autocatalysis occurs and the insulation surrounding it which prevents Signal from diffusing from the waveguide.

2.2 Results

Autocatalytic amplification enables super-diffusive transport of biochemical species in a reaction-diffusion waveguide model.

The reaction-diffusion waveguide model consisted of a two or three-dimensional path of DNA molecules conjugated to a hydrogel medium. The molecules along the path were the reactants and fuel needed to propagate an autocatalytic reaction. An insulator lined all sides of the waveguide; the insulator contained a high concentration of a DNA species that reacted to prevent the wave from diffusing from beyond the bounds of the waveguide. The following abstract reactions describe the basic function of the waveguide:

$$Signal + Carrier \xrightarrow{k_a} 2\ Signal \quad (1)$$

$$Signal + Sink \xrightarrow{k_d} \emptyset \quad (2)$$

$$\emptyset \xrightarrow{k_{pc}} Carrier \quad (3)$$

$$\emptyset \xrightarrow{k_{ps}} Sink \quad (4)$$

$$Carrier \xrightarrow{k_{dc}} \emptyset \quad (5)$$

$$Sink \xrightarrow{k_{ds}} \emptyset \quad (6)$$

Signal served as a trigger for the reaction cascade on the waveguide. The generation and diffusion of Signal at location A on the waveguide (**Figure 2.1a**) into the wire domain initiated the reaction of Signal and Carrier. This process could be initiated by the photo-directed release of oligonucleotides from a specific section of a hydrogel to trigger the wire at point A. Signal reacted autocatalytically to produce 2 molecules of Signal, which could diffuse and react with more Carrier, and thus generate more Signal. We designed a Sink molecule to react rapidly with Signal to convert it into waste, thus providing a way of removing Signal from the waveguide.

Within the waveguide core, Carrier and Sink were immobilized, and produced at a constant rate from a large inactive precursor reservoir patterned into the substrate. Carrier and Sink were also degraded slowly in a unimolecular reaction. We assumed that the size of the inactive precursor reservoir was in such excess of the steady state concentrations of Carrier and Sink that the production rate of both species obeyed a 0^{th} order rate law:

$$\text{production rate} \approx \mathrm{k_{pi}} \quad (7)$$

$$\text{degradation rate} \approx \mathrm{k_{di}}[M_i] \quad (8)$$

$$\frac{\partial[M_i]}{\partial \mathrm{t}} = \mathrm{k_{pi}} - \mathrm{k_{di}}[M_i] = \mathrm{k_{di}}\left(\frac{\mathrm{k_{pi}}}{\mathrm{k_{di}}} - [M_i]\right) \quad (9)$$

where M_i represents any of the species Carrier or Sink. Effectively, these production and degradation reactions enable the regeneration of the steady state concentrations, defined by k_{pi}/k_{di}, of Carrier and Sink after their consumption by the autocatalysis reaction. We discuss the full implications of these restorative behaviors for operation of a reaction-diffusion waveguide and for self-healing DNA-based materials in Supporting Information: Results & Discussion and Chapter 4 respectively. Similarly, the waveguide insulation consisted of a high concentration of Sink, which reacted with Signal at a high rate of reaction to prevent its diffusion from the waveguide. Importantly, the rate of this reaction must be an order of magnitude higher than the rate of Signal generation from autocatalysis to satisfy this requirement.

While the simplest method of transmitting molecules between two points in space is to allow them to passively diffuse from a region of higher concentration to one of lower concentration, the time for this process to occur over a distance of L scales with $O(L^2)$ according to Fick's 2^{nd} law. However, coupling a reaction to this diffusive process should accelerate the

rate of transport. Specifically, if a diffusing molecule, Signal, reacts with a patterned path of Carrier molecules to create copies of itself, then Signal will form a moving wave in which it diffuses and amplifies itself, causing formation of a stable traveling wave. These autocatalytic reactions change the scaling of the Laplacian at the leading edge of the wavefront, and can yield a linear rate of displacement with respect to time assuming a constant concentration of Carrier along the waveguide path. The existence of a stable asymptotic traveling wavefront and the exact relationship between reaction rate, diffusivity and wave velocity can be elucidated by adapting the Fisher-Kolomogorov-Petrovsky-Piskunov (FKPP) treatment[73–75] of a one-dimensional reaction-diffusion process for the autocatalytic network described above. To demonstrate this, we first examined the partial differential equation describing the rate of accumulation of Signal (abbreviated as Sg below) in space and time:

$$\frac{\partial Sg(x,t)}{\partial t} = D_{Sg}\frac{\partial^2 Sg(x,t)}{\partial x^2} + r\big(Sg(x,t)\big) \quad (10)$$

where D_{Sg} is the diffusion coefficient of Signal and r(Sg) in the net reaction rate of Signal. The initial conditions of the system are:

$$Sg(x,0) = 0 \text{ for all } x < x_1$$

$$Sg(x,0) = Sg_{max} \text{ for all } x > x_2 \geq x_1$$

The growth rate of Signal is assumed to be bounded:

$$r(Sg_{max}) = 0 \text{ and } r(0) = 0$$

Finally, several restrictions are placed on the growth rate of Signal. First, the reaction rate is assumed to be positive when $0 < Sg(x,t) < Sg_{max}$:

$$r(Sg) > 0$$

Second, the derivative of the reaction rate must satisfy the following inequalities:

$$r'(0) > 0$$

$$r'(Sg) < r'(0) \text{ when } 0 < Sg(x,t) \leq Sg_{max}$$

Far field conditions for the solution to the PDE are:

$$Sg(x,t) \xrightarrow[x \to -\infty]{} 0 \text{ and } Sg(x,t) \xrightarrow[x \to +\infty]{} Sg_{max}$$

We then looked for a solution to the PDE describing an asymptotic traveling wave: $Sg(x,t) = U(z)$, where $z = x + vt$ is a coordinate transformation into one dimension z. z reflects the new position of the wave after the passage of time t and rate of displacement v. The expression of the reaction-diffusion equation becomes:

$$\frac{v\partial U(z)}{\partial z} = D_{Sg}\frac{\partial^2 U(z)}{\partial z^2} + r\big(U(z)\big) (11)$$

This second order PDE can then be re-written as a system of first order differential equations. By letting $\frac{dU(z)}{dz} = M$, and substituting M back into equation 11, we get the following expression:

$$M = \frac{dU}{dz} \text{ and } vM = D_{Sg}\frac{dM}{dz} + r(U) \ (12 \ and \ 13)$$

Equation 13 can be approximated as a linear function of U by recalling that at the unreacted zone immediately preceding the wavefront, the far field condition $U(z) \xrightarrow[z \to -\infty]{} 0$ applies. We can therefore approximate the function $r(U)$ around $U = 0$ by performing a Taylor series expansion of $r(U)$ at this point and inserting the result into eqn. 13:

$$r(U) \approx r(0) + \frac{r'(0)U}{1!} = r'(0)U \ (14)$$

Equation 13 becomes: $\frac{dM}{dz} = \frac{vM - r'(0)U}{D_{Sg}}$ and the final form of the system of 1st order differential equations becomes:

$$\frac{dM}{dz} = \frac{vM - r'(0)U}{D_{Sg}} \text{ and } M = \frac{dU}{dz} (15 \ and \ 16)$$

This system can also be rewritten back in terms of $U(z)$ as a homogenous constant coefficient linear 2nd order differential equation:

$$D_{Sg}\frac{d^2U}{dz^2} - v\frac{dU}{dz} + r'(0)U = 0 (17)$$

The exponential solution to this ordinary differential equation will possess the roots of the characteristic equation as exponents. The characteristic equation is:

$$D_{Sg}g^2 - vg + r'(0) = 0 (18)$$

$$g = \frac{v \pm \sqrt{v^2 - 4D_{Sg}r'(0)}}{2D_{Sg}} (19)$$

The roots, g, must be real numbers so that the solution of $U(z)$ does not take negative values or exhibit oscillatory behavior. Therefore, the discriminant must be ≥ 0:

$$v^2 - 4D_{Sg}r'(0) \geq 0 \ (20)$$

By rearranging equation 20, we obtain a requirement for the of the minimum velocity required to from a stable asymptotic traveling wave.

$$v \geq 2\sqrt{D_{Sg}r'(0)} \text{ and } v_{min} = 2\sqrt{D_{Sg}r'(0)} \ (21 \ and \ 22)$$

It is important to note that the minimum rate of displacement does not depend on the initial conditions of the system. Additionally, $r'(0)$ can be determined for the for the autocatalytic circuit discussed previously in the absence of Sink:

$$r'(U(z)) = r'(Sg(x,t)) = \frac{\partial}{\partial Sg}[k_a C \times Sg] = k_a\left(C\frac{\partial Sg}{\partial Sg} + Sg\frac{\partial C}{\partial Sg}\right) (23)$$

$$r'(0) = k_a C_{max}$$

$$v \geq 2\sqrt{D_{Sg}k_a C_{max}} \text{ and } v_{min} = 2\sqrt{D_{Sg}k_a C_{max}} \ (24) \ and \ (25)$$

where the net reaction rate of Signal is differentiated with respect to Signal using the product rule and evaluated at [Signal] = 0; note that we assumed that at the leading edge of the wavefront where Signal approaches 0, Carrier takes its maximum concentration value, C_{max}. In the presence of Sink (Sk), $r'(0) = k_a C_{max} - k_a Sk_{max}$. This leads to the expressions:

$$v \geq 2\sqrt{D_A(k_a C_{max} - k_d S k_{max})} \text{ and } v_{min} = 2\sqrt{D_A(k_a C_{max} - k_d S k_{max})} \; (26) \; and \; 27)$$

A key result of the FKPP analysis of the Zhang amplifier is that the square of the effective change in displacement of the autocatalyst species in one-dimensional space over time is proportional to the square of the change in time $\delta L^2 \propto \delta t^2 * 4D_A r'(0)$, resulting in a power law dependence between $\delta L^2$and δt and a super-diffusive transport regime of Signal where the exponent of δt is greater than 1, whereas for diffusion in the absence of any reaction, $\delta L^2 \propto 2D_A \delta t$ which yields a linear relationship between the square of the displacement and time.

To verify that the idealized reaction-diffusion amplifier achieved super-diffusive transport of an autocatalyst species, we developed a reaction-diffusion model of an insulated waveguide. The model was implemented using Comsol Multiphysics and specifically, the Transport of Dilute Species physics node. The vertically positioned waveguide was 3000 μm long and 300 μm wide (**Figure 2.2a**). The insulation surrounding the edge of the waveguide was 50 μm wide. Additionally, we positioned a domain holding the initial stimulus of Signal to trigger the system at the top of the waveguide; this domain consisted of a 100 μm radius circle. The initial concentrations of reactants were selected from experimental ranges typically used in DNA strand displacement reactions[7,76].

Our first analysis modeled abstract reactions 1 and 2 and considered wave propagation when no Sink was patterned within the waveguide core. Again, it was our goal to determine if reactions 1 and 2 could form a stable traveling wave using reasonable estimates for strand displacement reaction rates and DNA diffusion coefficients. The rate constants for the modeled reactions were selected based on experimental values determined for bimolecular rate constants for toehold mediated strand displacement reactions at 25 C in standard buffer conditions (see Supporting Information: Materials and Methods). Strand displacement toeholds

typically range in length from 0 to 7 nucleotides. Above toeholds of 7 nucleotides in length, the magnitude of the biomolecular rate constant saturates. Therefore, in order to design an amplifier that reacted at the fastest rate possible, we designed these reactions to occur with rate constants at the upper end of this scale. Specifically, we chose k_a to be $2x10^5$ M^{-1} s^{-1}, the order of magnitude for a 6-nucleotide (nt) toehold strand displacement reaction; k_d was $3x10^6$ M^{-1} s^{-1}, which corresponded to the rate constant for a standard 7-nt toehold reaction[76]. To ensure that the Sink reaction could successfully perform its function of restricting amplification to the waveguide, we set the rate constant for its reaction with Signal to be an order of magnitude higher than rate constant for the Carrier and Signal reaction. Signal was assigned a diffusion coefficient of 60 μm^2 sec^{-1}, a typical value for the diffusivity of a 42-nt single stranded (ss) DNA oligonucleotide in poly(ethylene glycol) diacrylate (Mn = 575) hydrogels[77]. Sink and Carrier were immobilized within the waveguide. The concentration of Sink in the insulation was 500 nM. The initial concentration of Signal within the triggered domain was 90 nM. The initial concentration of Carrier in the waveguide was varied between 230 nM to 270 nM in each simulation.

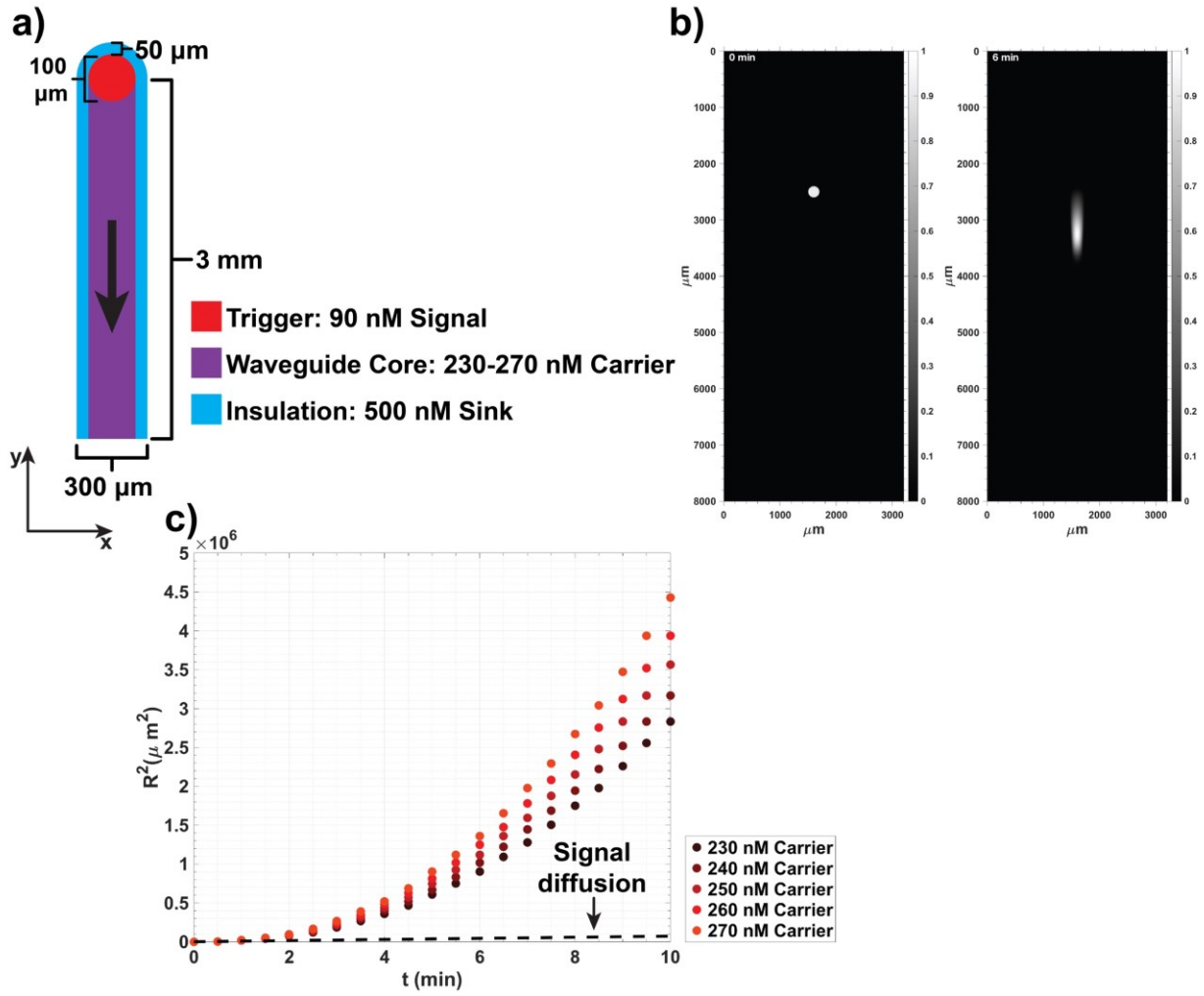

Figure 2.2. An idealized model of a reaction-diffusion waveguide. a) Geometry of the waveguide model and example initial concentrations used for the amplification reaction. b) Signal wave-front propagation down the wire over time. c) Square of the wavefront displacement vs. time across 5 different Carrier concentrations, dashed black line indicates the displacement of a 42 nucleotide-sized single stranded DNA molecule over time resulting from pure diffusion. Surface plots are non-dimensionalized by the maximum concentration of the stable traveling wave.

At the start of the simulation, Signal was allowed to diffuse in any direction; across all Carrier conditions tested, we observed the formation of a stable Signal wavefront that traveled down the waveguide as it consumed Carrier (**Figure 2.2b and c**). Additionally, the wave was constrained to the waveguide and did not spread outside of the insulation zone. We calculated the displacement of the wavefront in the center axis of the waveguide over time (**Figure 2.1b**) and observed that the square of the displacement, R^2, was proportional to t^{α}, with $\alpha > 1$, indicating

that the idealized system had achieved super-diffusive transport of Signal (see Supporting Information: Materials & Methods for calculation of wavefront displacement). The dashed black line in **Figure 2.2c** indicates the square of the displacement resulting from simple diffusion of a DNA oligonucleotide in one dimension.

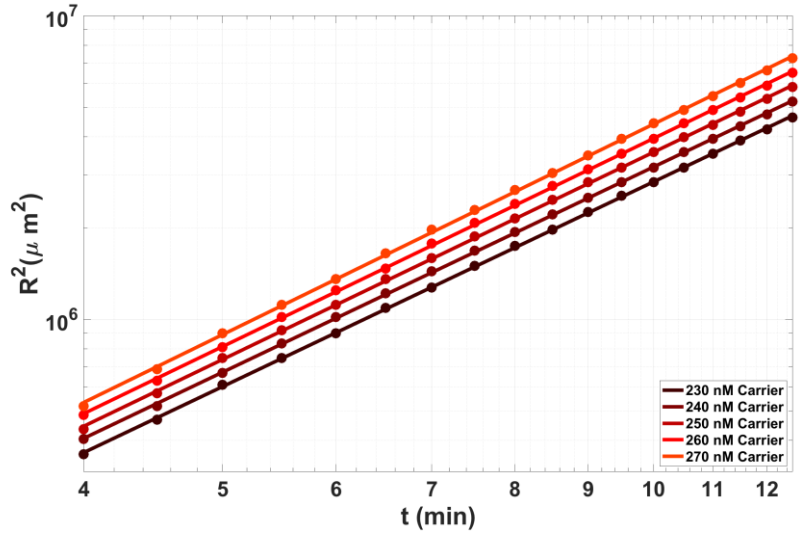

Figure 2.3. Logarithmic plot of wavefront displacement (R^2) vs. time of the idealized waveguide with no Sink present in the core path for varying Carrier concentrations. Dots indicate square displacement obtained from the spatial model. Lines are the linear least-squares fit of (R^2 vs. time. A linear relationship exists between log(R^2) and log(time), where the slope of each line is α.

While R^2 for the reaction network grows exponentially with time, R^2 in the case of simple diffusion grows linearly with time. Plots of R^2 vs. t on a logarithmic plot yielded straight lines across all Carrier concentrations (**Figure 2.3**), where the slope of the line was α. Across all Carrier concentrations, the average value of α calculated from the least-squares fit of R^2 vs. time in **Figure 2.3** was 1.89 ± 0.02 (95% confidence interval). The length of the spatial region of Signal grew over time, which was consistent with an increase in Signal concentration down the length of waveguide **(Figure 2.2b**). Additionally, we observed that at each individual timepoint, R^2 varied linearly with Carrier concentration, which was predicted by FKPP analysis eqn. 26.

Having established that the waveguide design could reliably propagate a spatiotemporal wave using known experimental ranges of parameters for DNA strand

displacement reactions and diffusion coefficients, we then tested whether it was possible to form a stable traveling wave with Sink patterned within the waveguide core in addition to being sequestered in the insulation. The simulation used all of the existing conditions described previously and included 35 nM of Sink sequestered within the waveguide core. The inclusion of Sink within the waveguide path provided two key functions. First, Sink can react with Signal at a faster rate than Carrier, serving as a threshold that can protect the waveguide from spurious activation by leak reactions that produce Signal.

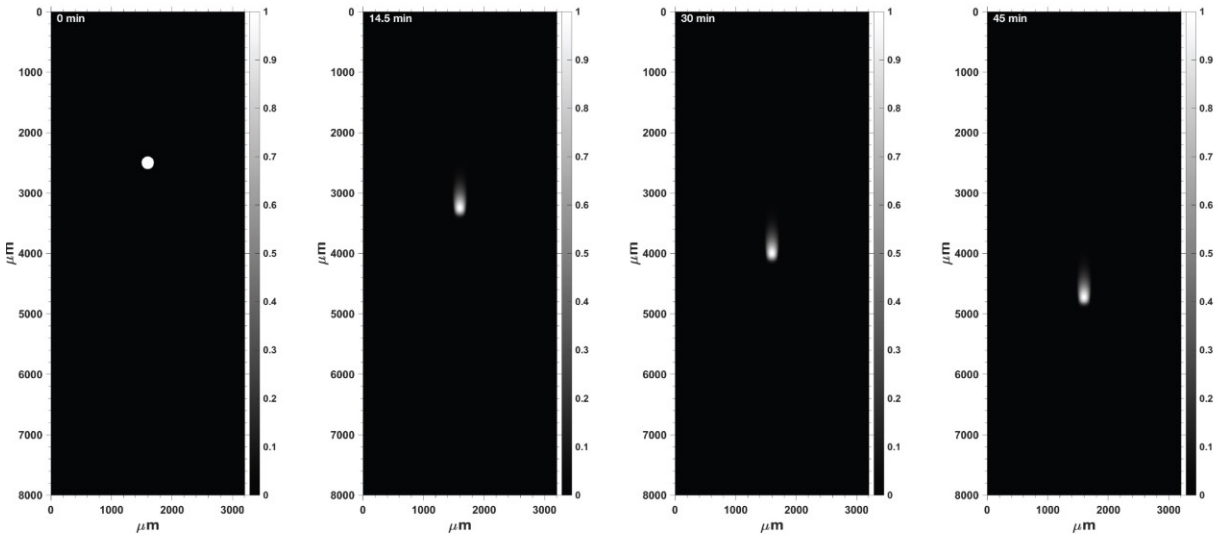

Figure 2.4. Wave propagation on reaction-diffusion waveguide with 35 nM Sink patterned in the wire core. Spatial propagation of the autocatalytic wavefront over time. Here, Signal trailing the wavefront is eventually degraded. Surface plots are non-dimensionalized by the maximum concentration of Signal within the stable traveling wavefront.

For spurious activation to occur within a specific point on the waveguide, the concentration of Signal produced via leak reactions in that location must consume the all of the local Sink present. Only after this threshold Sink concentration has been consumed can autocatalytic amplification occur. Second, the Sink residing within the waveguide removes Signal behind the wavefront, and thus resets the waveguide for future activation.

We observed formation of a stable traveling pulse, where the back edge of the zone of Signal was degraded into waste (**Figure 2.3**). We again observed a nonlinear dependence of R^2 with t (**Figure 2.5a**). Logarithmic plots of R^2 against t yielded a linear relationship across all Carrier concentrations (**Figure 2.5b**, diamonds & dashed lines). For comparison, the logarithmic R^2 vs. t plots from waveguide simulations without Sink in the waveguide core have been included (circles & solid lines). Interestingly, in the presence of 35 nM Sink, α, calculated by the line of best fit of R^2 vs. t, across all Carrier concentrations and plotted timepoints was 1.77 ± 0.04 (95% confidence interval), indicating that the dynamics of wavefront displacement were in between the thresholds of directed transport ($\alpha = 2$) and super-diffusive transport ($\alpha > 1$). Additionally, the presence of 35 nM Sink in the waveguide core resulted in lower R^2 values (a reduction by a factor of 10) at each timepoint compared to the values obtained from the simulation of wave propagation in the absence of Sink. The dashed black line in **Figure 2.5b** shows the expected R^2 value for a DNA molecule diffusing in one dimensional space and has a slope of 1.

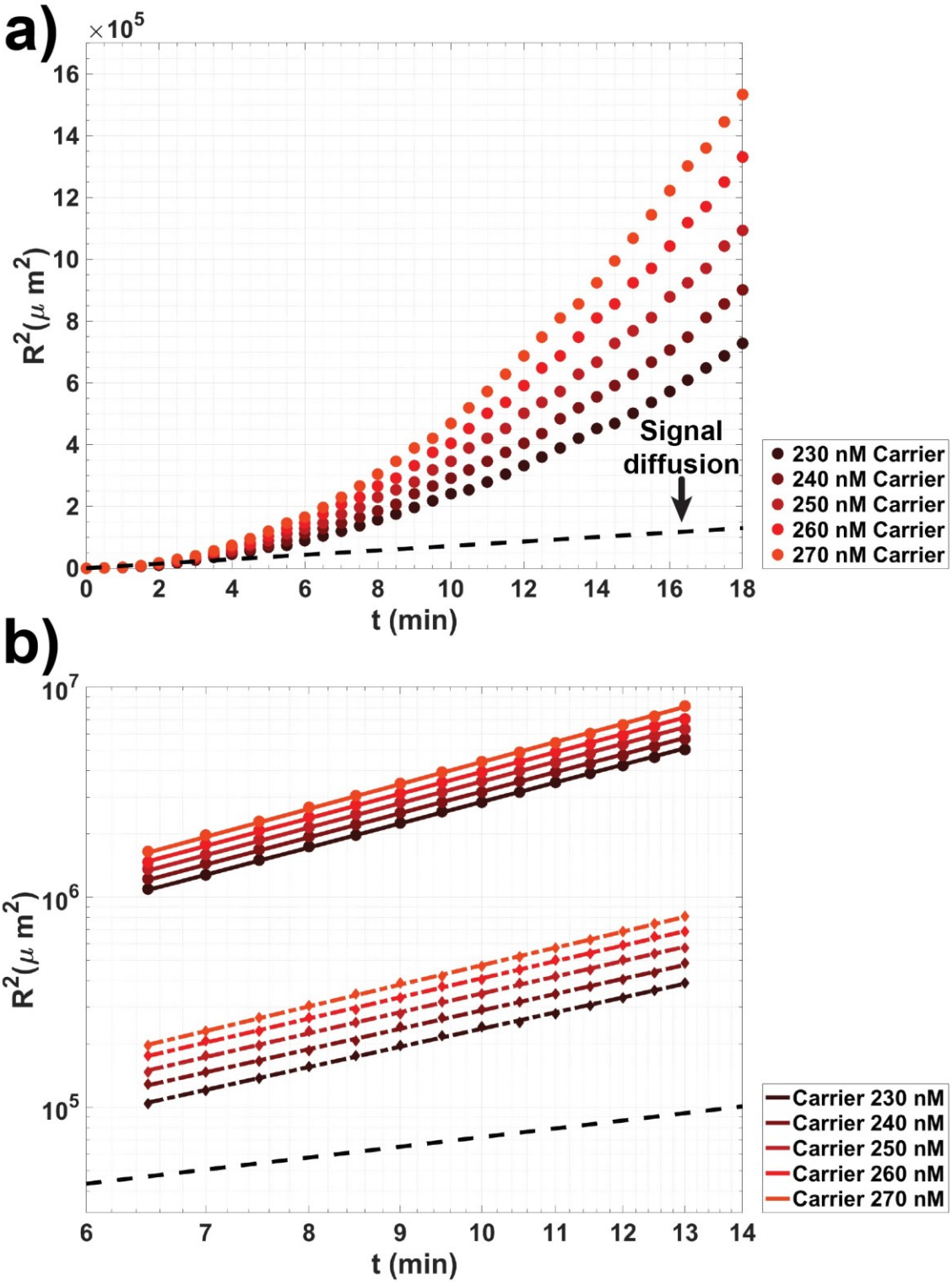

Figure 2.5. Idealized autocatalytic wavefront propagation in the presence of 35 nM Sink. a) Square of the wavefront displacement, R^2, vs. time. b) Comparison of R^2 is the without Sink (circles are results of PDE reaction-diffusion model & solid lines are the line of best fit for R^2 vs. time) and with 35 nM Sink (diamonds are the results of the PDE reaction-diffusion model & dashed lines are the line of best fit for R^2 vs. time) patterned in the waveguide core. Black dashed line in a) and b) indicates R^2 for pure diffusion 42 nucleotide sized DNA molecule over time.

A thresholding reaction mitigates spurious activation of strand displacement autocatalysis in well-mixed conditions.

In order to develop and implement the waveguide experimentally, we modified and characterized an autocatalytic DNA strand displacement amplifier previously designed by Zhang and colleagues[72]. Important differences exist between the abstract reactions previously described and the full autocatalytic circuit that we adapted for the system. First, the autocatalytic step comprising reaction 1 is in practice very difficult to implement using strand displacement processes alone and has yet to be designed as a single bimolecular reaction. Instead, reaction 1 is broken into a series of bimolecular strand displacement reactions involving the Carrier species (**Figure 2.6a**). Specifically, Signal, a single stranded autocatalytic (ss) DNA species first reacts with Carrier, a duplex, which contains another Signal strand and an Output strand hybridized to it. After binding of to the 5 nucleotide (nt) length toehold, Signal branch migrates to displace Output (reaction 7), forming Intermediate, a three-strand duplex with an exposed toehold (denoted 3') that Fuel can bind to. Reaction 7 is reversible because Output can also to rehybridize to this domain and initiate the reverse reaction.

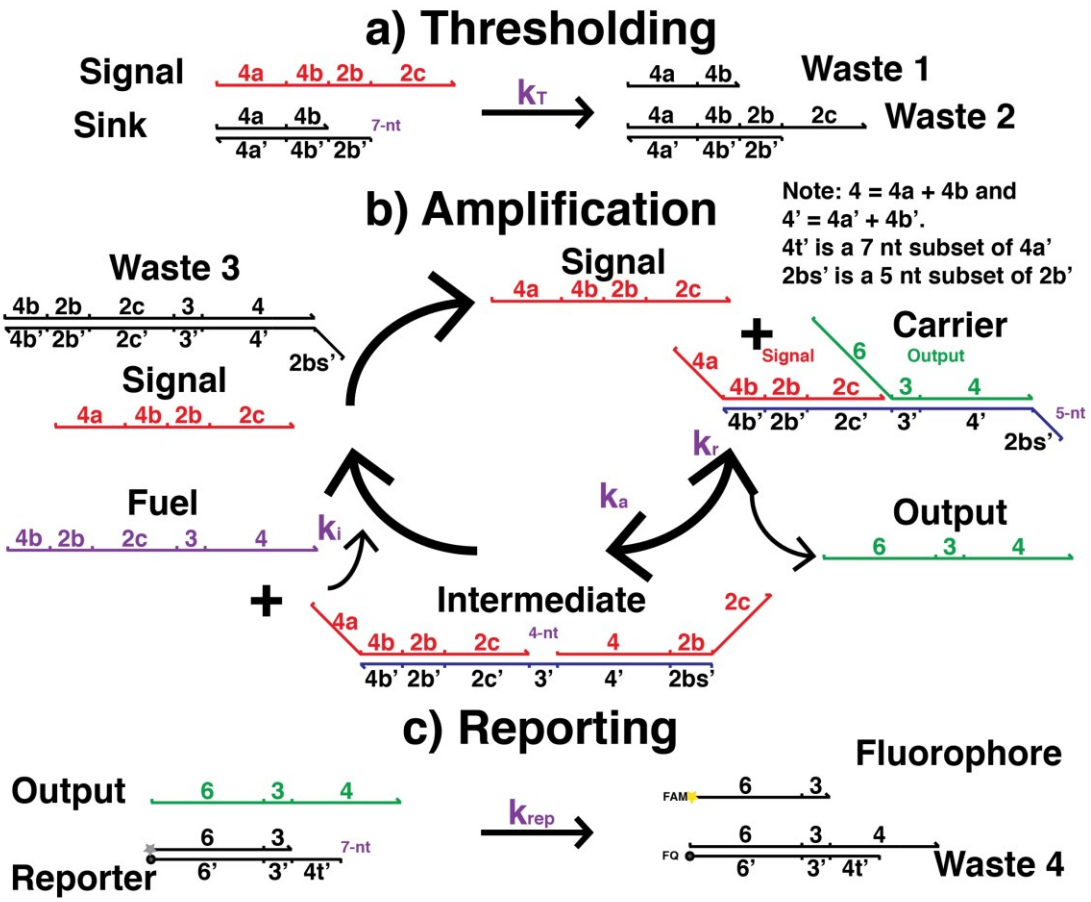

Figure 2.6. Autocatalytic amplification reactions with thresholding. a) Thresholding reaction module. b) Autocatalysis module. c) Fluorescence reporting reaction module for optical detection.

Importantly, a large reservoir of Fuel exists within the system, which drives the reaction in the forward direction and supplies the energetic driving force for the reaction, where Fuel transitions from a higher energy state as single stranded species to a lower free energy state in a DNA duplex. Fuel and Intermediate complex react through a 4- nt toehold (reaction 8) and release two Signal strand which can then react with more Carrier species. The molar Gibbs free energy change for completion of 1 cycle of amplification at 25 C and 12.5 mM Mg^{2+} (**Figure 2.6b**), as calculated by the nearest neighbor model of DNA hybridization and thermodynamics[78] is -0.67 kcal mol^{-1}(Supporting Information: Results & Discussion), a typical value for a DNA strand displacement reacting involving oligonucleotides of length 40 nucleotides and shorter. To

incorporate the insulating and thresholding functions that were key for waveguide function, we designed an irreversible thresholding reaction between a Sink duplex and Signal; Signal hybridized to Signal through a 7-nt toehold. Finally, the Output strand resulting from reaction 7 reacts with a Reporter duplex composed of a terminal fluorophore-quencher pair, the invading Output strand binds to the 7-bp toehold of Reporter and displaces its cover Fluorophore strand, enabling optical measurement of the circuit's reaction progress using quantitative PCR or fluorescence microscopy.

Fuel and Carrier can react spuriously to produce Signal, which leads to untriggered amplification; this presented a serious challenge for the use of the amplifier in a spatial system where reactants would be incubated with one another over potentially several hours within a waveguide. The bimolecular rate constant for the leak reaction has been previously measured as 23 M^{-1} s^{-1} and was attributed to a mechanism of base dehybridization at the Carrier duplex terminus and at the nick in the duplex between bound Output and Signal strands[72]. The end-fraying mechanism results in transiently exposing one or two duplex bases providing a nucleation site for an invading strand to hybridize and branch migrate to displace the incumbent oligonucleotide. The magnitude of the leak rate constant was ~ $O(10^{n-1})$ M^{-1} s^{-1}, where n = 2, is the number of nucleotides in the transiently exposed toehold. We developed a model of the full reaction network in well-mixed conditions to determine the timescale of spurious amplification over a range of concentration conditions. The model was composed of a system of partial differential equations and used measured values for the strand displacement rate constants[72,76] listed in **Figure 2.6** and for the Carrier-Fuel leak reaction (see Supporting Information: Materials & Methods). We observed that for 230-270 nM Carrier incubated with 500 nM Fuel, and 50 nM Sink, the circuit rapidly entered the growth phase of its sigmoidal activation curve after only 12

minutes. In the absence of any protection chemistry for the Carrier or Fuel species to prevent leakage upon mixing, such a short timescale of activation provided no feasible way for experimental construction of a hydrogel waveguide in a laboratory setting where experimental set up times range from tens of minutes to several hours.

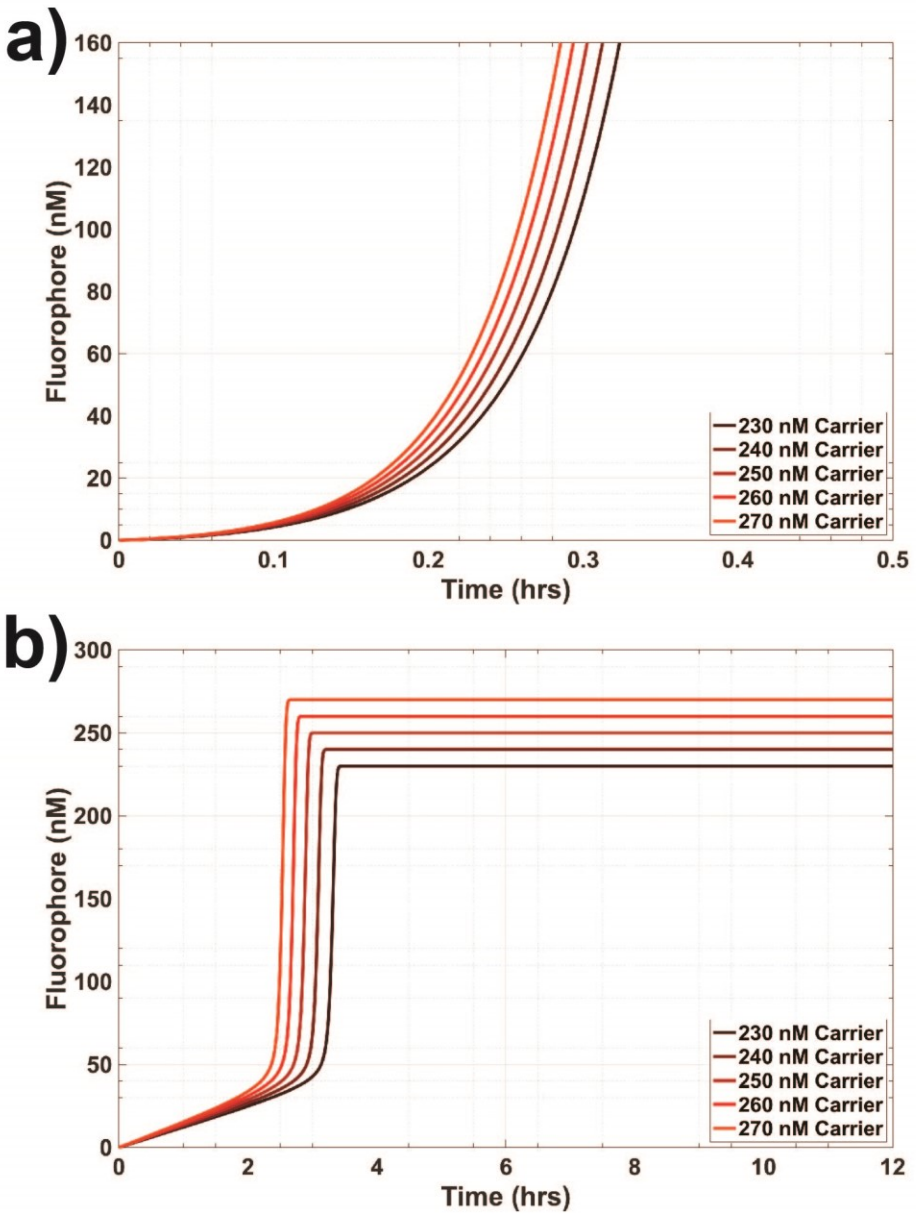

Figure 2.7. A Well-mixed reaction model of thresholded autocatalysis. a) Amplification resulting from a 6 nucleotide sized Carrier toehold. b) Amplification resulting from a 5 nucleotide sized Carrier toehold.

Several strategies could be employed to increase the lag phase of the circuit. Increasing the rate of the threshold reaction by increasing the Sink concentration delays amplification at the cost of creating a larger activation threshold concentration that must be overcome to trigger the circuit. Conversely, lowering the rate of amplification by either decreasing the concentrations of Carrier and Fuel or decreasing the rate constant for reaction 7 would also prolong the lag phase of the reaction. We chose to decrease the rate of amplification by decreasing the Carrier toehold, involved in reaction 7, from 6 nucleotides to 5 nucleotides in size, thereby decreasing the rate constant for the reaction by a factor of at least 10. With this modification, the model predicted the time to steady state (defined as the time at which the Fluorophore concentration first increased to within 5% of the average steady state concentration and stayed within that bound) of roughly 2.1-2.4 hours (**Figure 2.7**) which was a reasonable timescale for experimental implementation of the waveguide (see Supporting Information: Materials & Methods for the definition of reaction steady state concentration).

It is possible to trigger amplifier autocatalysis during its lag phase by supplying an external Signal perturbation.

In well-mixed experimental conditions, we tested whether it was possible to trigger the circuit by adding a stimulus of Signal while it was held in its lag phase by Sink. We attempted to experimentally measure and compare the timescales for the circuit to reach steady state for spurious activation where no initial Signal stimulus was added in the presence and absence of Sink. First we examined a range of Carrier concentrations (50 to 90 nM) that were mixed with 200 nM Fuel and 150 nM Reporter in the absence of Sink. The fluorescence intensity increase of each individual reaction was measured over time from the initiation of the reaction by the addition of fuel at 25 C in a Strategene quantitative PCR machine (see Supporting

Information: Materials & Methods). We calibrated and converted fluorescence intensity into Fluorophore concentration using separate calibration wells which were also measured during the experiment (see Supporting Information: Materials & Methods). Across all Carrier concentrations, we observed that the time to reach steady state was roughly under 40 minutes. The steady state times for each reaction condition are listed in **Table 2.1**. Additionally, the steady state timescale decreased linearly with increasing Carrier concentration. To calculate the reaction rate constants for the circuit, we fit a partial differential equation model of the amplification circuit to the data using nonlinear least squares regression for each Carrier concentration condition (Supporting Information: Materials & Methods). Discussion of the fitting analysis and fitted rate constants can be found in Supporting Information: Results & Discussion). The expected steady state Fluorophore concentration for each test condition was 50 nM, 60 nM, 70 nM, 80 nM, and 90 nM. Variation between the expected steady state, as predicted by the model, and the experimental data is visible in **Figure 2.8a**. The model also provided a reasonable estimation of the timescale to reach steady state as a function of Carrier concentration (**Figure 2.9a**) and was accurate to within 8 minutes. Across all conditions, the measured concentration of Fluorophore was slightly greater than the expected steady state concentration predicted by the complete reaction of Fuel and Carrier and we attribute this difference to cumulative effects of human experimental error from pipetting and measurement of DNA concentrations.

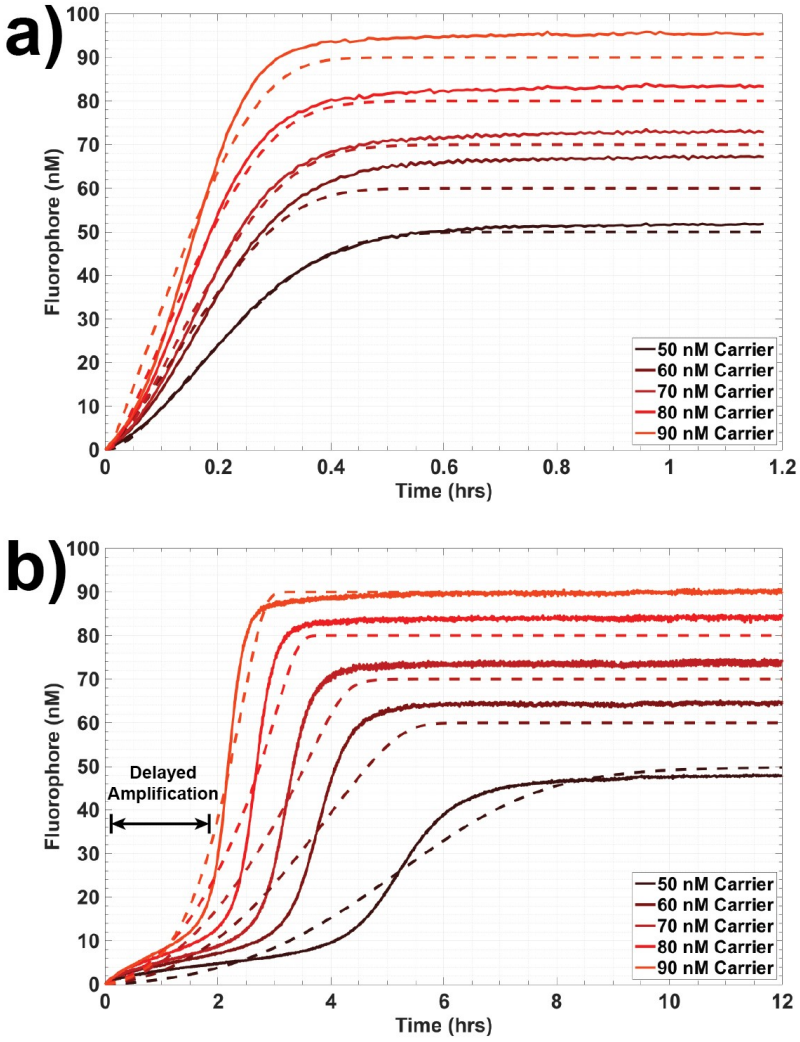

Figure 2.8. Well-mixed experimental fluorescence data of a) Autocatalysis without thresholding by Sink complex and b) autocatalysis in the presence of a thresholding reaction driven by a 50 nM Sink initial condition. Solid lines = experimentally measured concentration profiles, dashed lines = least-squares fit of reaction model model to experimental results.

Having determined the expected timescale of activation for the unthresholded amplifier, we then tested whether the addition of Sink would delay the onset of amplification and whether the circuit could be triggered while it was in a delayed phase. Importantly, the shape of the Fluorophore curve resulting from thresholded amplification should yield a sigmoidal shape, as was observed with the unthresholded amplifier, but with a longer period of pre-exponential growth (**Figure 2.8b**). Such behavior indicates that the circuit is eventually able to undergo

exponential growth as the concentration of Sink is depleted and the circuit transitions from its lag phase into exponential growth. Conversely, saturating the system with excess Sink such that $[Sink] \gg [Carrier]$ would prevent autocatalysis from occurring and the rate of Output production would only be coupled to the bimolecular reaction of Fuel and Carrier, which would not result in a sigmoidal growth curve. It was also our goal to identify a regime of delayed amplification experimentally. We repeated the experiments previously described under the same conditions but mixed 50 nM Sink into each reaction well at the start of the experiment. The timescale to reach steady state increased with the minimum time of 2.7 hours occurring at the highest Carrier concentration (**Table 2.1**). We again observed a roughly linear relationship between the steady state time and initial Carrier concentration in the presence of 50 nM Sink (**Figure 2.9b**). The increase in the steady state time between unthresholded and thresholded reactions are provided in third row of **Table 2.1**. On average, the addition of 50 nM Sink increased the steady state time by a factor of 10 ± 3 (95% confidence interval).

Table 2.1: Measured Steady State Times for unthresholded and thresholded amplification.

	50 nM Carrier	**60 nM Carrier**	**70 nM Carrier**	**80 nM Carrier**	**90 nM Carrier**
0 nM Sink	31 min	27 min	26 min	23 min	18 min
50 nM Sink	7.3 hrs	4.7 hrs	3.9 hrs	3.2 hrs	2.7 hrs
X-fold increase	14	11	9.1	8.4	8.4

We then sought to trigger the circuit during its lag phase by adding Signal to verify that amplification could occur and to identify the size of the Signal stimulus necessary to cause such a change. The experimental conditions were identical as those described previously. First, Sink, Fuel, and Reporter were each mixed together in 5 different reaction wells at a final concentration of 50 nM, 200 nM, and 200 nM respectively. Carrier was then added to each

reaction well at a final concentration ranging from 50 to 90 nM to initiate the reaction (**Figure 2.10a**). We observed a slow and gradual increase of Fluorophore concentration over 30 minutes. We then added and pipette mixed a 20 nM stimulus of Signal and observed a sharp increase in the Fluorophore concentration curve. Reactions across all Carrier concentrations reached to within roughly 7 nM of their theoretical steady Fluorophore concentrations determined by the complete reaction of Carrier and Fuel. The least-squares fit of the PDE model (**Figure 2.10a**, dashed lines provided) predicted formation of the steady state over the same timescale as the experimental data (see Supporting Information: Results& Discussion for analysis of fitted rate constants). To compare this result to the effect of further delaying autocatalysis by adding more Sink, which should provide additional energy to suppress autocatalysis, we conducted the same

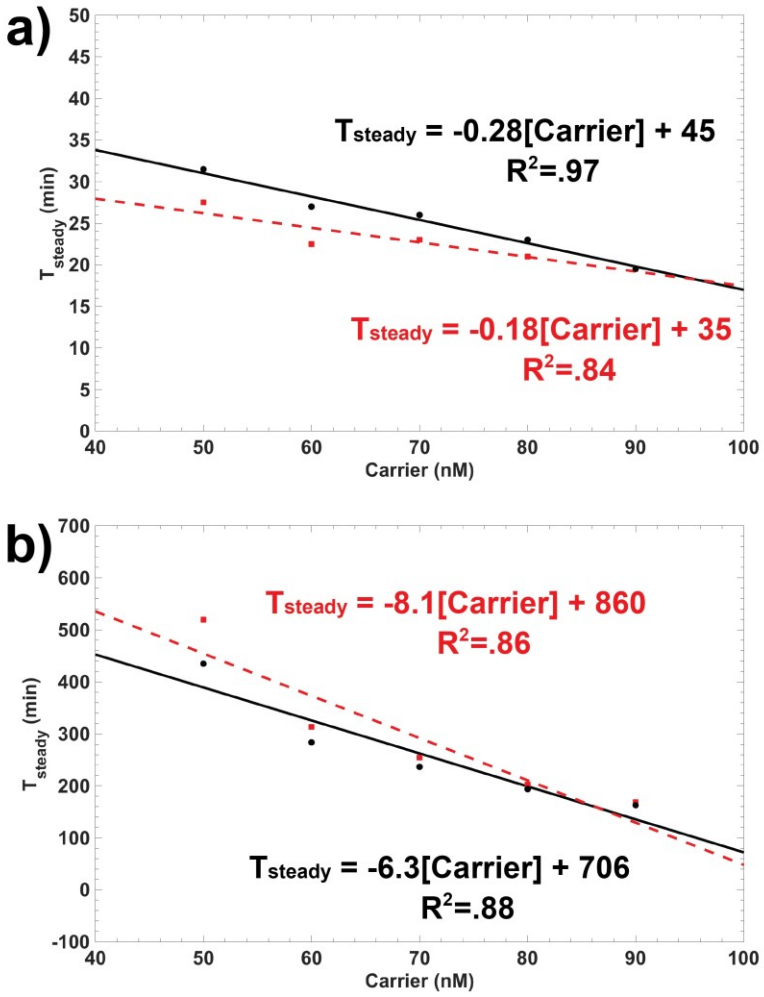

Figure 2.9. Steady state times for well-mixed autocatalysis: a) without thresholding and b) with 50 nM Sink. Black circles are experimental steady state times. Red squares indicate steady state times predicted by the well-mixed model resulting from nonlinear least squares curve fitting to experimental data. The solid black line is the linear least squares fit to the experimental steady state times (black circles). The red dashed line is the linear least squares fit resulting from model steady state times (red squares).

experiment and added 20 nM of Sink instead of 20 nM Signal 1 hour after initiating the reactions (**Figure 2.10b**). The addition of 20 nM of Sink increased the total concentration of Sink to 70 nM, which should saturate 50 nM and 60 nM Carrier concentrations and prevent amplification. The fluorescence curves for 60 nM-90 nM Carrier had a sigmoidal shape. At 50 nM Carrier, we observed the slowest increase in Fluorophore across all conditions and no visible inflection of the fluorescence curve, indicating an absence of exponential growth and inhibition of autocatalysis.

This condition did not reach steady state during the timescale of measurement suggesting that the circuit was saturated with Sink. At 60 nM Carrier, we observed a flattened sigmoidal curve, which could be the result of pipetting error, suggesting that either the concentration of Carrier in the well was higher than designed and/or that the concentration of Sink was lower than 70 nM, which enabled autocatalysis to occur. The least-squares fit of the PDE model underestimated the timescale of pre-exponential growth after the addition of 20 nM Sink, resulting in overestimation of the Fluorophore concentration before the inflection point of the experimental curves and underestimation of the concentration after the inflection point (see Supporting Information: Results& Discussion for analysis of fitted rate constants). Additionally, only Carrier concentrations of 80 and 90 nM reached their targeted steady state concentrations over the timescale of measurement and had steady state times of 6.1 hours and 5.5 hours respectively, which were both roughly a factor of 2 greater than the steady state times attained in the presence of an initial concentration of 50 nM Sink alone; thus indicating that for 80 nM and 90 nM Carrier, the addition of 70 nM final concentration of Sink mixed into to the circuit at different times before the onset of exponential growth, could extend the lag phase.

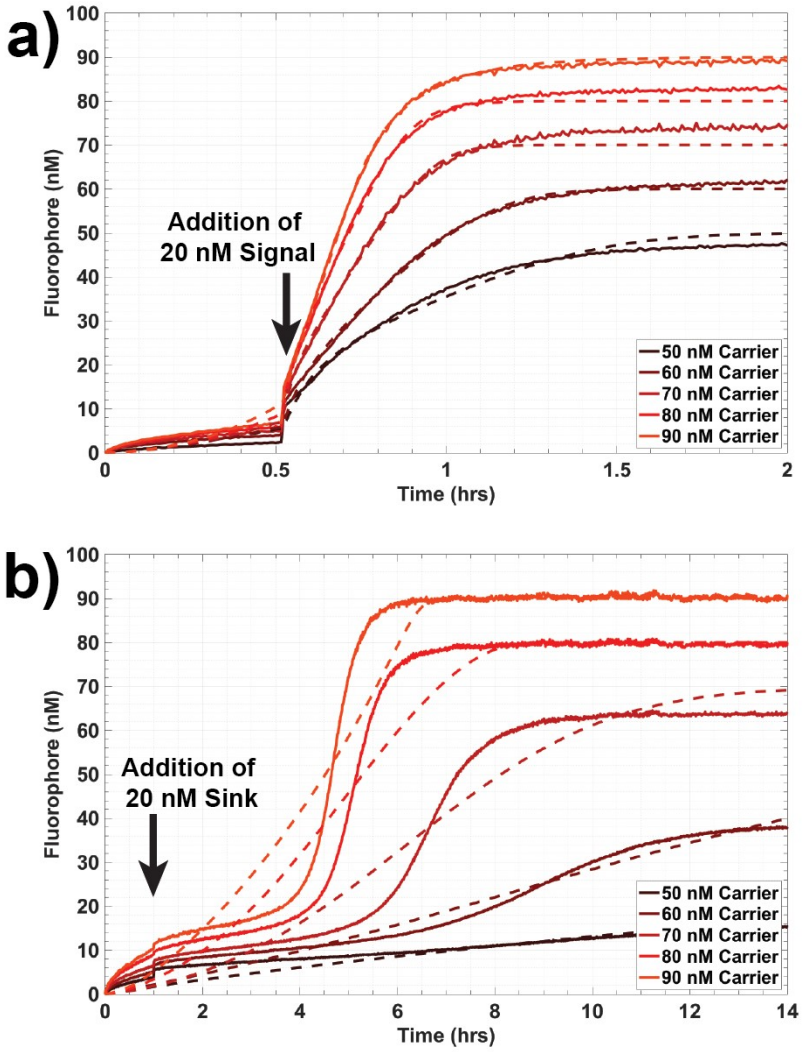

Figure 2.10. Perturbation of amplification during thresholding. Solid lines = experimental data, dashed lines = results of least-squares regression. a) Delayed triggering of autocatalysis via 20 nM addition of Signal 32 minutes after initiation of the experiment. b) Extended delay of autocatalysis by the addition of 20 nM Sink roughly 1 hr after initiation of the reaction.

The addition of clamping domains to Carrier species duplex ends fails to prevent leak reactions between Carrier and Fuel species.

After measuring the ranges of the rate constants of the designed and unintended leak reactions, we then modeled the full spatial reaction-diffusion waveguide excluding the reporting reaction shown in **Figure 2.6**. The model used the same initial conditions as those stated for previous spatial simulations where the Carrier concentration was 230 nM (**Figure 2.11**). In the absence of any Sink within the waveguide core, an initial wave of Signal is observed at 6

minutes. However, the spurious generation of Signal from the leak reaction between Fuel and Carrier within the body of the waveguide also emerges at this time point and quickly grows to turn the whole waveguide on before the wavefront has arrived (**Figure 2.11a**). When 35 nM of Sink is sequestered within the waveguide, a stable traveling wave of Signal is observed (**Figure 2.11b**). From this result, we proposed that patterning Sink within the waveguide would serve as an effective strategy for suppressing the autocatalytic leak reaction in single usage experiments. Moving beyond this analysis, we also asked whether there were molecular protection strategies that might further mitigate the risk of spurious triggering during waveguide construction (i.e. during photolithographic processes) by keeping Carrier in an inactive state until its required consumption during wave propagation.

We considered a variety of protection strategies that would make Carrier inactive to prevent the leak from occurring and identified a photo-deprotection method consisting of photocleavable 1-(2-nitrophenyl) ethyl linkers that can be incorporated into the phosphodiester backbone of synthetic oligonucleotides.

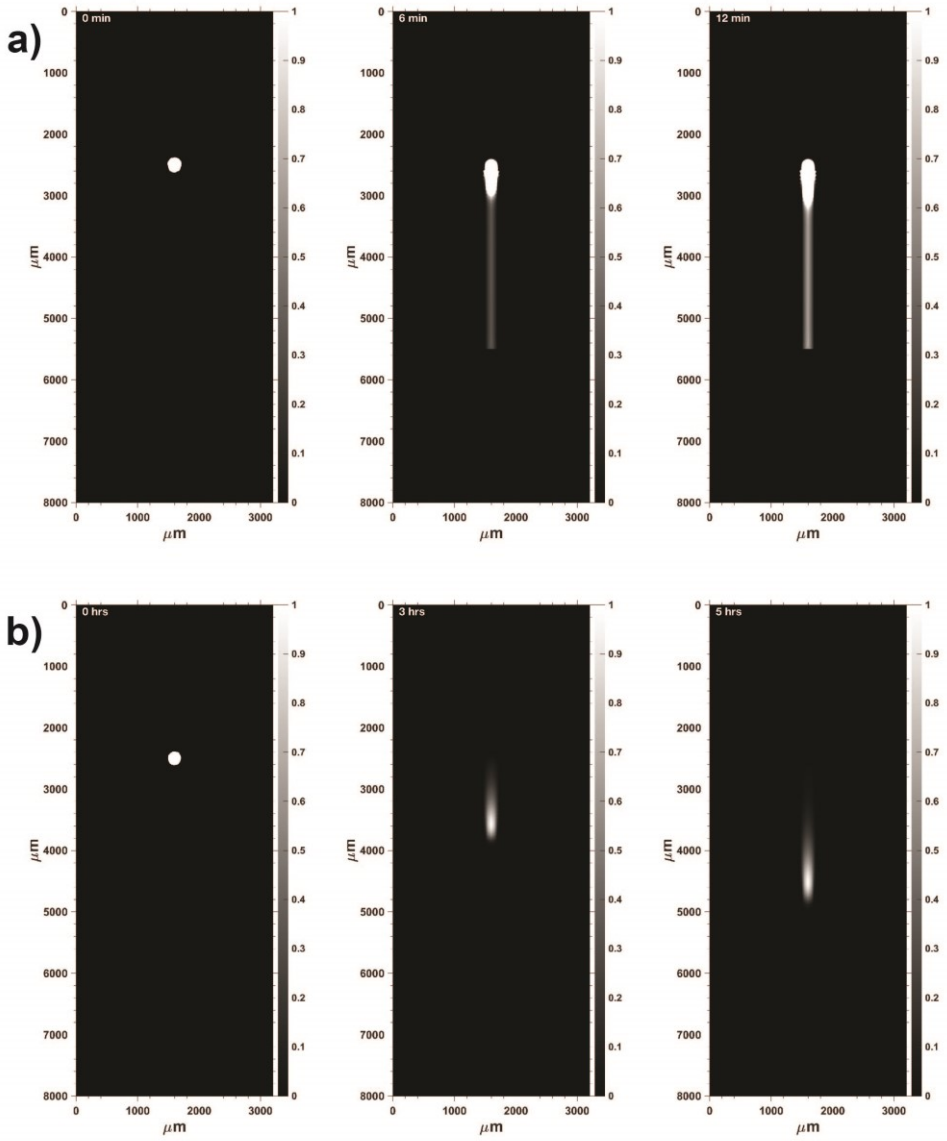

Figure 2.11. A model of spatiotemporal wavefront propagation with full non-idealized amplification, thresholding, and Fuel-Carrier leak reactions. a) Spurious waveguide activation during wave propagation without Sink due to Fuel-Carrier leakage. b) Stable wave propagation with 35 nM Sink patterned within the waveguide core. Surface plots are non-dimensionalized by the maximum Signal concentration on the stable traveling wavefront.

Photo-protection of DNA strand displacement reactions using nitro-benzyl chemistries has been implemented experimentally[79,80]. Additionally, light can be spatially modulated at the micron length scale using photolithographic techniques; we envisioned using UV light to photo-deprotect Carrier that was crosslinked to the waveguide as the wave of Signal traveled along the

length of the wire. This process would minimize the amount of time for active Carrier and Fuel to react before the arrival of the wavefront.

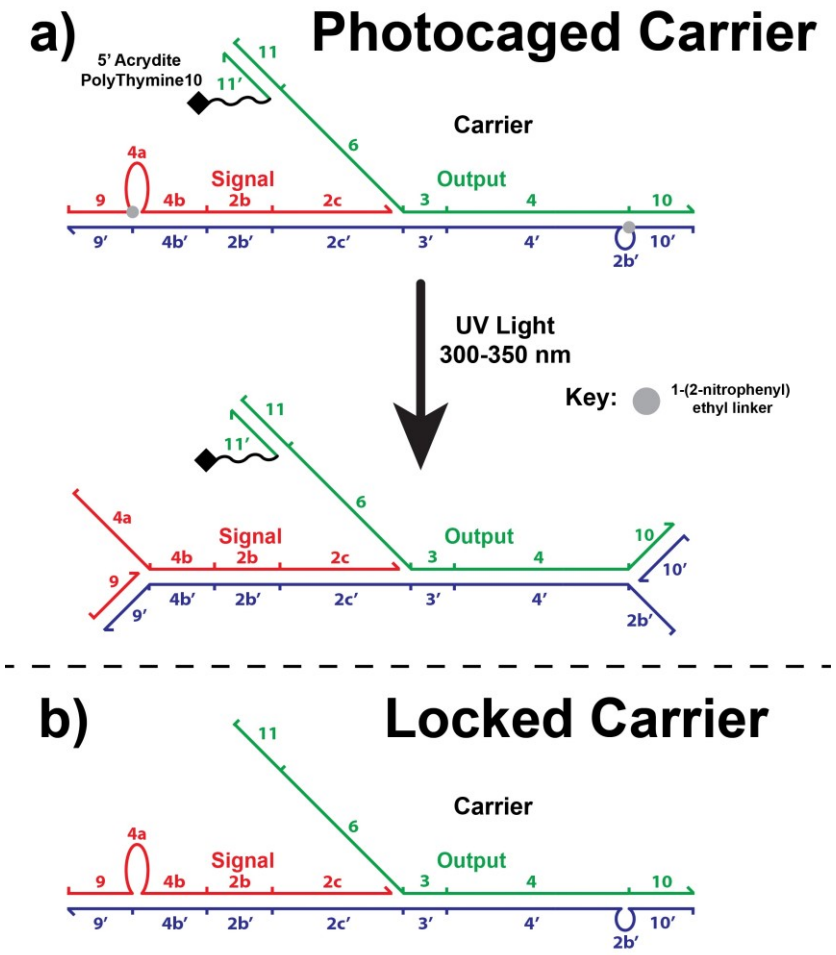

Figure 2.12. a) Carrier photoprotection strategy using nitrobenzyl modified clamp domains to prevent Fuel leakage with Carrier duplex ends. Photocleavage of 1-(2-nitrophenyl) ethyl linkers results in exposure of the 2b' toehold on Carrier and the activation of bound Signal. b) Locked Carrier substrate tested in well-mixed experiments for its ability to slow the Fuel-Carrier leak reaction.

As mentioned previously, initially we proposed that Fuel could react with Carrier to displace Output and Signal at three possible invasion points the duplex: the two duplex ends and the nick located between Output and Signal. As a first attempt to mitigate the leak, we chose to add 7-bp clamp domains to both ends of the duplex that had no complementarity to Fuel. To prevent Fuel from reacting with Carrier, we extended the length of Signal and Output to contain the reverse complement of the 7 nucleotide domains added to the bottom strand of Carrier (referred to as

$Carrier_B$). Importantly, the original unclamped sequence structure of Signal and Output, and $Carrier_B$ was retained. The toehold of $Carrier_B$ and 4a domain of Signal formed bulge loops (**Figure 2.12a**) in the duplex. The hypothesis of this design was that: 1) the presence of clamps would slow the rate at which Fuel could nucleate with frayed bases at the ends of $Carrier_B$ due to steric hindrance, and that 2) during partial displacement of Signal or Output by Fuel, the clamps would increase the rate of rehybridization and reverse branch migration of Signal and Output because these molecules possess a domain to reattach and/or remain attached to Carrier duplex, thereby forcing these oligos into a set of conformational configurations that lower the energy barrier for base nucleation with adjacent segments of Fuel-hybridized duplex. During the photo-deprotection process, Signal and Output would be attached to their clamp domains with 1-(2-nitrophenyl) ethyl linkers (**Figure 2.12b**). Exposure of Carrier to UV light would break these linkages and produce the functional form of Carrier where Signal and Output can be fully displaced from the complex during strand displacement. To verify that the protected form of Carrier, $Carrier_p$, reacted with Fuel at a slower rate or did not react at all, we first mixed 50 to 90 nM $Carrier_p$ with 200 nM Fuel and 150 nM Reporter in different reaction wells of a 96 well plate. We tracked the increase in Fluorophore concentration over time (**Figure 2.13**) and observed a slow and gradual increase in Fluorophore concentration, where the rate of increase over time appeared to be proportional to the initial Carrier concentration. Additionally, all kinetic traces maintained their concavity and no inflection points were visually observed over the timescale of measurement, suggesting that autocatalysis was inhibited and the rate of Fluorophore production was largely coupled to the bimolecular reaction of Fuel and $Carrier_p$. Based on these observations, we designed a PDE model of the reaction which assumed that autocatalysis was inhibited (i.e. Signal could not react with $Carrier_p$) and that Fuel was able to

react with $Carrier_P$ to produce Output (see Supporting Information: Materials & Methods for model equations). Nonlinear least-squares regression was performed to fit the model to the experimental data: k_{leak} and k_{rep} were the fitted parameters. The average values of k_{leak} and k_{rep} were 22 ± 1.9 M^{-1} s^{-1} and 3.3E6 ± 1.5E6 M^{-1} s^{-1}, which were within one order of magnitude of values obtained from previous fitting analyses of the leak and reporting reaction rates.

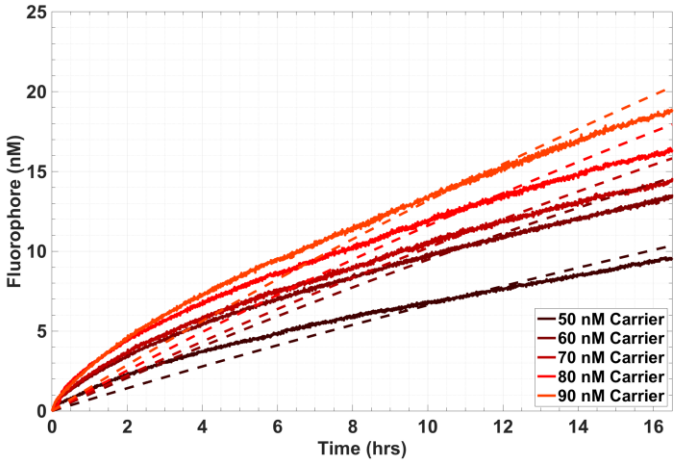

Figure 2.13. Fluorescence signal generated from incubation of 50-90 nM Locked Carrier with 200 nM Fuel.

More importantly, the persistence of the Carrier-Fuel leak reaction and the size of the fitted leak rate constant indicated that the protection strategy for the duplex ends was not effective in preventing the invasion of Fuel strand. This suggested that the dominant mechanism occurring during the leak reaction was Fuel hybridization to transiently exposed bases at the nick site within Carrier between Signal and Output. One possible way of occluding the nick to prevent the leak reaction is to introduce a non-canonical photocleavable attachment between the 5' end of the last Output nucleotide bound to $Carrier_B$ and the 3'carbon of the first Signal nucleotide hybridized to $Carrier_B$. The feasibility of incorporating this particular kind of photosensitive modification into a synthetic oligonucleotide has yet to be demonstrated using known photochemistries and synthesis methods.

2.3 Discussion

Overall, the results of computational analyses and experimental kinetics measured in well-mixed solution indicate that super-difusive propagation of chemical waves using DNA strand displacement amplification is feasible over length scales of hundreds of micron using concentration ranges of oligonucleotides typically used in strand displacement processes [27,81]. The use of thresholding reactions provides a way of mitigating deleterious Fuel-Carrier side reactions that might otherwise trigger spurious amplification. The integration of strand displacement waveguides into existing classes of DNA-based soft materials might enable chemical signal transmission within biomaterials and between separated devices over timescales orders of magnitude faster than what could be achieved with diffusion alone. Moreover, the ability to combine different sets of stimuli using wires will provide control over where and how chemical information is distributed within a biomaterial, enabling coordinated responses to complex sets of environmental cues[42,82,83].

To implement a full hydrogel waveguide system experimentally, further investigation of microfabrication methods and nucleic acid photo-chemistries that are DNA-compatible, and orthogonal to one another is required. Photolithographic techniques offer the capability of precisely designing patterned biomaterials at biologically relevant size scales within a controlled environment, a requirement for strand displacement reactions due to temperature and pH sensitivity. It is critical that the placement of oligonucleotides within a substrate, via photopolymerization for example, accommodates subsequent photo-directed release or activation of crosslinked species to enable spatiotemporal activation of waveguide architectures within a laboratory setting; this could take the form of light as a proxy for spatial biomolecular stimuli that might induce activation of a wire. Numerous challenges exist regarding the construction of

DNA-based materials capable of photo-directed release using lithographic technologies. We discuss these in more detail in Chapter 3.

2.4 Supporting Information

Materials and Methods:

DNA Sequences and Purification: All DNA sequences use in well-mixed experiments were purchased from Integrated DNA Technologies (Coralville, IA).

Table S 2.1. Waveguide Circuit DNA sequences.

Name	Sequence	Purification
Signal	CATTCAATAC CCTACG TCTCCA ACTAACTTACGG	Desalted
Output	ATCCACATACATCATATT CCCT CATTCAATAC CCTACG	Desalted
Carrier Bottom	GGAGA CGTAGG GTATTGAATG AGGG CCGTAAGTTAGT TGGAGA CGTAGG	Desalted
Sink Cover	CATTCAATAC CCTACG	Desalted
Sink Bottom	T TGGAGA CGTAGG GTATTGAATG	Desalted
Fuel	CCTACG TCTCCA ACTAACTTACGG CCCT CATTCAATAC CCTACG	Desalted
Reporter Bottom	TTGAATG AGGGAATATGATGTATGTGG/3IABKfQ/	HPLC
Reporter Cover	/56FAM/CCACATACATCATATT CCCT	HPLC
Clamped Output	CACATAACAA CCACATACATCATATT CCCT CATTCAATAC CCTACG CATACAA	Desalted
Clamped Signal	CACCATC CATTCAATAC CCTACG TCTCCA ACTAACTTACGG	Desalted
Clamped Carrier Bottom	TTGTATG GGAGA CGTAGG GTATTGAATG AGGG CCGTAAGTTAGT TGGAGA CGTAGG GATGGTG	Desalted

DNA complexes were annealed in 1X tris-acetate-EDTA buffer with 12.5 mM Mg^{2+}; the anneal protocol consisted of heating the solution up to 90 °C for 5 minutes and then cooling 1 °C every minute to 20 °C in an Eppendorf Mastercycler. Annealed complexes were then PAGE (polyacrylamide gel electrophoresis) gel purified to remove single stranded impurities; the conditions were 15% PAGE gels run at 150 V for 3 hours. For Carrier complex, two bands were

typically observed when visualized at 260 nm on; a dark top band was positioned ¼ of the total length of the gel, and a fainter thinner band was located at ½ of the gel length. The top band was cut from the gel and eluted in 1X TAE/Mg^{2+} buffer for 1 day. The elute was then centrifuged to remove small gel fragments from solution. For the Reporter and Sink complexes, one band was observed during PAGE gel visualization. These bands were cut from the gels, soaked in 1X TAE/Mg^{2+} buffer for 1 day to elute the DNA, and centrifuged to remove small polyacrylamide fragments from solution.

Well-Mixed Experiments: All well-mixed kinetic experiments were conducted using a Strategene MX3000 quantitative PCR machine at 25 C. We added reactants to 100 μL total volumes in individual wells of a 96-well plate. The concentrations of reactants listed in the main text are the final concentrations of the species in 100 μL total volume. Each reaction well contained 1X 1X TAE/Mg^{2+} buffer and 1 μM of PolyT20, a 20 nucleotide sized poly-thymine strand that acted as sacrificial DNA for adsorption to the polypropylene walls of the reaction wells. To initiate amplification reactions, reactants were added in the following order: Reporter, Carrier, Sink, a baseline fluorescence measurement was then made for 5 minutes. Finally, Fuel and Signal were added to trigger the reaction.

Modeling of Reaction-Diffusion Waveguides:

Spatial models of reaction-diffusion waveguides were implemented using finite element analysis software specifically Comsol Multiphysics – Transport of Dilute Species node. The waveguide geometry was meshed with a combination of free tetrahedral and mapped element types. For the idealized waveguide, the model was composed of the following partial-differential equations:

$$\frac{\partial[Signal](t,x)}{\partial t} = D_{ss}\nabla^2[Signal]](t,x) + k_a[Signal](t,x)[Carrier](t,x) - k_d[Signal](t,x)[Sink](t,x)$$

$$\frac{\partial[Carrier](t,x)}{\partial t} = -k_a[Signal](t,x)[Carrier](t,x)$$

$$\frac{\partial[Sink](t,x)}{\partial t} = -k_d[Signal](t,x)[Sink](t,x)$$

Only Signal was allowed to diffuse and it was assigned a diffusion coefficient of 60 $\mu m^2\ s^{-1}$, which was the average value measured for a 43 nucleotide sized single stranded oligonucleotide in a 30% (v/v) poly(ethylene-glycol) diacrylate hydrogel[84]. The diffusion coefficient for all other species was set to 0. For the full reaction-diffusion waveguide models, we constructed the system using the following PDEs:

$$\frac{\partial[Signal](t,x)}{\partial t} = D_{ss}\nabla^2[Signal]](t,x) + 2k_i[Fuel](t,x)[Intermediate](t,x) + k_r[Output](t,x)[Intermediate](t,x)$$
$$- [Signal](t,x)[Carrier](t,x) - k_T[Signal](t,x)[Sink](t,x)$$

$$\frac{\partial[Carrier](t,x)}{\partial t} = -k_a[Signal](t,x)[Carrier](t,x) + k_r[Output](t,x)[Intermediate](t,x) - k_{leak}[Fuel](t,x)[Carrier](t,x)$$

$$\frac{\partial[Sink](t,x)}{\partial t} = -k_T[Signal](t,x)[Sink](t,x)$$

$$\frac{\partial[Output](t,x)}{\partial t} = k_a[Signal](t,x)[Carrier](t,x) - k_r[Output](t,x)[Intermediate](t,x)$$

$$\frac{\partial[Reporter](t,x)}{\partial t} = -k_{rep}[Reporter](t,x)[Output](t,x)$$

$$\frac{\partial[Fuel](t,x)}{\partial t} = -k_{leak}[Fuel](t,x)[Carrier](t,x) - k_i[Fuel](t,x)[Intermediate](t,x)$$

$$\frac{\partial[Fluorophore](t,x)}{\partial t} = k_{rep}[Reporter](t,x)[Output](t,x)$$

Only the Signal species was allowed to diffuse, for all other species the diffusion coefficient was set to 0. Finally, the reaction-diffusion waveguide models incorporating proportional control equations for Carrier, Sink and Fuel incorporated the following additional reaction terms:

$$R_{pc} = k_{pc} - k_{dc}[Carrier]$$

$$R_{ps} = k_{ps} - k_{ds}[Sink]$$

$$R_{pf} = k_{pf} - k_{df}[Fuel]$$

Curve-fitting analysis of well-mixed data: Kinetic models of the amplifier were designed in MATLAB. All well mixed experimental fluorescence data was converted from raw fluorescence intensity into Fluorophore concentration by calibrating each experiment. Calibration as performed by adding a known amount of Output to a concentration Reporter within separate individual reaction wells during the experiment. **Figure S2.2** shows a typical calibration plot. This allowed us to calculate an average ratio, χ, between the average change in fluorescence intensity and the amount of output added:

$$\langle \chi \rangle = \langle \frac{[FCR]}{\Delta Counts} \rangle$$

$$[R_f(t)] = \langle \chi \rangle \Delta Counts(t)$$

We used $\langle \chi \rangle$ to convert all fluorescence counts into Fluorophore concentration. With this concentration time data, we performed nonlinear least-square regression using the *lsqcurvefit* Matlab function, which minimized the square of the y-error between each computed Fluorohpore time domain profile and the experimental profiles. The methods of integration used the Runge-Kutta method or the variable step variable order method which were implemented using Matlab's *ode45* and *ode15s* functions[85].

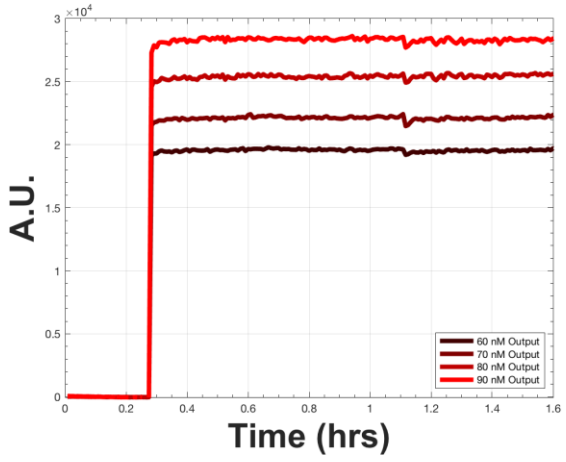

Figure S 2.1. An example calibration plot of 60 to 90 nM Output added separately to 4 reaction wells of 150 nM Reporter.

These models used the following PDEs describing the reaction rates of the system:

$$\frac{\partial[Signal](t,x)}{\partial t} = 2k_i[Fuel](t,x)[Intermediate](t,x) + k_r[Output](t,x)[Intermediate](t,x) - [Signal](t,x)[Carrier](t,x) - k_T[Signal](t,x)[Sink](t,x)$$

$$\frac{\partial[Carrier](t,x)}{\partial t} = -k_a[Signal](t,x)[Carrier](t,x) + k_r[Output](t,x)[Intermediate](t,x) - k_{leak}[Fuel](t,x)[Carrier](t,x)$$

$$\frac{\partial[Output](t,x)}{\partial t} = k_a[Signal](t,x)[Carrier](t,x) - k_r[Output](t,x)[Intermediate](t,x)$$

$$\frac{\partial[Reporter](t,x)}{\partial t} = -k_{rep}[Reporter](t,x)[Output](t,x)$$

$$\frac{\partial[Fuel](t,x)}{\partial t} = -k_{leak}[Fuel](t,x)[Carrier](t,x) - k_i[Fuel](t,x)[Intermediate](t,x)$$

$$\frac{\partial[Fluorophore](t,x)}{\partial t} = k_{rep}[Reporter](t,x)[Output](t,x)$$

The upper and lower bounds for the fitted rate constants were 4E6 M^{-1} s^{-1} and 0 M^{-1} s^{-1}, covering the range of rate constants for biomolecular strand displacement reactions in standard buffer conditions at 25 C up to a maximum toehold size of 7 nucleotides.

When performing least-squares regression on the amplification perturbation experiments (Section 2.4, **Figure 2.10**), our model first integrated the system of PDEs from the starting time to the time of perturbation. At this time point the model took the solution obtain from integration and updated the concentration Signal or Sink by adding 20 nM of either species to this existing concentration. Numerical integration was continued from the perturbation time to the end of the experiment. The curve fitting function called this model for each specific time point and chose the set of rate constants that minimized the square of the y-error between the model and data set. The steady state time for the reactions was defined as the time when the moving average of the Fluorophore concentration decreased below 8E-3 nM, where the window size for averaging was 3 consecutive timepoints.

Supplementary Results & Discussion:

Reaction-diffusion waveguide with proportional feedback control:

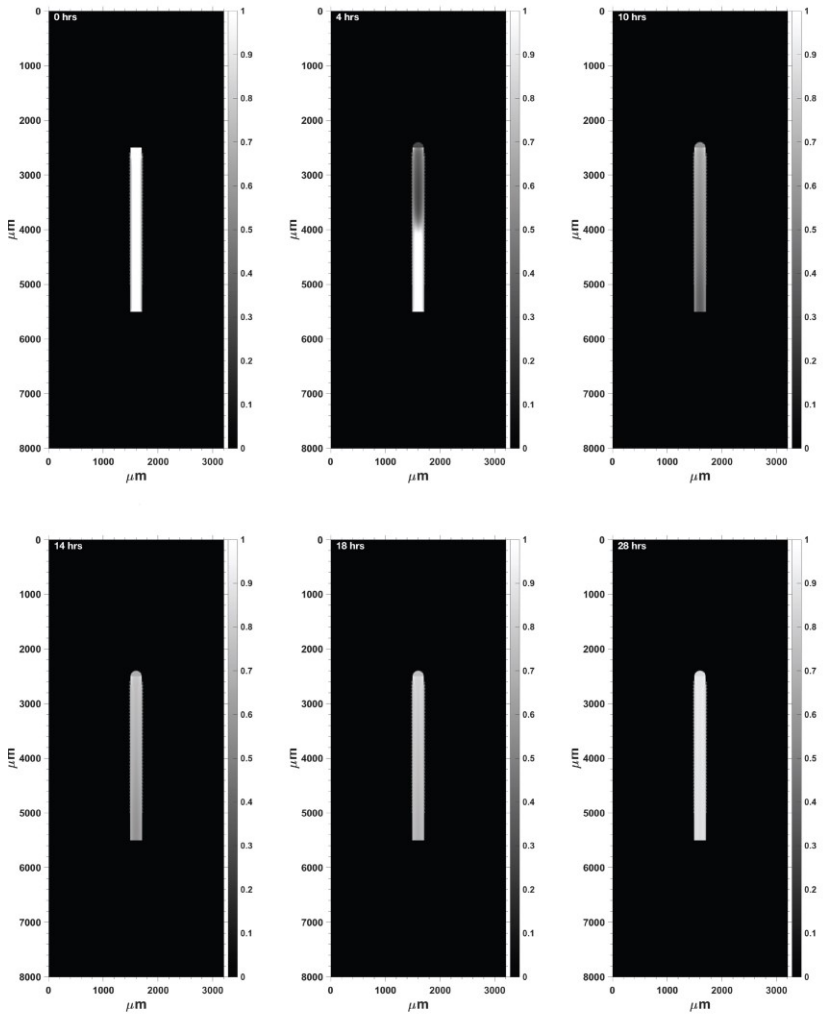

Figure S 2.2. Full reaction-diffusion waveguide circuit with negative feedback control to replenish key reactants Carrier, Fuel, and Sink. Here, Carrier is replenished over time to its steady state concentration after wave propagation.

Molar free energy change during strand displacement amplification:

The total Gibbs free energy change of the reaction can be expressed as the sum of the standard free energies of the species produced minus sum of the standard free energies of species consumed:

$$\Delta G_{rxn} = \sum_i x_i \, \Delta G^{\circ}_{product\ i} - \sum_i x_i \, \Delta G^{\circ}_{reactant\ i}$$

where ΔG_i° is the molar free energy of a particular DNA species and x_i is the number of moles produced or consumed during the reaction step. The total reaction for 1 cycle of amplification is:

$$Carrier + Fuel \xrightarrow{k} Signal + Output + Waste_3 \ (SI\ Rxn.\ 2.1)$$

The molar Gibbs free energy for each species at 25 C in standard buffer conditions can be calculated using the nearest-neighbor model for DNA structural motifs[78], which assumes that the stability of a given nucleotide depends on the composition of the base-pairs surrounding it. For DNA duplexes, each base-pair within the duplex is assigned a standard free energy based on the base pairing interaction (A-T/G-C), and the base-pairs directly adjacent to it to account for base stacking interactions. Additional factors for duplex stability accounted for by the model are the presence of terminal A-T and G-C pairings, the entropic penalty associated with nucleation of the first base-pair, and coordination of counter-ions with the backbone, which are all accounted for together with an initiation/terminal base-pairing term, and a symmetry term if the duplex is self-complementary. Together the standard free energy of each species can be expressed as:

$$\Delta G_i^\circ = \sum_j n_j \Delta G_j^\circ + \Delta G^\circ(init.term\ G-C) + \Delta G^\circ(init.term\ A-T) + \Delta G_{sym}^\circ$$

ΔG_j° is the standard free energy for the n_j possible base-pairs in the species. The values for these free energies have been computed and correlated across a variety of temperature and salt conditions[86–88]. Here, we use software tools, specifically NUPACK[89] to calculate the free energy of each species at the reaction conditions occurring in our experiments.

$$\Delta G_{Carrier}^\circ = -72.43\ kcal\ mol^{-1}$$

$$\Delta G_{Waste_3}^\circ = -73.10\ kcal\ mol^{-1}$$

$$\Delta G_{Signal}^\circ = -2.21\ kcal\ mol^{-1}$$

$$\Delta G_{Output}^\circ = 0.0\ kcal\ mol^{-1}$$

$$\Delta G^{\circ}_{Fuel} = -2.21\ kcal\ mol^{-1}$$

x_i = 1 for all species in SI reaction 1. Therefore, we expect $\Delta G_{rxn} = -0.67\ kcal\ mol^{-1}$. For comparison, the average molar thermal energy fluctuation from molecular collisions at 25 C is $kT * N_A = 0.59\ kcal\ mol^{-1}$, where k is the Boltzmann constant and N_A is Avogadro's number, illustrating how close the free energy change of the system is to the energy provided by random molecular collisions.

Measurement of Amplifier Rate Constants

We first measured reaction rate constants in well mixed conditions for the un-thresholded amplifier. The fitted parameters were the reaction rate constants k_a, k_r, k_{rep} and k_i shown in the main text reaction diagram Figure 2.6. The strand displacement mechanism for the reaction of Fuel and Intermediate and Signal and Intermediate occur through the same toehold and involve branch migration along specificity domains of roughly equal length and we assumed that the rate constants k_r and k_i are equivalent in our model. The average values for the fitted parameters are listed in **Table S2.2**. and the least-squares fit for each reaction is plotted as a dashed line in main text Figure 2.8a. We observed that the estimated magnitude of k_{rep}, k_r and k_i from the model fell within an order of magnitude of known experimental ranges for the corresponding toehold sizes within the circuit involved in those reactions. The expected magnitude of 7 nucleotide, 6 nucleotide, and 4 nucleotide toehold bimolecular rate constants are 3E6 M^{-1} s^{-1}, 5E5 M^{-1} s^{-1}, 5E3 M^{-1} s^{-1} respectively[76]. Interestingly, the magnitude of k_a was overestimated (which involved a 5 base-pair toehold ~ 10^4 M^{-1} s^{-1}) by a factor of 10. Additionally, the measured leak rate constant for the leak reaction between Fuel and Carrier was ~ 10^3 M^{-1} s^{-1}, roughly 2 orders of magnitude higher than the value previously reported by Zhang et al.[72]. Key differences exist between the purity of the strands used in their experiments and in

our experiments. Zhang et al. used HPLC purified DNA. All non-modified strands purchased from IDT in our experiments were ordered with standard desalting, which can yield a higher fraction of oligonucleotides with 5'end nucleotide deletion errors than what is found in HPLC purified DNA. 5' deletion errors could expose bases at the end of the 4b' domain of Carrier, effectively creating a permanent 1 or 2 nucleotide toehold for Fuel to hybridize to, in addition to the Carrier nick, and opposite duplex end which both offer possible invasion points for Fuel. Finally, subtle differences also existed between the duplex purification protocols used in both experiments. Zhang et al. purified DNA duplexes using 12% non-denaturing polyacrylamide gel electrophoresis gels using a power of 180V for 6 hours. Our protocol used 15% non-denaturing polyacrylamide gel electrophoresis gels run at 150V for 3 hours.

Similarly, the average rate constants fitted to the thresholded amplifier data yielded a similar trend to what was observed with the unthresholded system. Here, we fit k_a, k_r, k_{rep}, k_i, k_{leak}, and k_t. We observed that the magnitudes of k_r and k_i were in the expected range for a 4-nt toehold reaction. However, ka was an order of magnitude higher than its expected value. Additionally, k_t and k_{rep} were both one order of magnitude lower than the expected size corresponding to a 7 nucleotide toehold rate constant ~ 10^6 M^{-1} s^{-1}. Finally, the magnitude of k_{leak}, which was 26 M^{-1} $s^{-}1$, fell within the expected range for a 0-2 nucleotide toehold reaction ~ 10-100 M^{-1} s^{-1}. It is important to note that during purification of the Carrier complex, it was incredibly difficult to ensure consistency in the fraction of properly formed complex; different experiments used different batches of purified Carrier. Variation between these results across data sets may be attributed to differences in Carrier purity from batch to batch as was observed by Zhang et al.[72].

Table S 2.2: Un-thresholded and thresholded amplifier average fitted rate constants (95% confidence intervals)

	ka	kr	ki	kt	krep	kleak
0 nM Sink	1.9E5 ± 1.6E4 M^{-1} s^{-1}	8.9E3 ± 9.2E1 M^{-1} s^{-1}	8.9E3 ± 9.2E1 M^{-1} s^{-1}	N/A	2.4E6 M^{-1} s^{-1}	2.9E3 ± 4.6E2 M^{-1} s^{-1}
50 nM Sink	2.0E5 ± 4.8E3 M^{-1} s^{-1}	7.7E3 ± 1.8E3 M^{-1} s^{-1}	7.7E3 ± 1.8E3 M^{-1} s^{-1}	2.0E5 ± 5.7E4 M^{-1} s^{-1}	9.2E5 ± 1.9E6 M^{-1} s^{-1}	2.6E1 ± 1.3E1 M^{-1} s^{-1}

Table S 2.3: Average fitted rate constants for thresholded amplifier perturbation experiments (95% confidence intervals).

	ka	kr	ki	kt	krep	kleak
20 nM Signal Addition	2.1E6 ± 1.4E6 M^{-1} s^{-1}	5.0E3 ± 2.8E3 M^{-1} s^{-1}	5.0E3 ± 2.8E3 M^{-1} s^{-1}	3.7E4 ± 1.9E4 M^{-1} s^{-1}	5.1E5 ± 5.6E5 M^{-1} s^{-1}	1E2 ± 5.0E1 M^{-1} s^{-1}
20 nM Sink Addition	1.9E5 ± 7.0E3 M^{-1} s^{-1}	4.7E3 ± 4.2E3 M^{-1} s^{-1}	4.7E3 ± 4.2E3 M^{-1} s^{-1}	2.0E5 ± 1.2E5 M^{-1} s^{-1}	2.8E6 ± 2.1E6 M^{-1} s^{-1}	2.2E1 ± 7.3E0 M^{-1} s^{-1}

Fitted rate constants for the perturbation experiments are listed in **Table S2.3**. We again observed that the optimized magnitudes for the rate constants corresponded to toehold sizes that were within 1 nucleotide of with the actual sizes involved in the experimental system.

Chapter 3 Digital maskless photolithographic patterning of DNA-functionalized poly(ethylene -glycol) diacrylate hydrogels with visible light enabling photo-directed release of oligonucleotides

Summary

Soft biomaterials possessing structural hierarchy have growing applications in lab-on-chip devices, artificial tissues, and micromechanical and chemomechanical systems. The ability to integrate sets of biomolecules, specifically DNA, within hydrogel substrates at precise locations could offer the potential to form and modulate complex biochemical processes with DNA-based molecular switches in such materials, and provide a means of creating dynamic spatial patterns, thus enabling spatiotemporal control of a wide array of reaction-diffusion phenomena prevalent in biological systems. Here we develop a means of photopatterning two-dimensional DNA-functionalized poly(ethylene glycol) diacrylate (PEGDA) hydrogels architectures with an aim toward these applications. While PEGDA photopatterning methods are well-established for the fabrication of hydrogels, including those containing oligonucleotides, the photoinitiators typically used have significant crosstalk with many UV-photoswitchable chemistries including nitrobenzyl derivatives. We demonstrate the digital photopatterning of PEGDA-*co*-DNA hydrogels using a blue light-absorbing (470 nm peak) photoinitiator system and macromer comprised of camphorquinone, triethanolamine, and poly(ethylene glycol) diacrylate (Mn = 575) that minimizes absorption in the UV-A wavelength range commonly used to trigger photoswitchable chemistries. We demonstrate this method using digital maskless photolithography within microfluidic devices which allows for the reliable construction of multidomain structures. The method achieves feature resolutions as small as 25 μm and the resulting materials allow for lateral isotropic bulk diffusion of short single-stranded (ss) DNA

oligonucleotides. Finally, we show how the use of these photoinitiators allows for orthogonal control of photopolymerization and UV-photoscission of acrylate-modified DNA containing a 1-(2-nitrophenyl) ethyl spacer to selectively cleave DNA from regions of a PEGDA substrate.

3.1 Introduction

Biomaterials that combine multiple spatial-scales, heterogenous structural and compositional features, and chemical reaction networks could create systems with the ability to sense and respond to their environment with complex spatiotemporal dynamics. Towards this goal, synthetic biologists and DNA nanotechnologists have employed a variety of approaches for constructing and studying the behaviors of synthetic DNA-based reaction networks that mimic biological processes. These systems include microfluidic networks for examining the effects of boundary conditions on the propagation rates of chemical waves of DNA-based oscillators in Predator-Prey systems[37], electrochemical desorption processes within microfluidic devices to spatiotemporally activate such oscillators[90], and glass capillary tubes that DNA-based recapitulations of Wolpert's French Flag model of pattern development during embryogenesis are implemented within[40].

The incorporation of DNA within crosslinked polymer networks makes it possible to program the interplay of chemical reactions with a hydrogel's structure and mechanics. For example, DNA crosslinks can allow for reversible gel-sol processes modulated by temperature[91] or chemical stimuli in the form of pH, enzymes[92], or molecular markers sensed by aptamers[93]. Oligonucleotides can also trigger hydrogel shape change[42,81]. By incorporating orthogonal photolabile chemistries, [7-(diethylamino) coumarin-4-yl] methyl and p-dialkylaminonitrobiphenyl respectively, into the phosphodiester backbone of DNA, Fichte et al.

demonstrated the three-dimensional photoactivation of a DNA strand displacement fluorescence reporting reaction within a chemically crosslinked maleimide-modified hydrogel using two-photon uncaging.[80] This approach enabled the use of two different wavelengths of light to spatially stimulate regions of the hydrogel, initiating two orthogonal photosensitive strand displacement reactions with precision below 10 μm. Inspired by pattern sensing and processing algorithms, Chirieleison et al. integrated a photosensitive DNA strand displacement reaction, consisting of an incoherent feedforward loop, within a chemically crosslinked bis-acrylamide hydrogel to perform edge-detection of millimeter-sized patterns of UV-light exposed onto the surface of the substrate.[79] However, the development of systems that integrate both advanced material and chemical features remains challenging. Most studies of responsive, DNA-based soft materials have relied upon chemical polymerization or molding, which complicates the assembly of multidomain structures with different species sequestered in different substrate locations. Photolithographic processes typically require a clean room and/or specialized microscopy equipment. Approaches for rapid prototyping that avoid such technlogies[94–96] and can yield structured, DNA-embedded hydrogels could make it possible to more easily design DNA-based soft materials with sophisticated structural and functional capabilities.

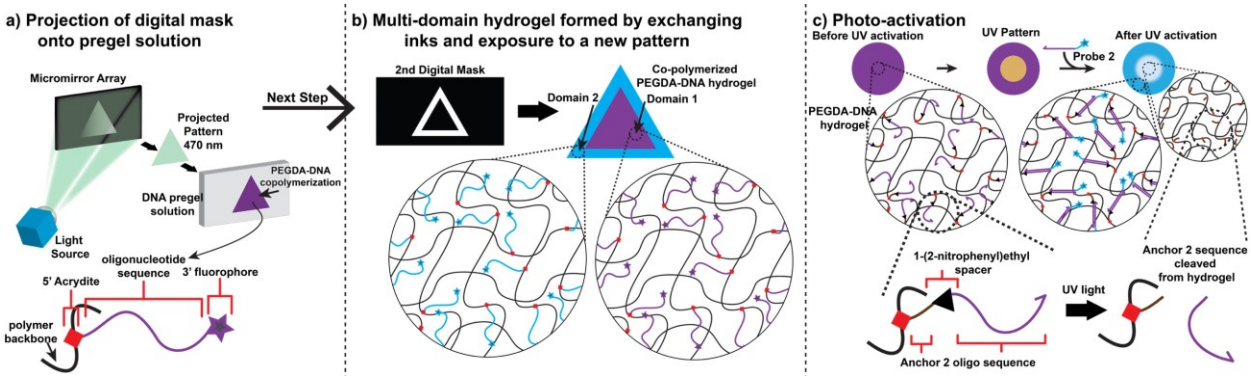

Figure 3.1. Schematic of two-dimensional, multi-step digital maskless photolithography and spatial photo-uncaging of DNA within two-dimensional architected hydrogels. a) Spatial patterns of arbitrary shape are printed into a PEGDA-DNA pre-gel solution containing a 470 nm absorbing CQ-TEA photoinitiator system using digital photomasks. b) Digital photopolymerization in a flow cell facilitates multi-step patterning where new prepolymer solutions are sequentially washed into the flow cell and

crosslinked in different, defined region without the need for registration. Here multiple domains each containing different types of acrydite-modified DNA oligonucleotides are patterned together to produce an architected structure. c) Photo-uncaging of a photosensitive 1-(2-nitrophenyl) ethyl linker using UV light results in cleavage of DNA within selected regions of the hydrogel. In the example depicted, UV light cleaves the binding domain (purple) of an oligonucleotide crosslinked to the hydrogel polymer, allowing the domain to diffuse out of the gel. The process can be visualized via the selective binding of a fluorophore-modified DNA probe containing the complement of the cleavable domain to the un-cleaved binding domains left in the gel.

Digital maskless photolithography has emerged as an economical method for printing soft materials without the need for specialized microscopy equipment or clean room facilities[97,98]. This approach has been used to produce structures that mimic the functions of organs[99] and undergo stimuli-induced shape change[100]. Structures with features on length scales of microns to millimeters can be patterned on time scales of seconds to minutes[101,102]. In digital maskless photolithography, patterns are generated by reflecting a beam of light off of an array of several hundred thousand to one million individually triggered mirrors onto the substrate of interest (**Figure 3.1a**). Unlike mask-based photolithography, this process does not require that a physical photo-mask be placed in contact with the patterned substrate.[103–105] The ability to photopattern a material without physically contacting it presents several key advantages: 1) structurally delicate materials can be assembled within an enclosed chamber without the need for repeated alignment and direct contact with a photomask and 2) when coupled with a microfluidic assembly platform, maskless photolithography provides an automated and highly parallel process for designing multi-domain hydrogels[106] with a spatial resolution of tens of microns. In this paper we sought to demonstrate how digital maskless photolithography could be used as a standard tool to construct hydrogel systems incorporating biomolecules, specifically, DNA.

Another key tool for manipulating DNA-based materials is the direction of where or when chemical cues are released into solution using UV light[107,108], which can enable spatiotemporal control of biochemical processes within biomaterials[109,110]. UV light can expose chemical groups through photo-uncaging[111] or conformational change[112] and direct the photocleavage of bonds between oligonucleotides and hydrogel networks. A standard toolkit for

independent control of photopolymerization, (i.e. the placement of biomolecules) and photo-deprotection of caged molecules after photopolymerization, would make it possible to build DNA-based soft materials that could execute sophisticated responses to stimuli and be simultaneously modulated spatiotemporally with light.

However, combining photopatterning methods with photocleavable chemistries presents a key obstacle: standard commercial photoinitiators used in soft materials patterning are also UV-absorbing, and this overlap interferes with UV-light directed material responses. Furthermore, photoinitiators generally have poor water solubility and typically remain sequestered within crosslinked polymer networks after photopolymerization has completed, with leaching timescales on the order of tens of hours to days.[113–115] Specifically, the persistence of widely utilized UV-wavelength excitable photoinitiators in photolithographic applications, such as Darocur and OmniRad diminishes the activity of large classes of UV photoswitchable chemistries with potential therapeutic applications.[80,116–121]

Camphorquinone (CQ), a commercially available visible-light photoinitiator commonly used in dental resins, enables the use of 470 nm light for photopolymerization[122–124] and also has minimal absorbance in the UV-A spectrum. Photopolymerization of hydrogels with CQ might therefore permit subsequent UV-triggered activation of UV-sensitive moieties in patterned hydrogels without spuriously activating the moiety during photopolymerization. When utilized as a class II photoinitiator, CQ acts as the excitation molecule for a free-radical generating species, commonly a tertiary amine. Additionally, CQ should not interfere with UV light-triggered reactions: initial tests in solution revealed that the presence of CQ does not significantly affect the photocleavage activity of a non-nucleosidic 1-(2-nitrophenyl)ethyl photolabile linker incorporated within DNA (Supporting Information **Figure S3.1a**). To make

use of photocleavage reactions, biomolecules attached to the polymer network need to be able to diffuse through the hydrogel after being cleaved, ideally isotropically, and at rates similar to those found in biological conditions[125]. Rates of diffusive transport of DNA oligonucleotides have not been characterized for camphorquinone-polymerized hydrogels. In this study, we develop a toolkit for digital maskless photopatterning of hydrogels that incorporate DNA and allow for DNA photocleavage in well-defined regions using UV light. We show how camphorquinone (CQ) and triethanolamine (TEA), a tertiary amine, can be used with digital photolithographic techniques to pattern PEGDA hydrogels into arbitrary shapes and multidomain structures where each domain contains specific DNA molecules conjugated to the hydrogel network with feature resolutions of 25 μm and higher (**Figure 3.1a and 3.1b**). We then show how digital maskless photolithography can be used to photopattern hydrogels that short DNA molecules can diffuse through by demonstrating how such molecules can form gradients within them. Finally, we demonstrate that the process we develop can be used to crosslink and then selectively photo-uncage DNA oligonucleotides containing acrylate and UV sensitive 1-(2-nitrophenyl) ethyl linker modifications (**Figure 3.1c**), overcoming the limitation of other methods for photopatterning similar materials.

3.2 Results

Digital photolithography enables fabrication of multidomain DNA functionalized poly(ethylene glycol) diacrylate hydrogels with a minimum feature size of 25 μm.

We first attempted to pattern PEGDA gels containing DNA using CQ and TEA in a pregel solution consisting of 75% (v/v) poly(ethylene glycol) diacrylate (PEGDA) / 0.8% (w/v) CQ / 0.5 % (v/v) triethanolamine (TEA) and 1 μM acrydite-modified DNA within a 100 μm-

thick microfluidic chamber (**Figure 3.2a**). Crosslinking reactions for the macromer and acrydite-modified DNA occurred via identical mechanisms (see Supporting Information **Figure S3.5/S3.6** for DNA and PEGDA crosslinking schematics). Photolithographic patterning was conducted using a Mightex Systems Polygon 400 Dense Pixel micromirror device mounted on a compound inverted microscope; 470 nm light was routed from a 50-Watt 470 nm light guide coupled LED to the micromirror array and was projected onto the sample stage through a 4X microscope objective (Supporting Information: Methods and Materials). We observed that a dosage of 57 mJ cm^{-2} resulted in fully exposed patterns with minimal amounts of webbed gel around the perimeter due to overexposure (**Figure 3.2b**). Dark spots observed in patterns were indicative of a lower amount of crosslinked DNA in those locations. The polymerization time to yield well-defined patterns from a digital mask with minimum features of 25 μm was 5 seconds.

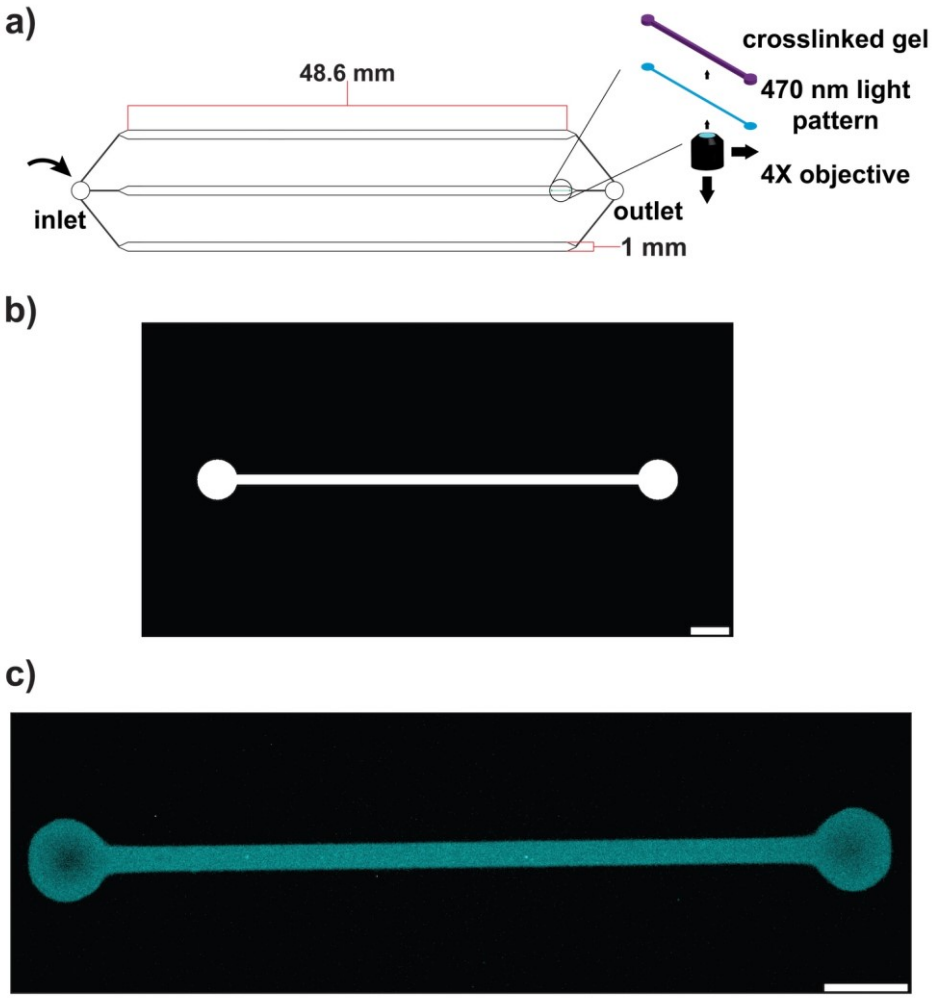

Figure 3.2. (a) Layout of the branched flow cell in which hydrogels were photopatterning. (b) AutoCAD digital mask (scale bar = 100 μm) (c) Fluorescence micrograph of a PEGDA hydrogel photopolymerized with 1 μM acrydite polyT20-FAM (scale bar = 100 μm) (See Supporting Information: Materials and Methods for sequences and protocol details).

We extended this method to photopattern multi-domain 75% (v/v) PEGDA-*co*-DNA hydrogels where each domain contained a different DNA species (**Figure 3.3).** DNA crosslinked in each domain of the resulting hydrogel contained a fluorescent label for visualization purposes. At each patterning step, one type of DNA-prepolymer solution was injected into the device, which was washed between blue light exposures to remove un-crosslinked polymer from the channels. Patterns for the domains in the hydrogels were formed from AutoCAD designs (**Figure 3.3a**) and rastered onto the digital micromirror array. We observed reliable patterning and were able to

visually resolve the different domains of the gels using visible light microscopy for a variety of shapes (**Figure 3.3b**).

To ensure that the patterned hydrogels might be isolated as structurally intact freely mobile structures, we determined whether the gels possessed some degree of elasticity and did not fragment upon deformation. Specifically, we characterized their response to roughly 50 PSI of pressure-driven flow that pushed them into a polydimethylsiloxane (PDMS) wall. Under this force, 75% (v/v) multidomain hydrogels were sheared from the surface of the flow cell which they were adhered to. During application of flow, free-floating structures were deformed as they were pushed into the PDMS walls of the microchannels. Patterned structures were elastic enough to quickly relax to their original shape after flow ceased (**Figure 3.3c**).

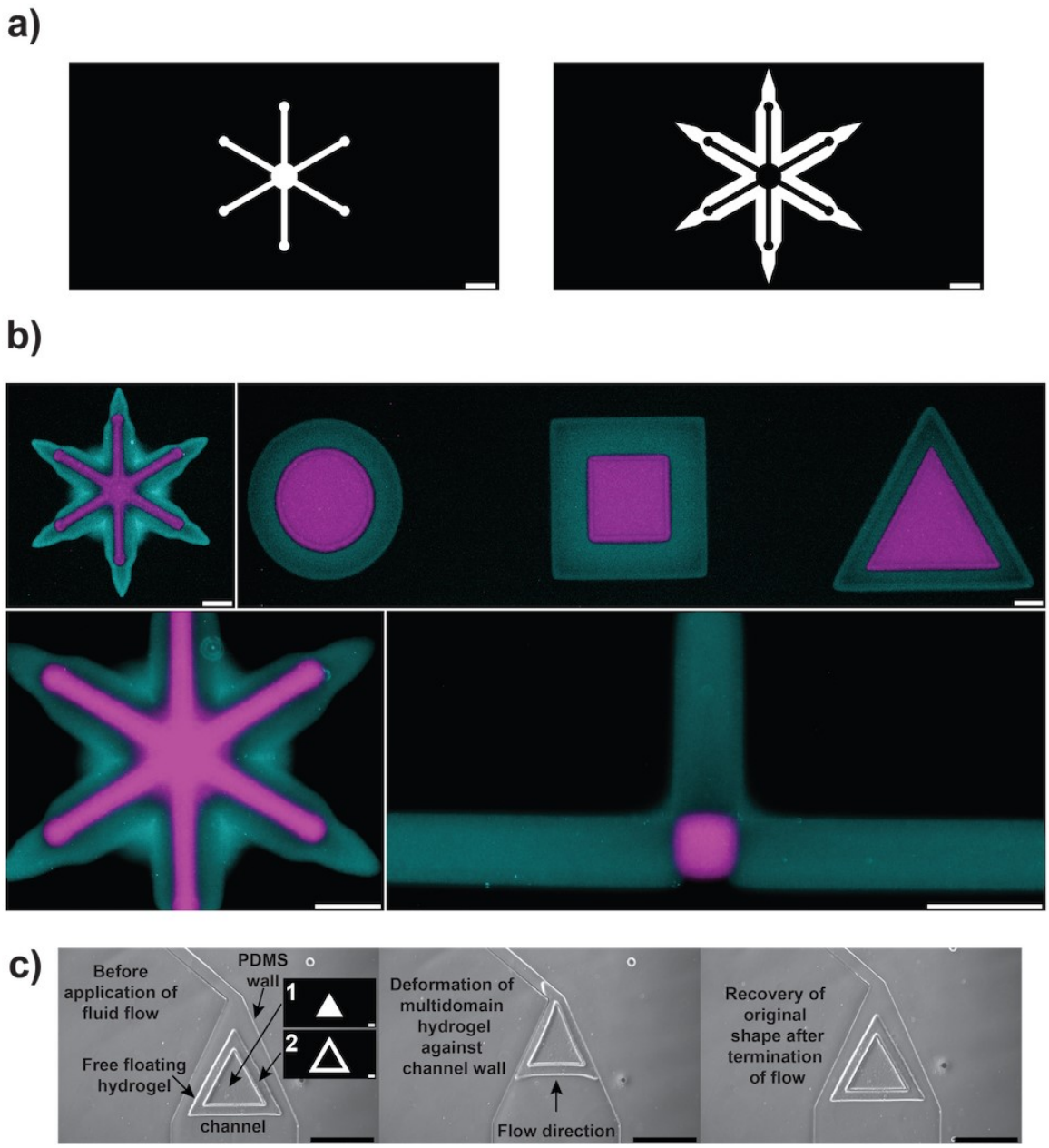

Figure 3.3. (a) Examples of digital masks for the different domains of a multidomain hydrogel structure (scale bars = 100 μm). (b) Fluorescence images of multi-domain PEGDA-co-DNA hydrogels in which the different domains were polymerized with either 1 μM acrydite polyT20-FAM (cyan) or 1 μM acrydite polyT20-Texas-615 (magenta) (see Supporting Information: Materials and Methods). (scale bar = 100 μm). (c) Bright field images of flow-induced deformation and shape recovery of a multidomain PEGDA-co-DNA structure; polymerized with 1 μM acrydite polyT20-Texas-615 in domain 1 or 1 μM acrydite polyT20-FAM in domain 2. Digital masks indicate the two domains of the hydrogel (black scale bars = 500 μm, white scale bars on masks = 100 μm).

42 nucleotide and 31 nucleotide-sized single stranded DNA species are able to diffuse through 30% (v/v) poly(ethylene glycol) and 75% (v/v) diacrylate hydrogels respectively.

Next, we developed a protocol for fabricating PEGDA hydrogels using CQ and TEA that single-stranded (ss) DNA could diffuse through isotropically at rates comparable (within an order of magnitude or so) to diffusion rates in cytoplasmic conditions and in aqueous solutions[125]. To show uniform diffusion of DNA molecules at the desired rate, we measured the dynamics of formation of stable diffusive gradients within hydrogels. In order to set up linear diffusive gradients while mitigating the presence of convection, we used a microfluidic gradient generator modified from previous designs by Ibo et al. and Paliwal et al.[126,127], and a pressure-driven flow controller[128] (**Figure 3.4a**). In our system, a series of rectangular diffusion cells spanned a length of 1500 μm between two liquid delivery channels (Supporting Information: Materials and Methods); 30 % (v/v) PEDGA hydrogels containing 0.8% (w/v) CQ and .5% (v/v) TEA were polymerized in the diffusion cells (Dosage = 228 mJ cm^{-2}). To ensure that the hydrogels were anchored to the walls of the diffusion cells, all surfaces within the microfluidic device were functionalized with methacrylate groups before PEGDA photopolymerization, which allowed the hydrogel to be chemically crosslinked to the device walls (Supporting Information: Materials and Methods).

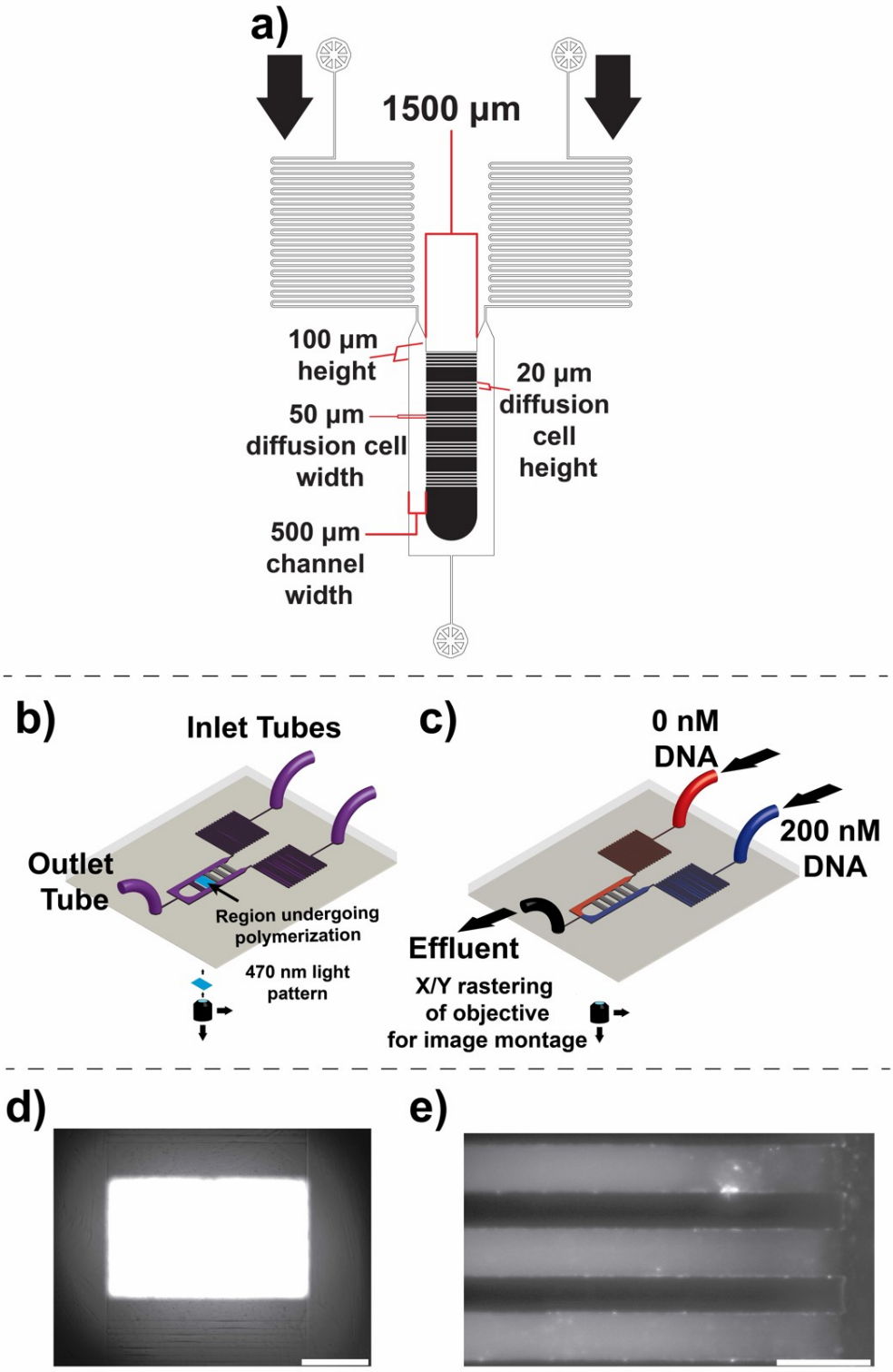

Figure 3.4. (a) Geometry of the microfluidic gradient generator, arrows indicate the direction of flow through the device. (b) Region where the hydrogel is polymerized within the device and (c) application of boundary conditions to create a linear gradient of DNA via diffusion. (d) Exposure of the microchannel array with a fully triggered mirror set (scale bar = 500 µm) and (e) visualization of anchored PEGDA hydrogels in diffusion cells with fluorescence microscopy (PEGDA co-polymerized with 500 nM 5'acrydite polyT20-Texas-615, scale bar = 100 µm).

Diffusion of Probe 1, a 5' Cyanine 3 dye-modified DNA strand (See Supporting Information: Materials and Methods for oligonucleotide sequence) with a size of 42 nucleotides, a typical oligonucleotide size utilized in common DNA strand displacement reactions, was visualized with time-lapse fluorescence microscopy. Within the gradient generator, DNA solutions flowing past either end of the patterned hydrogel formed a constant concentration boundary condition (**Figure 3.3c**). Over time, as the system reached steady state, a linear gradient of Probe 1 formed within the hydrogels (see Supporting Information for details regarding the calculation of diffusion coefficients). Linear gradients formed in the channels by roughly 4 hours and remained stable during the time course of the experiment, about 38 hours (**Figure 3.5b**), across all channels in the array, indicating the reproducibility of gradient formation within the patterned hydrogels, and thus the ability to reliably control the diffusion coefficient of DNA species in the structures. We used least-squares fitting of fluorescent count data to the solution of the 1-D diffusion equation for our boundary conditions to calculate a diffusion coefficient of Probe 1 of 60 ± 28 μm^2 sec^{-1} (mean ± s.d.). This value was similar to the coefficient measured for 23-base ssDNA in 1% (v/v) agarose hydrogels[39] and of those of short oligonucleotide fragments in cytoplasmic conditions and aqueous solution[125], suggesting that the DNA could migrate readily through the patterned gel.

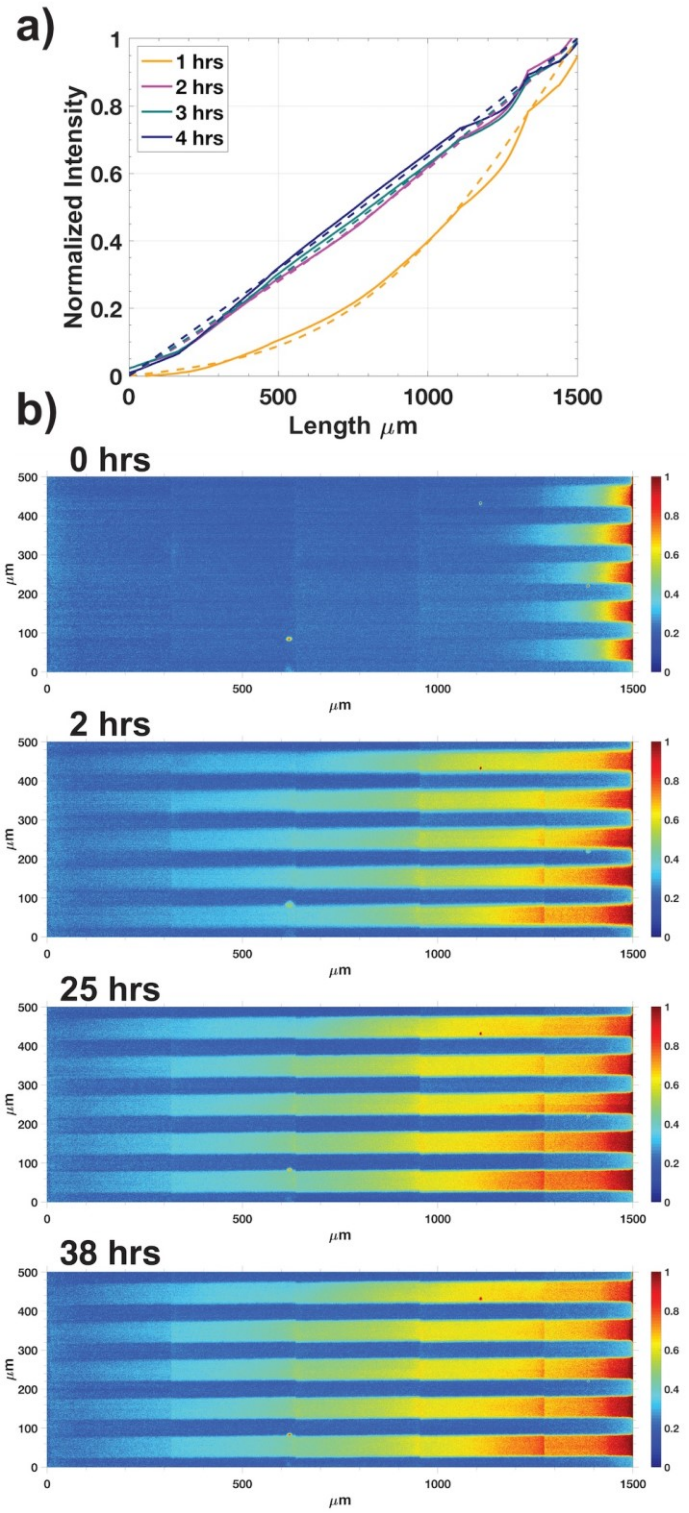

Figure 3.5. The formation of diffusive gradients within channels where the boundaries are reservoirs containing (left) no DNA and (right) 200 nM of a Cy3 dye-modified oligonucleotide. (a) Fluorescence intensity as a function of time and position within the channel. Dashed lines indicate the least-squares fit to the solution of the diffusion equation. (b) Fluorescence micrographs of 5 growing and stabilizing gradients within 5 channels at different time points.

We also performed additional diffusion experiments using a 31 base long fluorophore-modified oligonucleotide, denoted as Probe 2 (See Supporting Information: Materials and Methods for oligonucleotide sequence), to estimate this molecule's diffusivity in hydrogels photopatterned from the 75% (v/v) PEGDA formulation and exposed over dosages of 22 mJ cm^{-2}, 34 mJ cm^{-2}, 47 mJ cm^{-2}, and 57 mJ cm^{2}. We observed lateral isotropic diffusion in the resulting materials and obtained diffusion coefficients of 18 ± 7 μm^2 sec^{-1}, 16 ± 6 μm^2 sec^{-1}, 15 ± 6 μm^2 sec^{-1}, and 10 ± 5 μm^2 sec^{-1} respectively for hydrogels patterned with these dosages (mean ± s.d., see Supporting Information and Figure S3 for experimental details).

Having established that PEGDA gels could be photopatterned to allow crosslinking of acrylate-DNA in different gel domains and that DNA could diffuse through the hydrogels, we tested the use of CQ and TEA for photopatterning materials where acrylate-DNA could be sequestered through PEGDA-DNA co-polymerization and then released by UV photo-triggered cleavage of a 1-(2-nitrophenyl)ethyl spacer in its phosphodiester backbone (see Supporting Information **Figure S3.7** for schematic of spacer photocleavage).

Hydrogels photopolymerized using 0.8% (w/v) camphorquinone mixed with a 75% (v/v) poly(ethylene glycol) diacrylate pregel solutions retain DNA with 12% efficiency.

To determine the photoinitiator's efficiency of crosslinking acrydite modified DNA, we first measured how much of the DNA remained inside the hydrogel over time while washing out the uncrosslinked prepolymer and DNA with water. We crosslinked Anchor 1, a 5' acrydite-polyThymine oligonucleotide containing an internal UV-photocleavable spacer inserted in the middle of its 10 bases and a 3' Cyanine3 dye modification (2 μM concentration of DNA in the pregel solution, see Supporting Information for sequence) within 750 μm-diameter photopatterned PEGDA hydrogel circles using the aforementioned photopatterning method

within the branched flow cell. The average final intensity within the centers of the hydrogels was 12% of the initial intensity prior to washing, suggesting that 12% of the DNA in the prepolymer solution was crosslinked in the center of the hydrogel (Supporting Information Figure S3.4).

25-30% of 1-(2-nitrophenyl)ethyl-functionalized DNA is cleaved from 75% (v/v) poly(ethylene glycol) diacrylate hydrogels with UV light over a dosage range of 0.75 mJ cm^{-2} to 15 mJ cm^{-2}.

To determine whether UV light could be used to direct the release of conjugated DNA by cleaving its backbone, we patterned 750 μm diameter circles containing Anchor 2, a 23 nucleotide long strand with a 5' acrydite modification and a photocleavable spacer. Anchor 2 contained a 20 nucleotide binding domain extending from its 3' end complementary to Probe 2. This binding domain was separated from the 5' acrydite modification by a 1-(2-nitrophenyl)ethyl spacer (see Supporting Information: Materials and Methods for oligonucleotide sequence). In UV-exposed areas of the hydrogels, photocleavage and diffusion of the Anchor 2 binding domain from the gel should result in a lower amount of sequestered Probe 2 (which has a fluorescent tag) compared to unexposed areas where no binding domains have been removed because the cleaved domain can diffuse away from the location where it was conjugated. We chose to separate acrydite and fluorophore modifications between Anchor 2 and Probe 2, which can hybridize to one another, because we observed that Cy3 dye had an unintended interaction with CQ during UV exposure that diminished its ability to fluoresce afterwards (Supporting Information: Supplemental Data 2.2). We exposed 500 μm diameter circles within 750 μm patterned hydrogels to either 0.75 J cm^{-2}, 7.5 J cm^{-2}, or 15 J cm^{-2} of 365 nm light (intensity = 25 mW cm^{-2}). After UV exposure, hydrogels were washed for 24 hours to remove cleaved Anchor 2 fragments. We injected 2 μM of Probe 2 in 1X tris-acetate-EDTA (TAE) buffer with 12.5 mM

magnesium acetate into the flow cell and allowed it to diffuse into the hydrogels for 24 hours. The hydrogels were washed again for 5 hours and imaged.

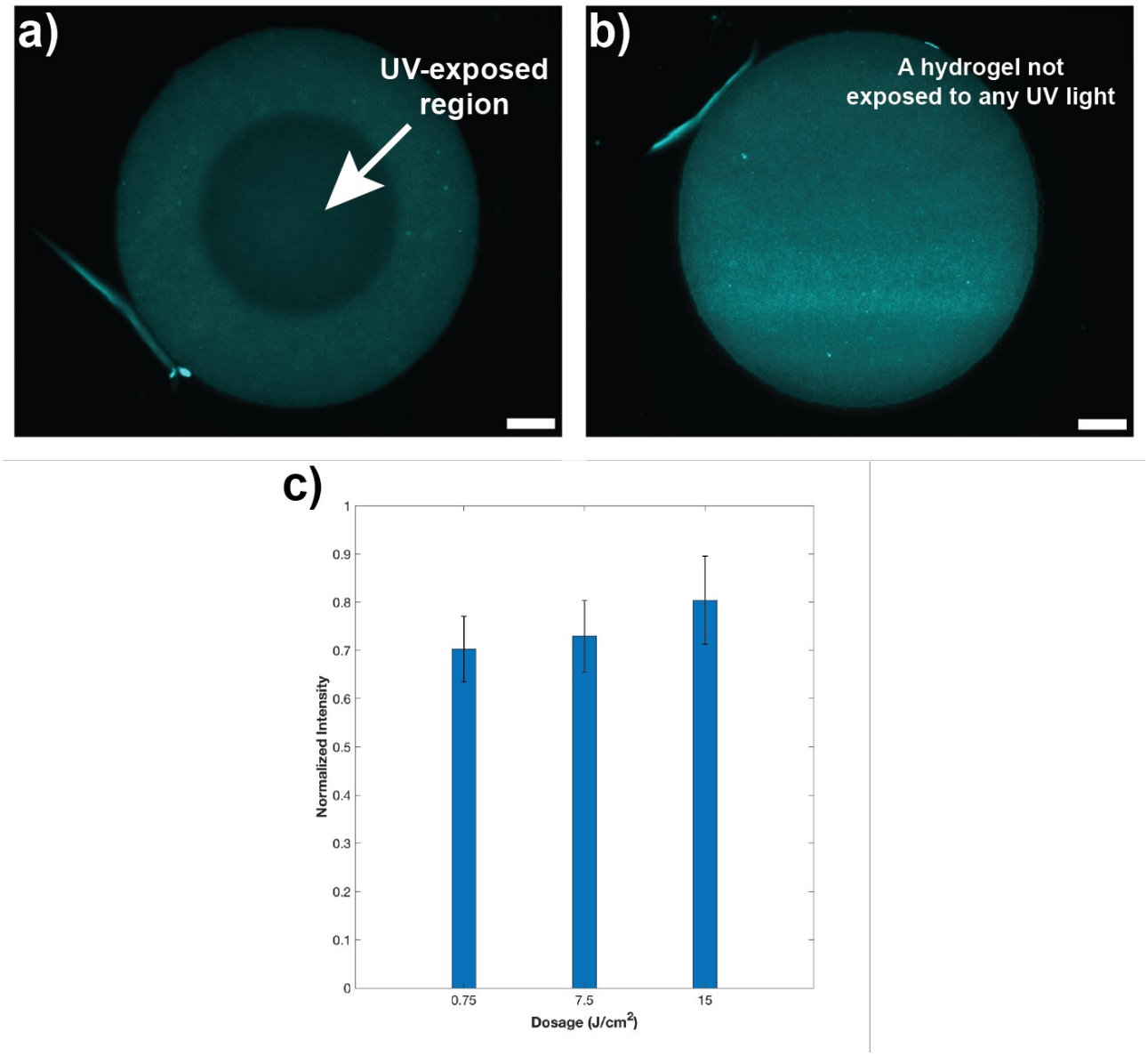

Figure 3.6. Patterned 75% (v/v) PEGDA-co-Anchor 2 DNA hydrogel (a) after exposure to a 500 μm UV pattern, Dosage = 7.5 J cm^{-2} and (b) a control gel that was not exposed to any UV pattern (scale bars = 100 μm). (c) normalized fluorescence intensities in the UV-exposed center of the hydrogels as a function of UV dosage (average ± s.d.) The reported intensity for each gel is the average intensity within 200 μm around the gel center divided by the average intensity within the annulus surrounding the center.

Fluorescent micrographs of UV-exposed 75% (v/v) hydrogels showed decreased fluorescence intensity in the exposed centers compared to their unexposed annular region (**Figure 3.6a, c**).

No decrease was observed in hydrogels that weren't exposed to a UV light pattern (**Figure 3.6b**). Reduction in the relative intensity in exposed areas, plotted as the average normalized intensity in Figure 6c, therefore indicated a lower amount of Probe 2 hybridized to crosslinked Anchor 2 in those locations resulting from photocleavage of the 1-(2-nitrophenyl) ethyl linker, and diffusion of the cleaved Anchor 2 binding domain out of the gel. While we only observed roughly 70-80% cleavage and diffusion of Anchor 2 from the gels over a dosage range of 0.75 J/cm^2 to 15 J/cm^2, it is important to note that a variety of system and geometric factors influence the overall cleavage efficiency, including the UV transmission efficiency of the DMD device, microscope projection optics employed, and gel physical properties[129,130] (see Supporting Information for discussion of factors impacting digital photocleavage efficiency within PEGDA-*co*-DNA gels).

3.3 Discussion

In this study, we demonstrate digital photolithographic patterning of DNA-functionalized PEGDA hydrogels using a blue light-activated camphorquinone-triethanolamine photoinitiator system. DNA diffuses through the resulting hydrogels and DNA with a photocleavable linker can be released via selective photocleavage. DNA diffusion within the hydrogels is isotropic in the lateral x and y dimensions. The practical limit for patterning resolution depends on the size of the individual mirrors, which are roughly 10 μm in dimension for our system without magnification (Supporting Information). Our observed minimum feature size of about 25 μm is consistent with feature sizes obtained in other digital photolithographic processes[102,106]. We also demonstrate that multiple PEGDA domains can be patterned next to one another to create a composite material. No visible interpenetration of these domains was

observed, suggesting that DNA molecules of the size we used (MW ~ 10,000 g/mole) or larger could be separated between domains. Additionally, multi-domain structures were elastic enough to recover their original shape upon flow-induced deformation against a polydimethylsiloxane surface.

The techniques outlined in this work suggest that PEGDA-*co*-DNA hydrogel formulations comprised of camphorquinone and triethanolamine, when combined with digital maskless photolithography, open up new possibilities for assembling structurally complex stimuli-responsive DNA-based biomaterials compatible with a wide array of UV-sensitive photolabile chemistries[131–133]. The formation of stable DNA gradients highlights this technique's potential usefulness for applications requiring patterned substrates that can incorporate DNA-based reaction-diffusion networks and exchange nucleic acid signals between different locations through UV-light activated reactions. Applications of this approach could include photoactivated release of small interfering RNA oligos from implantable tissue scaffolds[134,135] and photoregulation of enzymatic circuits[136]. Such a platform might also facilitate studies of transcriptional networks and DNA-based pattern sensing in dynamic microenvironments where environmental cues in the form of chemotactic gradients or UV-photolabile ligands can be modulated in a spatiotemporal manner.

3.4 Acknowledgements

This work was supported by the Department of Energy (Grant No. DE-SC0015906). The authors also acknowledge Dr. Dominic Scalise, Dr. Nicholas Mavrogiannis, Dr. Francesca Crivellari, Dr. Sarah Friedrich, and Prof. Zachary Gagnon for helpful discussions.

3.5 Supporting Information

Materials and Methods

Materials: All materials were purchased from commercial vendors and used as received. Poly(ethylene) glycol diacrylate (Mn = 575, 437441) was ordered from Sigma Aldrich and camphorquinone (A14967) and triethanolamine (L04486) were ordered from Alfa Aesar. All oligonucleotides were purchased from Integrated DNA Technologies HPLC purified.

Microfluidic device fabrication: SU-8 photoresist molds for the flow cell and gradient generator were fabricated on 4-inch silicon wafers with standard contact photolithography. Molds for the gradient generator required two different heights of photoresist which was achieved by first spin coating SU-8 10 (Microchem) to a target height of 20 μm, exposing the wafer to a UV dosage of 225 mJ/cm^2 (i-line), and immersing it in SU-8 developer for 5-10 minutes. After confirming the integrity of the mold of the diffusion cells, a second layer of SU-8 3050 (Microchem) was spin coated over the existing pattern for a target height of 100 μm. Care was taken to make sure that the alignment keys of the first patterned layer weren't covered by the second photoresist layer and these keys were used to align the wafer to the second photomask on a mask aligner. The same exposure dosage and development times described above were used to lift off un-crosslinked photoresist. Poly-dimethyl-siloxane microchannels were made by crosslinking Sylgard 184 (Dow-Corning) in a 10:1 ratio of base elastomer to curing agent. After thermally curing the PDMS mold for 2 hours at 70 °C, devices were cut from the mold, hole punched (3 mm diameter), cleaned in a UV-ozone oven with glass coverslips and annealed together for 2 hours at 80 °C. Photomasks for the branched flow cell and gradient generator are provided as separate CAD documents.

Digital mask design: Digital masks were generated in AutoCAD and were scaled to fit the areas of the projected micromirror array through a U Plan Fluorite 4X microscope objective.

Multidomain hydrogel formulation: Two-color hydrogels were fabricated by crosslinking 1 μM fluorescently tagged DNA with a mixture of 75%(v/v) PEGDA 575, 0.8%(w/v) CQ, and 0.5% (v/v) TEA in deionized water. CQ was diluted from a 10% (w/w) stock in 1-butanol. The DNA tag consisted of a 20 bp poly-Thymine strand with a 5' acrydite-modification and a 3' fluorescein or Texas-615 dye modification.

Photopolymerization platform and procedure: The digital light projection apparatus utilized in our experiments consisted of a Mightex Systems Polygon 400 Dense Pixel micromirror array fitted into the light port of an inverted Olympus IX73 microscope. Blue light was routed from an LED head through a liquid light guide and reflected off of the digital micro-mirror array into the light path of the microscope. We conducted all polymerizations with a 4X microscope objective, which resulted in a maximum exposed rectangular area of 1500 μm in width by 787 μm in height (height = 1.21 μm, width = 2.24 μm per pixel of projected light). We measured the intensity of 470 nm light at the sample stage to be 11.4 mW cm^{-2}. Each digital mask was designed in AutoCAD and rastered onto the digital micromirror array (DMD) through a software interface.

Multi-domain hydrogel procedure: Prior to conducting polyethylene glycol diacrylate (PEGDA) photopolymerization within the branched flow cell, the device was treated with a solution of 12% (v/v) 3-(trimethoxysily)propyl methacrylate in acidic methanol to functionalize the channel surface with pendant methacrylate groups in order anchor the hydrogel within the channels. Tygon tubing (Cole Parmer - 0.060 in. OD) was inserted into its inlet and outlet, and the outlet tube was placed into a 50 mL Falcon tube to collect effluent. Solutions were injected manually into the device using a 1mL syringe (Becton Dickinson). The 75% (v/v) PEGDA-DNA prepolymer formulation consisted of 75% (v/v) PEGDA (Sigma Aldrich), 0.8% (w/v) (±)

camphorquinone (CQ), and 0.5% (v/v) triethanolamine (TEA) (Alfa Aesar). To promote its solubility in the final pregel blend, CQ was first dissolved in a 10% (w/w) solution of 1-butanol and diluted down to a final 0.8% (w/v) in the pregel solution. The device was placed on the microscope stage and prepolymer solutions were injected serially into the channels. Exposure to patterns of blue light were 5 seconds long. After each set of patterns was generated, water was injected into the device manually for several minutes; the syringe was then replaced with a new syringe holding the second DNA pregel solution, and the injection and exposure process was repeated a second time. Images were obtained using time-lapse fluorescence microscopy using a 16-bit Infinity 3 CCD camera.

Gradient generation procedure: The microfluidic network utilized in the diffusion experiments consisted of up to 25 diffusion cells lined on each side by a liquid delivery channel; each diffusion cell was 1500 μm long, 50 μm in width, and 20 μm in height. Cells were grouped into arrays of 5 channels with an inter-channel spacing of 50 μm; we designed each array of cells to fight exactly within the projected area of the entire array of exposed mirrors. The gradient generator was first methacrylated with 12% (v/v) 3-(trimethoxysily)propyl methacrylate in acidic methanol as previously described before we conducted experiments. The prepolymer blend utilized in the gradient experiments consisted of 30% (v/v) PEGDA 575, 0.5% (v/v) TEA, 0.8% (w/v) CQ, and 1X tris-acetate-EDTA (TAE) buffer with 12.5 mM Mg^{2+}. To produce a gradient of DNA within the patterned substrates, a 30% (v/v) PEGDA prepolymer solution was first injected into the diffusion cells manually and exposed to the full array projected from the 4X objective for a dosage of 228 mJ cm^{-2}. The polymerization was conducted for 20 s on each array of 5 microchannels in the gradient generator (5 total arrays per device). Tygon tubes were then connected to the device inlet and outlet ports and a fluidic controller[128] supplied constant

pressure-driven flow of a DNA oligonucleotide and non-DNA solution (both contained 1X TAE Mg^{2+} buffer) to opposite sides of the diffusion cells; liquid was routed through a resistor upstream of the diffusion cells to mitigate convection due to minute pressure imbalances on the two side of the diffusion channels. Images were obtained using time-lapse fluorescence microscopy using a 16-bit Infinity 3 CCD camera at 400 ms exposure. Dark frame correction was performed on individual images to remove artifacts from uneven signal intensity across the CCD array. We constructed montages of the microchannel arrays by digitally appending individual images with overlapping fields of view and smoothing of the montage to remove residual noise.

Crosslinking Efficiency & Photocleavage of DNA within hydrogels: DNA photocleavage experiments in the hydrogels were conducted in the methacrylated branched flow cells using the 75% PEGDA formulation. To determine the crosslinking efficiency of CQ and TEA with acrydite modified DNA, 2 μM of Anchor 1 was mixed into the pregel solution and injected into the microfluidic device. 750 μm diameter circles were patterned in the flow cell at a dosage of 57 mJ cm^{-2}. To quantify how much DNA was crosslinked during photopolymerization, a New Era NE-500 syringe pump holding a 20 mL syringe of water was connected to the flow cell with Tygon tubing and the gels were washed within the channels with for several hours and imaged over time using a 10X UPlan FL N microscope objective. The reduction of the fluorescence intensity profile in the hydrogel was normalized by the intensity profile obtained immediately after photopolymerization and before the washing step (**Figure S3.4**). Roughly 12% of the DNA was retained after the wash step. An identical experimental set up was used to examine UV-triggered cleavage and release of Anchor 2 from 75% PEDGA hydrogels. 750 μm diameter circles were patterned in the flow cell at a blue light dosage of 57 mJ cm^{-2} and were washed with

water for 24 hours using a syringe pump. After UV exposure, 2 μM of Probe 2 in 1X TAE Mg^{2+} buffer was then washed into the flow cells and allowed to diffuse into the hydrogels for 24 hours, the flow cell was then washed with 1X TAE Mg^{2+} buffer for another 5 hours and the gels were imaged.

Synthetic Oligonucleotides:

The sequences of the DNA strands utilized in this study are listed below:

Multi-domain DNA Hydrogels:

/5Acryd/TTTTTTTTTTTTTTTTTTTT/36-FAM/

/5Acryd/TTTTTTTTTTTTTTTTTTTT/3TEX615/

Diffusion Gradient (Probe 1):

/5Cy3/TCTACGGAAATGTGGCAGAATCAATCATAAGACACCAGTCGG

Simple Diffusion Experiment (Probe 2):

/5Cy3/CATCTCATAACACATCTCACAATCCATCTCA

Acrydite-DNA anchoring and photocleavage experiments:

Anchor 1: /5Acryd/TTTTT/iSpPC/TTTTT/3Cy3Sp/

Anchor 2: /5Acryd/TTT/iSpPC/TGAGATGGATTGTGAGATGT

Camphorquinone/1-(2-nitrophenyl)ethyl linker compatibility:

S1_PC_S4: TCCATTCCACT/iSpPC/CATAACAACCA

S4'_PC_S1': TGGTTGTTATG/iSpPC/AGTGGAATGGA

Characterization of DNA diffusivity in 30% PEGDA hydrogels:

Within the channels of the microfluidic gradient generator, if different concentrations of a DNA strand exist at opposite ends of the hydrogel, a linear gradient should form at steady state, assuming homogenous diffusion. In order to determine the diffusion

coefficient of the DNA probe in the hydrogel, we treated the dynamics of diffusion within the channel as a one-dimensional diffusion process. The steady state solution to the 1-D diffusion equation with Dirichlet boundary conditions is a line:

$$\frac{\partial C(x,t)}{\partial t} = D\nabla^2 C(x,t) \text{ (1)}$$

$$C(x,t)|_{x=0} = 0 \text{ (2)}$$

$$C(x,t)|_{x=L} = C_0 \text{ (3)}$$

$$\frac{C(x,t)}{C_0} = \frac{x}{L} + 2\sum_{i=1}^{\infty}\left(\frac{i\pi\cos i\pi - \sin i\pi}{i^2\pi^2}\right)\sin\left(\frac{i\pi x}{L}\right)e^{-(i\pi)^2 t\frac{D}{L^2}} \text{ (4)}$$

In this 1-D diffusion process, a linear gradient exists at steady state only if there is no convection and isotropic diffusion across the channels. The concentrations at the left-hand-side and right-hand-side boundaries of the channels were 0 and 200 nM of Probe 1. In our experiments, we observed that linear gradients formed in the channels and remained stable during the entire time course of the experiment, suggesting that these conditions were met. We used least-squares fitting of fluorescent count data to the solution of the 1-D diffusion equation for our specific boundary conditions to calculate the diffusion coefficient of the oligonucleotide. The solution is the superposition of time-independent and time-decaying solutions (eqn. 4).

The exact derivation of the analytical solution occurred in the following steps. We non-dimensionalized the diffusion equation and boundary conditions and then assumed the solution for transient diffusion leasing to a steady state can be written as the linear superposition of time-decaying and time independent solutions:

$$\frac{\partial C_s(x_s,t_s)}{\partial t_s} = \nabla^2 C_s(x_s,t_s) \text{ (5)}$$

$$C_s(x_s,t_s)|_{x=0} = 0 \text{ (6)}$$

$$C_s(x_s, t_s)|_{x=1} = 1 \ (7)$$

$$C_s(x_s, t_s)|_{t_s=0} = 0 \ (8)$$

$$C_s(x_s, t_s) = C_D(x_s, t_s) + C_\infty(x_s, t_s) \ (9)$$

Plugging expression 9 into eqn. 5 and transforming the boundary and initial conditions from eqns. 6-7 we get:

$$\frac{\partial C_d}{\partial t_s} = \frac{\partial^2 C_d}{\partial x_s^2} + \frac{\partial^2 C_\infty}{\partial x_s^2} (10)$$

$$C_d(x_s, t_s)|_{x=0} = -C_\infty(x_s)|_{x=0} \ (11)$$

$$C_d(x_s, t_s)|_{x=1} = 1 - C_\infty(x_s)|_{x=1} \ (12)$$

$$C_D(x_s, t_s)|_{t_s=0} = -C_\infty(x_s)|_{t_s=0} (13)$$

The partial differential equation and boundary conditions for the steady state problem are:

$$\frac{\partial^2 C_\infty}{\partial x_s^2} = 0 (14)$$

$$C_\infty(x_s)|_{x=1} = 1 \ (15)$$

$$C_\infty(x_s, t_s)|_{t_s=0} = 0 \ (16)$$

which is an ordinary second order differential equation and can be integrated twice to yield:

$$C_\infty = a_1 x_s + a_2 (17)$$

a_1 and a_2 are constants of integration. Substituting boundary conditions into the eqn. 17 yields the steady state solution:

$$C_\infty = x_s (18)$$

The partial differential equation for the time decaying solution is a function of time and space with the following conditions and cannot be solved using separation of variables:

$$\frac{\partial C_d}{\partial t_s} = \frac{\partial^2 C_d}{\partial x_s^2} (19)$$

$$C_d(x_s, t_s)|_{x=0} = 0 (20)$$

$$C_d(x_s, t_s)|_{x=1} = 0 (21)$$

$$C_D(x_s, t_s)|_{t_s=0} = -x_s (22)$$

To solve this partial differential equation with the following boundary and initial conditions, we performed a finite Fourier transform. We first assumed that the solution can be expanded in the following form:

$$C_d(x_s, t_s) = \sum_{n=1}^{\infty} A_n(t_s)\varphi_n(x_s) (23)$$

We defined the finite Fourier transform using a basis function in the spatial domain which allowed us to handle the Dirichlet boundary conditions:

$$C_d(t_s) = \int_0^1 C_d(x_s, t_s)\varphi_n(x_s)dx_s (24)$$

We defined the basis function, $\varphi(x_s)$, to account for the two homogenous boundary conditions for the time decaying solution:

$$\varphi_n(x_s) = \sqrt{2}\sin(n\pi x_s) (25)$$

$$\varphi_n(0) = 0 (26)$$

$$\varphi_n(1) = 0 (27)$$

We then substitute eqn. 24 into eqn. 19 for the time and spatial derivatives of the diffusion equation:

$$\int_0^1 \frac{\partial C_d(x_s, t_s)}{\partial t_s}\varphi_n(x_s)dx = \frac{dC_d(t_s)}{dt_s} (28)$$

$$\int_0^1 \frac{\partial^2 C_d(x_s, t_s)}{\partial {x_s}^2}\ \varphi_n(x_s)dx\ (29)$$

Equation 29 must be integrated by parts twice to reduce it to a form suitable for applying isolating the definition of the finite Fourier transform:

$$\int_0^1 \frac{\partial^2 C_d(x_s,t_s)}{\partial {x_s}^2}\,\varphi_n(x_s)dx_s = \frac{\partial C_d}{\partial x_s}\varphi_n\Big|_0^1 - \int_0^1 \frac{\partial C_d}{\partial x_s}\frac{d\varphi_n}{dx}dx_s = \frac{\partial C_d}{\partial x_s}\varphi_n\Big|_0^1 - C_d\frac{d\varphi_n}{dx}\Big|_0^1 + \int_0^1 C_d\frac{d^2\varphi_n}{{dx_s}^2}dx_s \quad (30)$$

The first two terms are 0 leaving the definite integral as the only remaining term. The second derivative of the basis function can be determined from eqn. 25 and substituted into the integral to produce the definition of the FFT:

$$\frac{d^2\varphi_n}{{dx_s}^2} = -\sqrt{2}(n\pi)^2\sin(n\pi x_s) \quad (31)$$

$$\int_0^1 C_d\frac{d^2\varphi_n}{{dx_s}^2}dx_s = -(n\pi)^2\int_0^1 C_d\sqrt{2}\sin(n\pi x_s)\,dx_s = -(n\pi)^2\int_0^1 C_d\varphi_n dx_s = -(n\pi)^2 C_d(\,t_s) \quad (32)$$

Using the solution from eqn. 32 and eqn. 28, we can express the original partial differential equation as a first order ordinary differential equation (eqn. 33) which can be integrated to yield eqn. 34:

$$\frac{dC_d(t_s)}{dt_s} + (n\pi)^2 C_d(\,t_s) = 0 \quad (33)$$

$$C_d(\,t_s) = Ae^{-(n\pi)^2 t_s} \quad (34)$$

The initial condition (eqn. 22) was transformed using the FFT definition and integration by parts to solve for A, the constant on integration.

$$C_d(0) = \int_0^1 C_d(x_s,0)\varphi_n(x_s)dx_s = \int_0^1 -x_s\sqrt{2}\sin(n\pi x_s)dx_s = \frac{\sqrt{2}\cos(n\pi)}{n\pi} - \frac{\sqrt{2}\sin(n\pi)}{(n\pi)^2} = A \quad (35)$$

Therefore:

$$C_d(\,t_s) = \frac{\sqrt{2}\,n\pi\cos(n\pi) - \sqrt{2}\sin(n\pi)}{(n\pi)^2}e^{-(n\pi)^2 t_s} \quad (36)$$

Substitution of eqn. 36 into eqn. 23 and substitution of eqn. 23 into eqn. 9 and dimensionalization produces eqn. 9.

Characterization of DNA diffusivity in 75% PEGDA hydrogels:

To determine the diffusivity of a 31-base long oligonucleotide in the 75% (v/v) PEGDA formulation, we first polymerized 500 μm diameter circles in the branched flow cell for dosages of 22, 34, 47, and 57 mJ cm^{-2}. A solution of 2 μM of Probe 2 in water was injected into the device for roughly 2 minutes. The device was then time lapse imaged to measure the rate of diffusion of the DNA into the hydrogels. In order to calculate the diffusion coefficient of the DNA, intensity profiles of the DNA were least-squares fit to the solution to the diffusion equation in cylindrical coordinates (eqn. 9) with the following boundary and initial conditions:

$$\frac{\partial C(r,t)}{\partial t} = D\nabla^2 C(r,t) \quad (5)$$

$$\left.\frac{\partial C(r,t)}{\partial r}\right|_{r=0} = 0 \quad (6)$$

$$C(r,t)|_{r=R} = C_0 \quad (7)$$

$$C(r,t)|_{0<r<R,t=0} = 0 \quad (8)$$

$$\frac{C(r,t)}{C_0} = 1 - \sum_{n=1}^{\infty}\left(\frac{J_1(\lambda_n)}{\frac{\lambda_n^2}{2}\left(J_o^2(\lambda_n) + J_1^2(\lambda_n)\right)}\right) J_o\left(\frac{r}{R}\right) e^{-{\lambda_n}^2 t\frac{D}{R^2}} \quad (9)$$

where are J_o and J_1 Bessel functions of order 0 and 1 of the first kind respectively. Graphs of the normalized intensity profile in the hydrogels over the dosage range tested are listed in **Figure S3.3**. The derivation of the time-dependent solution of the diffusion equation was obtained through separation of variables. We first non-dimensionalized the partial differential equation, boundary and initial conditions:

$$\frac{\partial C_s(r_s,t_s)}{\partial t_s} = \nabla^2 C_s(r_s,t_s) \quad (10)$$

$$\left.\frac{\partial C_s(r_s,t_s)}{\partial r_s}\right|_{r_s=0} = 0 \quad (11)$$

$$C_s(r_s, t_s)|_{r_s=1} = 1\ (12)$$

$$C_s(r_s, t_s)|_{0<r_s<1,\ t_s=0} = 0\ (13)$$

We assumed the solution could be written as the linear superposition of steady state and time-decaying solutions:

$$C_s = C_d + C_\infty (14)$$

$$C_\infty = 1 (15)$$

$$C_d(r_s, t_s)|_{r_s=1} = 0 (16)$$

$$\frac{\partial C_d(r_s, t_s)}{\partial r_s}\Big|_{r_s=0} = 0 (17)$$

$$C_d(r_s, t_s)|_{0<r_s<1,\ t_s=0} = -C_\infty = -1 (18)$$

We assumed that the solution of the time decaying PDE took the following form:

$$C_d = F(r_s)G(\ t_s)\ (19)$$

Substituting eqn. 19 back into eqn. 10 and algebraic rearrangement gave the following equations:

$$\frac{G'}{G} = \frac{1}{r_s\, F}\frac{\partial(r_s\, F')}{\partial r_s} = -\lambda^2 (20)$$

$$\frac{1}{F}\frac{\partial(r_s\, F')}{\partial r_s} + r_s\lambda^2 = 0\ (21)$$

$$G' + G\lambda^2 = 0\ (22)$$

Eqns. 21 and 22 were solved separately. The solution to eqn. 16 is the Bessel function which takes the form of eqn. 18 with the following transformed boundary conditions:

$$F(r_s) = AJ_0(\lambda r_s) + BY_0(\lambda r_s)\ (23)$$

Y_0 is the Bessel function of order 0 and is unbounded at $r_s = 0$. Therefore, its coefficient must be 0 because the solution is bounded at $r_s = 0$.

$$F'(0) = 0 \xrightarrow{yields} \frac{\partial J_0(\lambda r_s)}{\partial r_s} = -\lambda J_1(\lambda r_s)$$

$$F(1) = 0 \xrightarrow{yields} AJ_0(\lambda r_s) = 0$$

Additionally, eqn. 22 was a first order ode and was integrated to obtain eqn. 24:

$$G = Ce^{-\lambda^2 t_s} (24)$$

After combining eqns. 24 and 23 into a series solution and consolidating coefficients, we rewrote eqn. 19 as a series solution:

$$C_d = \sum_{n=1}^{\infty} A_n J_0(\lambda_n r_s) e^{-\lambda_n{}^2 t_s} (25)$$

We used the initial condition and orthonormal property of Bessel functions to solve for the coefficient A_n:

$$C_d(r_s, t_s)|_{0<r_s<1,\, t_s=0} = -1 = \sum_{n=1}^{\infty} A_n J_0(\lambda_n r_s) (26)$$

$$-\sum_{m=1}^{\infty} J_0(\lambda_m r_s) = \sum_{n=1}^{\infty} A_n J_0(\lambda_n r_s) * \sum_{m=1}^{\infty} J_0(\lambda_m r_s) (27)$$

The inner product of the right-hand side of eqn. is 0 unless m = n. We can rewrite the summations as definite integrals from 0 to 1 and evaluate them to obtain A_n:

$$-\int_0^1 J_0(\lambda_n r_s) r_s dr_s = A_n \int_0^1 J_0^2(\lambda_n r_s) r_s dr_s (28)$$

$$A_n = \frac{-J_1(\lambda_n)}{\frac{\lambda_n^2}{2}(J_o^2(\lambda_n) + J_1^2(\lambda_n))} (29)$$

Substitution of An back into eqn. 25 and substitution of eqn. 25 into eqn. 14 yielded the final solution.

An important consideration for understanding the diffusive properties of the photopolymerized hydrogels is the relative size of the hydrogel mesh and hydrodynamic radius of the DNA species. The correlation length is typically used to describe hydrogel mesh size and

is defined as the average spacing between consecutive crosslinks in a hydrogel network.[137] As the correlation length decreases, approaching the size of a diffusing solute, transport of the solute can no longer be described by a molecular diffusion regime alone; collisions between the solute and solvent do not predominate and solute-hydrogel pore interactions must be taken into account, this is commonly referred to as a Knudsen diffusion. Specifically, this phenomenon and related theories describe the rate of collisions between the solute and crosslinked polymer, adsorption to the polymer, the average pore radius and tortuosity, all of which impacts the hydrodynamic drag on a diffusing molecule.[138,139] Here, we estimate the average mesh size of 75% (v/v) and 30% (v/v) PEGDA hydrogels fabricated in our experiments. Flory-Rehner theory, which describes the relationship between hydrogel swelling and crosslinked polymer properties, is a well-established approach for determining the diffusive properties of hydrogel composed of uncharged polymers. A crosslinked and swollen hydrogel is subject to two forces, the elastic retractive force of the crosslinked polymer chains and thermodynamic force of mixing which minimizes the entropy of the system.[140–143] A swollen hydrogel that is at or near equilibrium with its environment balances these two forces which can be expressed as contributors to the Gibbs free energy of the system:

$$\Delta G_{Total} = \Delta G_{Elastic} + \Delta G_{Mixing} (1)$$

$$\mu_{Solvent\ in\ gel} - \mu_{Pure\ solvent} = \Delta \mu_{Elastic} + \Delta \mu_{Mixing} (2)$$

where partial differentiation of eqn. 1 with respect to the moles of solvent yields eqn. 2. Based on this definition, a variety of equations and correlations have been developed to express hydrogel correlation length as a function of its composition. To determine the correlation length, we first estimated the hydrogel's equilibrium polymer volume fraction, $v_{2,s}$, after swelling in an aqueous solvent, specifically water:

$$\frac{1}{v_{2,s}} = q \frac{\rho_{polymer}}{\rho_{gel}} (3)$$

The density of the polymer, PEGDA (Mn = 575) at 25 C and atmospheric pressure, is 1.12 g mL^{-1}. The density of the crosslinked hydrogel was assumed at be that of water, 1 g mL^{-1}, at 25 C and atmospheric pressure. q is the equilibrium weight swelling ratio which we assumed to be roughly between 2 and 2.5 based on experimental observations by Wang 2019.[144] Therefore, we estimated the value of $v_{2,s}$ to be between .36 and .45. The polymer volume fraction prior to swelling, $v_{2,r}$, was assumed to be the same as the volume fraction added to the pregel solution was .75. Using $v_{2,r}$ and $v_{2,s}$ we then determined the number average molecular weight between crosslinks in the hydrogel, $\overline{M_c}$:

$$\frac{1}{\overline{M_c}} = \frac{1}{\overline{M_n}} - \frac{\frac{\bar{v}}{V_1}\left[\ln\left(1 - v_{2,s}\right) + v_{2,s} + \chi_1 v_{2,s}^2\right]}{v_{2,r}\left[\left(\frac{v_{2,s}}{v_{2,r}}\right)^{\frac{1}{3}} - \left(\frac{v_{2,s}}{2v_{2,r}}\right)\right]} \quad (4)$$

where $\overline{M_n}$ is the number average molecular weight of the polymer chains in the absence of the crosslinking agent ($\overline{M_n}$= 575 g mol^{-1}), $\bar{v}$ is the specific volume of polyethylene glycol at 25 C and atmospheric pressure ($\bar{v}$ = 0.89 mL g^{-1}), V_1 is the molar volume of water at 25 (V_1 = 18 mL mol^{-1}), χ_1 is the Flory-Huggins interaction parameter for PEDGA in water (χ_1= 0.426)[145]. Knowing $\overline{M_c}$ allowed us to calculate the root-mean-square, unperturbed end-to-end distance of the PEDGA chains between crosslinks, $(\bar{r}_o^2)^{1/2}$, which was used to directly calculate the correlation length, ξ:

$$\xi = {v_{2,s}}^{-\frac{1}{3}}(\bar{r}_o^2)^{\frac{1}{2}} \quad (5)$$

$$(\bar{r}_o^2)^{1/2} = l(C_n N)^{\frac{1}{2}} \quad (6)$$

$$N = \frac{2\,\overline{M_c}}{M_r} \quad (7)$$

where N is the number of polymer links per chain, C_n is the Flory characteristic ratio, which is the ratio of the square of the unperturbed to the square of the random flight end-to-end distance and has been tabulated for many polymers (C_n= 6.9). M_r is the molecular weight of the poly(ethylene glycol) repeat units within the polymer chain (M_r = 44 g mol^{-1}) and l is the average bond length of the polymer backbone obtained by averaging one carbon oxygen and one carbon-carbon bond (l = .30 nm). Based on the range of swelling weight ratios we estimated, ξ = 2.3 nm – 3.2 nm.

For the 30% (v/v) PEGDA hydrogels, we assumed $v_{2,r}$ = 0.3. The equilibrium volume and weight swelling ratios are inversely proportional to a hydrogel's equilibrium volume fraction. Based on this simple relationship we assumed that decreasing the volume fraction of polymer within the hydrogel by a factor of 2.5 from .75 to .3 would thereby increase the weight swelling ratio of the gel by a factor of 2.5 (q = 5 – 6.25). Using this estimation, we determined that the correlation length for 30% (v/v) PEGDA hydrogels varied between 5.3 nm – 6.4 nm.

Having determined the mesh size of the hydrogels, we then calculated the hydrodynamic radius of the single stranded oligos used in our experiments. By calculating the hydrodynamic radius of the DNA species, we were able to compare the relative sizes of the species and mesh size and estimated the theoretical diffusion coefficients of the species using the Stokes-Einstein equation. We first determined the hydrodynamic radius of short single stranded DNA, which forms hydrated coil in aqueous solution assuming the polymer has no self-complementarity. A coiled oligonucleotide can be approximated as a spherical object having a minimum radius of:

$$R_{min} = \left(\frac{3M\bar{v}_2}{4\pi N_A}\right)^{\frac{1}{3}} \quad (8)$$

M is the molecular weight of the oligonucleotide (M_{42} = 12964.6 g mol^{-1} and M_{31} = 9287.1 g mol^{-1}) and $\bar{v}_2$ is its partial specific volume which is assigned a value of 0.56 cm g^{-1}. $\bar{v}_2$ underestimates the actual specific volume of hydrate DNA, and a correction factor is substituted for it to account for the specific volume, v_1^0(1.0 cm^3 g^{-1}), of δ_1 grams (0.5 g g^{-1}) of water bound to 1 g of DNA in its first hydration shell:

$$\bar{v}_2 = \bar{v}_2 + \delta_1 v_1^0 (9)$$

$$R_0 = R_{min}\left(1 + \frac{\delta_1 v_1^0}{\bar{v}_2}\right)^{\frac{1}{3}} (10)$$

For each oligonucleotide, we estimated R_{42} = 1.76 nm and R_{31} = 1.57 nm corresponding to diameters of 3.52 nm and 3.15 nm which were smaller than the mesh size of the 30% (v/v) PEDGA hydrogels. Probe 2 which was 31 nucleotides in size, was tested in the 75% (v/v) hydrogels; its diameter was within 2% of the maximum estimated correlation length. Using the Stokes-Einstein equation, we calculated the molecular diffusion coefficients for the strands based on their hydrodynamic drag coefficients and assumed the systems were in a dilute concentration regime:

$$D = \frac{kT}{6\pi\eta R} (11)$$

kT is the energy provided for molecular collisions by random thermal fluctuations in the system (4.1E-21 J), η is the viscosity of water at 25 C and atmospheric pressure (8.9E-4 Pa sec^{-1}), and R is the hydrodynamic radius of the DNA species. Overall, the denominator is the hydrodynamic drag coefficient of the species. We estimated that D_{42} = 139 μm^2 sec^{-1} and that D_{31} = 155 μm^2 sec^{-1}. The value of the diffusivity measured for Probe 1 in 30% (v/v) hydrogels was roughly 60 μm^2 sec^{-1} and varied between 10 and 18 μm^2 sec^{-1} for Probe 2 in 75% (v/v) hydrogels, indicating that the effective diffusivity of the oligonucleotides in our hydrogels was lower their molecular

diffusivity; this suggests that Knudsen diffusion may have a strong effect on the observed transport of DNA in the hydrogel formulations tested.

Supplemental Data

Camphorquinone compatibility with a photocleavable oligonucleotide 1-(2-nitrophenyl)ethyl spacer: We verified that the presence of camphorquinone does not inhibit UV-triggered photocleavage of an internally placed 1-(2-nitrophenyl)ethyl linker in a 22 bp DNA duplex. The specific sequence of the duplex (consisting of strands S1_PC_S4 and S4'_PC_S1') was adapted from a library of domains provided in Qian and Winfree 2011[146]. We hybridized the DNA duplex by mixing equimolar amounts of each strand with 1X TAE Mg^{2+} buffer in an Eppendorf Mastercycler PCR; the anneal protocol consisted of heating the solution up to 90 °C for 5 minutes and then cooling 1 °C every minute to 20 °C. The position of the PC spacer is the same on each strand, so that photocleavage should result in the scission of the duplex into two 11-bp fragments, which exhibit a different electrophoretic mobility than the full duplex.[147–150] 1 μM of the DNA duplex was mixed with 1% (v/v) Irgacure 2100 (BASF), a UV photoinitiator with peak absorbances at 275 and 370 nm, or 0.8% (w/v) CQ and exposed to 1, 5, and 10 minutes of 302 nm radiation from a UVP benchtop transilluminator. DNA from the exposed solutions was separated using polyacrylamide gel electrophoresis (PAGE) with a 10% polyacrylamide gel run at 120 V for 1.5 hours. PAGE gels were stained with Sybr Gold (ThermoFisher), a DNA intercalating dye, and visualized on a gel imager. A 100 bp double stranded DNA ladder (ThermoFisher) was used to track the size-dependent separation of the DNA fragments. The presence of 1% (v/v) Irgacure 2100 significantly diminished photo-scission of the duplex across all exposure times. However, the duplex exhibited cleavage at all exposure times when mixed with 0.8% (w/v) camphorquinone.

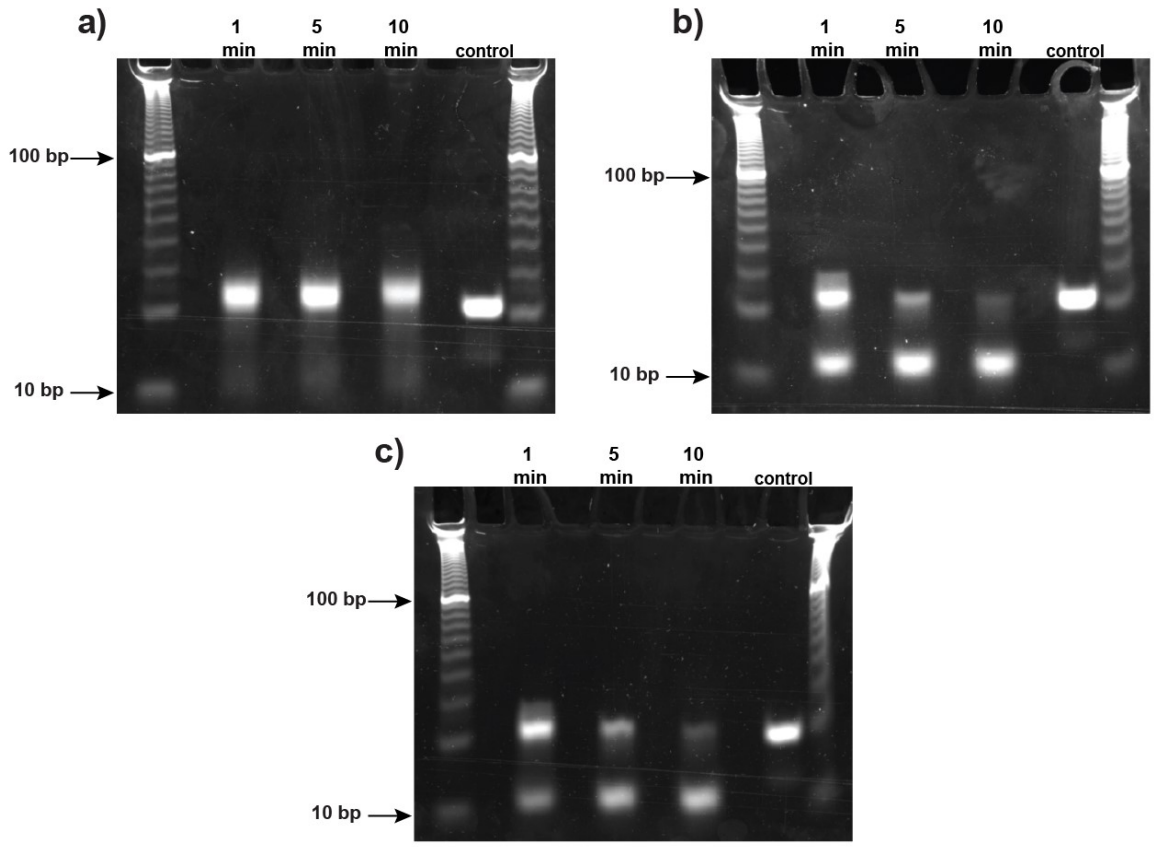

Figure S 3.1. DNA duplex PC-linker cleavage in the presence of a) 1% (v/v) OmniRad/Irgacure 2100 b) 0.8% (w/v) CQ, and c) 1X TAE Mg^{2+} buffer.

Fluorophore compatibility with UV light exposure:

We identified Cyanine 3 as a DNA dye modification that exhibited minimal photobleaching when exposed to UV-A light. To confirm its behavior, we first exposed solutions of 1 μM Cyanine 3 labeled DNA in 1X TAE Mg^{2+} buffer to UV-A light emitted from a UVP benchtop transilluminator for 2 hours and observed a 5% average change in the average fluorescence intensity of the solution over that period of time (Figure S2). To determine whether camphorquinone potentially degraded Cy3 dye fluorescence activity during excitation under UV light, we also exposed solutions of Cyanine 3 labeled DNA mixed with 0.8 % (w/v) CQ for 2 hours and observed an average reduction in fluorescence intensity of 38% (**Figure S3.2**). Having established that CQ and Cy3 had a deleterious interaction during exposure to UV light, we

visualized the UV-directed release of DNA from CQ photopolymerized hydrogels (see main text) by allowing a Cy3-modified strand to diffuse into the gels and hybridize to its crosslinked photocleavable reverse complement several hours after UV exposure.

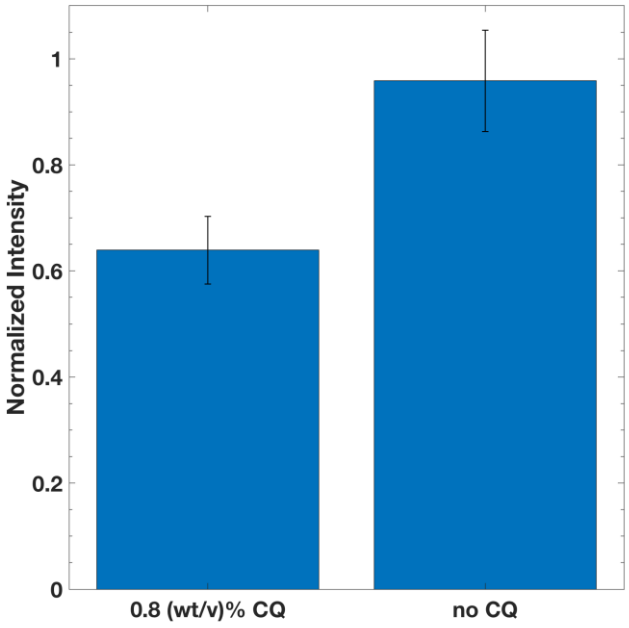

Figure S 3.2. Fluorescence intensities of solutions of Cy3-labeled DNA exposed 2 hours of UV-A radiation on a UVP benchtop transilluminator in the presence and absence of CQ (mean ± s.d.). Normalized intensity is intensity as compared to initial intensity before UV exposure.

Estimation of DNA diffusion coefficients within 75%(v/v) PEGDA hydrogels:

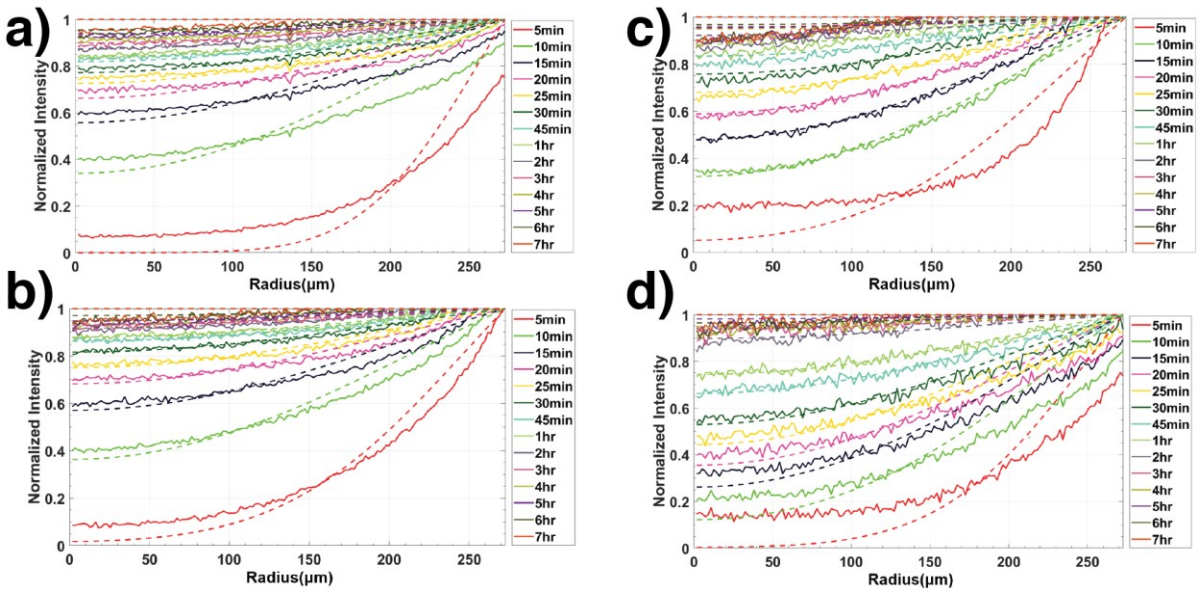

Figure S 3.3. Graphs of radial fluorescence intensity profiles of Probe 2 (see Materials and Methods: Synthetic Oligonucleotides for sequence) diffusing into 500 μm diameter 75% (v/v) PEGDA hydrogels photopolymerized for dosages of (a) 22 mJ cm^{-2} (b) 34 mJ cm^{-2} (c) 47 mJ cm^{-2} (d) 57 mJ cm^{-2}.

Notes on the uniformity of hydrogel height resulting from digital photopolymerization process: While we did not characterize the uniformity of DNA diffusivity with respect to hydrogel height or z-dimension, we expect that DNA also diffuses uniformly through the hydrogels in this dimension as well. The physics of the decay of light intensity across the z-depth are well-studied in the context of digital light projection photolithography[151,152], for bulk photopolymerization of macroscope volumes of acrylate resins with CQ[153], and obey the Beer-Lampert law. We estimate that the ratio of the intensity of 470 nm light at a depth of z in our devices to its incident intensity (I_z/I_o) drops to .97 and .87 for depths of 20 μm and 100 μm respectively.[154] A 13% drop in light intensity may result in variations in the microstructure of the hydrogel, specifically with its pore size. However, keeping the CQ photoinitiator concentration below 1% mass of the prepolymer solution is known to mitigate its screening effects across the polymerized depth, which was the case for the formulations presented in this work.[153]

System factors impacting digital photocleavage efficiency within PEGDA-*co*-DNA hydrogels: The efficiency of the photocleavage reaction is highly dependent on the reflectivity of the micromirrors and transmittance of the microscope projection optics; certain aspects of our projection system were not optimized for UV transmission. The extinction coefficient of the 1-(2-nitrophenyl)ethyl linker is optimized to absorb and cleave radiation below 350 nm. At 365 nm and above, the moiety's quantum yield drops significantly. While the UV mercury lamp we used for photocleavage emitted lines from 320 nm to 400 nm, the mirror set of the DMD only transmits light at 350 nm and above. Moreover, the transmission of the multipurpose 4X UPlan Fluorite objective used in our study cuts off around 350 nm and has a transmittance of 50% at 365 nm.[151] Our system is highly inefficient for transmitting UV light onto the hydrogel substrate. As such, it is not surprising that the photocleavage efficiency we measured over the range of exposure dosages was low. The quality of the moiety incorporated during DNA synthesis by the manufacturer (Integrated DNA Technologies) may also play a role in its cleavage efficiency, defective or non-reactive moieties will contribute to the overall efficiency observed. It is also important to note that unlike the blue-light photopolymerization process which occurred in seconds of exposure time, during the photocleavage exposure, UV light travels through densely crosslinked polymer across the entire microchannel thickness; attenuation of UV light intensity at increasing depth due to scattering and absorption by the crosslinked PEGDA macromer[129,130] could also diminish the ability to cleave the 1-(2-nitrophenyl)ethyl linker.

DNA Crosslinking Efficiency of CQ/TEA in 75% (v/v) PEGDA:

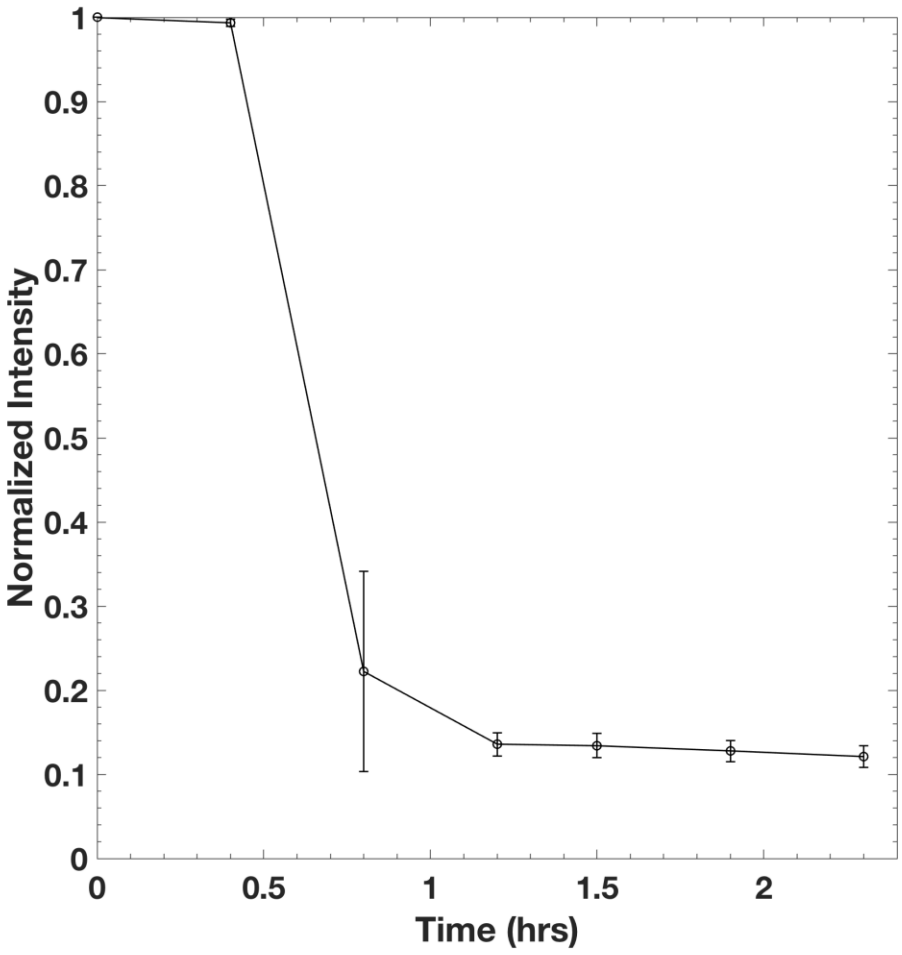

Figure S 3.4. Fraction of Anchor 1 retained during washing of 75% (v/v) PEGDA hydrogels, average center intensity (mean ± s.d.) for 11 gels.

PEGDA-DNA hydrogel crosslinking schematic:

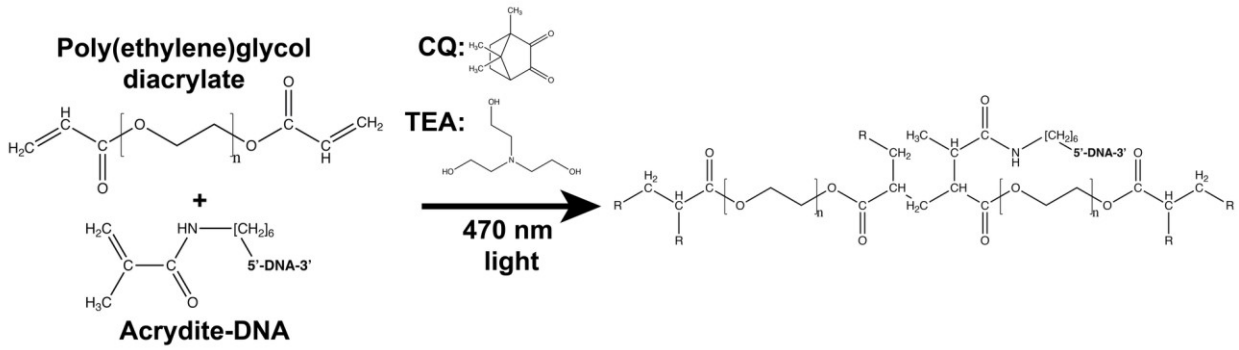

Figure S 3.5. Co-photopolymerization of PEGDA and 5' acrylate-modified DNA.

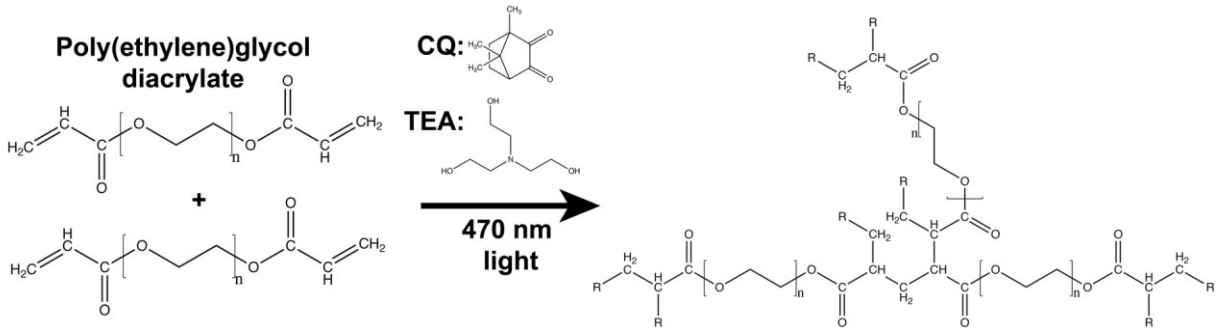

Figure S 3.6. PEGDA macromer photopolymerization.

UV photoscission of 1-(2-nitrophenyl)ethyl linker schematic:

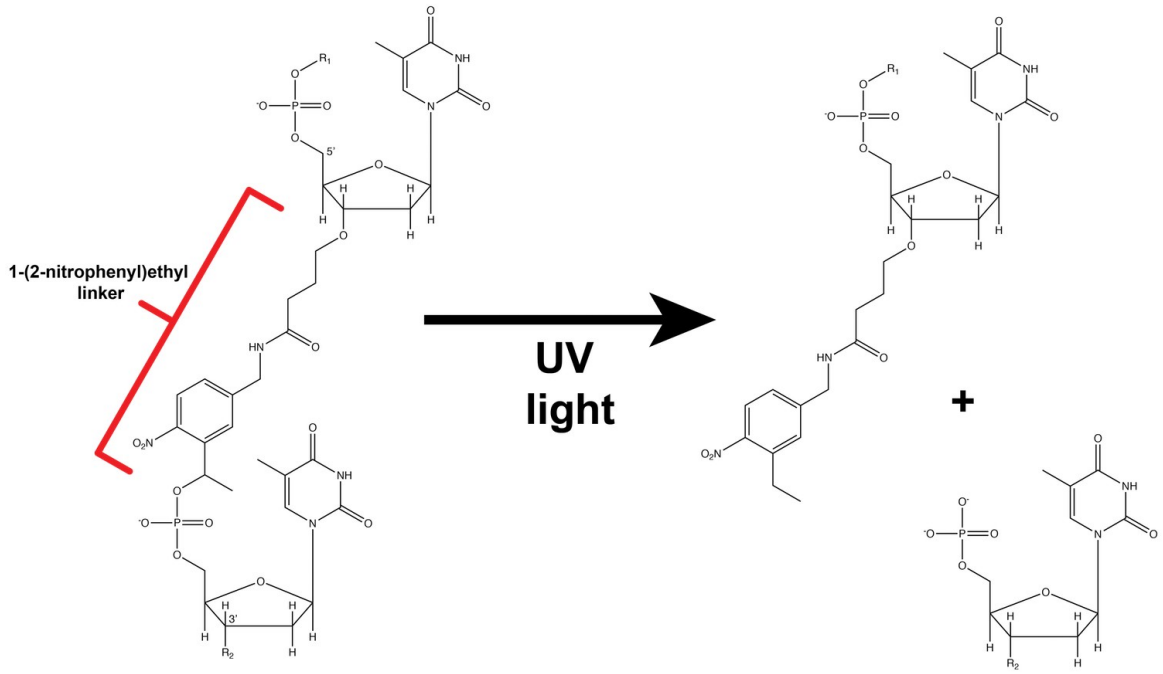

Figure S 3.7. UV triggered photocleavage of a 1-(2-nitrophenyl)ethyl linker inserted in the backbone between two Thymine bases.

Chapter 4 DNA Reaction-Diffusion Attractor Patterns

Summary

Living systems can form and recover complex chemical patterns extending hundreds of microns in length at prescribed locations. We show how designed reaction-diffusion processes can likewise produce precise patterns, termed attractor patterns, that reform when perturbed. We use oligonucleotide reaction networks, photolithography and microfluidic delivery to systematically form attractor patterns and study the responses of these patterns to different localized perturbations. Linear and 'hill'-shaped patterns formed and stabilized into shapes and at time scales consistent with reaction-diffusion models. When patterns were perturbed in particular locations with UV light, they reliably reformed their steady state profiles. Recovery also occurred after repeated perturbations. By engineering the far-from-equilibrium dynamics of a chemical system, this study shows how it is possible to design spatial patterns of molecules that are sustained and regenerated by continually evolving towards a specific steady state configuration.

4.1 Introduction

Precisely controlled biomolecular reaction-diffusion processes regulate and maintain chemical gradients of proteins, nutrients and cytokines across cells within tissues. These gradients coordinate the behaviors of tissues over length scales of hundreds of microns, including differentiation[155], vascularization[156] and healing[157]. These gradients must be formed and then maintained long enough to complete these processes [158]. Synthetic reaction-diffusion systems can also form and maintain patterns over similar length scales. Chemical waves are propagated in Belousov-Zhabotinsky processes[71,159], and in spatial implementations of Predator-Prey

oscillators[37]. Designed reaction-diffusion processes can also recapitulate Wolpert's French Flag model of threshold-dependent sensing[40]. As in biological systems, the inputs and outputs of synthetic reaction-diffusion processes can direct downstream chemical processes. Reaction-diffusion networks in hydrogels have been used to trigger chemomechanical actuation in response to chemical stimuli[42], and to direct chemical transformation with light-based[79] stimuli.

The formation of specific chemical patterns using reaction-diffusion processes generally requires precise ratios of reaction and diffusion rates[160]. Producing complex patterns also requires complex networks of reactions. DNA oligonucleotides reaction networks offer a means to control reaction and diffusion rates and to scale the complexity of the reaction networks required for multicomponent reaction-diffusion processes.[161,162] The rates of DNA strand-displacement reactions can be tuned precisely over a range of 10^6 by changing the length of DNA toehold domains[163] and the diffusion constants for DNA oligonucleotides and complexes are well-characterized in different media and obey simple scaling laws[164]. A combinatorial number of inputs can be encoded as different sequences and DNA circuits can perform complex operations on these inputs[3] . Many such DNA-based reactions can also occur reliably in tandem with limited crosstalk[7]. .

One function of reaction-diffusion systems in vivo is to robustly encode spatial information: for example, biological spatial gradients can often converge to back to their steady states after external perturbation or loading[165]. Synthetic chemical patterns able to recover their spatial profile could offer a robust means of directing the assembly or healing of the shape or structure of a heterogeneous material. A particularly useful type of reaction-diffusion process would be one that could exactly recover its steady state spatial distributions of chemical species after disturbances. If $\xi_i(x, y, t_i)$ defines the concentrations of species in a reaction-diffusion

process at time t_i the criteria for such recovery is that $\xi_1(x, y, t_1)$, the steady state pattern in the absence of perturbation and the recovered pattern after perturbation after steady state, $\xi_2(x, y, t_2)$, match exactly, *i.e.* $\xi_2 - \xi_1 = 0$ for all x and y and for appropriate times t_1 and t_2. We term the patterns produced by these reaction-diffusion processes attractor patterns.

One mechanism of creating an attractor in concentration space is through feedback that in response to perturbations drives the system back to a stable state. For example, in biological systems, genetic regulatory feedback processes stabilize gradients that control dorsal-ventral axis patterning in the blastoderm of vertebrate and invertebrate organisms.[32,166–168] Feedback loops could likewise regulate spatial patterns and restore chemical information in synthetic systems. For example, Scalise et al. developed a DNA-based buffer that can repeatedly restore the concentration of a specific DNA species to a setpoint concentration after perturbations in well-mixed solution.[27]

Attractor patterns result if feedback ensures that the rates of production and degradation or efflux of patterned species are balanced at each point in space at steady state. In such a case, damage to the spatial profile of the patterned species changes the pattern's shape but not the relative rates of production and degradation/efflux of the patterned species. As a result, after the pattern is perturbed, the system converges toward, and eventually reaches, its previous steady state (the attractor), effectively healing the pattern. One such feedback mechanism is a proportional-control loop, where the rate at which a particular species converges to its steady state concentration is proportional to the difference between the current concentration and the steady state concentration. Such a mechanism naturally occurs in chemical systems where the rate of production of a species is effectively zeroth order and its rate of degradation is first-order. In principle such coupled feedback loops along with chemical reactions that implement logic can

be used to generate arbitrary spatial patterns from simple initial conditions.[161] Here, we construct attractor patterns using synthetic DNA strand displacement networks (**Figure 4.1a**). We show how such patterns form as designed and can recover their original shapes after perturbations, specifically UV light-triggered strand displacement reactions that degrade the patterned species (**Figure 4.1b-c**). We demonstrate that the dynamics of pattern formation and recovery are consistent with the predictions of partial differential equations models of the reaction-diffusion process and how patterns can recover from repeated perturbations.

4.2 Results

The DNA reaction-diffusion processes we designed (**Figure 4.2**) employed active boundaries where the concentrations of input species are maintained at constant concentrations. These active boundaries served as a source of chemical energy, allowing the systems to remain far from equilibrium throughout their operation. We achieved these conditions within a microfluidic device containing diffusion cells of 1500 μm length, 50 μm width, and 20 μm height [84]. Reactants were supplied and waste was removed by pressure balanced flows perpendicular to the diffusion cells. Perturbations were induced *via* UV photocleavage of a 1-(2-nitrophenyl) ethyl linker within the phosphodiester backbone of a double stranded (ds) competitor complexes, exposing previously occluded toeholds that allow binding and degradation of the patterned species. 30% (v/v) poly(ethylene glycol) diacrylate (PEGDA Mn = 575) was photopatterned with a camphorquinone (470 nm excitation) photoinitiator[84] within each diffusion cell as a medium for reaction-diffusion that minimizes convection. Camphorquinone does not strongly absorb UV light, making it possible to trigger the UV-photosensitive reaction. Using this platform, we implemented systems of one dimensional 'attractor' patterns and

characterized the dynamics of pattern formation and repair using time-lapse fluorescence microscopy.

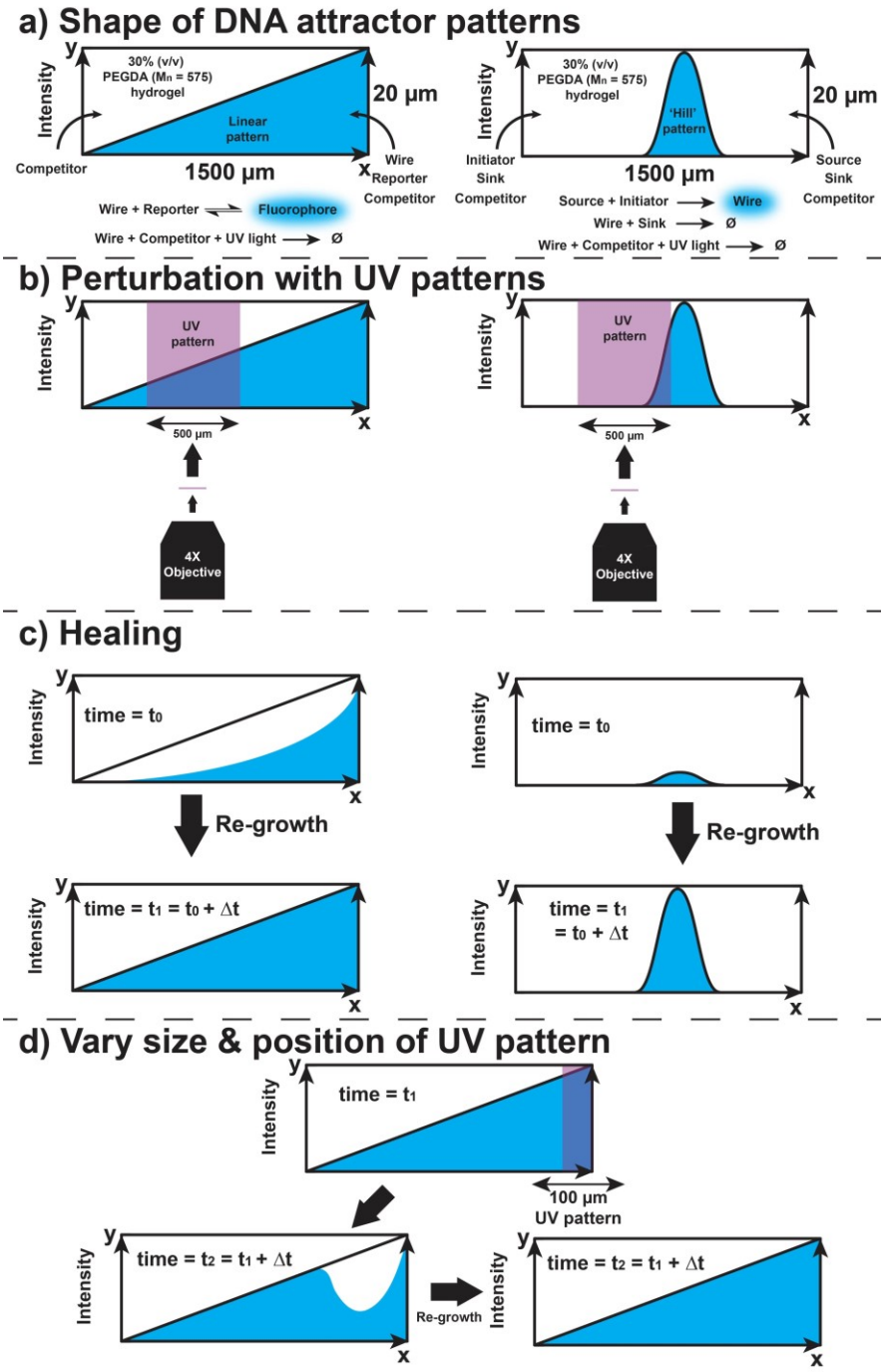

Figure 4.1. Schematic of linear and hill-shaped DNA pattern the formation and perturbation within a reaction cell. a) Specific reactants diffuse into the cell from boundaries at either end. Concentrations of the input species are kept constant at boundaries, providing an energy source to drive the far-from-equilibrium patterning process. DNA strand displacement reactions generate patterns characterized using the distribution of fluorescence within the diffusion cell. b) Patterns are perturbed in specific regions by exposing them to a patterns of UV light. c) Perturbed patterns eventually return to their original steady state (the attractor). d) The size and location of the region damaged by UV light can be varied.

Linear patterns form within 4 hours & reassemble after spatial damage by activation of a competitor species.

To initially study the process of attractor pattern formation, damage, and recovery, we created linear gradients of a Linear Wire (LW) strand that could react reversibly via toehold-mediated strand displacement with a Reporter complex to generate fluorescence (**Figure 4.2a, 4.3a**). In a process where the concentration of Reporter-Wire mixture is 0 along one side of the diffusion cell boundary and > 0 at the other boundary, a linear gradient of LW should form between the two boundaries and persist as long as the concentrations of the inputs are sustained via flow (**Figure 4.3a**). To make it possible to perturb LW's concentration at specific locations using light, a photoactivatable Competitor complex (**Figure 4.2a**) was also supplied on both sides of the diffusion cell (**Figure 4.3a**, SI: Results & Discussion 4). Upon irradiation of UV light, a 7-bp toehold cover on Inactive Linear Competitor (ILC) was cleaved, allowing it to detach, exposing the toehold. The resulting Active Linear Competitor (ALC) could then consume Wire (Figure 3a). 500 nM Reporter and 400 nM LW were allowed to react and equilibrate in an upstream reservoir prior to setting up the linear gradient (**Figure 4.3a**). A small fraction of spuriously generated ALC was assumed to present in any mixture of ILC prior to UV exposure, the total concentration of this Competitor mixture is referred to as Pre-active Linear Competitor (PLC). 500 nM PLC was also mixed into reservoirs that supplied reactants to both ends of the hydrogels (**Figure 4.3a**). The formation of the expected linear gradient was observed. We defined the formation timescale to be the period of time over which the change in fluorescence intensity in the center of the diffusion cell became less than 10% of the final steady state profile measured during pattern formation. The timescale of linear gradient formation was 4 hours (Figure 3b).

We then perturbed the linear patterns by exposing the diffusion cells containing the linear gradients to 500 μm-wide bands of 15 J cm^{-2} UV-A light. This exposure perturbed the entire pattern. After UV exposure, patterns began to reform, achieving a steady state indistinguishable from the original profile over 2.2 hours (**Figure 4.3c**). The linear reaction-diffusion process therefore formed and could recover the designed stable linear pattern. We then asked whether the linear pattern shape and the observed timescales of pattern formation and healing were consistent with the designed reaction network. We performed nonlinear least-squares regression to fit a one-dimensional PDE model using the rate constants of the strand displacement reactions and diffusion coefficients of the DNA species as optimization parameters to the dynamics of pattern formation (see SI: Results & Discussion 5). In addition to accounting for the designed reactions, the model incorporated a leak reaction between LW and spuriously generated ALC. The fitted rate constants and diffusion coefficients (SI: **Table S4.1**) fell within established ranges for toehold-mediated strand displacement reactions at 25 C in standard buffers and DNA diffusion coefficients in hydrogels. Importantly, the simulated formation timescale was 4.3 hours, which was within a factor of 2 of the experimentally observed timescale. To further validate that the proposed reaction-diffusion mechanism was responsible for the recovery of the pattern shape, we then simulated the process of pattern healing using the optimized parameters as model inputs and the fluorescence profile of the pattern measured directly after perturbation as the initial condition. We observed that the model also predicted shape recovery after perturbation, suggesting that we could effectively rationally design self-regenerating DNA patterns within our experimental platform.

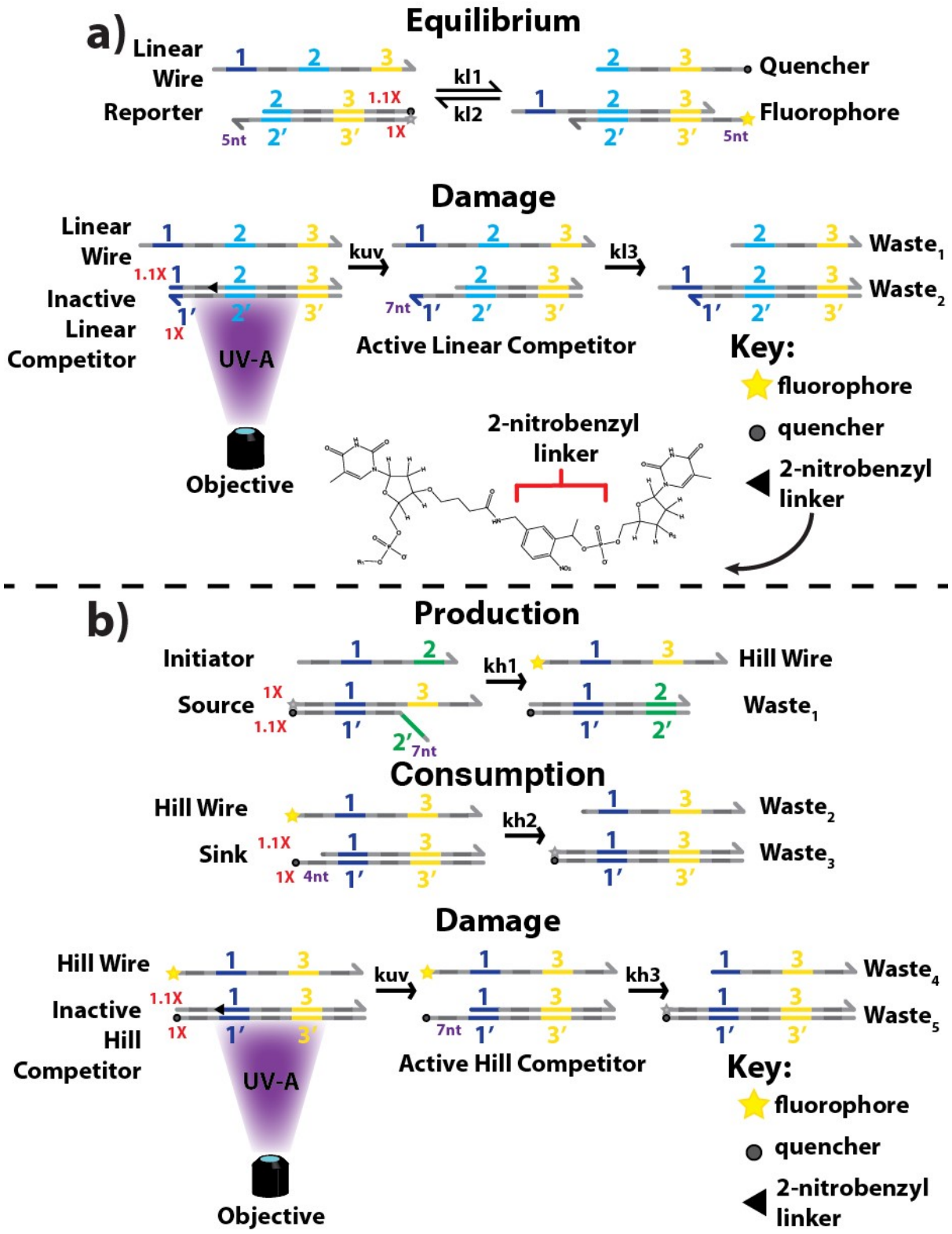

Figure 4.2. Coupled reactions used to produce a) Linear b) hill-shaped patterns along with respective photosensitive competition reactions. Red numbers indicate the relative concentrations of single stranded oligonucleotides annealed to form DNA duplexes and purple denotes the sizes of the toehold binding domains between species.

We then studied the dynamics of pattern healing after only a portion of a linear pattern was perturbed. After the patterns had recovered after the first 500 μm UV exposure, we applied 15 J cm^{-2} UV light to the right-most 100 μm of each pattern. Roughly 2/3 of each pattern was perturbed after this application of UV; the patterned reformed within 2.1 hours after perturbation (**Figure 4.4a**). The same UV dose was then applied to the same 100 μm region. This dose created a perturbation of the same size and scale as the first 100 μm-sized perturbation. After this perturbation, recovery occurred within 1 hour (**Figure 4.4b**). The linear patterns could therefore recover reliably after multiple perturbations. We used the reaction-diffusion model to simulate

recovery after both perturbations; the model predicted a pattern recovery timescale of 1 hour for both perturbations, consistent with the observed timescales of both perturbations.

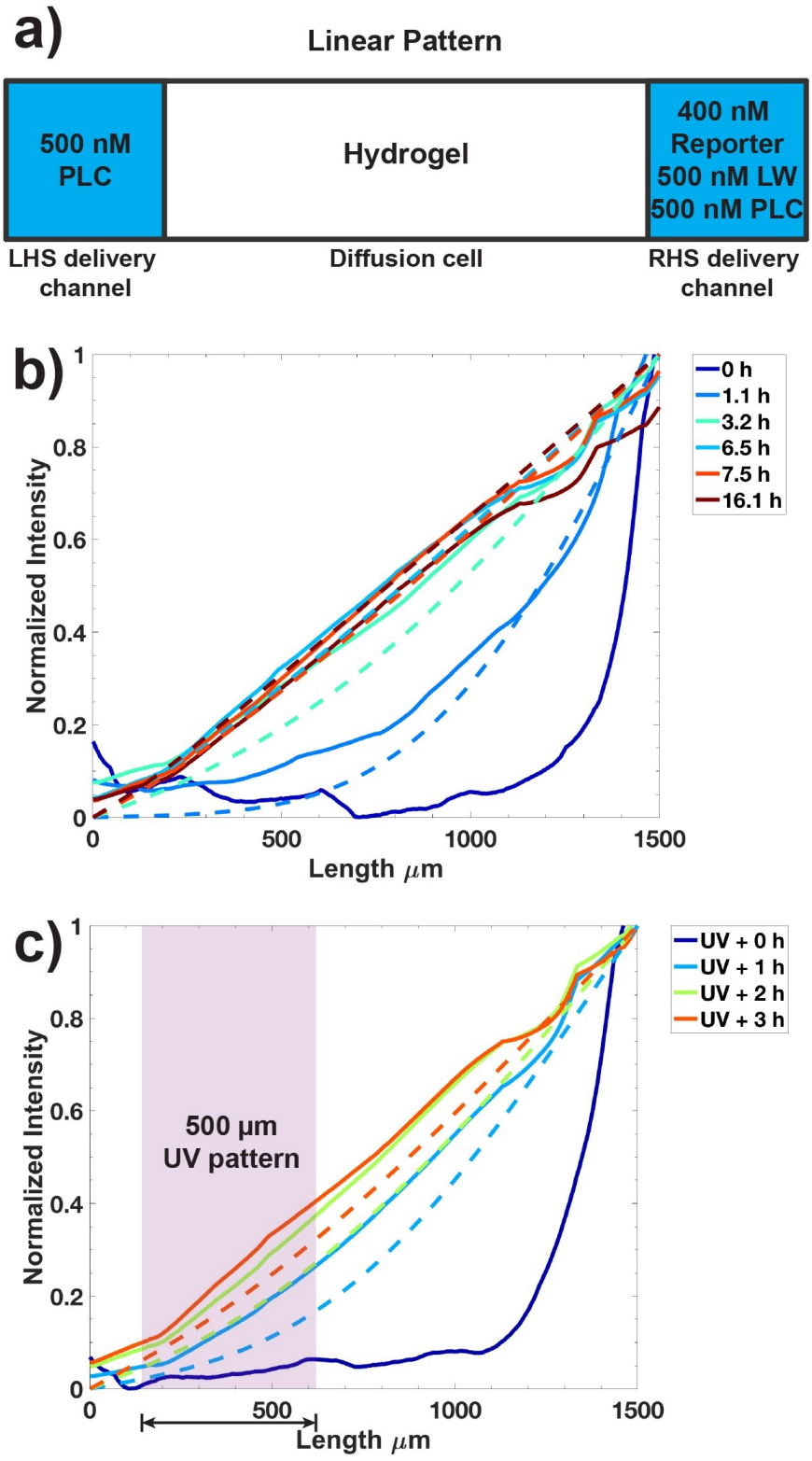

Figure 4.3. Formation of a linear pattern and its regrowth after perturbation. Solid lines = experimental data, dashed lines = simulations. a) Cross-section showing a diffusion cell's boundary conditions. b) Formation and stabilization of a linear gradient c) Pattern equilibration after UV exposure, which activates the Competitor. Red arrow indicates 500 μm region exposure to UV.

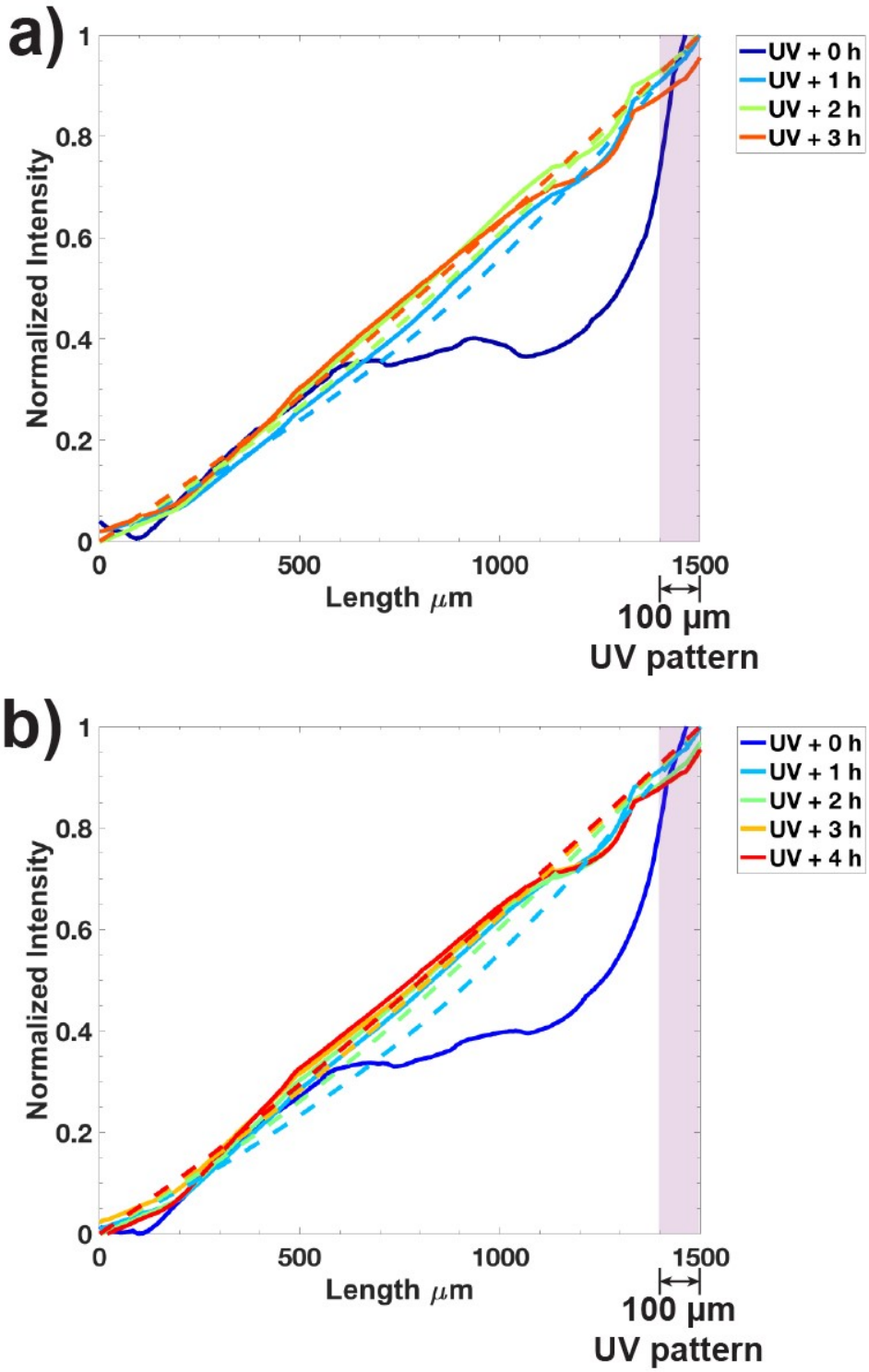

Figure 4.4. Repeated partial damage and healing of linear patterns. a) First UV exposure. Solid lines indicate the experimental results, dashed lines indicate simulations (red arrow indicates 100 μm region of UV pattern). b) Second UV exposure. Solid lines indicate the experimental results, dashed lines indicate simulations.

'Hill' patterns assemble within 9 hours & reform after spatial damage by activation of a competitor species.

In the linear pattern, the shape is stabilized solely by diffusion of the patterned species to and from each location within the hydrogel; our results showed that these patterns can recover in response to chemical perturbations that degrade the patterned species. We then showed that the same principles of damage and recovery applied when a stable pattern is the result of balanced rates of diffusion and production and degradation of the patterned species by chemical reactions. We designed a reaction-diffusion process in which the concentration of a single stranded DNA species, Hill Wire (HW), is a hill shape at steady state (see SI: Results & Discussion 1). The reaction network included Production and Consumption reactions (**Figure 4.2b**) that produced and degraded HW. Source and Initiator were supplied at opposite ends of the diffusion cell, so that HW was produced at the intersection of the diffusive fronts of the two species. After it was produced, HW was then degraded by Sink molecule so that its steady state concentration decreased with increasing distance from the site of production. This decrease is due to both diffusion and degradation, and the concentration profile is expected to decay exponentially with distance from the point of production. In one-dimensional space this process therefore forms a 'hill'-shaped profile of HW. The steady state is formed because the rates of HW production and degradation, and diffusion are equal at each point along the pattern; the hill shape is an attractor pattern that should be able to recover its shape after perturbations in HW concentration.

To form hill-shaped patterns using these reactions, we allowed solutions containing 2.5 μM Initiator to diffuse from the left-side boundary and 2.5 μM Source to diffuse from the right-side boundary (**Figure 4.5a**) into the diffusion cell. Source and Initiator reacted in a 7-nucleotide toehold-mediated strand displacement process to release Wire, causing an increase in fluorescence.

This reaction should proceed at the fastest rate near the center of cell, where the product of the local concentrations of Initiator and Source is expected to be at a maximum. Sink could bind and sequester HW through a 4-nucleotide length toehold-mediated strand displacement reaction, thereby quenching it. We designed a Damage reaction consisting of a UV-triggered Hill Competitor that could consume HW when activated by UV light, thus perturbing the patterned HW from its steady state shape. As we assumed for the linear pattern system, prior to UV exposure, the Pre-active Hill Competitor (PHC) likewise was a mixture of Inactive Hill Competitor (IHC) and Active Hill Competitor (AHC). 1.4 μM Sink and 1 μM PHC diffused into the diffusion cell at both boundaries.

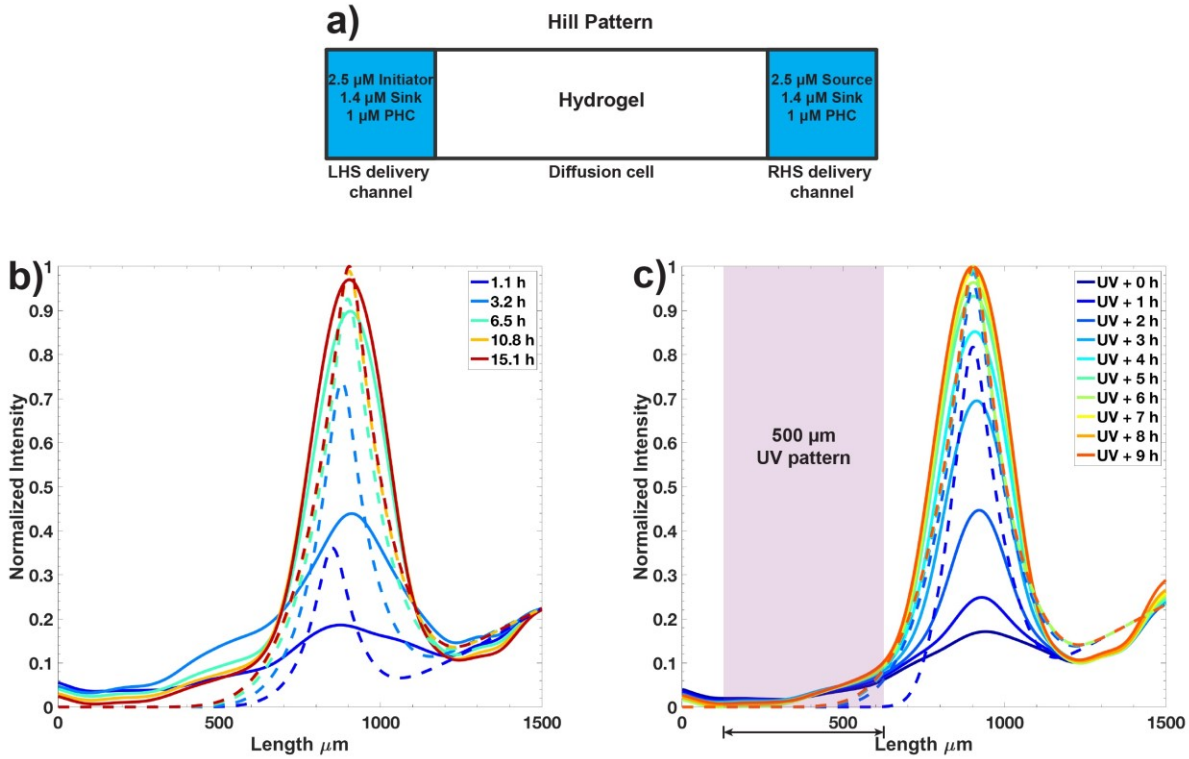

Figure 4.5. Growth, perturbation, and equilibration of hill-shaped patterns. In b and c, solid lines = experimental data, dashed lines = simulations. a) Diffusion cell boundary conditions. b) Formation and stabilization of a single hill-shaped pattern. c) Pattern recovery after 15 J cm^{-2} UV is applied in the region indicated by the red arrow.

Hill-shaped patterns formed over 7.6 hrs (**Figure 4.5b,d**). After 15 hours, we perturbed the patterns by applying 15 J cm^{-2} UV light in a 500 μm wide region of each diffusion cell (**Figure**

4.5c). This exposure decreased the heights of the patterns' peaks to 10% of their heights at steady state (Figure 5d). The peaks returned to within 10% of the steady state peak intensity within 5 hrs after perturbation (**Figure 4.5c, d**). We observed variations of 1-5% between the steady state peak heights before and after perturbations in some patterns; **Figures 4.5b and c** have been normalized to the minimum and maximum values attained by the specific pattern shown before and after a single perturbation.

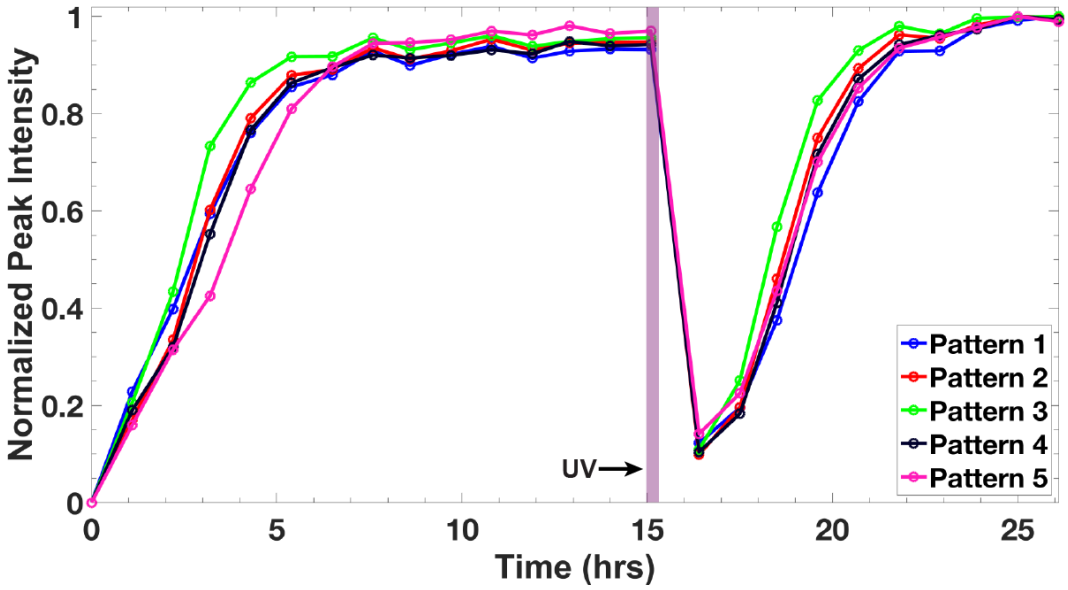

Figure 4.6. Intensity of the peak of 5 hill-shaped patterns during formation and recovery.

To understand whether hill pattern formation and recovery was consistent with the designed attractor pattern forming behavior, we first determined whether hill-shaped patterns formed because of the designed reaction and diffusion mechanism. We fit the diffusion coefficients and strand displacement rate constants to a one-dimensional PDE reaction-diffusion model using the fluorescence profiles measured during formation. The model fit leak reaction rate constants between HW and IHC, HW and AHC. Experimentally, we observed that the Source complex generated a baseline fluorescent signal that resulted in an offset between the intensities at the left and right-side boundaries of the diffusion channel (SI: **Figure S4.2**). The

model accounted for this offset with an empirical factor correction factor fit to the data. The simulation also incorporated literature value rate constants, based on toehold size, to model the leak reactions between Initiator and AHC, and Initiator and Source Bottom (SB) (SI: **Figure S4.4**). Specifically, Initiator can reversibly bind to AHC and can irreversibly bind to SB, its full reverse complement.

Using the fit parameters and literature rate constants, the model recapitulated the size and formation time of the hill gradients. The fitted rate constants and diffusion coefficients were consistent to within in one order of magnitude of literature values for standard strand displacement reactions and measured DNA diffusion coefficients in 30% (v/v) PEGDA hydrogels[84] (SI: **Table S4.2**). The predicted timescale of formation was 6.5 hrs, which was within a factor of 2 of the experimental timescale. When pattern recovery was simulated using the rate constants and diffusion coefficients as model inputs, and the fluorescence profile after perturbation as an initial condition, the model predicted a recovery timescale of 2.1 hrs, which differed from the experimental timescale by only a factor of 2.4, which suggested that feedback control could be effectively used as form of programming chemical patterning processes and recovering chemical patterns in the hydrogels.

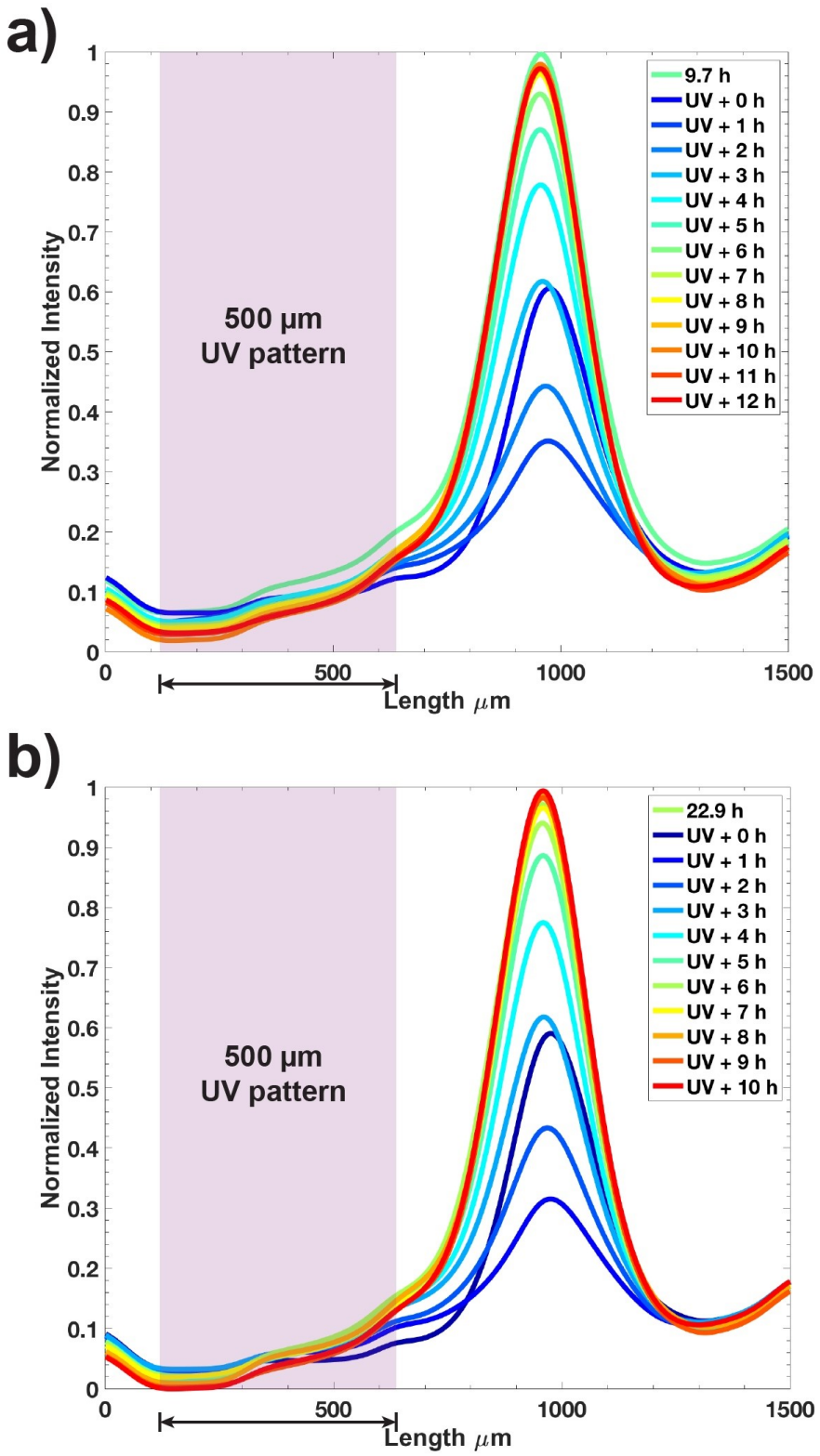

Figure 4.7. Repeated perturbation and healing of hill-shaped patterns. a) Recovery of a pattern after a first UV exposure of 1.5 J cm^{-2}. Solid line indicates the steady state profile prior to UV perturbation, dashed lines denote fluorescence profiles after UV perturbation (red arrow indicates 500 µm region of UV pattern). b) Second UV exposure of 1.5 J cm^{-2}. Solid line indicates the

steady state profile prior to UV perturbation, dashed lines denote profiles after UV damage (red arrow indicates 500 μm region of UV pattern.

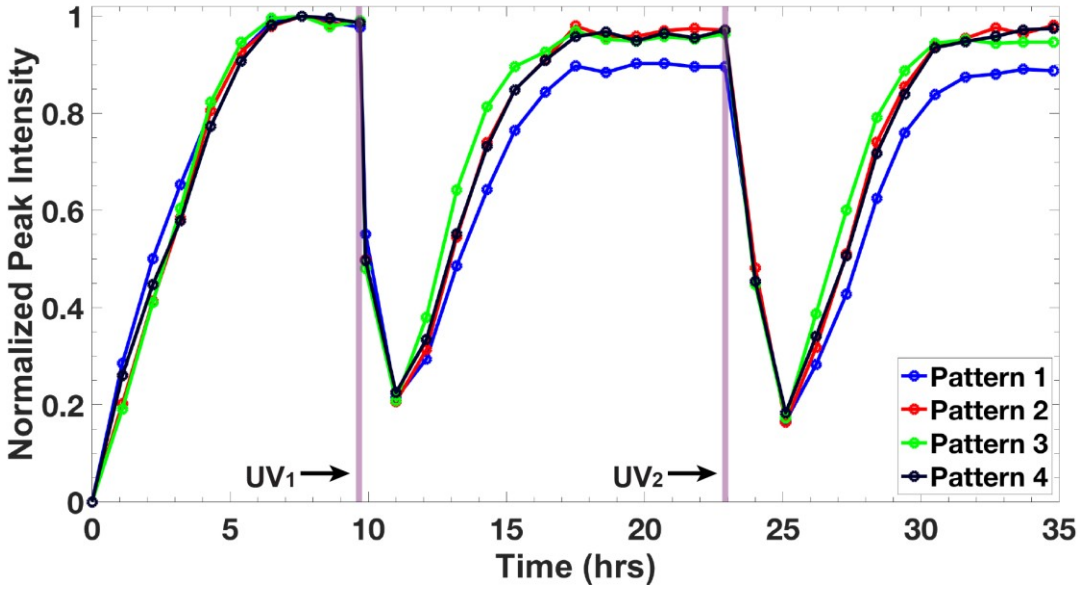

Figure 4.8. Intensities of the peaks of 4 hill-shaped patterns during growth and healing periods.

We then characterized the patterns' responses to multiple UV perturbations to test how well our designed attractor patterns could repeatedly recover their programmed shapes. We first formed hill-shaped patterns, allowed them to reach steady state and then exposed them to a 500 μm wide zone of 1.5 J cm^{-2} UV light (**Figure 4.7a**). After the first perturbation, the peak intensities of the hill-shaped patterns dropped to 21% (**Figure 4.8**) of their initial steady state intensities and then recovered over 5.6-7.8 hrs (Supporting Information **Table S4.3**). After returning to steady state, we exposed patterns to a second dosage of 1.5 J cm^{-2} (**Figure 4.7b**), resulting in an average 85% decrease in peak heights. We observed that after the UV exposure, the patterns recovered to their initial heights with 5% variation in the average center peak intensity for Patterns 1 through 3 in **Figure 4.8** before and after perturbation. Pattern 4 exhibited a slight decrease in average peak intensity, dropping 10% from its initial steady state after the

first perturbation and 3% from its second steady state after the second perturbation (Supporting Information **Table S4.3**, row 2). These results indicate how attractor patterns can be designed to recover a specific shape in response to repeated perturbation and return to their exact form.

4.3 Discussion

In this study, we provide an example of how classes of reaction-diffusion patterns heal spatial damage after multiple perturbations. Linear and hill-shaped DNA-based patterns stabilized in 4.3 and 7.6 hours respectively and recovered in response to multiple UV perturbations of varying size and dosage over a timescale of roughly 1 to 10 hours within PEGDA hydrogels. The measured timescales of pattern formation and recovery after UV-photoactivation were consistent with theoretical predictions of the designed CRN mechanisms to within an order of magnitude. Fitted rate constants and diffusion coefficients for the strand-displacement reactions provided confirmation regarding the role of the designed circuit behavior in the measured dynamics. Additionally, fitted ss and ds diffusion coefficients were consistent with existing measurements of DNA diffusivity in 30% PEDGA hydrogels respectively. Future work will be necessary to better characterize the photocleavage rate and efficiency of 1-(2-nitrophenyl) ethyl spacer functionalized DNA for the systems used in this study and the impact of light scattering through the depth of the substrates fabricated in the microfluidic platforms incorporated in this study.

DNA reaction-diffusion networks that can form and recover precise gradient shapes could be used to assemble more complex self-healing patterns by coupling multiple sets of feedback mechanisms demonstrated here. These self-healing patterns might regulate material composition, selectively heal chemical or structural damage, or buffer otherwise transient patterns of molecules as a means of storing information indefinitely. More generally, the

attractor patterns in this work are the sole stable steady states of the reaction-diffusion processes. These processes might be augmented to have multiple stable steady states which would make it possible to recover a spatial pattern after a small perturbation but switch to a distinct profile in response to a different stimulus. Such attractor dynamics are characteristic of associative memories[169] and neural systems[170].

Acknowledgements

This work was supported by the Department of Energy (Grant No. DE-SC0015906) and a Johns Hopkins Catalyst Award. The authors also thank Dr. Nicholas Mavrogiannis, Dr. Francesca Crivellari, Dr. Sarah Friedrich, Prof. Zachary Gagnon, and all of the members of the Schulman lab for helpful discussions.

4.4 Supporting Information

Experimental Procedures

Reagents:

All materials were purchased from commercial vendors and used as received. Poly(ethylene) glycol diacrylate (Avg. Mn = 575, 437441) was ordered from Millipore Sigma and camphorquinone (A14967) and triethanolamine (L04486) were ordered from Alfa Aesar. All oligonucleotides were purchased from Integrated DNA Technologies. All other reagents and materials are listed in the sections below detailing their use. DNA strands used for in this paper are listed in **Table S4.1** and **Table S4.2** along with the purification method. We annealed all complexes at the relative concentrations provided in **Figure 4. 2** of the main text. DNA complexes were annealed in 1X tris-acetate-EDTA buffer with 12.5 mM Mg^{2+}; the anneal

protocol consisted of heating the solution up to 90 °C for 5 minutes and then cooling 1 °C every minute to 20 °C in an Eppendorf Mastercycler PCR.

Table S 4.1. DNA sequences used in linear pattern experiments listed from 5' to 3' direction. IDT chemical modifications are bracketed by / /.

Linear Pattern	Sequence	Purification
Hill Wire	CA TAACA CA TCT CA CAATC CA TCT CA CCACC CA	Desalted
Reporter Cover	CAATC CA TCT CA CCACC CA TCT CA/3BHQ_2/	HPLC
Reporter Bottom	/5Cy3/TG AGA TG GGTGG TG AGA TG GATTG TG AGA	HPLC
Reporter Bottom (used in some qPCR mixed experiments)	/56-FAM/TG AGA TG GGTGG TG AGA TG GATTG TG AGA	HPLC
Linear Competitor Cover	TA CA TCT /iSpPC/ CA CAATC CA TCT CA CCACC CA	HPLC
Linear Competitor Bottom	TG GGTGG TG AGA TG GATTG TG AGA TG TA	PAGE
Full Complement of Reporter	TCT CA CAATC CA TCT CA CCACC CA TCT CA	PAGE

Table S 4.2. DNA strands for hill-shaped patterns listed from 5' to 3' direction. IDT chemical modifications are bracketed by / /.

Hill-shaped Pattern	Sequence	Purification
Hill Wire (Source Cover)	/5Cy3/CA TCT CA TAACA CA TCT CA CAATC CA TCT CA	HPLC
Source Bottom	TG ACATA TG AGA TG TGTTA TG AGA TG/3BHQ_2/	HPLC
Initiator	CA TCT CA TAACA CA TCT CA TATGT CA	PAGE
Sink Cover	T CA TAACA CA TCT CA CAATC CA TCT CA	PAGE
Sink Bottom	TG AGA TG GATTG TG AGA TG TGTTA TG AGA TG/3BHQ_2/	HPLC
Hill Competitor Cover	CA TCT CA/iSpPC/TAACA CA TCT CA CAATC CA TCT CA	HPLC
Hill Competitor Bottom (same as Sink Bottom)	TG AGA TG GATTG TG AGA TG TGTTA TG AGA TG/3BHQ_2/	HPLC
Sink/Competitor Bottom (noQ)	TG AGA TG GATTG TG AGA TG TGTTA TG AGA TG	Desalted

Microfluidic Device Design and Fabrication

The microfluidic network used in all experiments had the layout of the gradient generator previously described by Dorsey et al.[84] Each diffusion cell within the gradient generator was 1500 μm long, 50 μm in width, and 20 μm in height. Cells were grouped into arrays, each consisting of 5 cells with an inter-channel spacing of 50 μm; we designed each array of cells to fit exactly within the entire area of light projected (at 4X magnification) from a Polygon 400 DP digital micromirror array. Positive molds of SU-8 photoresist for the microfluidic device were fabricated on 4-inch silicon wafers using standard contact photolithography. Molds for the microfluidic device required two different heights of photoresist. Patterning this two-height device was achieved by first spin coating SU-8 10 (Microchem) to a target height of 20 μm, exposing the wafer to a UV dosage of 225 mJ/cm^2 (i-line), and then immersing it in SU-8 developer for 5-10 minutes. After confirming the integrity of the first stage of the mold, a second layer of SU-8 3050 (Microchem) was spin coated over the existing pattern for a target height of 100 μm. Care was taken to make sure that the alignment keys of the first patterned layer weren't covered by the second photoresist layer. These keys were used to align the wafer to the second photomask on a mask aligner. The same exposure dosage and development times described above were used to lift off un-crosslinked photoresist. The molds were then hardbaked overnight at 200 °C. Poly-dimethyl-siloxane microchannels were made by crosslinking Sylgard 184 (Dow-Corning) in a 10:1 ratio of base elastomer to curing agent. Wafers were used repeatedly to make PDMS devices; Sylgard 184 elastomer and crosslinker were mixed and then poured into a weigh boat holding the wafer. The mold was then degassed in a vacuum chamber to remove air bubbles. After thermally curing the PDMS mold for at least 2 hours at 70 °C, devices were removed from the mold, biopsy-punched to create device inlets and outlets, and cleaned in a UV-

ozone oven with glass coverslips. Each device was bonded to a glass coverslip for 2 hours at 80 °C.

Digital Micromirror Array Operation

The digital light projection apparatus utilized in our experiments to photopolymerize hydrogels and perturb patterns consisted of a Mightex Systems Polygon 400 Dense Pixel array fitted into the light port of an inverted Olympus IX73 microscope. Blue light was routed from an LED through a liquid light guide and reflected off of the digital micro-mirror array into the light path of the microscope. We conducted all polymerizations with an Olympus 4X UPlan FL N 0.13 NA microscope objective, which resulted in a maximum exposed rectangular area of 1500 μm in width by 787 μm in height (height = 1.21 μm, width = 2.24 μm per pixel of projected light). We measured the intensity of 470 nm light at the sample stage to be 11.4 mW cm^{-2}; the intensity of UV light at 365nm passed from a GreenSpot UV Curing system (GS2, America Ultraviolet Company) was 25 mW cm^{-2}. Each digital mask was designed in AutoCAD and rastered onto the digital micromirror array (DMD) through a software interface.

Reaction-Diffusion Hydrogel and UV Perturbation Setup

Before conducting polyethylene glycol diacrylate (PEGDA) photopolymerization within the microfluidic device, we treated the devices with a solution of 12% (v/v) 3-(trimethoxysily)propyl methacrylate (Millipore Sigma) in acidic methanol to functionalize the channel surface with pendant methacrylate groups in order to anchor the hydrogel to the surfaces of the channels. The pre-gel blend used in the experiments consisted of 30% (v/v) PEGDA 575 (Millipore Sigma), 0.5% (v/v) triethanolamine (TEA) (Alfa Aesar), 0.8% (w/v) (±) camphorquinone (CQ), and 1X Tris-acetate-EDTA buffer with 12.5 mM magnesium acetate (1X TAE/Mg^{2+}). CQ was first dissolved in a 10% (w/w) solution of 1-butanol and diluted down to a

final concentration of 0.8% (w/v) in order to promote its solubility in TAE/ Mg^{2+} buffer. The photopolymerization was conducted for 20 s (228 mJ cm^{-2}) on each array of microchannels. Tygon tubing was then inserted into the outlet and inlets. The inlets were connected to two upstream reservoirs containing the DNA reactants for the pattern forming reaction in 1X TAE/ Mg^{2+} buffer. A fluidic controller[128] provided constant pressure-driven flow of DNA oligonucleotides through both sides of the diffusion cells; liquid was routed through a resistor upstream of the diffusion cells to mitigate convection due to pressure imbalances on either side of the diffusion channels. Equal pressures of 1.3 PSI were applied to each reservoir.

Images were obtained via time-lapse fluorescence microscopy using a 16-bit Infinity 3 CCD camera at 400-900 ms exposure. During UV exposures, light from the blue LED was used to position the digital UV mask (500 μm or 100 μm width by 787 μm height) over the array. Light was then routed from a GreenSpot2 UV lamp into the Polygon 400 DP through a liquid light guide and exposed onto the array for a defined period of time. Imaging resumed immediately after UV exposure. Dark frame correction was performed on individual images to remove artifacts from uneven signal intensity across the CCD array. We constructed montages of the microchannel arrays by digitally appending individual images with overlapping fields of view and smoothing of the montage to remove residual noise.

Supporting Information Results & Discussion

4.4.1 Design of hill-shaped pattern reaction network: The Source and Consumption reactions were designed to produce and degrade Hill Wire (HW) according to 0^{th} order and 1^{st} order reaction kinetics respectively. These kinetics were achieved using bimolecular reactions, while maintaining constant concentrations of the reactants used to produce and consume HW. At each

location in space the reactions were designed so that the total flux of HW at each time point (excluding diffusion) obeys the following reaction rules:

$$\text{Source rate} = k_a[\text{Source}][\text{Initiator}] \approx k_p \quad (1)$$

$$\text{Consumption rate} = k_b[\text{Sink}][\text{Hill Wire}] \approx k_d[\text{Hill Wire}] \quad (2)$$

$$\frac{d[\text{Hill Wire}]}{dt} = k_p - k_d[\text{Hill Wire}] = k_d\left(\frac{k_p}{k_d} - [\text{Hill Wire}]\right) \quad (3)$$

The reaction network (equations 1 and 2) is designed so that it regulates the concentration of Wire in a manner similar the behavior of a negative-feedback proportional controller (equation 3) that resists changes in HW concentration. Here, k_a and k_b are the second order rate constants for the designed reactions and k_p and k_d represent the effective rate constants of Wire production and degradation when [Source], [Initiator] and [Sink] remain approximately constant during the experiment. In the analogy to a proportional controller, k_d and k_p/k_d are the controller gain and set-point respectively. The rate of growth and magnitude of the steady state profile of the HW patterns were then determined by the values of the constant concentrations of reactants in the system and the reaction rate constants. Specifically, in a spatial context, HW is produced at a particular location in space at a 0^{th} order rate. HW is then degraded in a 1^{st} order reaction as it diffuses away from its point source. The resulting shape of the profile is a hill, where the concentration of Wire decreases with increasing distance from the source of generation.

4.4.2 Cyanine 3 fluorophore insensitivity to UV light exposure in 30% PEGDA hydrogels:

Prior to conducting pattern perturbation experiments, we identified Cyanine 3 as a DNA dye modification that exhibited minimal photobleaching when exposed to UV light. We used this

dye to track patterns with minimal interference to the tracking process from the UV light used to perturb them. To measure the extent of photobleaching of Cy3 after UV exposure in a hydrogel, we formed linear gradients of the Reporter Bottom strand, which has an attached Cy3 dye (sequence, **Table S4.1**) in the microfluidic diffusion cells with a boundary condition of 200 nM of at the right hand side. After the patterns reached steady state, cells were subjected to either 30 seconds, 1 minute, 5 minutes and 10 minutes (equivalent to the maximum exposure time across all experiments) of UV light (intensity = 25 mW cm^{-2}) across the entire channel length. We then measured the change in profile intensity along the channel as (Intensity After UV exposure(t) – Intensity before UV exposure)/(Intensity at Right Boundary) at different time after exposure. At all exposure dosages, the patterns exhibited minimal deviation relative to the concentration boundary condition (**Figure S4.1**).

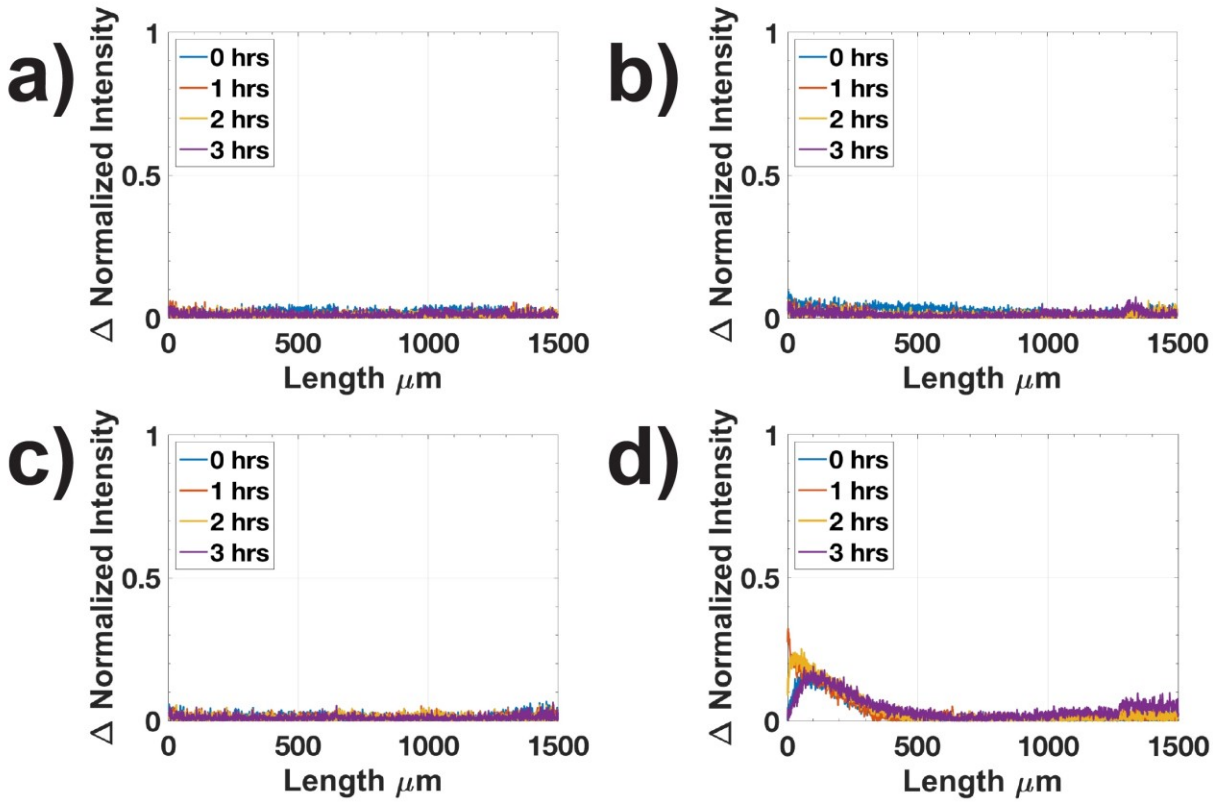

Figure S 4.1. Changes in normalized profile intensity of a linear diffusive gradient of Reporter Bottom at different times after UV exposure at a) 30 seconds, b) 1 minute and c) 5 minutes and d) 10 minutes. Δ normalized intensity = (Intensity After UV exposure (t) – Intensity before UV exposure)/(Intensity at Right Boundary).

4.4.3 The fluorescence intensity signal of the hill-shaped pattern contains artifacts due to Source fluorescence:

We observed that during hill-shaped pattern formation, the fluorescence intensity at the boundary of a diffusion cell where Source entered was roughly 25% higher than the fluorescence intensity at than the opposite boundary; the hill pattern should produce a concentration profile and resulting fluorescence intensity profile that is symmetric at both ends of the diffusion cell. The Source has a fluorophore-quencher pair, whereas the species entering the diffusion cell from the opposite site had no fluorophores. We hypothesized that difference in observed fluorescence intensities between the two boundaries was due to imperfect quenching of the fluorophore on the Wire strand while it was hybridized to Source Bottom Bottom (*i.e.* fluorescence from the Source

complex). To test this hypothesis, we measured the fluorescence intensity of a gradient of Source complex (**Figure S4.2**). We observed the formation a linear Source gradient with difference in fluorescence intensity of roughly 2000 counts between its boundaries; this value was 25% of the typical peak hill intensities measured during an experiment which ranged from 8000-10000 counts in magnitude. This experiment demonstrated that the Source complex alone formed a linear gradient that was detectable within the diffusion cells and that the magnitude of this gradient was sufficient to explain the observed difference. We account for this artifact in our reaction-diffusion model of hill patterns (see Results & Discussion 4.4.5).

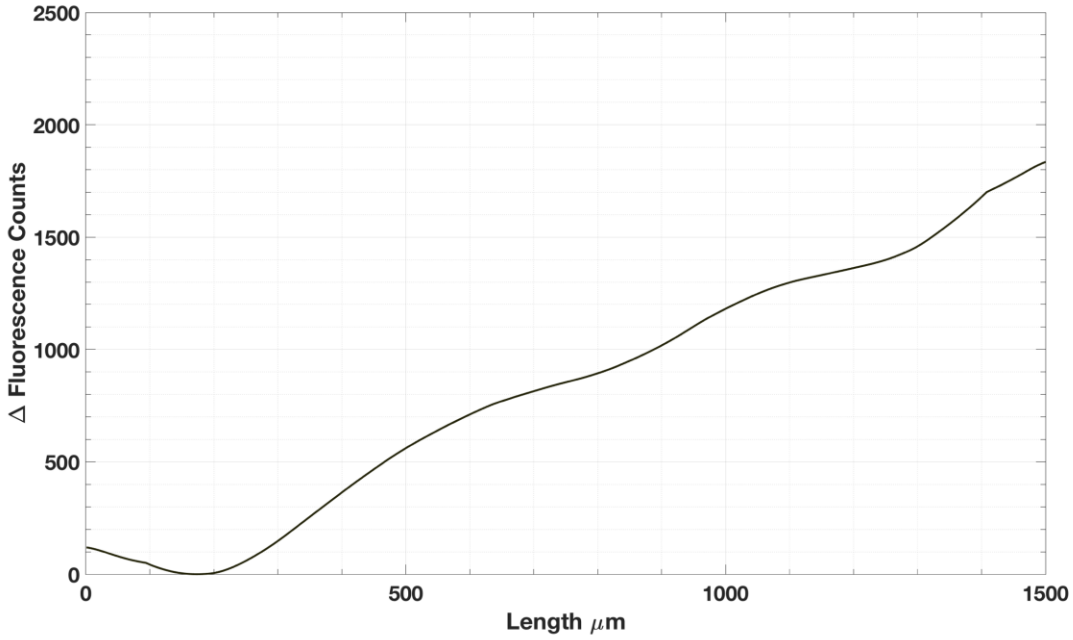

Figure S 4.2. Raw fluorescence intensity profile of Source diffusing into a diffusion cell at 18 hours. 2.5 μM Source entered the hydrogel from the right-side boundary and was roughly 2000 counts higher than the left-side boundary. Here, the difference in Source gradient fluorescence intensity between left and right boundaries is shown.

4.4.4 Characterization of leak reactions in linear and hill attractor patterns:

Undesired side-reactions have the potential to influence the experimentally observed dynamics of formation of the linear and hill patterns. To understand how leaks resulting from

undesired side reactions might impact the reaction-diffusion processes studied here, we first enumerated the side-reactions occurring between single stranded (ss) DNA and double stranded (ds) DNA species through three-way branch migration. The potential reactions for each of the pattern systems are given in **Figures S4.3 and S4.4** respectively. To understand the influence of these leaks, we measured the rates of key leak reactions, and the rates for some designed reactions, in well-mixed solution. The measured rate constants for these reactions were included in reaction-diffusion models of the linear and hill pattern systems. All experiments discussed in the following section were conducted in 96-well plates in TAE/ Mg^{2+} buffer and in the presence of 10 μM of polyT20 DNA (to prevent surface adsoprtion between the DNA species and pipette tips or the plates) and were measured on a BioTek plate reader or Stratagene qPCR at 25 C.

Linear Patterns:

For linear patterns, we hypothesized that some of the Pre-Active Linear Competitor (PLC), containing the UV-cleavable linker, had been cleaved before the experiment and was therefore spuriously active. This spuriously active Linear Competitor (ALC) could sequester Linear Wire (LW) through its exposed toehold (we refer to spuriously generated ALC as either a complex containing a toehold cover that was cleaved and dissociated so that the bases of its toehold are exposed) (Figure S3, reaction 1). We sought to determine the rate constant of this leak reaction in well-mixed solution by measuring the degree to which the addition of different concentrations of PLC, which contained ALC and Inactive Linear Competitor (ILC), shifted the fluorescence intensity of a reversible LW-Reporter reaction that had been allowed to reach equilibrium. We mixed 20 nM of Reporter with 200 nM of LW in multiple wells of a 96-well plate. After the reaction reached steady state (as measured by a constant level of fluorescence intensity), we then added PLC to final concentrations of 0 to 1000 nM. This PLC solution

presumably contained a proportion of ALC. After the addition of PLC, we observed a sharp drop in fluorescence intensity roughly proportional to the amount of PLC added (**Figure S4.5**), consistent with this hypothesis.

Calibration of linear pattern reactions:

To measure the leak rate constant, kl4, of Reaction 1 in Figure S3, we had to determine the concentrations of Fluorophore and LW over time from measured fluorescence intensities. As such, we performed a calibration by mixing known amounts of Full Complement of the Reporter (FCR) with 20 nM Reporter, which is a standard practice for calibrating strand displacement reactions[72]. FCR reacts irreversibly with Reporter to release Fluorophore (R_f), and Quencher strands; we assumed that the concentration of Fluorophore was equal to the concentration of FCR added. To convert raw fluorescence counts into R_f, we first added 0 to 20 nM of FCR in separate wells, to 20 nM Reporter (**Figure S4.6a**). We then measured the change in fluorescence at steady state between: 5 nM and 0 nM FCR wells, 10 nM and 5 nM FCR wells, 15, nM and 10 nM FCR wells, 20 nM and 15 nM FCR wells, and 25 nM and 20 nM FCR wells. Each of these values was defined as α, which is the ratio of Δ [FCR]/Δcounts. We calculated the average value of α which provided a proportionality to convert raw counts to [R_f]:

$$\langle \alpha \rangle = \langle \frac{\Delta[FCR]}{\Delta Counts} \rangle \quad (4)$$

$$\left[R_f(t)\right] = \langle \alpha \rangle \Delta Counts(t) \quad (5)$$

To determine the concentration of LW from [R_f], we used the definition of the equilibrium constant and the known initial conditions of the reaction. We calculated the equilibrium constant after the reaction reached equilibrium using the initial concentrations of species and [$R_f(t_{eq})$]:

$$K_{eq}(t_{eq}) = \frac{[R_f(t_{eq})][Quencher_0 + R_f(t_{eq})]}{[Reporter_0 - R_f(t)][LW_0 - R_f(t_{eq})]} \quad (6)$$

After having determined K_{eq}, we calculated the average K_{eq} at steady state for the reversible reaction across the 5 well calibration conditions. We then used this calculated K_{eq} to calculate the concentration of LW(t) for all reaction wells:

$$LW(t) = \frac{[R_f(t)][Quencher_0 + R_f(t)]}{[Reporter_0 - R_f(t)]\langle K_{eq}\rangle} \quad (7)$$

Using this transformation, after 200 nM LW equilibrated with 20 nM Reporter, we then calculated the initial concentrations of Wire Quencher, Reporter from R_f at the time when PLC was added to the wells. We fit the kinetic traces following the time of PLC addition to a least-squares regression model (**Figure S4.6a**) where the fit parameters included the fraction of spuriously generated ALC and biomolecular rate constant for the LW/ALC leak reaction, kl4. The average fraction of ALC was estimated to be roughly 0.07 ± 3.0E-3 (95% confidence interval) of the total PLC concentration. The average value of kl4 was 1.47E6 ± 0.052 E6 M^{-1} s^{-1}(95% confidence interval), which is consistent with literature for the magnitude an effective 6-bp toehold rate constant[76]. As the toehold of PLC was 7 nucleotides in length, we assumed that our fitted parameter provided a reasonable estimate of the possible leak mechanism between ALC and LW. We also fitted forward and reverse rate constants, kl1 and kl2, for the Reporting reaction using the reverse calibration kinetic traces (**Figure S4.6b**). The average values of kl1

and kl2 were 6.4E4 ± 0.5E4 M^{-1} s^{-1} and 2.6E5 ± 0.3E5 M^{-1} s^{-1}, which were within an order of magnitude of literature values for 5-bp length toeholds[76].It is important to note that the Reporter duplex possessed a quencher and fluorophore at its duplex end. This pair terminated the end of toehold binding domain for the reverse reaction (kl2); fluorescent dyes and quencher pairings are known to significantly stabilize the ends of DNA and RNA duplexes, effectively acting as an extra base-pair on the duplex[171,172]. Therefore, the magnitude of kl2 is reasonable because its toehold was effectively 6 nucleotides long.

Hill-shaped patterns:

For hill-shaped patterns, we enumerated key potential side reactions mainly occurring through three-way branch migration with Source, Competitor and Sink duplexes (**Figure S4.4**). Reaction 1 in Figure S4 can occur because Source complex is annealed with 1.1X excess Source bottom strand which can fully hybridize with Initiator, its reverse complement. The bimolecular rate constant for two single stranded oligonucleotides hybridizing to form a duplex in standard buffer conditions at 25 ºC has been characterized previously [76] to be 3.5E6 M^{-1} s^{-1}. kh8 was the rate constant for this reaction.

Pre-active Hill Competitor (PHC) and Sink are annealed with 1.1X excess cover strands and these excess cover strands have the potential to react with the Source complex. Specifically, Inactive Hill Competitor (IHC) Cover can initiate a 0-nt toehold reaction with Source to form $Waste_2$ and produce Hill Wire (HW); this reaction can also proceed in the reverse direction through a 0-nt toehold initiated step. For reaction 3, Sink Cover could initiate a 0-nt toehold reaction with Source to generate Wire and $Waste_3$; this reaction is also reversible via a 0 nt toehold initiation step. To determine the importance of leak reactions 2 and 3, we measured the rates of the leak reactions involving IHC Cover, Sink Cover, and Source complex. We incubated

varying concentrations of Sink complex and PHC complex with constant concentrations of Source; where the Sink or PHC complexes were annealed with 1.1X of the cover strand. In the strand displacement reactions used reaction-diffusion experiments, Sink and PHC and 3' quenchers terminated the ends of the duplexes. Upon hybridization of HW to these complexes, HW was not able to fluoresce because its 5' fluorophore was quenched by the 3' quencher on the Sink and PHC bottom strand. Importantly, to determine if Sink and PHC complex reacted with Source in well-mixed conditions to generate HW, these complexes could not have 3' quenchers at their ends so that the leak reactions could be tracked using the fluorescence of HW once it had been displaced from Source Bottom. The Sink and PHC complexes used in these experiments lacked 3' quenchers so that the generation of free HW could therefore be measured in solution and would not be quenched by hybridization of Wire to IC or Sink complex (see Table S1 for sequence information).

To estimate the rate constant of Reaction 2, the fluorescence change over time was monitored after PHC was added to final concentrations ranging from 0 to 1 μM to solution containing 2.5 μM of Source (**Figure S4.7a**). To estimate the rate of Reaction 3, the fluorescence change was monitored over time after Sink was added to final concentrations ranging from 0 to 1.4 μM to solutions containing 2.5 μM of Source (**Figure S4.7b**). We then calibrated the fluorescence change in these reactions by comparing it to the change in fluorescence change observed during an irreversible reaction of 0 to 2.5 μM of Initiator added to 2.5 μM of Source (Figure S7c). The intensity increase observed 10 hours after each of the concentrations of PHC was added to Source were on order 50 counts, which was 0.1% of the steady state intensity generated by mixing 2.5 μM Initiator and Source (40,000 counts). Therefore, the amount of Wire generated by this reaction accounted for only 0.1% of the amount of HW generated by the

reaction of 2.5 μM Source and Initiator. The reaction of Sink and Source generated less than 200 counts across all concentrations of Sink added after 10 hours of measurement. This count change was less than 1% of the change in fluorescence intensity generated by the reaction of 2.5 μM Initiator and 2.5 μM of Source. The maximum concentrations of PHC and Sink used in these experiments were as large as the maximum concentrations used in the reaction-diffusion experiment; the measured rates of Reactions 2-3 should represent a maximum of the rates of these reactions in the hill reaction-diffusion process. Therefore, the rates of Reactions 2-3 are small enough to be neglected in reaction-diffusion models of hill-pattern formation (see Results and Discussion 4.4.5).

In reaction 4, excess IHC Cover reacts with Sink complex in a 4-nt toehold strand displacement reaction to generate IHC complex and Sink Cover. At the concentration of IHC complex mixed in the upstream reservoirs during pattern formation experiments (1 μM) there should be maximum 100 nM of IHC Cover (if no spuriously cleaved AHC Cover is present) available to react with 1.4 μM Sink; resulting in a final reservoir Sink concentration of 1.3 μM upon completion of the reaction. This reaction is assumed to proceed with a 4-nt bimolecular rate constant of 5E3 M^{-1} s^{-1}, a standard value strand displacement reactions at 25 ºC in normal buffer conditions[76]. At this rate, the reaction of 1.4 μM Sink and 100 nM IC Cover would reach steady state roughly 12 minutes after initial mixing during reservoir preparation. As this time period was much shorter than the 1.5 hours of additional set up time following reservoir preparation, we neglected modeling this reaction in reaction-diffusion models and instead correct the boundary concentrations of Sink and IHC cover to their expected steady state values.

We also considered reactions in which non-UV exposed IHC could sequester HW. In this reaction, HW may bind to IHC and undergo strand displacement by hybridizing to exposed bases

on IHC Bottom, which may become exposed because of reversible fraying of bases at the end of the duplex or 5' truncation errors in the toehold cover **(Figure S4.4**, reaction 5). Additionally, the 10 atom-length 2-nitrobenzyl linker, which is the length of approximately 3 bases, attaches the 7-nucleotide long toehold cover domain to the rest of Competitor Cover. Its presence in the phosphodiester backbone potentially disrupts local base stacking interactions and increases the rate of end fraying of the duplex. Spurious cleavage of the 2-nitrobenzyl linker resulting in the unbinding of the toehold cover (**Figure S4.4**, reaction) could also create an AHC species that could react with and sequester HW. Sequestration of HW could also occur because of some combination of these factors.

To classify the ways that the Pre-active Hill Competitor mixture might react with HW, we assumed that PHC was initially composed of two populations, Inactive (IC) Competitor and spuriously generated AHC. AHC refers to Hill Competitor that had its 2-nitrobenzyl linker photocleaved, and its cover dissociated, so that it could react rapidly with HW and sequester it via a 7-nt toehold initiated reaction. IHC refers to Competitor that had its 2-nitrobenzyl linker intact and may or may not have had 5' truncation errors on its cover strand, possibly exposing a few end bases of the toehold to initiate binding of HW. AHC and IHC should sequester Wire at different rates; the AHC reaction proceeding with a rate constant for 7-nt toehold strand displacement reaction, on order 10^6 M^{-1} s^{-1} and IHC with an effective rate constant that reflects the collection of duplexes in truncated or frayed states with exposed toeholds, which we hypothesized would be on order the rate constant for a toehold mediated strand displacement reaction initiated by a toehold of 0 ~ 4 nucleotides. The rate constant for the reaction between IHC and HW should therefore be several orders of magnitude lower than the rate constant for the reaction between AHC and HW. To measure these rate constants, we first compared the rates of

reaction of HW with a PHC solution (which presumably also contained some AHC) and with a solution of AHC that was generated by exposing PHC to 302 nm UV light on a UVP bench top transilluminator for 30 minutes. We mixed 200 nM Source and 200 nM Initiator in multiple wells of a 96-well plate. After this reaction reached steady state, we added 0 to 1000 nM AHC or PHC separately to the wells and tracked the decreases in fluorescence over time (**Figure S4.8**). We observed rapid drops in fluorescence after the addition of AHC and the signal generated was completely quenched at AHC concentrations of 200 nM and higher (**Figure S4.8a**). For PHC, we observed an initial sharp decrease in fluorescence intensity followed by a slower decrease that appeared exponential in character (Figure **S54.8b**). The magnitude of the initial rapid fluorescence intensity decrease appeared roughly proportional to the concentration of PHC added, suggesting that PHC contained two populations of complex, one reacting quickly and the other reacting more slowly. These results supported the hypothesis that the PHC solution was composed of some fast-reacting AHC and IHC that reacted with HW at a slower rate.

We conducted experiments with lower concentrations of PHC, Source and Initiator to measure the effective reaction rate between IHC and HW and the fraction of AHC in a solution of PHC. We calibrated these reactions by measuring the change in fluorescence at steady state between the wells. First, 0 to 22 nM of Initiator was added to individual wells of 20 nM of Source. Similar to the FCR calibration we employed in the linear pattern system (SI Section 4 above), we then measured the fluorescence change at steady state between: 7 nM and 0 nM Initiator wells, 12 nM and 7 nM Initiator wells, 17 nM and 12 nM Initiator wells, and 22 nM and 17 nM Initiator wells. The average fluorescence change corresponded to a HW concentration change of 5 nM and allowed us to convert all fluorescence traces into a change in HW concentration.

The steps for measuring the leak rate constants proceed as follows. We mixed 20 nM Source and 22 nM Initiator in separate wells of a 96-well plate. After the irreversible reaction between Source and Initiator had gone to completion, PHC was added to each well to final concentrations of 5 to 100 nM (**Figure S4.9**). As we observed previously in experiments with higher concentrations of Source, Initiator and PHC, upon addition of PHC, the HW concentration in the wells initially dropped sharply then decayed more gradually over 17 hours of measurement. For each kinetic trace, we determined the fraction of AHC present within the Competitor mixture by calculating the ratio of the initial sharp decrease in HW concentration, HW_d, to the initial total concentration of PHC, $[HW_d]/[PHC]$. We assumed that the concentration of HW_d consumed corresponded to the concentration of AHC in the added PHC mixture; $[HW_d]/[PHC] = [AHC]/[PHC]$. The average fraction of AHC was 0.15 ± 0.09 (mean ± standard deviation). Having determined the initial fractions of IHC and AHC, we estimated the rate constants for slow (kh4) and fast (kh5) HW degradation reactions by fitting simulated kinetic traces to the experimental data using least-squares regression; the values of kh4 and kh5 were 1.1E3 ± 0.2E3 M^{-1} s^{-1} and 2.5E5 ± 0.4E5 M^{-1} s^{-1} (95% CI) respectively. These rate constants were used in subsequent reaction-diffusion models of hill patterns.

Importantly, we did not model the effects of toehold occlusion by photocleaved Competitor Cover on the toehold of AHC (**Figure S4.4**, reaction 6). Assuming the cleaved cover had a bimolecular rate constant of hybridization to the toehold of 3E6 M^{-1} s^{-1} (an established value for bimolecular rate constants of 7-nucleotide length) and that the toehold composition consisted equally of A/T and G/C nucleotide content, resulting in a free energy change of $\Delta G° =$ -9.2 kcal mol^{-1} upon hybridization, we calculated the fraction of unbound and bound toehold

cover at equilibrium at 25 C. To do this we estimated the rate of toehold cover unbinding from its toehold domain:

$$k_{off} = k_{on} e^{\frac{\Delta G^\circ}{RT}} \text{ (8)}$$

The k_{off} value is 0.54 s^{-1}. At equilibrium, approximately 70% of the toehold is uncovered and the characteristic time for unbinding of the cleaved cover is $1/k_{off}$ or 1.86 seconds. Therefore, because the dynamics of hill pattern formation and recovery occured over a timescale of at least 10 hours and the timescale for equilibration of cleaved cover is under 10 seconds, we excluded toehold occlusion by the cleaved cover fragment in well-mixed models and reaction-diffusion models of hill pattern dynamics.

The final leak reaction we considered was reaction 8 (**Figure S4.4**). Initiator could bind to the exposed toehold on AHC and branch migrate to become partially hybridized to it. We assumed that Initiator reacted with AHC by hybridizing to its 7-nucleotide length toehold using the same literature value for the bimolecular rate constant assumed for 7 nt toehold mediated strand displacement reaction throughout this work, i.e. 3E6 M^{-1} s^{-1}. We incorporated this rate constant into hill pattern reaction-diffusion models as kh6. We also assumed that the Initiator:AHC complex could undergo branch migration and toehold unbinding to reform Initiator and AHC complex; we adapted the form of the effective unimolecular rate constant for this type of dissociation reaction which has been determined previously[76]:

$$k_{off} = k_{on} \frac{1}{N} e^{\frac{\Delta G^\circ}{RT}} \text{ (9)}$$

where N is the length of the branch migration domain available to Initiator for hybridization after toehold binding to form the three-strand intermediate complex. Here N has a length of 12 nucleotides. 1/N is a correction term that accounts for the number of iso-energetic branch migration states that contribute to the three-strand complex and accounts for the additional time

the complex spends in these microstates, which lowers the rate of disassociation relative to that of a unimolecular reaction lacking these states. The dissociation rate constant of Initiator:AHC, kh7, as computed using Equation 9, is 0.045 s^{-1} at 25 C; this value was used in reaction diffusion models.

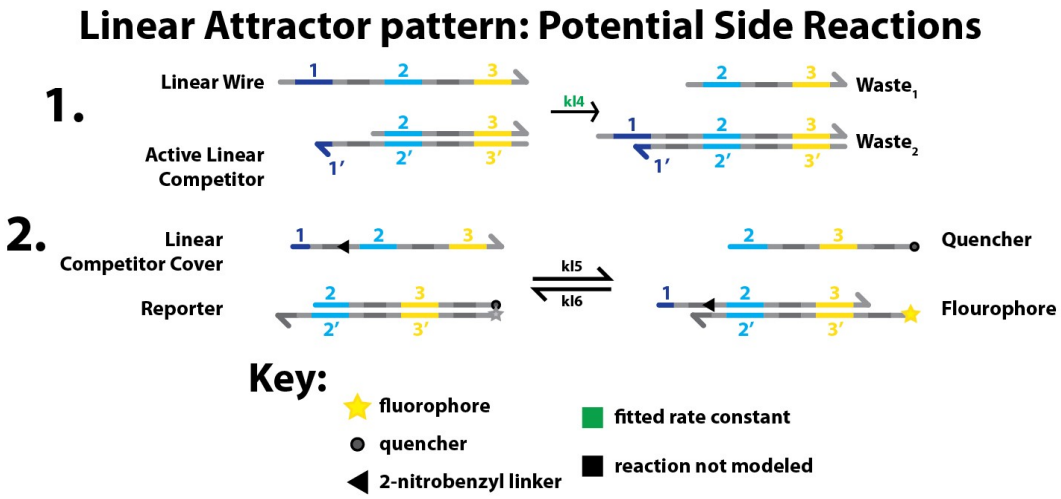

Figure S 4.3. Linear pattern side reactions.

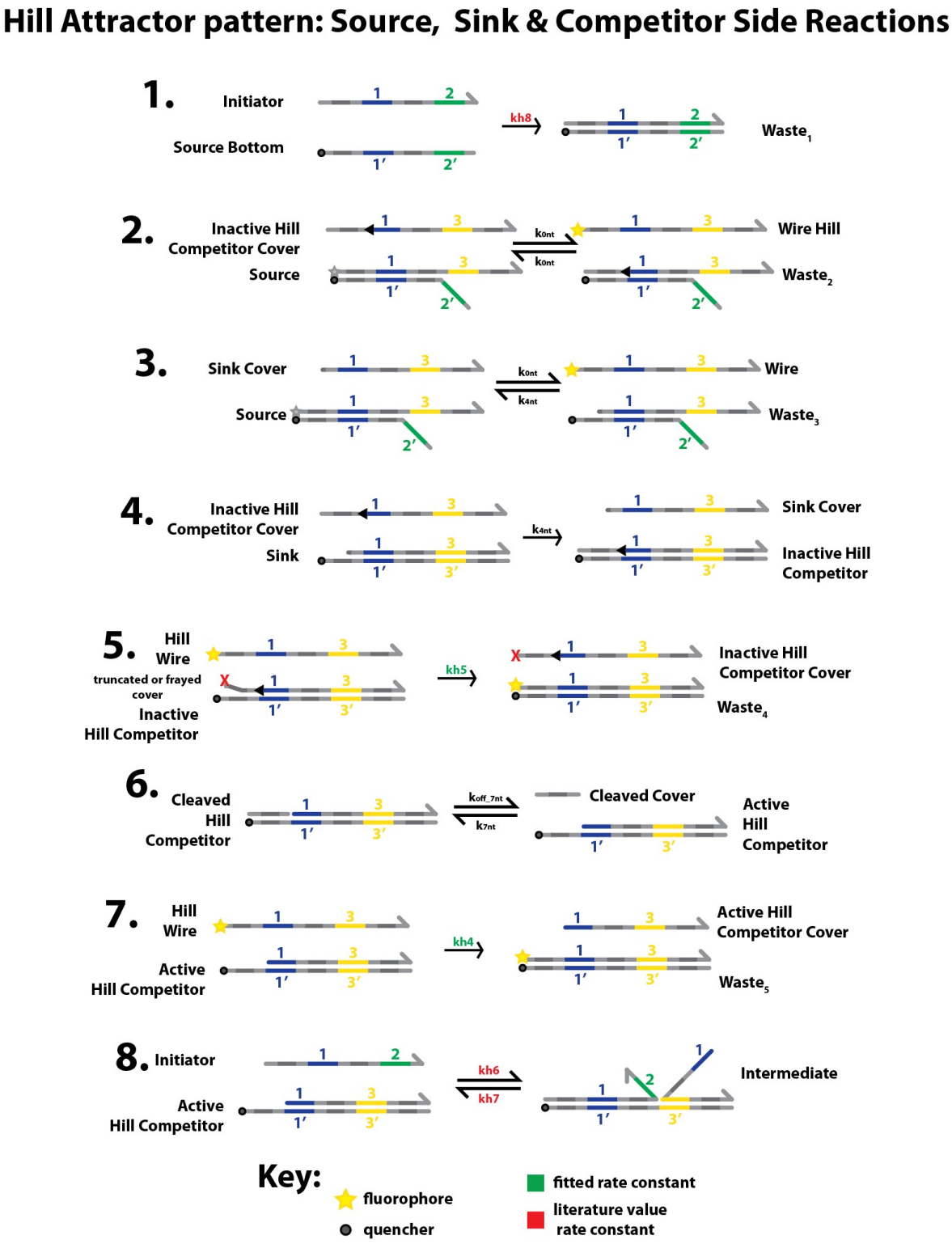

Figure S 4.4. Potential unintended side reactions occurring hill-pattern formation and recovery.

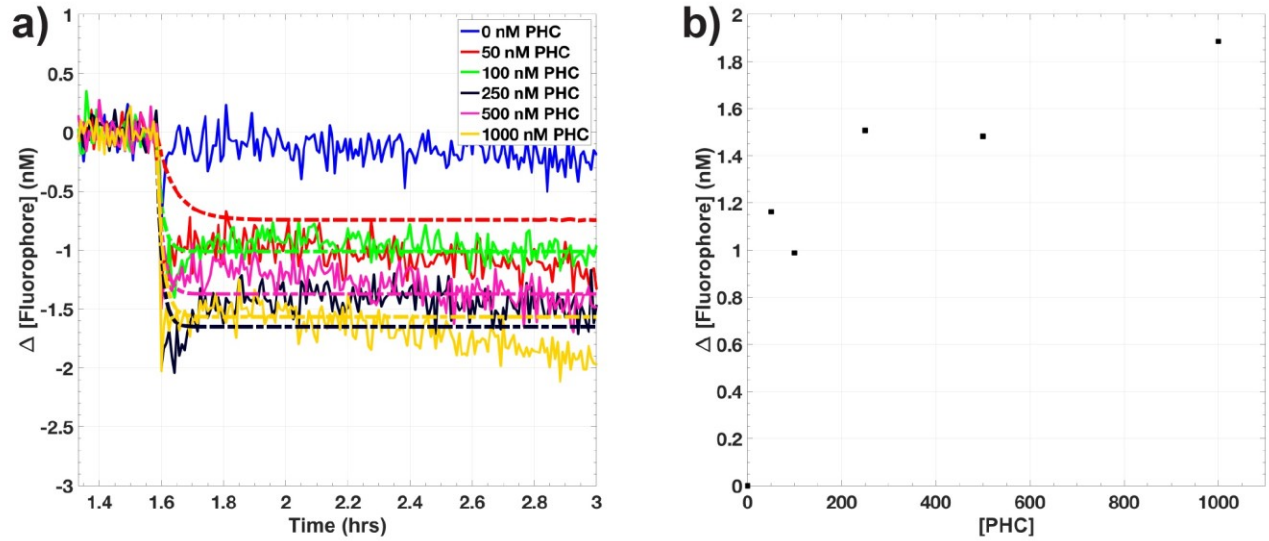

Figure S 4.5. a) Addition of 0 to 1000 nM Pre-active Hill Competitor (PHC) to an equilibrated reaction of 200 nM Linear Wire (LW) and 20 nM Reporter. Dashed lines indicate results of the least squares fit of the ALC-LW leak rate constant kl4. b) Total change in Fluorophore concentration vs. concentration of PHC added to each reaction well.

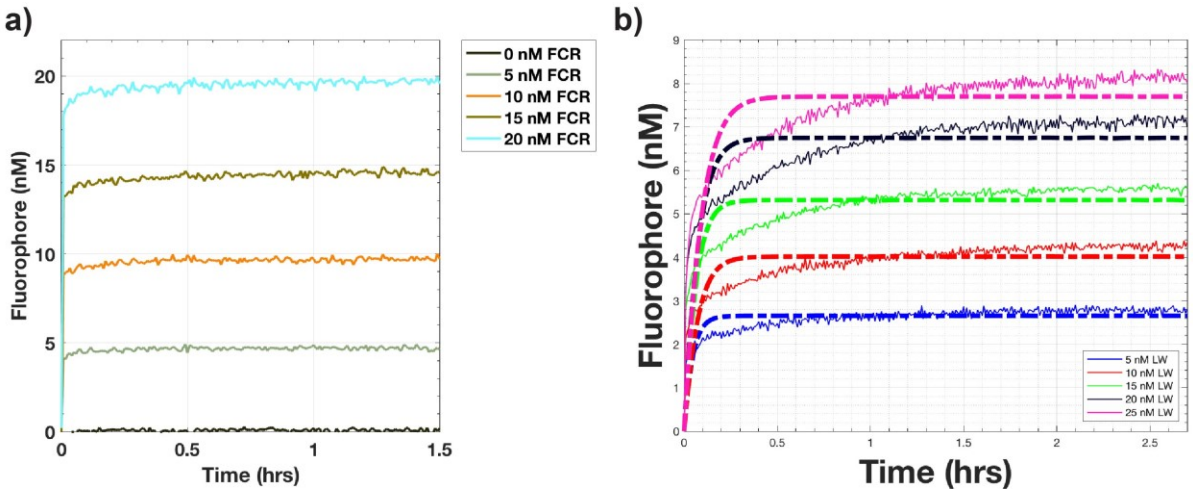

Figure S 4.6. a) Addition of 0 to 20 nM Full Complement of the Reporter (FCR) to 20 nM of Reporter. b) Concentration of Fluorophore released after adding 5 to 25 nM of Wire to 20 nM Reporter. Dashed lines show results of least squares fit of model. These results were used to determine the concentration of Linear Wire (LW) released in characterizations of the leak reaction for the linear pattern network (See SI Section 4 text).

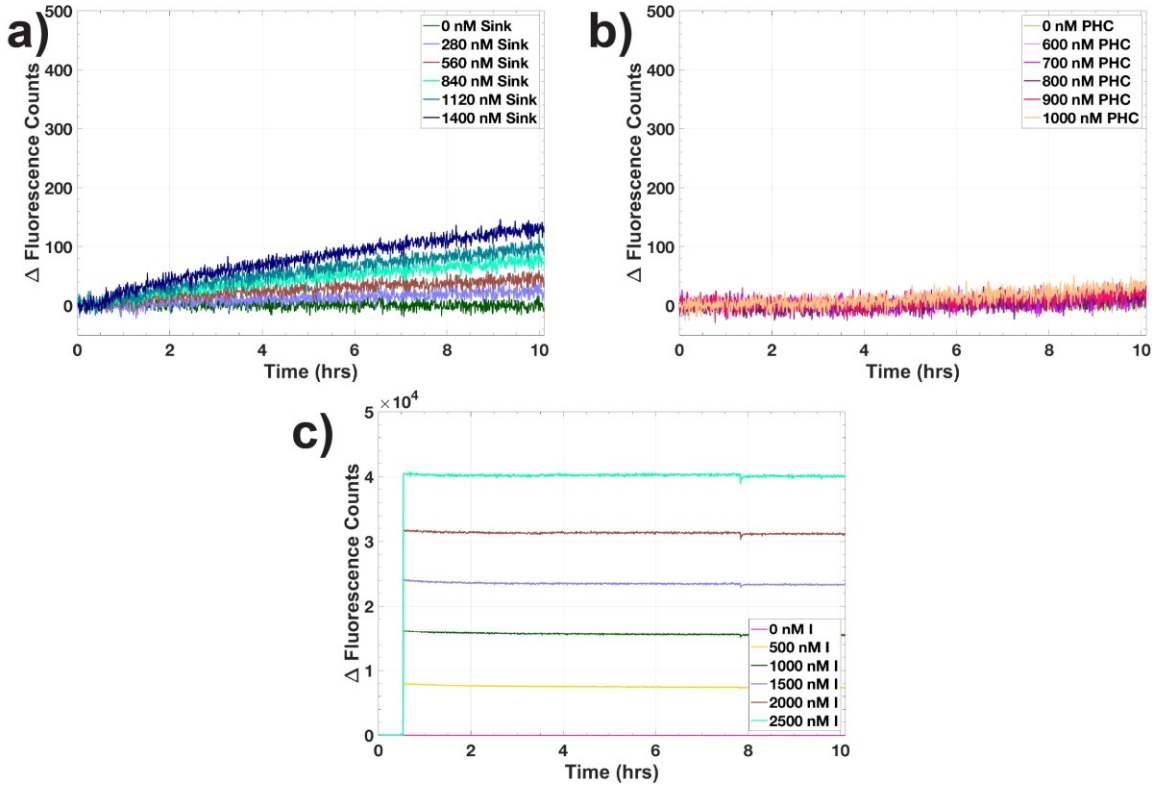

Figure S 4.7. Changes in solution fluorescence intensity after c) 0 to 2500 nM Initiator (I) was added to 2500 nM Source. b) 0 to 1000 nM PHC was added to 2500 nM Source. b) 0 to 1400 nM Sink was added to 2500 nM Source.

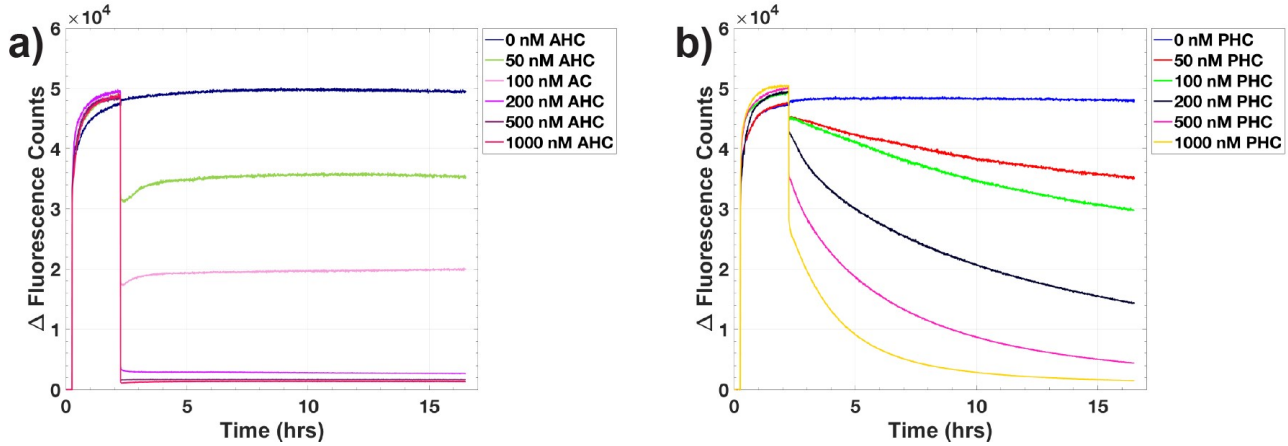

Figure S 4.8. Changes in solution fluorescence intensity after a) 0 to 1000 nM Active Hill Competitor (AHC) was added to a solution containing 200 nM Source and 200 nM Initiator that were allowed to react to completion. b) 0 to 1000 nM Pre-active Hill Competitor (PHC) was added to a solution containing 200 nM Source and 200 nM Initiator that were allowed to react to completion.

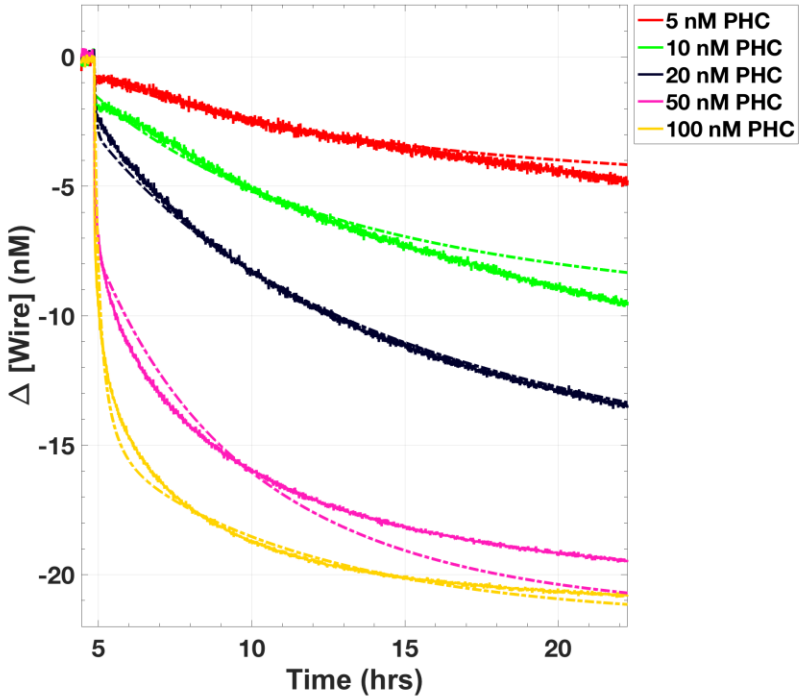

Figure S 4.9. Measured changes in HW concentration after 5 to 100 nM PHC was added a solution where 22 nM Initiator and 20 nM Source were allowed to reaction to completion to produce 20 nM HW.

4.4.5 Reaction-diffusion models:

Models were implemented in MATLAB and consisted of a system of coupled 1-dimensional reaction-diffusion partial differential equations solved over a domain of 1500 microns. One reaction is included for each chemical species, where S_i, D_i and R_i are the species concentration, diffusion coefficient, and total reaction rate respectively:

$$\frac{\partial [S_i](t,x)}{\partial t} = D_i \nabla^2 [S_i](t,x) + R_i \quad (10)$$

Model Objectives:

For both linear and hill pattern systems, we first sought to use models of the reaction-diffusion processes to determine whether the proposed reactions coupled to diffusion of the species within a diffusion cell would produce stable patterns; we also sought to determine how fast patterns would form. Second, it was our objective to determine whether the experimental dynamics yielded rate constants and diffusion coefficients in reasonable agreement, within roughly an order of magnitude or so, of literature values for toehold-mediated strand displacement rate constants and measured values of DNA diffusion coefficients in 30%(v/v) PEDGA hydrogels to demonstrate that the observed dynamics were the result of the designed reaction networks. Lastly, using optimized parameters obtained by fitting the models to the experimental dynamics of pattern formation, we sought to establish whether the circuit recovered its original steady state in accordance with its intended behavior as an attractor pattern.

While designing the microfluidic platform, we initially used the 1-D models of hill pattern dynamics to specify the dimensions required for the diffusion cells so that 1) the entire width of the hill patterns fit within the center third of the diffusion cell length and 2) to ensure that degradation of Wire occurred within the cell and to mitigate diffusive flux of Wire at the cell

boundaries. Additionally, we selected the toeholds of the designed reactions and concentrations of supplied reactants to satisfy this condition. Both linear and hill pattern models initially used literature values for bimolecular and unimolecular strand displacement rate constants, and values of single and double stranded DNA diffusion coefficients measured in separate experiments (SI: Results & Discussion: Section 4.4.7 and Dorsey et al.[84]).

We then performed least-squares regression to fit the rate constants of key reactions and fit ss and ds diffusion coefficients for all species to experimental formation data for both sets of patterns to. Again, it was our goal to determine whether the dynamics of the stable patterns we observed experimentally produced rate constants and diffusion coefficients in reasonable agreement, (to within roughly an order of magnitude) of known literature values for strand displacement reaction and DNA diffusivity. This agreement would support our claim that the observed dynamics of pattern formation were the result of the designed reaction networks. We then supplied the fitted parameters to the models as well as the pattern profile measured immediately after UV perturbation as an initial condition from which the system could recover; we compared the predicted timescale of recovery to the experimentally measured timescale of recovery with the objective that both recovery timescales should be on the same order of magnitude. Correspondence between recovery timescales would provide additional support for the designed systems' function as attractor patterns.

During least-squares regression, the following general constraints were employed: the lower and upper bounds for fitted bimolecular rate constants were 0 M^{-1} s^{-1} and 4E6 M^{-1} s^{-1}; the lower and upper bounds for fitted ss and ds diffusion coefficients were 0 and 150 um^2 s^{-1}, which was chosen based on previous diffusion measurements of a 42 nucleotide strand in 30%(v/v) PEDGA hydrogels[84] where the magnitude of the diffusion coefficient was 60 ± 28 um^2 s^{-1} (mean

± standard deviation). All single stranded species were assigned the same single stranded diffusion coefficient. All double stranded species were assigned the same double stranded diffusion coefficient. All simulated results of linear and hill attractor pattern formation are presented in the main text figures as dashed lines. We used the same definition of pattern formation and recovery timescale defined in the main text during discussion of the model construction and dynamics in the sections below.

Linear Pattern Models:

The reaction-diffusion equations comprising the PDE model were:

$$\frac{\partial[LW](t,x)}{\partial t} = D_{ss}\nabla^2[LW](t,x) - k_{l1}[LW](t,x)[Reporter](t,x) - k_{l4}[LW](t,x)[ALC](t,x) + k_{l2}[Quencher](t,x)[Fluorophore](t,x)$$

$$\frac{\partial[Reporter](t,x)}{\partial t} = D_{ds}\nabla^2[Reporter](t,x) - k_{l1}[LW](t,x)[Reporter](t,x) + k_{l2}[Quencher](t,x)[Fluorophore](t,x)$$

$$\frac{\partial[Fluorophore](t,x)}{\partial t} = D_{ds}\nabla^2[Fluorophore](t,x) - k_{l2}[Quencher](t,x)[Fluorophore](t,x) + k_{l1}[LW](t,x)[Reporter](t,x)$$

$$\frac{\partial[Quencher](t,x)}{\partial t} = D_{ss}\nabla^2[Quencher](t,x) - k_{l2}[Quencher](t,x)[Fluorophore](t,x) + k_{l1}[LW](t,x)[Reporter](t,x)$$

$$\frac{\partial[ALC](t,x)}{\partial t} = D_{ds}\nabla^2[ALC](t,x) - k_{l4}[ALC](t,x)[LW](t,x)$$

The fit parameters for the linear pattern model were the forward and reverse Reporting rate constants (**Figure 2a** main text), kl1 and kl2, leak rate constant kl4 between Linear Wire (LW) and spuriously activated Competitor (ALC), and ss and ds diffusion coefficients for all species in the reaction network. The reaction rate constants kI1, kI2 and kI4 were estimated by fitting the nondimensionalized solution of the partial differential equation model to normalized experimental fluorescence profiles of pattern growth and stabilization (described below) using MATLAB's built-in *lsqcurvefit* function. A single experimental fluorescence profile consisted of a 1-

dimensional vector of normalized fluorescence intensity pixels spanning the entire 1500 um length of a single diffusion cell at a given time point. The values of the profiles for a single pattern were normalized to the maximum and minimum intensities measured over all x-values and over all time points for that specific pattern so that the rescaled intensities ranged from 0 to 1. Fluorescence profiles for 7 individual time points were used to fit the model parameters to the normalized intensity data for a single pattern (main text **Figure 4.3b**). All single stranded species were assigned the same diffusion coefficient, D_{ss}. All double stranded species were assigned the same diffusion coefficient, D_{ds}. The initial concentrations of all species in the diffusion cells was 0. The concentrations of Pre-active Linear Competitor at the left and right boundaries of the diffusion cell were set to the concentrations used in the experiment. We set the right-side boundary concentrations of LW, Reporter, Quencher and Fluorophore species by assuming that the reporting reaction had reached equilibrium in the upstream reservoir; the initial reservoir concentrations of Reporter and LW (before the equilibration of the reporting reaction, **Figure 4.3a**, main text) were 400 nM and 500 nM; the equilibrated boundary concentrations of LW, Reporter, Quencher, and Fluorophore were determined from the definition of the reporting reaction equilibrium constant, K_{eq} = kl1/kl2, and incorporated mass balances reflecting the change in concentration, X, as a function of the initial concentration and fitted rate constants:

$$K_{eq} = \frac{[X][Quencher_0 + X]}{[Reporter_0 - X][LW_0 - X]} = \frac{kl1}{kl2} \quad (11)$$

Solving for the unknown X as a function for a particular set of rate constants and the known initial concentrations gives the concentrations of the different species at the right hand boundary; the PDE model performed this calculation during regression.

The model incorporated the leak reaction between LW and spuriously generated ALC (**Figure S4.3**, Reaction 1) by assuming that this reaction went to completion within the upstream reservoir holding LW, Reporter, and PLC. We made this assumption about the reservoir concentrations because typically 1.5 hours passed between reservoir preparation and the start of an experiment, and well-mixed kinetic models predicted that the coupled reactions between LW and ALC and LW and Reporter reached steady state within 1 minute after initial mixing (Figure S10) assuming that the reactions proceeded with the fitted rate constants obtained from the experiments discussed in SI Results & Discussion: Section 4.4.4. **Figure S4.10** shows how this assumption results in the same steady state as a system where the LW-ALC reaction is initiated at time t = 0. The reaction of 500 nM LW with 400 nM Reporter, 70 nM ALC (which is 7% of [PLC] = 1000 nM) and 40 nM Quencher are the dashed lines in the figure. After roughly 30 seconds, this reaction reaches the same concentrations as a reversible reporting reaction with initial concentrations of 430 nM LW, 400 nM Reporter, and 40 nM Quencher (solid lines), suggesting that the consumption of LW by 70 nM ALC, at long times, yields the same steady state solution as assuming an initial LW concentration of 430 nM, where 70 nM ALC has already reacted with an initial concentration of 500 nM Wire. As such, we assumed that no AC was present in the RHS reservoir and that its concentration at the RHS boundary of the diffusion cell was 0. At the LHS boundary, 7% of the PLC concentration was assumed to be ALC.

The average values of the fit-parameters are listed in **Table S4.3**. The predicted timescale of pattern formation was roughly 4.3 hours, which exactly matched the experimentally observed timescale of formation of 4.3 hours. The fitted reporting rate constants for the reporting reaction, kl1 and kl2, were around 10^4 M^{-1} s^{-1}. The expected order of magnitude of a bimolecular rate constant for a 5-nt toehold is, correspondingly 10^4 M^{-1} s^{-1} [76]. We observed that the fitted value of

kl4 depended on the initial guess supplied during regression. An initial guess of 3E4 M^{-1} s^{-1} resulted in an average fit value of 2.1E4 ± 1.1E4 M^{-1} s^{-1} (95% CI). An initial guess of 1.5E6 M^{-1} s^{-1}, based on the average value of kl4 determined in well-mixed experiments, resulted in an average fit value of 1.5E6 ± 1.5E4 M^{-1} s^{-1} (95% CI). Both values of rate constant kl4 did not appear to change the formation or recovery dynamics of the model; additionally, the fluorescence profiles predicted at each timepoint, as shown in Figure 3 and Figure 4 of the main text, appeared identical in both cases. The fitted value of kl4 determined in well-mixed experiments was 1.47E6 ± 0.052 M^{-1} s^{-1} (95% CI). This result suggested that the optimization phase space for kl4 was flat and that the system may be specified by kl1, kl2, and the single and double stranded diffusion coefficients. As such, based on or previous estimation of this rate constant in well mixed solution, and the fact that the toehold size for ALC was 7 nucleotides, corresponding to an expected bimolecular rate constant around 10^6 M^{-1} s^{-1}[176], we report the value of kl4 obtained from the reaction-diffusion model as 1.5E6 ± 1.5E4 M^{-1} s^{-1} (95% CI).

Several additional factors could influence our estimation of kl4. . First, the uncertainty in the fraction of ALC and ILC in the PLC mixture may have contributed to overestimation of the leak reaction rate in time at particular points in space. Additionally, the accuracy of the solution obtained from numerical integration and regression analysis could have been affected by noise in the fluorescence intensity profiles used to fit the model. In Dorsey et al., the average diffusion coefficient for a 42 nucleotide long DNA strand was 60 ± 28 μm^2 sec^{-1} (± standard deviation)[84]. The mean of the fitted ss DNA diffusion coefficient was 41 ± 11 μm^2 sec^{-1} (95% CI) and fell within one standard deviation of mean value for single stranded DNA diffusion coefficients previously measured in 30% (v/v) PEGDA hydrogels[84]. The mean of the fitted ds DNA diffusion coefficient was 29 ± 3 μm^2 sec^{-1}(95% CI) and fell within one standard deviation of the mean value for a double

stranded diffusion coefficient measured in a separate diffusion-only experiment in 30% (v/v) PEGDA hydrogels (see Results and Discussion 4.4.7 for measurement of ds DNA diffusion coefficient); the mean value of the ds diffusion coefficient was 23 ± 6 μm^{-1} s^{-1} (mean ± standard deviation).

We then simulated linear pattern recovery after UV exposure using the parameters fit to the dynamics of pattern formation. The model used the fluorescence intensity profile of the pattern present immediately after UV exposure as the initial Fluorophore concentration condition within the channel; this dimensionless intensity profile was converted into a Fluorophore concentration profile for the model by multiplying it by the Fluorophore concentration at the right boundary. The model predicted pattern recovery in 3 hours after the first UV exposure which was 1 hour longer than the 2 hr experimental recovery timescale. For the 2nd and 3rd UV perturbations, the model predicted pattern stabilization within 1 hour which agreed with the experimental recovery timescales of 1 hour. Given these results, we concluded that the proposed linear pattern reaction-diffusion mechanism recapitulated the experimentally observed formation and recovery dynamics.

Hill Pattern Models:

Reaction-diffusion models of hill pattern formation and recovery after UV-perturbation were set up following the same approach for modeling the formation and recovery of linear patterns. These models used the designed reactions and and relevant leak reactions (see SI: Results & Discussion, Section 4.4.4) for the hill pattern formation process. The models were composed of the following partial differential equations:

$$\frac{\partial [HW](t,x)}{\partial t} = D_{ss}\nabla^2[Wire](t,x) - k_{h2}[HW](t,x)[Sink](t,x) - k_{h4}[HW](t,x)[AHC](t,x) - k_{h5}[HW](t,x)[IC](t,x) + k_{h1}[Source](t,x)[Initiator](t,x)$$

$$\frac{\partial[Source](t,x)}{\partial t} = D_{ds}\nabla^2[Source]](t,x) - k_{h1}[Source](t,x)[Initiator](t,x)$$

$$\frac{\partial[Initiator](t,x)}{\partial t} = D_{ss}\nabla^2[Initiator]](t,x) - k_{h1}[Source](t,x)[Initiator](t,x) - k_{h5}[ACH](t,x)[Initiator](t,x) - k_{h8}[SB](t,x)[Initiator](t,x)$$

$$\frac{\partial[Sink](t,x)}{\partial t} = D_{ds}\nabla^2[Sink]](t,x) - k_{h2}[Sink](t,x)[HW](t,x)$$

$$\frac{\partial[IHC](t,x)}{\partial t} = D_{ds}\nabla^2[IHC]](t,x) - k_{h5}[IC](t,x)[HW](t,x)$$

$$\frac{\partial[AHC](t,x)}{\partial t} = D_{ds}\nabla^2[AHC]](t,x) - k_{h4}[AHC](t,x)[HW](t,x) - k_{h6}[AHC](t,x)[Initiator](t,x) + k_{h7}[Intermediate](t,x)$$

$$\frac{\partial[Intermediate](t,x)}{\partial t} = D_{ds}\nabla^2[Intermediate]](t,x) - k_{h7}[Intermediate](t,x) + k_{h6}[AHC](t,x)[Initiator](t,x)$$

$$\frac{\partial[SB](t,x)}{\partial t} = D_{ss}\nabla^2[SB](t,x) - k_{h8}[SB](t,x)[Initiator](t,x)$$

We first used this reaction-diffusion model to determine whether the observed dynamics of hill pattern formation (**Figure 4.5b**) were consistent with the designed reactions, and predicted rate constants and diffusion coefficients on the order of those expected from literature. The Hill Wire (HW) production rate constant, kh1, sink rate constant, kh2, and diffusion coefficients for ss and ds DNA D_{ss} and D_{ds} were fit to the measured fluorescence intensity profiles of hill pattern formation (**Figure 4.5a**, main text). All ss species were assigned the same ss DNA diffusion coefficient as a fit parameter; all ds complexes were assigned the same ds DNA diffusion coefficient as a fit parameter.

The leak rate constants for reactions between Wire and Inactive Hill Competitor (IHC), kh3, and Wire and Active Hill Competitor (AHC), kh4, measured in well-mixed solution were incorporated into the model as constants and assigned the value that was measured in well-mixed solution. Side reactions between excess Source Bottom strand (SB) and Initiator, and Initiator and AHC were assigned literature values for their bimolecular rate constants of kh7, and kh5 and kh6

based on the toehold size that initiated these reactions. kh7 was 3.5E6 M^{-1} s^{-1}, which is the biomolecular rate of two single oligos hybridizing at 25 ºC in standard buffer conditions[76]. For kh5 and kh6, spuriously active Competitor (AC) binds and unbinds Initiator through toehold binding, branch migration, and unbinding. The value of kh6 and kh7 was 3E6 $M^{-1}s^{-1}$ and 0.045 s^{-1} as explained previously in discussion of reaction network characterization in well-mixed conditions. The concentration of AHC at each boundary was set to be 15% of the total Pre-active Hill Competitor (PHC) concentration with the remaining fraction being IHC (see SI Results & Discussion: Section 4.4.4). The initial concentrations of all species in the diffusion cell were set to 0. The concentrations of species on the boundary were set to be the same as those in experiments (Figure 5a). The model for the hill patterns also took into account the fact that the Source complex was imperfectly quenched, which created a linearly increasing fluorescence background signal, increasing from the left to the right hand side of the hydrogel. To account for this effect in our model, we introduced an empirical parameter, γ, which was a scale factor between 0 and 1 reflecting the relative contribution of Source to the observed total fluorescence intensity. Therefore, the contribution of Source to the normalized intensity of fluorophore observed is:

$$Normalized\ Intensity(x,t) = \frac{[HW](x,t) + \gamma[Source](x,t)}{[HW](x_m,t_m) + \gamma[Source](x_m,t_m)} \quad (12)$$

where x_m, is the position where the summation of [HW] and γ*[Source] takes its maximum value which occurs at the peak position and t_m is the timepoint of the profile at steady state. The values of fitted parameters are listed in Table S4. The PDE model predicted pattern formation in roughly 6.5 hours which was within an hour of the average measured formation time of 6.9 ± 0.94 hours. The expected values for kh1 and kh2 were 3E6 M^{-1} s^{-1} and 5E3 M^{-1} s^{-1}, which was based on the toeholds sizes for these reactions (7 nucleotides and 4 nucleotides respectively).[76] These values

assume there are no modifications to or adjacent to the bases comprising the toehold. The values of fit parameters kh1 and kh2 obtained from the model were 3E6 M^{-1} s^{-1} and 5E4 M^{-1} s^{-1}, respectively. The average fitted value of kh1 matched the magnitude for the rate constant of a 7-nucleotide toehold initiated strand displacement reaction. The average fitted value of kh2 was one order of magnitude larger than its expected value and had same magnitude as a 5-bp toehold. Importantly, Sink:HW complex possessed a quencher and fluorophore at its duplex end. This pair terminated the end of toehold binding domain; Cyanine 3 fluorescent dye and its quencher pairing are known to significantly stabilize the ends of DNA and RNA duplexes, effectively acting as an extra base-pair on the duplex[171,172]. Therefore, the fitted value of kh2 is a reasonable expectation for the specific design of the circuit. The fits to the ss and ds diffusion coefficients were 35 ± 0.2 um^2 s^{-1} and 23 ± 0.2 um^2 s^{-1} respectively (95% CI). The fit to the ss DNA diffusion coefficient was statistically consistent with a previously measured diffusion coefficient, 60 um^2 s^{-1} ± 28 um^2 s^{-1} (mean ± st. dev.), for ss DNA in 30%(v/v) PEGDA hydrogels[84]. The, average value of the fitted ds DNA diffusion coefficient was also within 1 standard deviation of the diffusion coefficient for a ds complex that we measured (see SI Results & Discussion: Section 4.4.7).

We simulated hill pattern recovery by supplying the model with the mean values of fit parameters kh1, kh2, D_{ss}, D_{ds}, and γ. The initial HW profile for the model was the fluorescence intensity profile measured immediately after UV perturbation (**Figure 4.5c** main text). The intensity profile was converted into Fluorophore concentration by re-arranging equation 12 to solve for the concentration of HW using γ, the steady state peak intensity, and the Source concentration profile at steady state, which was determined from the pattern formation model. The predicted dynamics are shown as normalized intensity in **Figure 4.5c** of the main text alongside the experimentally measure dynamics of pattern recovery. Recovery of the pattern after

perturbation took 2.1 hours to reach steady state; this recovery time differed by a factor of 2.4 from the recovery time of 5 hours measured in experiments. While the predicted timescale of recovery was within an order of magnitude of the experimental timescale, we attribute the underestimation of the experimental timescale to our inability to measure the photocleavage efficiency of the 2-nitrobenzyl linker in the Competitor duplex within the microfluidic apparatus and degree of UV light attenuation across the hydrogel depth. Additionally, the cumulative effect of these unknowns and the uncertainties in key estimated leak rate constants affect the model's accuracy. Moreover, the relative amount of AHC generated from IHC during photocleavage impacts the rates at which IHC and AHC can react with HW and reversibly sequester Initiator respectively, which can then influence the timescale of recovery.

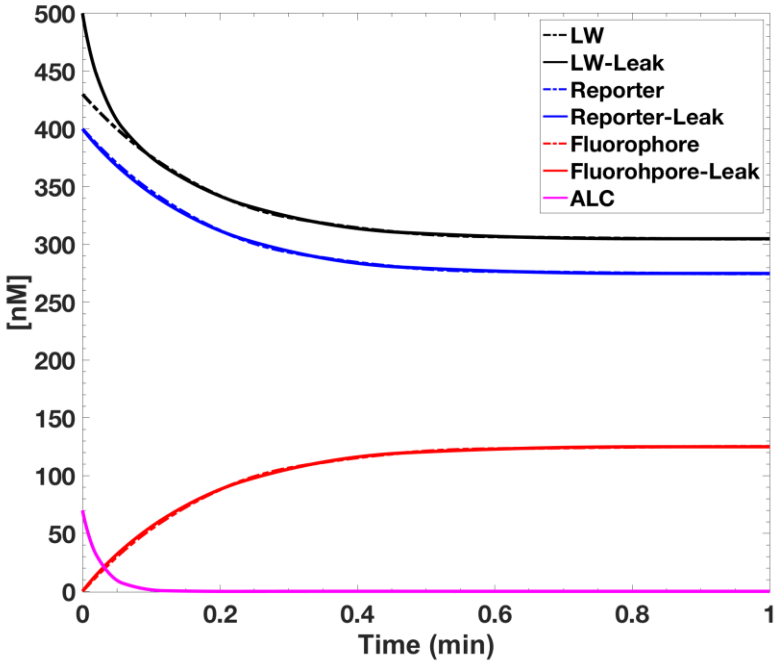

Figure S 4.10. A well-mixed reservoir reaction model of Linear Wire-Active Linear Competitor (ALC) leak. Dashed lines: initial concentrations of 500 nM LW, 400 nM Reporter, 40 nM Quencher, and 70 nM ALC. Solid lines: 200 nM Wire, 400 nM Reporter, 40 nM Quencher.

Table S 4.3 . Linear pattern fit parameters (95% CI)

Parameters	kl1	kl2	kl4	D_{ss}	D_{ds}
	2.8E4 ± 2.1E4 M^{-1} s^{-1}	8.7E4 ± 7.3E3 M^{-1} s^{-1}	2.1E4 ± 1.1E4 M^{-1} s^{-1}	41 ± 11 μm^2 s^{-1}	29 ± 3 μm^2 s^{-1}

Table S 4.4. Hill pattern fit parameters (95% CI)

Parameters	kh1	kh2	D_{ss}	D_{ds}	γ
	3.0E6 ± 5.5E3 M^{-1} s^{-1}	5.0E4 ± 210 M^{-1} s^{-1}	35 ± 0.20 μm^2 s^{-1}	23 ± 0.20 μm^2 s^{-1}	6.5E-3 ± 1.9E-3

4.4.6 Timescale for the average peak intensity of hill-shaped patterns to return to within 10% of steady state intensity after repeated UV-induced perturbation:

The range of the recovery times was 2.2 hours respectively for the first and second perturbations. The average time across all 4 patterns to return to 10% of the final measured steady state before any UV perturbation was 6.7 hours for the first perturbation and 8 hours for the second perturbation.

Table S 4.5. Measured times for peak intensity to return to within 10% of its maximum value after pattern perturbation

	Cell 1	Cell 2	Cell 3	Cell 4
First perturbation	7.8 hrs	6.7 hrs	5.6 hrs	6.7 hrs
Second perturbation	9.8 hrs	7.6 hrs	7.6 hrs	7.6 hrs

4.4.7 Determination of double stranded DNA diffusion coefficient in the hydrogel medium:

We separately measured the diffusion coefficient of ds DNA in 30%(v/v) PEGDA hydrogels. Wire:Sink(noQ) was allowed to diffuse into the hydrogel from a boundary concentration of 200 nM at the right-side of the gel. The constant was determined using methods

previously described in Dorsey et al.[84] where the diffusion constant is fit, using nonlinear least-squares regression, to time-lapsed fluorescent profiles of the DNA as it diffused into 30% (v/v) PEGDA hydrogels. A graph of the diffusion profile and fit are shown in **Figure S4.11**. The diffusion coefficient was 23 ± 6 μm^{-1} s^{-1} (mean ± standard deviation).

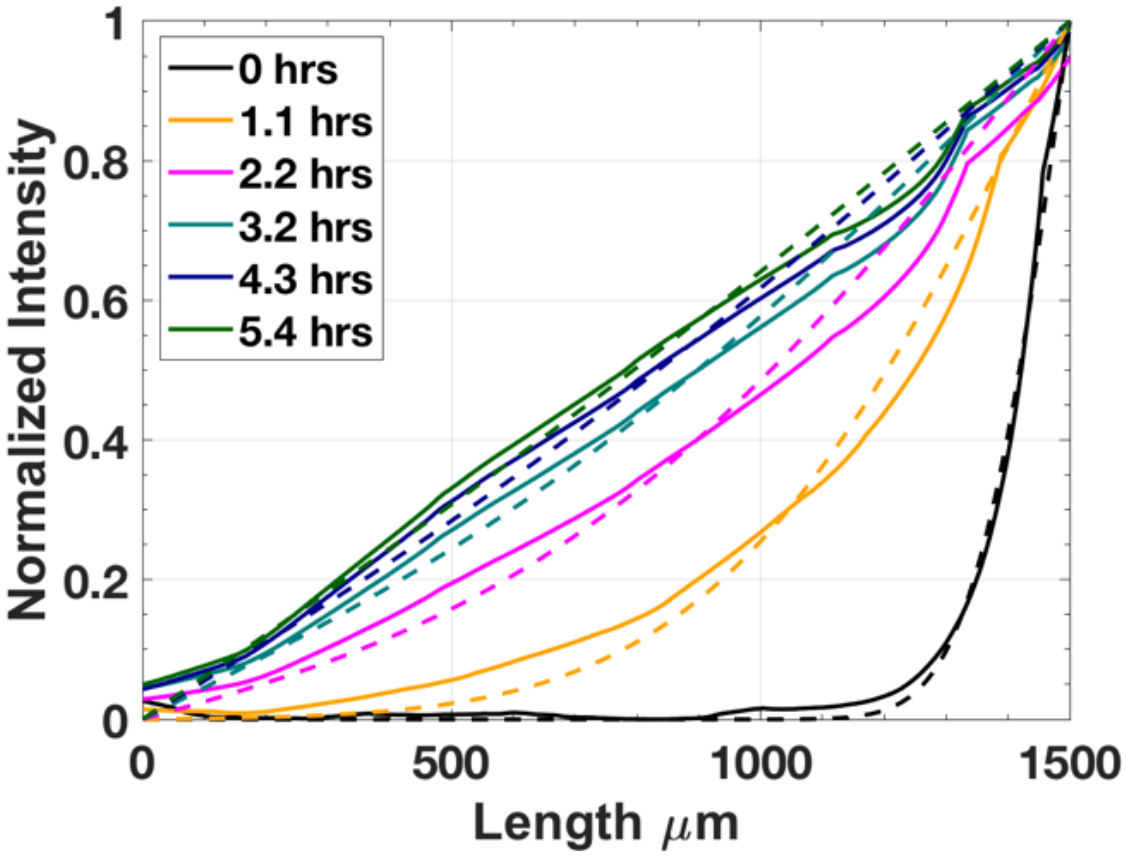

Figure S 4.11. Formation of a diffusive gradient in a diffusion cell. The boundary conditions consisted of a solution of 200 nM of a Hill Wire:Sink(noQ) complex in 1X TAE /Mg^{2+} buffer at the right side boundary and 1X TAE Mg^{2+} buffer with no DNA at the left side boundary. Solid lines indicate experimental data while dashed lines indicate the least-squares fit to the solution of the 1-D diffusion equation with homogenous boundary conditions

Chapter 5 A DNA-based reaction-diffusion associative memory for storage & repair of spatial molecular patterns

Summary:

Networks of chemical reactions control the behavior of cells; a major goal of chemistry is to understand how coupled reactions can likewise control designed materials and devices. Such coupled reactions could cause a material to change shape, synthesize or degrade its components or change its structural organization. While large chemical reaction networks, such as those based on DNA hybridization or enzymatic interactions, have been designed to perform these tasks in well-mixed solution using concentrations of biomolecular species as input and outputs, a key challenge to the design of these systems is to coordinate sensing and information flow spatiotemporally. Here, we sought to develop a key form of spatial integration of information using chemical reactions and signal transport via diffusion: an adaptive associative memory that stores and repairs spatial patterns using a consensus algorithm. We asked whether a material composed of these functionalities was capable of storing two dimensional patterns across a distributed network, and what its limitations were for repairing point mutations that might occur to stored patterns. We observed that a distributed two-dimensional network of nodes was capable of repairing a single pulse of mutations impacting up to 30% of its nodes. Additionally, when networks were damaged continuously overtime, the rate at which mutations accumulated was proportional to the rate of mutation; suggesting that a reliance on point mutation correction via neighboring signals alone is not suitable for combating continuous mutation at a frequency of damage approaching the rate of repair.

5.1 Introduction

During biological programs of morphogenesis, complex spatial patterns develop within tissues as a result of complex morphogenic cues, intracellular signaling cascades, and external biochemical stimuli. Fundamentally, such processes are governed by reaction-diffusion phenomena, where populations of cells and tissues constantly sense and integrate large and often noisy sets of biological cues in the form of diffusing signals. Importantly, information about an organism's homeostasis and surrounding environment can be sensed, stored, and communicated across a decentralized network of cells. Similarly, during processes of tissue injury and subsequent wound-healing, damaged and inflamed tissues release a myriad of diffusing cytokine factors which are sensed by surrounding healthy tissues, resulting in coordinated and directed growth and formation of blood vessels towards the site of injury as part of a complex spatiotemporal response.[173,174] Such complex behaviors are not limited to multicellular organisms, single-cell organisms such as bacteria have developed quorum sensing circuits that allow colonies of cells to make population dependent decisions regarding initiation of metabolically intensive processes like biofilm formation or degradation.[44,175] Pattern formation and damage repair mechanisms in biological tissues invariably involve a sub-population of cells exchanging chemical information about their current state with nearby neighbors through coupled sets of reactions to exert control or effect a response.

A strategic goal for synthetic biology and DNA nanotechnology is to understand how rationally designed networks of reactions can likewise be used to encode information within synthetic materials to manipulate their structure using biologically inspired machinery. While chemical reaction networks, such as those based on DNA hybridization or enzymatic interactions, have been designed to perform these tasks in a well-mixed solution, where the

concentration of different chemical species serve as inputs and outputs to the system[3,4,27], a key challenge to the design of these systems is to coordinate sensing, information flow, and direction of material behavior spatiotemporally in response to chemical processes. In order to address how self-assembly processes for synthetic biological systems might correct synthesis errors and damage in spatial contexts, a variety of theoretical and experimental systems have been postulated and investigated.[176,177] Winfree's model of abstract tile assembly provided a theoretical framework for understanding how self-assembling DNA tiles could be designed to repair pointwise random defects or fragmentation to their lattice structure via block transformations of bond types between individual tiles that enforce repair to occur in the same direction as the lattice's original growth.[16] Chen et al. improved upon this framework to design an abstract tile construction that is resilient to tile-loss of arbitrary size by implementing a set of rules that prohibit incorrect tile attachment and ensure that only certain terminal assemblies are capable of being formed during growth.[178] Some consideration has been devoted to how synthetic reaction-diffusion systems might be used to sense information and compute. Kaminaga et al. and Kuhnhert et al. developed photosensitive Belousov-Zhabotinsky (BZ) reactions capable of maintaining stationary Turing patterns over 1 hour triggered by spatial light stimuli.[159,179] Chirieleison et al. developed a DNA strand displacement pattern edge detection circuit embedded within a bis-acrylamide hydrogel responsive to light.[180] More recently, Scalise and Schulman demonstrated in silico how reaction-diffusion systems can operate as cellular automata, where diffusing chemical signals are exchanged between cells; their system was able to recapitulate 'Rule 110' and 'Rule 60'.[162] More specifically, reaction-diffusion algorithms abstracted from chemical and biological systems have been proposed as image processing and computer vision algorithms for edge detection and edge enhancement functions.[181] Typically,

such algorithms involve the transformation of spatial patterns through a sequence of Gaussian convolutions, which can be interpreted as the diffusive exchange of material from an initial condition, followed by additional transformations of the pattern involving nonlinear oscillators such as the BZ reaction or FitzHugh-Nagumo model of action potential initiation in neurons.[182,183] While easily implementable as computational algorithms for computer vision problems, these specific reaction-diffusion transformations involve highly nonlinear reactions and trimolecular reaction mechanisms, significantly complicating their potential development as experimental systems using chemical methods and more specifically, DNA based machinery.

In this work, we sought to determine the efficiency of spatial pattern storage and repair in an abstracted chemical node network where signals are exchanged between nodes through isotropic diffusion processes, analogous to Gaussian blurring. We then analyzed how a modification of node computation in this diffusive problem using the difference of Gaussians method (DOG) impacted pattern edge preservation and the network's capability repair random pointwise mutations. We then addressed the shortcomings of these two approaches and outline additional pattern transformation and preservation methods that are compatible with the proposed framework and are mechanistically compatible with experimental implementation.

Analyses of systems that rely upon dissipative chemical mechanisms to sense, store, and repair spatial information as part of large distributed networks remain underdeveloped. As such, we proposed a simple architecture for the integration and repair of spatial information using chemical reactions and signal transport via diffusion: a distributed network consisting of discreet, spatially defined nodes that encodes and maintains molecular patterns using a consensus algorithm; nodes emit signals and sense those of nearby neighbors to make decisions about the encoded information they store. Overall, it was our goal to design the system using mechanisms

that could be realistically implemented experimentally. We explored the capabilities and limitations of this architecture for encoding patterns into a set of states denoting patterns' interior, edge, and exterior, and the ability to recover the shape of stored patterns in the presence of random pointwise mutations. We considered lattices of regularly spaced nodes occupying a two-dimensional plane and first asked whether bits of binary chemical patterns can be stably stored across the network without significant loss of features. We then sought to determine how effective a node self-correction consensus algorithm might be for healing pointwise random mutations to spatial patterns that are stored as bits within each node of the array. We observed that a consensus algorithm employing a simple diffusive signal exchange process, where individual nodes used the concentration of emitted signals from nearby neighbors to determine their correct state in a randomized process, was an effective method for repairing pulses of random mutations occurring in patterns' encoded states stored in nodes. This approach reduced the error in the stored pattern from 30% of the network size to roughly 0.5%. The incorporation of the difference of Gaussians method in node computation improved the preservation of edge features but decreased the network's overall ability to correct pointwise mutations. Finally, to recapitulate node sensing and computation dependent on the consumption of energy and availability of reactants, we modeled network resilience using in a stochastic simulation algorithm in the presence of a continuous rate of pointwise mutations.

5.2 Materials & Methods

Functions of Consensus Algorithm: Using a distributed network for chemical information storage provides several advantages (**Figure 5.1**): 1) specific bits of information regarding the pattern's concentration, as a function of position, are stored with redundancy across the network assuming the feature size of the network is much smaller than the features of the pattern being

encoded, and 2) preservation of the pattern can be achieved by implementing a consensus algorithm that enables nodes to sense the states of their surrounding neighbors and update or correct their damaged state to reflect the surrounding neighborhood.

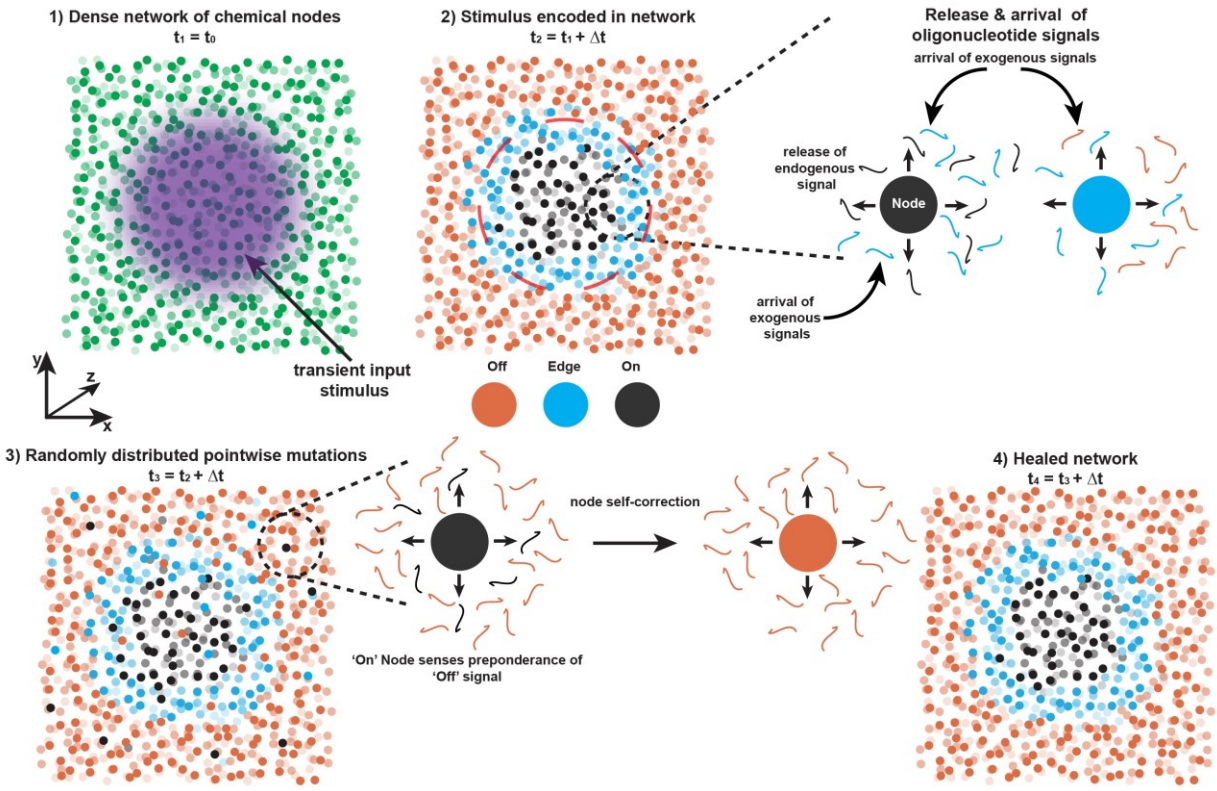

Figure 5.1. High-level schematic of a reaction-diffusion associative memory. 1) A dense network of chemical nodes comprising the associative memory are exposed to a transient spatial stimulus. 2) The node network encodes the transient stimulus into a series of encoded states that denote the position of the stimulus in the network. This pattern is maintained by nodes exchanging diffusing oligonucleotide signals with neighboring nodes. 3) In the presence of pointwise mutations, which cause nodes to express the wrong encoded state, sensing of the signals from the local environment allow nodes to retrieve the correct encoded state shown in 4).

Our analyses of the reaction-diffusion network made assumptions about the relative timescales at which diffusive transport of chemical signals between nodes and chemical computation within nodes occurred. Nodes performed computation in discreet steps and discreet time intervals. Each step began with an individual node initiating sensing of the concentration of signals diffusing within its location, and ended with the continuous emission of an updated signal that communicated the node's new state to its neighbors. In between sensing and emission steps, the node supplied the sensed signals as inputs to its consensus algorithm to determine what new

state to express based on the input from its surrounding neighbors. We first assumed that the timescale of node computation is much longer than the timescale for lateral diffusion of signaling molecules between nodes. We expressed this assumption in terms of the characteristic time for diffusion in two-dimensions in: $t_c \gg t_d = \frac{\langle R_0 \rangle^2}{4D}$, where t_c is the characteristic time for node computation and t_d is the characteristic time for diffusion of a signaling molecule. $\langle R_0 \rangle$ is the average distance between node locations and D is the diffusion coefficient of a signaling molecule.

Therefore, in our framework, diffusion of signals between nodes were not modeled explicitly and we assumed that a node calculates its state by sensing the steady state concentration of signals emanating from surround nodes. The magnitude of such the concentration was a function of the Euclidean distance between any two given nodes. The shape of the concentration profile emitted from a node was assumed to be static and the concentration profile itself was dimensionless, ranging between minimum and maximum values of 0 and 1. After calculating its new state, a node's existing emitted profile instantaneously changed to the steady state profile of a signaling molecule indicating its new state. The form of the diffusion profile for signals was the complementary error function, *erfc()*, which is the solution of the diffusion equation in a semi-infinite domain, where the concentration of a signal decays from 1 to 0 as the Euclidean distance, r, from its point source increases such that $\lim_{r \to \infty} C = 0$ where C is the dimensionless concentration of the signal. It is important to note that for our system, the complementary error function acted as a one-dimensional potential function that described the influence nodes have on each other and was solely a function of the Euclidean distance between any two nodes; we do not incorporate the form of the Laplacian operator in two-dimensional cartesian space or cylindrical coordinates:

$$\frac{\partial C(r,t)}{\partial t} = D\nabla^2 C(r,t) \ (1)$$

$$C(r,t)|_{r=0} = 1 \ (2)$$

$$C(r,t)|_{r\to\infty} = 0 \ (3)$$

$$C = \frac{2}{\sqrt{\pi}}\int_{\eta}^{\infty} e^{-z^2} dz \ (4)$$

$$\eta = \frac{r}{\sqrt{4Dt}} \ (5)$$

Construction of regularly spaced node array:

Secondly, we abstracted node chemical computation to a series of mathematical operations. To expand upon these functions, we explain the overall functions of the system for encoding patterns, updating nodes, and repairing pointwise damage. The regularly-spaced node network consisted of an N by N lattice of nodes, where $\{i,j|\ i,j \in \mathbb{N},\ 0 < i,j \leq N\}$. Each node_{ij} denoted a region in space where localized computation occured. At time t = 0, a transient binary pattern of size N by N was superimposed over the node network. The pixels in the binary pattern had the value of 1 and 0, corresponding to on and off values. The network then encoded the binary pattern into its nodes.

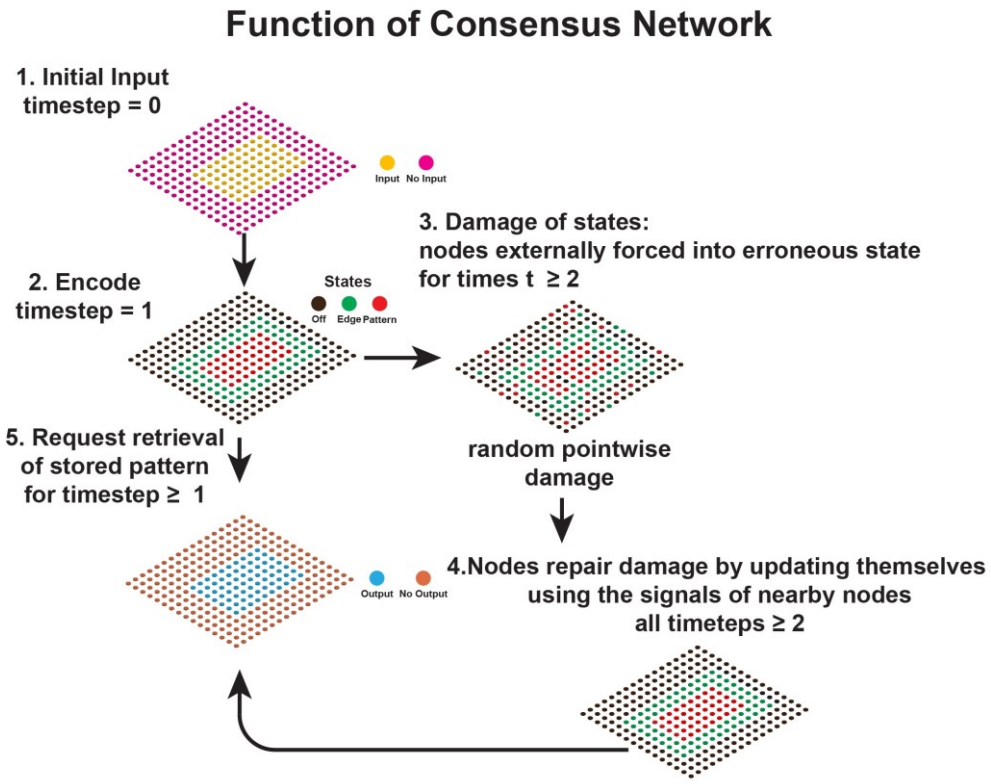

Figure 5.2. Process flow of the consensus network model.

The encoding process occurred with the following steps. Each $node_{ij}$ calculated a value from a weighted average composed of its initial binary input $signal_{ij}$ and the binary input signals emitted from neighbor nodes. The relative magnitude of the neighbor signals at node location ij was weighted by the complementary error function, which is a function of the Euclidian distance between $pixel_{ij}$ and a given $pixel_{kl}$, where $\{k, l | \, k, l \in \mathbb{N}, \; 0 < k, l \leq N\}$ (Figure 3). The signal strength of the surrounding nodes signals was assumed to be dimensionless, with values ranging from 1, corresponding to a Euclidian distance of 0, to 0, corresponding to a Euclidian distance of 10 nodes. All nodes performed this computation at time t = 0, and nodes weighted their own binary input value with an encoding self-weight, $w_{eij} = 0.05$. For all variables containing subscripted triplet indices, the first index indicates what step of computation is occurring, either the encoding step, denoted with a subscript e, or the node updating step, denoted with the

subscript u, which will be discussed in the next section. The next two indices to the right of this index indicate the node's identity in the lattice. A node performing a computation step had the indices ij. All neighbor nodes were assigned the indices kl. w_0 is a constant multiplied by each C_{ekl}(eqn. 6) to ensure that the weights of the average sum to 1 (eqn. 7).

$$w_{ekl} = w_0 C_{ekl} (6)$$

$$value_{eij} = w_{eij} B_{ij} + \sum_k \sum_l w_{ekl} B_{kl} (7)$$

$$w_{eij} + \sum_k \sum_l w_{kl} = 1 (8)$$

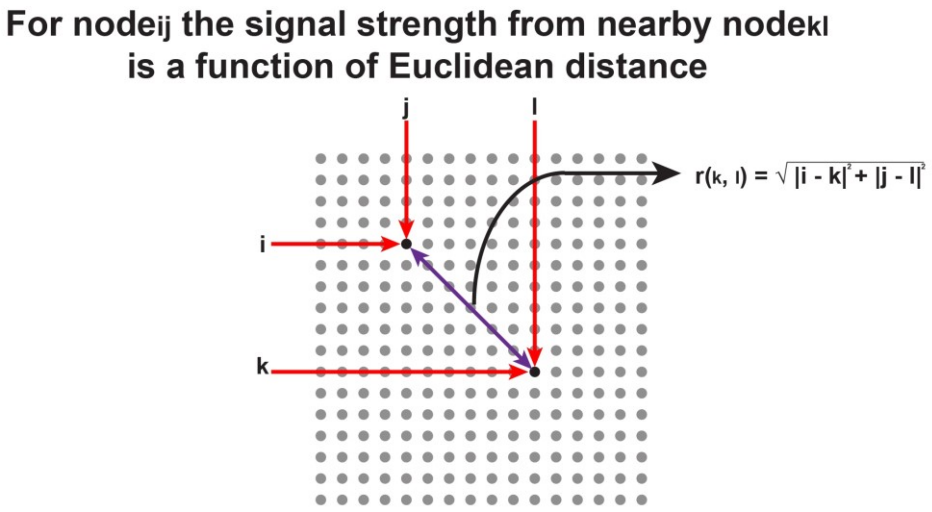

Figure 5.3. Illustration of Euclidean distance calculation, which determined the signal strength between nodes.

The resulting weighted average (equation 7) calculated across the network blurred the initial binary input pattern to a distribution of values between 0 and 1. Using these directory $values_{ij}$, each node then determined what state to encode itself as in a separate computation step by performing a thresholding operation to determine whether its calculated value corresponded to a state of ON, EDGE or OFF. This step concluded the initial encoding process of the network. A state of ON indicated that the node occupied a position that was within the boundaries of the

initial binary input pattern; ON had a numerical value of 3. A state of EDGE indicated that the node occupied a position that was at the edge of the binary input pattern; EDGE had a numerical value of 2. A state of OFF indicated that the node occupied a position that was outside of the binary input pattern's original boundaries; EDGE had a numerical value of 1. Two constant thresholds were defined for determining whether states of ON, EDGE, and OFF, were assigned to a node; $T_{on} = 0.8$, and $T_{edge} = 0.55$. If $value_{eij} > T_{on}$ an ON state was assigned to the node; if $T_{on} \geq value_{eij} \geq T_{edge}$ an EDGE state was assigned to the node; if $value_{eij} < T_{edge}$ an OFF state was assigned to the node. The overall, these calculations blurred the original binary image, recapitulating what would occur in a process of diffusive signal exchange between nodes.

Having encoded the binary input pattern into a set of states stored within individual nodes. The network then began its time evolution. Each node had a probability or rate at which it sensed its local environment and updated its state based on the encoded signals it received from its neighbor nodes. We assumed this process occurred randomly across the entire network and used Gillespie's sampling algorithm[184] to determine the time to the next updating reaction. p_u was the probability of a node performing a sensing and update operation per unit time, where time was dimensionless; $p_u = 1$ for all simulations presented. We first assumed that the rate of node sensing was constant, and sampled an exponential distribution with a mean value of $\frac{1}{T}$, where, $T = N^2 p_u$, was the total reaction propensity of the network, to determine the time to the next node updating event. During a sensing updating step, a node sensed the encoded signals of its neighbors and calculated a weighted average of those signals and of its own encoded signal. The node's self-weight was w_{uij}, $w_{uij} = 0.5$. Here, the dimensionless concentration, C_{ukl}, of an encoded $signal_{kl}$ decayed to 0 at a distance of 4 nodes. w_0 was a constant multiplied by each

$C_{ukl}$to ensure that the weights of the average sum to 1 (eqn. 10). The weighted average (eqn. 11) took the encoded states, S, as inputs to the function.

$$w_{ukl} = w_0 C_{ukl} (9)$$

$$w_{uij} + \sum_k \sum_l w_{ukl} = 1 (10)$$

$$value_{uij} = w_{uij} S_{ij} + \sum_k \sum_l w_{ukl} S_{kl} (11)$$

$value_{uij}$ was then compared against two thresholds to determine if the updated state variable should take a value of ON, EDGE, or OFF. $T_{on} = 0.8 * ON$, and $T_{edge} = 0.57 * ON$. If $value_{uij} > T_{on}$ an ON state was assigned to the node; if $T_{on} \geq value_{uij} \geq T_{edge}$ an EDGE state was assigned to the node; if $value_{uij} < T_{edge}$ an OFF state was assigned to the node. The random selection of a specific node for a reaction was implemented using Matlab's *randsample* function. Each node was assigned a unique reaction identifier from 1 to N^2 which was supplied to *randsample*. Additionally, a vector of reaction propensities for all nodes, listed in the same node order as the reaction identification vector, was supplied to *randsample*. This vector functioned as the weights *randsample* used to randomly select a reaction identifier; in this case the weights were all the same. *randsample* then selected a reaction identifier based on the relative weights, $\frac{p_u}{T}$, of each identifier. The process then repeated itself to select the next node that was randomly sampled and simultaneously evolved the time of the system by adding the time to the next reaction to a time counter. At each time step, the binary output image was calculated using the following rule: encoded node states of ON and EGDE were assigned a binary output value of 1 while OFF was assigned a binary output value of 0.

For models incorporating rates of random pointwise mutation reactions to encoded node states, we modified the sampling process to account for the probability of a node being randomly

damaged per unit time, p_m. We defined a damage reaction as the spurious random assignment of EGDE, OFF, or ON to a given node. Here, a separate set of reaction identifiers, accounting for random pointwise damage reactions, was numbered from N^2+1 to $2N^2$ and was concatenated to the end of the existing reaction identifier vector, which held identifiers for node updating reactions. Additionally, the reaction propensity vector was concatenated with an N^2 long vector containing the damage propensity of each node, which was initially treated as a constant probability. The updated reaction identifier and propensity matrices were supplied to *randsample* in order to determine the next reaction and its location. The time step until the next reaction was calculated using the updated total reaction propensity, $T = N^2 p_u + N^2 p_d$. As will be demonstrated later, adjustment of these reaction propensities to account for the consumption and replenishment of limited resources required for node function significantly impacted the behavior of the system. After each time step of the model, the output pattern of the network was captured using a Boolean retrieval function that decoded the network's encoded states into a binary output pattern; encoded states of ON or EDGE were assigned an output value of 1 while OFF was assigned an output value of 0. The fraction of pixels with flipped binary values from the input pattern were recorded as the output error fraction over the total time course of the simulation.

An important consideration for our models was the number of simulated events required to ensure that at least every node had been updated. The minimum number of simulated steps to satisfy this requirement adhered to Coupon Collector's problem[185] which asks how many times a set of X items must be sampled with replacement such that each item has been drawn at least once. In the simplifying case where $X = N^2$ items, or in this case nodes, and all nodes have a

constant and equal probability of being selected, the expected number of sampling steps, $E(X)$ obeys a geometric distribution and approximately scales as:

$$E(N^2) = N^2 \log N^2 + N^2\gamma + \frac{1}{2} + O\left(\frac{1}{N^2}\right)$$

where γ is the Euler-Mascheroni constant. For our models, lattices were 350 by 350 nodes in size, corresponding to 122,500 individual nodes and $E(N^2) = 1.51E6$. We ensured that the number of steps provided for the simulations was roughly 40% larger than $E(N^2)$.

5.3 Results

In the absence of damaging events, encoded patterns of arbitrary shape and concavity are encoded into an ensemble of states and were stable over time.

In the absence of any damage, the algorithm was able to encode patterns of patterns of arbitrary shape into states of ON, EDGE and OFF, denoting the relative position of the nodes to the original binary pattern (**Figure 5.4**). The shape of the encoded pattern was stable over the entire time course of the simulation with no variation between ON, EDGE and OFF populations. The average fraction of mutated nodes between original binary input matrix and output binary matrix at each time point is plotted in **Figure 5.5**. We observed that the error fraction maintained an average value of 3.7E-3 ± 1.1E-3 (mean ± standard deviation), corresponding to roughly .37 ± .11% of all nodes changing binary values between input and output patterns. For a variety of shapes, the encoding algorithm failed to preserve sharp edge features of the original binary pattern, whereas encoding of pattern edges with lower curvature yielded a higher degree of preservation (**Figure 5.4b, c**). Mathematically, this was due to the fact that nodes occupying the vertices of a pattern were surrounded by a higher number of OFF binary nodes that fell within the Gaussian filter kernel (the zone of diffusive signal exchange) compared to nodes positioned

at a flat edge of the original binary pattern; the weighted average calculated during the encoding step produced $value_{eij}$ that fell below the threshold for assignment of an EDGE state.

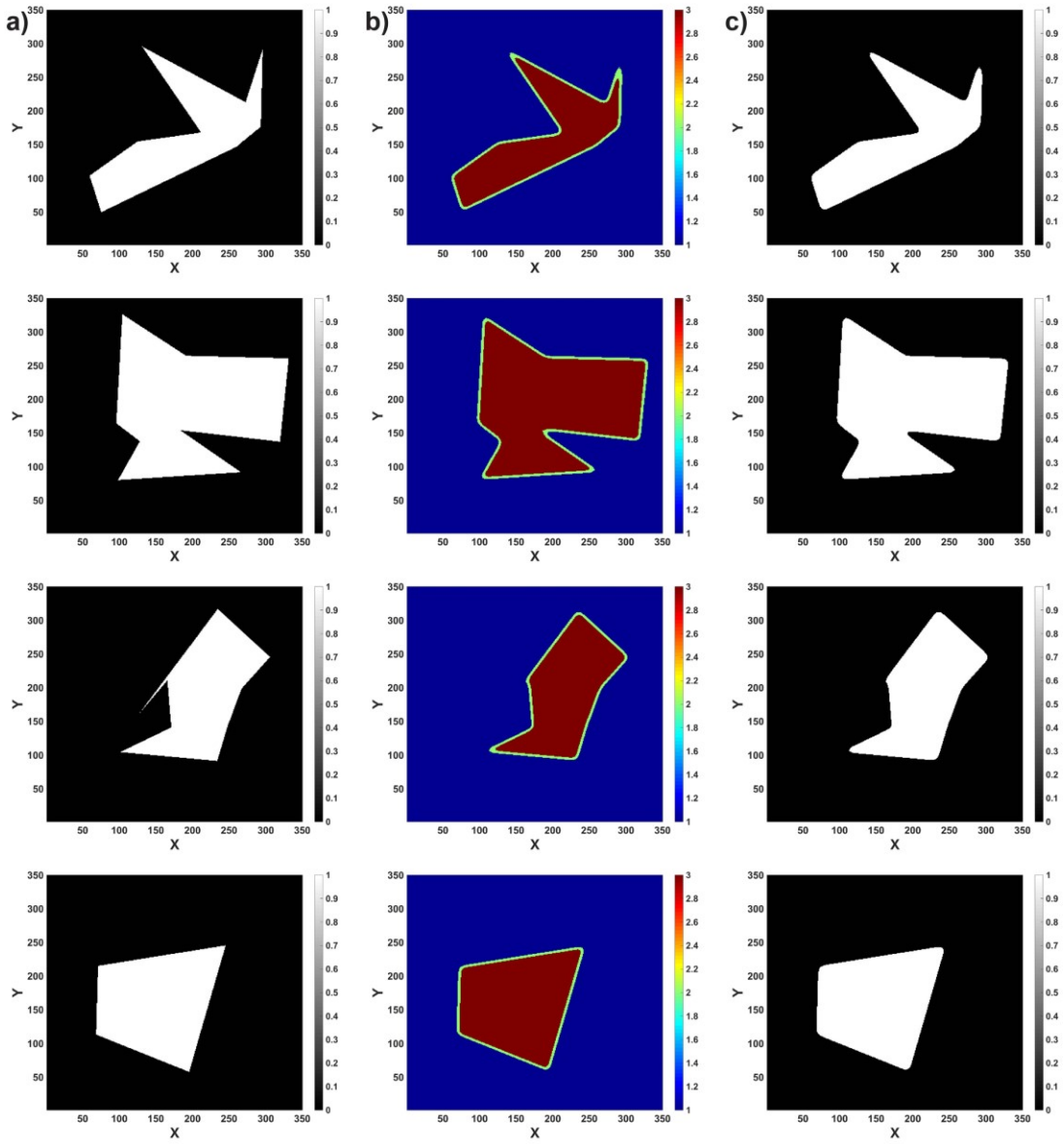

Figure 5.4. Results of 4 different pattern shapes. a) Binary input patterns, b) encoded state matrices at the last timepoint of simulation, and c) binary output matrices produced from b) final encoded state matrices.

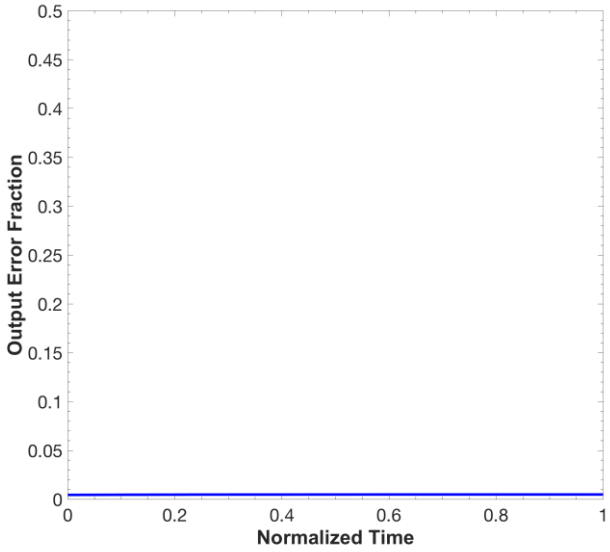

Figure 5.5. Fraction of nodes assigned the wrong binary output value as a function of normalized reaction time in the absence of any mutations.

The consensus algorithm reduced a single pulse of mutations that initially affected 30% of the network's nodes to 0.7% of the nodes.

We then asked whether the consensus algorithm could repair damage induced by a single pulse of random pointwise mutations distributed across the node network. The model construction was the same as previously mentioned. At a random timestep, 30% of the nodes within the network were randomly mutated to a new encoded state of ON, EDGE or OFF. Figure 6 shows the decrease in the output error fraction as a function of normalized reaction time.

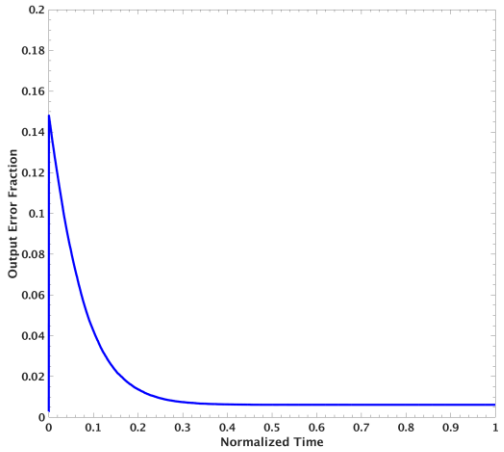

Figure 5.6. Output error fraction as a function of time after application of a pulse of random point mutations to the network.

After the mutation event, the output error fraction decreased to 0.7%. **Figure 5.7a, b** displays the input and final output pattern after mutation and healing; **Figure 5.7c, d** illustrates the encoded states resulting from mutation and the final matrix of encoded states at the end of the simulated reaction. The consensus algorithm was able to recover the correct encoded states in regions where one type of state predominated, specifically ON or OFF. However, within the edges of the encoded pattern and near the interior edge, mutated nodes persisted. For example, a mixture of nodes encoded with EDGE and OFF persisted despite being in a region of ON and EDGE nodes respectively. The sensing radius for a given node was designed to be 4 node lengths, which is the same length as the encoded edge layer of the original pattern. On average, the calculated value, $value_{uij}$, for these particular nodes approached to within 0.03 of $T_{on} = 0.8 * ON$. Roughly a third to one half of the neighboring nodes within their vicinity were distributed between EDGE and ON states. In the absence of an overwhelming majority of neighboring nodes of one state, nodes residing at the pattern edge did not possess $value_{uij}$ high enough to be assigned an EDGE state by the consensus algorithm.

Difference of Gaussians edge preservation impeded the network's ability to repair mutations arriving at a constant rate.

Isotropic diffusion alone results in the rounding of pattern edges and vertices. Difference of Gaussians filtering is a linear edge enhancement transformation involving the subtraction of Gaussian convolutions of differing diffusivities resulting in an image that exhibits large deviations from 0 that correspond to sharp transitions the feature intensities of the original input convolutions (Supporting Information: **Figure S5.1**). The implementation of this method chemically would involve the emission short and long-range signals from nodes. Each node

would then integrate both types of signals from neighbors and perform subtraction of the concentrations corresponding to the calculated values of each convolution. Mechanistically, subtraction would entail the bimolecular reaction of the two species generated from sensing of short and long-rang signals to generate waste, leaving the residual concentration of the species in excess to react with a register to store the difference and sign of the concentration. It was our goal to determine whether this process could be operated in random pointwise fashion to preserve encoded pattern edges while enabling repair resulting from a pulse of mutations. The existing algorithm was modified to include three additional parameters to aide in edge preservation, $\delta G1$, $\delta G2$, $\delta G3$:

$$\delta G1 = value_{eij} - value_{aij}$$

$$\delta G2 = value_{uij} - value_{bij}$$

$$\delta G3 = value_{uij} - 10 * value_{cij}$$

where, for example, $value_{aij}$, $value_{aij}$, and $value_{cij}$ are the result of a Gaussian convolution using a diffusion coefficient of 0.05, which is 5% of the original diffusion coefficient used to calculate $value_{uij}$. During pattern encoding, $\delta G1$ was calculated across all nodes in the network. Empirically, we observed that locations where $\delta G1 < -0.1$ corresponded to the edges of the original binary pattern, and this inequality was included as a condition for encoding nodes as EDGE (Supporting Information: Figure S1). Similarly, during node updating, $\delta G2$ and $\delta G3$ were added as additional Boolean requirements for identification of nodes positioned within the boundary of the binary pattern, specifically, $\delta G3 > -5$, AND $\delta G2 < -0.045$ & $\delta G2 \geq 0.045$ denoting whether nodes were located at the edges of the input pattern. In the presence of a random pulse of mutations to encoded states (**Figure 5.8**), the network's ability to repair pointwise random damage was compromised, resulting in an output error fraction of roughly

10%. This was due to the choice of threshold values set for the δG functions and the algorithm's inability to distinguish between high frequency noise and sharp features of the actual pattern. Although a tradeoff exists between low-pass filtering and edge preservation in regards to linear Gaussian convolution, further analysis is needed to refine the exact degree of this tradeoff and whether additional mechanisms are required for suitable implementation as a chemical method for pattern edge maintenance in response to mutation or damage.

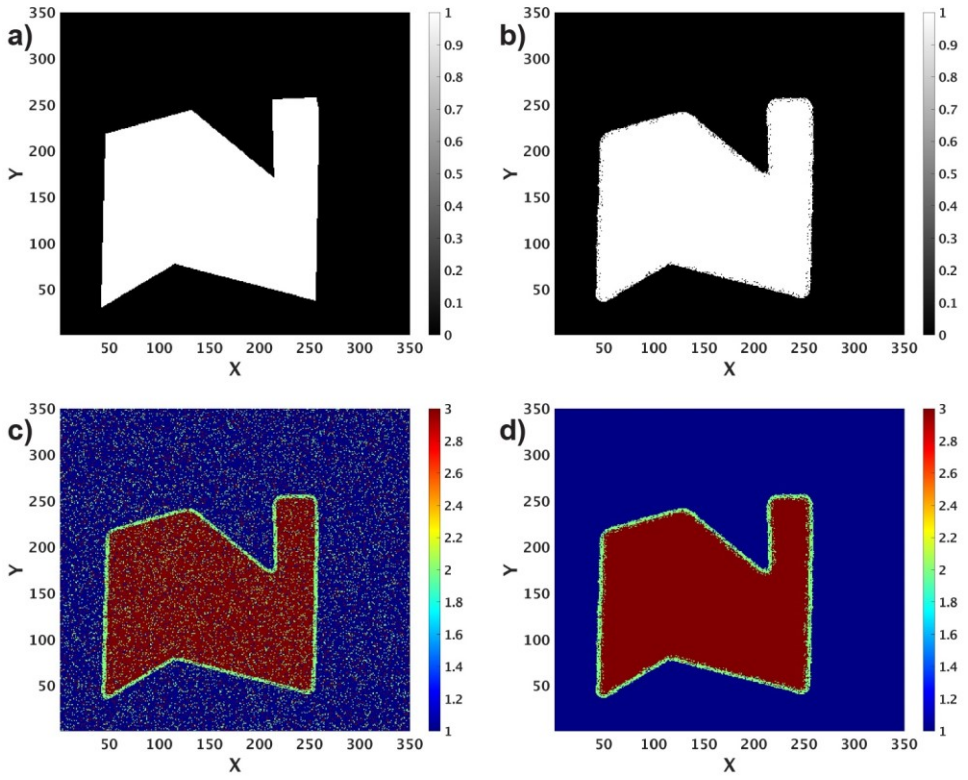

Figure 5.7. A pattern before and after a pulsed mutation event. a) Binary input pattern. b) Binary output pattern at the conclusion of the model. c) Pattern encoded states after the mutation event. d) Pattern encoded states at the conclusion of the model.

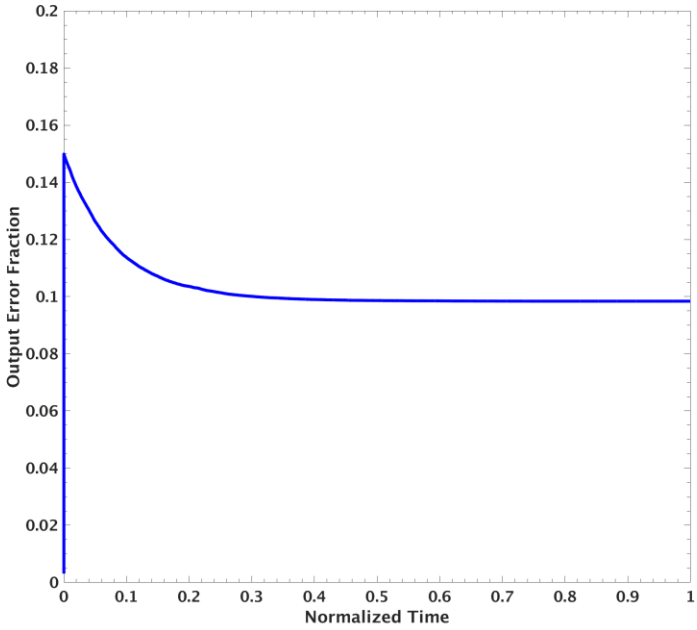

Figure 5.8. Output error fraction after a pulse of mutations to the network. Here, the difference of Gaussians method was employed to preserve pattern edges.

When networks were damaged continuously over time, the rate at which mutations accumulated was linearly proportional to the rate of mutation.

Finally, we characterized the network's ability to correct random pointwise mutations arriving at a constant rate, p_m. The rate of node updating was 1 event per unit time; three different values of p_m were used in three separate simulations. p_m was varied from N^{-2} events per unit time to 0.01 events per unit time, where N was the number of nodes along one dimension of the array. We first considered a constant rate of node updating. For each rate of mutation, the output error fraction initially grew and approached a steady state (Supporting Information: **Figure S5.2**). The final output fraction obtained from the three conditions tested was linearly proportional to the rate of damage (**Figure 5.9**).

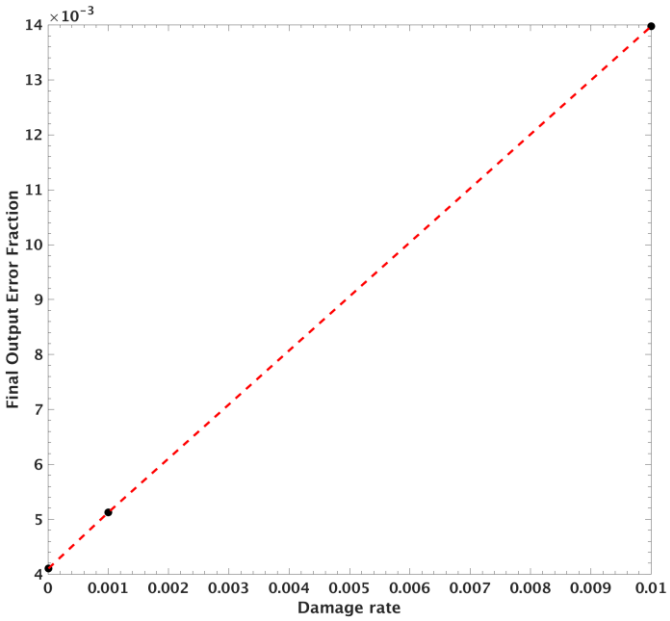

Figure 5.9. Final Output error fraction as a function of the damage rate applied to the network.

In order to recapitulate processes where node function was dependent on the presence of a nutrient or fuel, we imposed a refractory period in which nodes that had either undergone mutation or updated their encoded state had their update propensity, p_u, and damage propensity, p_d, lowered as part of a Gillespie algorithm incorporating negative feedback control to account for the replenishment of fuel from a reservoir (Supporting Information: **Figure S5.3**). For example, during a refueling reaction, a randomly selected node increased its update and damage propensities following a negative disturbance (which as proportional to $\alpha * p_u$, where $\alpha < 1$) according to the following equation:

$$p_{u\,new} = p_u + \beta(p_i - p_u)$$

p_i is the set point for update propensity. Refueling reactions were assumed to occur with a constant propensity $p_r = 0.5$ events per unit time. For set point propensities of $p_u = 1$ and $p_d =$

0.1, the output error fraction obtained from simulation exhibited a sigmoidal shape and grew linearly between 0.2 and 0.7 of its normalized time (**Figure 5.10**).

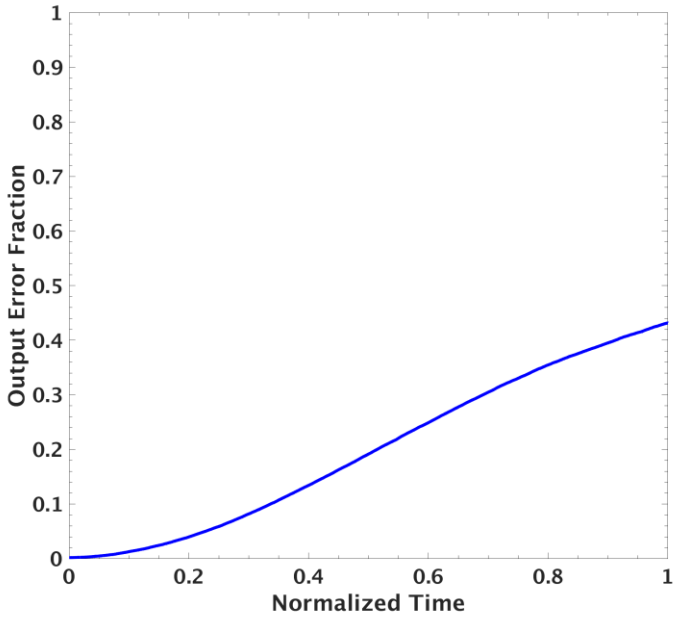

Figure 5.10. Output error fraction resulting a continuous rate of mutations where nodes enter refractory periods corresponding to the consumption of fuel during a sensing or mutation reaction. The set point update and damage propensities were 1 and 0.1 events time^{-1}.

Over the timescale of simulation, the network became overwhelmed and failed to repair mutations faster than their net rate of production. This result indicated that when accounting for node refractory periods that were 4 orders of magnitude less than the total number of timesteps allowed during computation, there was limit to the rate of damage that the system could accommodate, suggesting that the proposed consensus algorithm may be suitable for maintenance and repair applications in which the rate of node sensing and rate of damage are separated by at least several orders of magnitude.

5.4 Discussion

The consensus network outlined in this study enables stable storage of patterns of arbitrary shape in the absence of damage. Incorporation of edge preservation and enhancement functions are necessary for preventing loss of sharp pattern features during convolution operations. Importantly, edge preservation algorithms must not impede the network's ability to remove point mutations and must offer a realistic mechanism of operation as a chemical system. While our initial analysis of the difference of Gaussian's method demonstrated this tradeoff, alternative edge enhancement methods, such as anisotropic diffusion, provide alternative routes towards ensuring edge preservation and are potentially implementable as chemical systems. Future analyses will explore the exact relationship between node refractory behavior and the ability to correct point mutations to encoded patterns.

5.5 Supporting Information

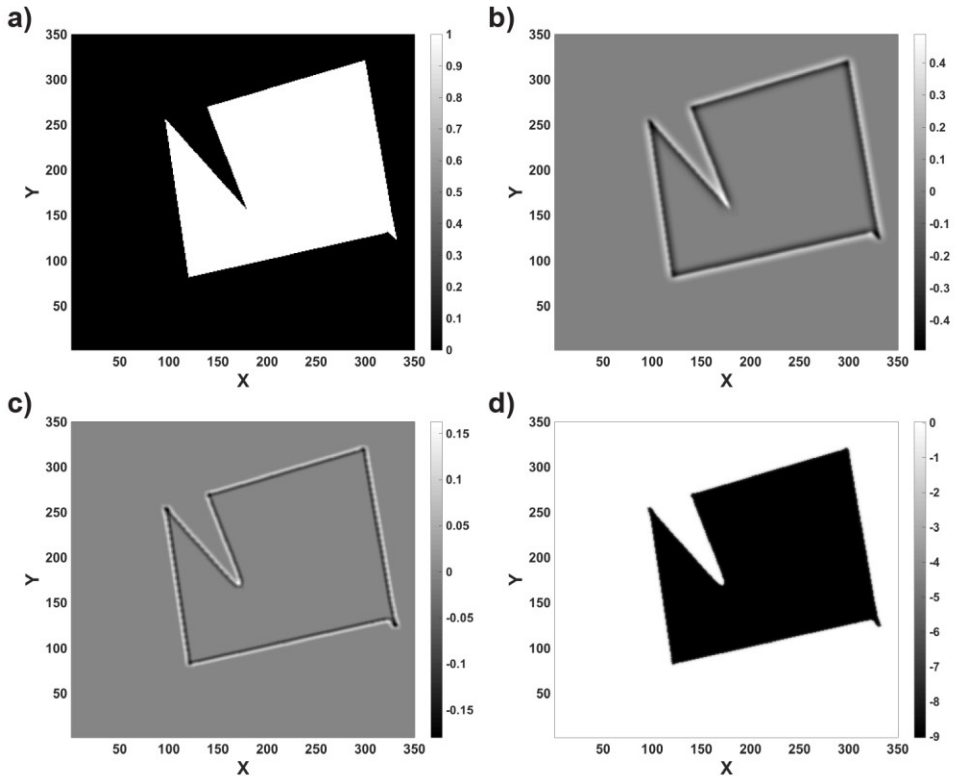

Figure S 5.1. Edge detection using the difference of Gaussians method. a) Binary input pattern. b) A detected edge using function δG1 (see main text). c) A detected edge using function δG2 (see main text). d) A detected edge using function δG3 (see main text).

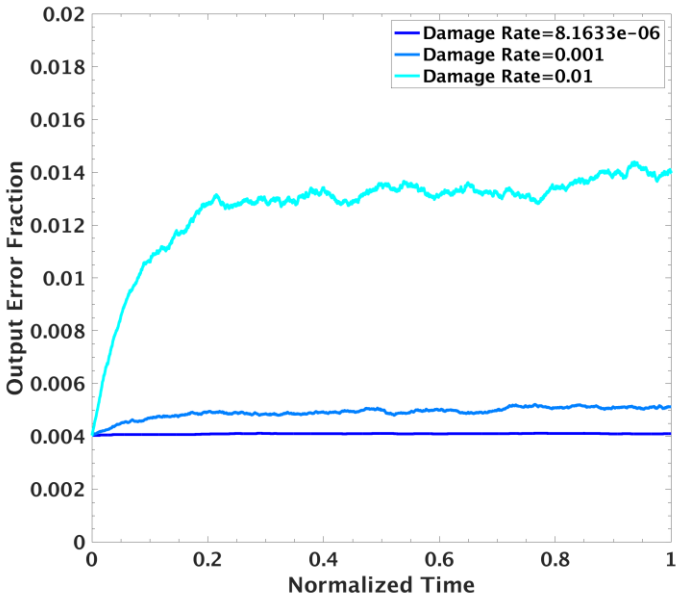

Figure S 5.2. Pattern output error fractions during application of a constant rate of damage to the network. Pd = 1/N, 0.001, 0.01. Pu = 1.

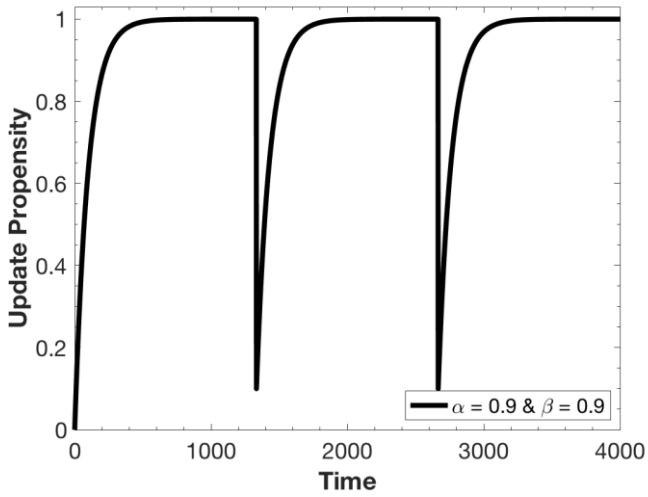

Figure S 5.3. Example node refractory function using a set point reaction propensity of 1. Two negative perturbations are applied over the course of 4000 timesteps.

Chapter 6 Conclusion & Future Directions

In this thesis I provide a groundwork for designing DNA-based systems that transmit and store chemical information spatiotemporally. Currently, the construction of multi-domain DNA-functionalized hydrogels is restricted by a small set of photoinitiators that can be used in photolithographic approaches incorporating DNA, which limits the types of materials that can be constructed and the physical properties they possess. Additionally, a limited set of DNA compatible UV photo-responsive chemistries exists. The creation of a larger set of photocleavable moieties with orthogonal spectra in the UV-B and UV-A range would enable the design of model systems composed of DNA-based hydrogels that could initiate more sophisticated responses to light stimuli and improve the ability to test and validate the types of systems that are suitable for further development for spatial computation. This is an active area of photochemistry research. DNA and RNA microarray design technology represents a well-developed application that leverages sophisticated nucleic acid chemistry and photolithography

and may possibly provide additional routes for overcoming these fabrication challenges. As DNA reaction-diffusion systems designed for hydrogel networks become more complex, more research into fabrication methods to construct two and three-dimensional micro-materials in high-through-put is necessary. Specific techniques include 3D micro-stereolithographic printing[186] and two-photon laser-scanning lithography[95,187]. Importantly, the DNA nanotechnology and soft materials research communities will significantly benefit from the development of a robust set of systems design principles for integrating DNA circuitry within hydrogels. For example, as was discussed in Chapter 3, the yield of crosslinking acrylate-modified oligonucleotides with camphorquinone photopolymerized PEDGA hydrogels was roughly 12%, resulting in a highly inefficient process for incorporating modified strands (which remain costly to synthesize) within polymer substrates.

Leaks and unintended side reactions are another a major challenge for designing larger more sophisticated circuits using DNA strand displacement. Although a variety of approaches exist for minimizing the rate of leak reactions for double stranded DNA species that can undergo three-way and 4-way branch migration (including the use of a leakless strand displacement architecture which was employed in Chapter 4 and using oligonucleotides composed of locked nucleic acids) photo-responsive DNA strand displacement circuits containing oligos synthesized with photocleavable chemistries present a particularly difficult challenge; the presence of such chemistries provides potential points for invading strands to spuriously react with DNA duplexes.

Leak reactions also pose a significant challenge for designing nonlinear strand displacement reactions, as was observed in Chapters 2 and 4. Mechanistically, coupling DNA strand displacement circuits with enzymatic systems such as transcriptional switches and genetic

regulatory networks provides a way of augmenting the kinds of nonlinear responses currently prohibited by strand displacement processes alone. The use of machine learning algorithms to screen out sets of nucleotide sequences prone to leakage or spurious transcription by polymerases will be a requirement for designing future systems. Finally, I believe the most rapid areas of growth for synthetic biology during the next decade lie in molecular diagnostics and therapeutic applications, particularly as 'smart' targeted drug delivery systems capable of molecular recognition in varying physiological conditions. Incorporation of DNA logic circuits within viral and non-viral gene delivery platforms and CRISPR-Cas editing technologies coupled with growing trends in biotechnology towards implantable, long acting drug depots will create a unique niche poised to benefit from the design principles currently being established for DNA reaction-diffusion systems. Moving beyond the next 10 years, it will become possible to design increasingly sophisticated DNA-integrated micromaterials approaching the function of chemical computers that can recapitulate and significantly augment functions once associated with cells and tissues.

References

(1) Seeman, N. C. Nucleic-Acid Junctions and Lattices. *J. Theor. Biol.* **1982**, *99* (2), 237–247.
(2) Adleman, L. M. Molecular Computation of Solutions to Combinatorial Problems. *Science (80-.).* **1994**, *266*, 1021–1024.
(3) Qian, L.; Winfree, E. Scaling Up Digital Circuit Computation with DNA Strand Displacement Cascades. *Science (80-.).* **2011**, *99* (June), 1196–1202.
(4) Qian, L.; Winfree, E.; Bruck, J. Neural Network Computation with DNA Strand Displacement Cascades. *Nature* **2011**, *475*, 368.
(5) Zhirnov, V.; Zadegan, R. M.; Sandhu, G. S.; Church, G. M.; Hughes, W. L. Nucleic Acid Memory. *Nat. Mater.* **2016**, *15* (4), 366–370.
(6) Yurke, B.; Turberfield, A. J.; Mills, A. P.; Simmel, F. C.; Neumann, J. L. A DNA-Fuelled Molecular Machine Made of DNA. *Nature* **2000**, *406* (6796), 605–608.
(7) Cherry, K. M.; Qian, L. Scaling up Molecular Pattern Recognition with DNA-Based Winner-Take-All Neural Networks. *Nature* **2018**, *559* (7714), 370–376.
(8) Thubagere, A. J.; Li, W.; Johnson, R. F.; Chen, Z.; Doroudi, S.; Lee, Y. L.; Izatt, G.; Wittman, S.; Srinivas, N.; Woods, D.; Winfree, E.; Qian, L. A Cargo-Sorting DNA Robot. *Science (80-.).* **2017**, *357* (6356), eaan6558.
(9) Li, S.; Jiang, Q.; Liu, S.; Zhang, Y.; Tian, Y.; Song, C.; Wang, J.; Zou, Y.; Anderson, G. J.; Han, J.-Y.; Chang, Y.; Liu, Y.; Zhang, C.; Chen, L.; Zhou, G.; Nie, G.; Yan, H.; Ding, B.; Zhao, Y. A DNA Nanorobot Functions as a Cancer Therapeutic in Response to a Molecular Trigger in Vivo. *Nat. Biotechnol.* **2018**, *36* (3), 258–264.
(10) Janssen, B. M. G.; van Rosmalen, M.; van Beek, L.; Merkx, M. Antibody Activation Using DNA-Based Logic Gates. *Angew. Chemie Int. Ed.* **2015**, *54* (8), 2530–2533.
(11) Groves, B.; Chen, Y.-J.; Zurla, C.; Pochekailov, S.; Kirschman, J. L.; Santangelo, P. J.; Seelig, G. Computing in Mammalian Cells with Nucleic Acid Strand Exchange. *Nat. Nanotechnol.* **2016**, *11* (3), 287–294.
(12) Douglas, S. M.; Bachelet, I.; Church, G. M. A Logic-Gated Nanorobot for Targeted Transport of Molecular Payloads. **2012**, *335* (6070), 831–834.
(13) Huo, S.; Gong, N.; Jiang, Y.; Chen, F.; Guo, H.; Gan, Y.; Wang, Z.; Herrmann, A.; Liang, X.-J. Gold-DNA Nanosunflowers for Efficient Gene Silencing with Controllable Transformation. *Sci. Adv.* **2019**, *5* (10), eaaw6264.
(14) Zhang, H.; Demirer, G. S.; Zhang, H.; Ye, T.; Goh, N. S.; Aditham, A. J.; Cunningham, F. J.; Fan, C.; Landry, M. P. DNA Nanostructures Coordinate Gene Silencing in Mature Plants. *Proc. Natl. Acad. Sci.* **2019**, *116* (15), 7543 LP – 7548.
(15) Yin, P.; Choi, H. M. T.; Calvert, C. R.; Pierce, N. A. Programming Biomolecular Self-Assembly Pathways. *Nature* **2008**, *451* (7176), 318–322.
(16) Winfree, E. Self-Healing Tile Sets BT - Nanotechnology: Science and Computation; Chen, J., Jonoska, N., Rozenberg, G., Eds.; Springer Berlin Heidelberg: Berlin, Heidelberg, 2006; pp 55–78.
(17) Schulman, R.; Winfree, E. Synthesis of Crystals with a Programmable Kinetic Barrier to Nucleation. **2007**, *104* (39), 15236–15241.
(18) Rothemund, P. W. K. Folding {DNA} to Create Nanoscale Shapes and Patterns. *Nature* **2006**, *440*, 297–302.
(19) Winfree, E.; Liu, F.; Wenzler, L. A.; Seeman, N. C. Design and Self-Assembly of Two-

Dimensional {DNA} Crystals. *Nature* **1998**, *394*, 539–544.
(20) Freije, C. A.; Myhrvold, C.; Boehm, C. K.; Lin, A. E.; Welch, N. L.; Carter, A.; Metsky, H. C.; Luo, C. Y.; Abudayyeh, O. O.; Gootenberg, J. S.; Yozwiak, N. L.; Zhang, F.; Sabeti, P. C. Programmable Inhibition and Detection of RNA Viruses Using Cas13. *Mol. Cell* **2019**, *76* (5), 826-837.e11.
(21) Chen, G.; Liu, D.; He, C.; Gannett, T. R.; Lin, W.; Weizmann, Y. Enzymatic Synthesis of Periodic DNA Nanoribbons for Intracellular PH Sensing and Gene Silencing. *J. Am. Chem. Soc.* **2015**, *137* (11), 3844–3851.
(22) Leung, K.; Chakraborty, K.; Saminathan, A.; Krishnan, Y. A DNA Nanomachine Chemically Resolves Lysosomes in Live Cells. *Nat. Nanotechnol.* **2019**, *14* (2), 176–183.
(23) Spruijt, E.; Tusk, S. E.; Bayley, H. DNA Scaffolds Support Stable and Uniform Peptide Nanopores. *Nat. Nanotechnol.* **2018**, *13* (8), 739–745.
(24) Ketterer, P.; Ananth, A. N.; Laman Trip, D. S.; Mishra, A.; Bertosin, E.; Ganji, M.; van der Torre, J.; Onck, P.; Dietz, H.; Dekker, C. DNA Origami Scaffold for Studying Intrinsically Disordered Proteins of the Nuclear Pore Complex. *Nat. Commun.* **2018**, *9* (1), 902.
(25) Swenson, C. S.; Velusamy, A.; Argueta-Gonzalez, H. S.; Heemstra, J. M. Bilingual Peptide Nucleic Acids: Encoding the Languages of Nucleic Acids and Proteins in a Single Self-Assembling Biopolymer. *J. Am. Chem. Soc.* **2019**, *141* (48), 19038–19047.
(26) Shastri, A.; McGregor, L. M.; Liu, Y.; Harris, V.; Nan, H.; Mujica, M.; Vasquez, Y.; Bhattacharya, A.; Ma, Y.; Aizenberg, M.; Kuksenok, O.; Balazs, A. C.; Aizenberg, J.; He, X. An Aptamer-Functionalized Chemomechanically Modulated Biomolecule Catch-and-Release System. *Nat. Chem.* **2015**, *7*, 447.
(27) Scalise, D.; Dutta, N.; Schulman, R. DNA Strand Buffers. *J. Am. Chem. Soc.* **2018**, *140* (38), 12069–12076.
(28) Schaffter, S. W.; Schulman, R. Building in Vitro Transcriptional Regulatory Networks by Successively Integrating Multiple Functional Circuit Modules. *Nat. Chem.* **2019**, *11* (9), 829–838.
(29) Kahn, J. S.; Hu, Y.; Willner, I. Stimuli-Responsive DNA-Based Hydrogels: From Basic Principles to Applications. *Acc. Chem. Res.* **2017**, *50* (4), 680–690.
(30) Shim, T. S.; Estephan, Z. G.; Qian, Z.; Prosser, J. H.; Lee, S. Y.; Chenoweth, D. M.; Lee, D.; Park, S.-J.; Crocker, J. C. Shape Changing Thin Films Powered by DNA Hybridization. *Nat. Nanotechnol.* **2017**, *12* (1), 41–47.
(31) Mohammed, A. M.; Šulc, P.; Zenk, J.; Schulman, R. Self-Assembling DNA Nanotubes to Connect Molecular Landmarks. *Nat. Nanotechnol.* **2017**, *12* (4), 312–316.
(32) Bier, E.; De Robertis, E. M. BMP Gradients: A Paradigm for Morphogen-Mediated Developmental Patterning. *Science (80-.).* **2015**, *348* (6242), aaa5838.
(33) Turing, A. The Chemical Basis of Morphogenesis. *Phil. Trans. R. Soc. Lond. B.* **1952**, *237*.
(34) Field, R. J.; Noyes, R. M. Oscillations in Chemical Systems. IV. Limit Cycle Behavior in a Model of a Real Chemical Reaction. *J. Chem. Phys.* **1974**, *60* (5), 1877–1884.
(35) Gierer, A.; Meinhardt, H. A Theory of Biological Pattern Formation. *Kybernetik* **1972**, *12* (1), 30–39.
(36) Lengyel, I.; Epstein, I. R. A Chemical Approach to Designing Turing Patterns in Reaction-Diffusion Systems. *Proc. Natl. Acad. Sci. U. S. A.* **1992**, *89* (9), 3977–3979.
(37) Zambrano, A.; Zadorin, A. S.; Rondelez, Y.; Estévez-Torres, A.; Galas, J.-C. Pursuit-and-

Evasion Reaction-Diffusion Waves in Microreactors with Tailored Geometry. *J. Phys. Chem. B* **2015**, *119* (17), 5349–5355.
(38) Joesaar, A.; Yang, S.; Bögels, B.; van der Linden, A.; Pieters, P.; Kumar, B. V. V. S. P.; Dalchau, N.; Phillips, A.; Mann, S.; de Greef, T. F. A. DNA-Based Communication in Populations of Synthetic Protocells. *Nat. Nanotechnol.* **2019**, *14* (4), 369–378.
(39) Zenk, J.; Scalise, D.; Wang, K.; Dorsey, P.; Fern, J.; Cruz, A.; Schulman, R. Stable DNA-Based Reaction-Diffusion Patterns. *RSC Adv.* **2017**, *7* (29), 18032–18040.
(40) Zadorin, A. S.; Rondelez, Y.; Gines, G.; Dilhas, V.; Urtel, G.; Zambrano, A.; Galas, J.-C.; Estevez-Torres, A. Synthesis and Materialization of a Reaction–Diffusion French Flag Pattern. *Nat. Chem.* **2017**, *9*, 990.
(41) Gines, G.; Zadorin, A. S.; Galas, J.; Fujii, T.; Rondelez, Y. Microscopic Agents Programmed by DNA Circuits. *Nat. Nanotechnol.* **2017**, No. January.
(42) Cangialosi, A.; Yoon, C.; Liu, J.; Huang, Q.; Guo, J.; Nguyen, T. D.; Gracias, D. H.; Schulman, R. DNA Sequence–Directed Shape Change of Photopatterned Hydrogels via High-Degree Swelling. *Science (80-.).* **2017**, *357* (6356), 1126 LP – 1130.
(43) Muskavitch, M. A. T. Delta-Notch Signaling and Drosophila Cell Fate Choice. *Dev. Biol.* **1994**, *166* (2), 415–430.
(44) Miller, M. B.; Bassler, B. L. Quorum Sensing in Bacteria. *Annu Rev Microbiol.* **2001**, *55*, 165–199.
(45) Demain, A. L.; Fang, A. The Natural Functions of Secondary Metabolites. In *History of Modern Biotechnology I*; Fiechter, A., Ed.; Springer Berlin Heidelberg: Berlin, Heidelberg, 2000; pp 1–39.
(46) Venayak, N.; Anesiadis, N.; Cluett, W. R.; Mahadevan, R. Engineering Metabolism through Dynamic Control. *Curr. Opin. Biotechnol.* **2015**, *34* (Supplement C), 142–152.
(47) Sadowski, J. P.; Calvert, C. R.; Zhang, D. Y.; Pierce, N. A.; Yin, P. Developmental Self-Assembly of a DNA Tetrahedron. *ACS Nano* **2014**, *8* (4), 3251–3259.
(48) Lu, L.; Oswald, S. J.; Ngu, H.; Yin, F. C.-P. Mechanical Properties of Actin Stress Fibers in Living Cells. *Biophys. J.* **2008**, *95* (12), 6060–6071.
(49) Beenakker, J.-W. M.; Ashcroft, B. A.; Lindeman, J. H.; Oosterkamp, T. H. Mechanical Properties of the Extracellular Matrix of the Aorta Studied by Enzymatic Treatments. *Biophys. J.* **2012**, *102* (8), 1731–1737.
(50) Makowski, M. S.; Ivanisevic, A. Molecular Analysis of Blood with Micro-/Nanoscale Field-Effect-Transistor Biosensors. *Small* **2011**, *7* (14), 1863–1875.
(51) Werkmeister, F. X.; Nickel, B. A. Fast Detection of Blood Gases by Solution Gated Organic Field Effect Transistors. *Org. Electron.* **2016**, *39* (Supplement C), 113–117.
(52) Pardee, K.; Green, A. A.; Ferrante, T.; Cameron, D. E.; DaleyKeyser, A.; Yin, P.; Collins, J. J. Paper-Based Synthetic Gene Networks. *Cell* **2017**, *159* (4), 940–954.
(53) Fritz, J.; Cooper, E. B.; Gaudet, S.; Sorger, P. K.; Manalis, S. R. Electronic Detection of DNA by Its Intrinsic Molecular Charge. *Proc. Natl. Acad. Sci.* **2002**, *99* (22), 14142–14146.
(54) Tabata, M.; Goda, T.; Matsumoto, A.; Miyahara, Y. Field-Effect Transistors for Detection of Biomolecular Recognition. In *Intelligent Nanosystems for Energy, Information and Biological Technologies*; Sone, J., Tsuji, S., Eds.; Springer Japan: Tokyo, 2016; pp 13–25.
(55) Rosales, A. M.; Anseth, K. S. The Design of Reversible Hydrogels to Capture Extracellular Matrix Dynamics. *Nat. Rev. Mater.* **2016**, *1* (2), 15012.
(56) Bryant, S. J.; Anseth, K. S. Controlling the Spatial Distribution of ECM Components in

Degradable PEG Hydrogels for Tissue Engineering Cartilage. *J. Biomed. Mater. Res. Part A* **2003**, *64A* (1), 70–79.
(57) Rambhia, K. J.; Ma, P. X. Controlled Drug Release for Tissue Engineering. *J. Control. Release* **2015**, *219* (Supplement C), 119–128.
(58) Wehner, M.; Truby, R. L.; Fitzgerald, D. J.; Mosadegh, B.; Whitesides, G. M.; Lewis, J. A.; Wood, R. J. An Integrated Design and Fabrication Strategy for Entirely Soft, Autonomous Robots. *Nature* **2016**, *536* (7617), 451–455.
(59) Kaminaga, A.; Vanag, V. K.; Epstein, I. R. "Black Spots" in a Surfactant-Rich Belousov–Zhabotinsky Reaction Dispersed in a Water-in-Oil Microemulsion System. *J. Chem. Phys.* **2005**, *122* (17), 174706.
(60) Castets, V.; Dulos, E.; Boissonade, J.; De Kepper, P. Experimental Evidence of a Sustained Standing Turing-Type Nonequilibrium Chemical Pattern. *Phys. Rev. Lett.* **1990**, *64* (24), 2953–2956.
(61) Turberfield, A. J.; Yurke, B.; Mills Jr., A. P. DNA Hybridization Catalysts and Molecular Tweezers. In *DNA Based Computers V*; 1999.
(62) Zhang, D. Y.; Seelig, G. Dynamic DNA Nanotechnology Using Strand Displacement Reactions. *Nat. Chem.* **2011**, *3*, 103–113.
(63) Kahn, J. S.; Hu, Y.; Willner, I. Stimuli-Responsive DNA-Based Hydrogels: From Basic Principles to Applications. *Acc. Chem. Res.* **2017**, *50* (5), 680–690.
(64) Liao, W.-C.; Al., E. PH- and Ligand-Induced Release of Loads from DNA–Acrylamide Hydrogel Microcapsules. *Chem. Sci.* **2017**, *8*, 3362–3373.
(65) Zenk, J.; Schulman, R. The Kinetics and Thermodynamics of Watson-Crick Base Pair-Driven DNA Origami Dimerization. *J. Am. Chem. Soc.* **2016**, *138* (10), 3346–3354.
(66) Mirkin, C. A.; Letsinger, R. L.; Mucic, R. C.; Storhoff, J. J. A DNA-Based Method for Rationally Assembling Nanoparticles into Macroscopic Materials. *Nature* **1996**, *382*, 607–609.
(67) Vinkenborg, J. L.; Karnowski, N.; Famulok, M. Aptamers for Allosteric Regulation. *Nat. Chem. Biol.* **2011**, *7* (8), nchembio.609.
(68) Seymour, E.; Daaboul, G. G.; Zhang, X.; Scherr, S. M.; Ünlü, N. L.; Connor, J. H.; Ünlü, M. S. DNA-Directed Antibody Immobilization for Enhanced Detection of Single Viral Pathogens. *Anal. Chem.* **2015**, *87* (20), 10505–10512.
(69) Seelig, G.; Soloveichik, D.; Zhang, D. Y.; Winfree, E. Enzyme-Free Nucleic Acid Logic Circuits. *Science (80-.).* **2006**, *314* (5805), 1585–1588.
(70) Seelig, G.; Yurke, B.; Winfree, E. Catalyzed Relaxation of a Metastable DNA Fuel. *J Am Chem Soc.* **2006**, *128* (37), 12211–12220.
(71) Zadorin, A. S.; Rondelez, Y.; Galas, J.-C.; Estevez-Torres, A. Synthesis of Programmable Reaction-Diffusion Fronts Using DNA Catalyzers. *Phys. Rev. Lett.* **2015**, *114* (6), 068301.
(72) Zhang, D. Y.; Turberfield, A. J.; Yurke, B.; Winfree, E. Engineering Entropy-Driven Reactions and Networks Catalyzed by DNA. *Science (80-.).* **2007**, *318* (5853), 1121–1125.
(73) Bacaër, N. The Diffusion of Genes (1937) BT - A Short History of Mathematical Population Dynamics; Bacaër, N., Ed.; Springer London: London, 2011; pp 111–116.
(74) Ablowitz, M. J.; Zeppetella, A. Explicit Solutions of Fisher's Equation for a Special Wave Speed. *Bull. Math. Biol.* **1979**, *41* (6), 835–840.
(75) Kolmogoroff, A.; Petrovsky, I.; Piscounoff, N. Study of the Diffusion Equation with Growth of the Quantity of Matter and Its Application to a Biology Problem. In *Dynamics*

of Curved Fronts; Pelcé, P. B. T.-D. of C. F., Ed.; Academic Press: San Diego, 1988; pp 105–130.
(76) Zhang, D. Y.; Winfree, E. Control of DNA Strand Displacement Kinetics Using Toehold Exchange. *J. Am. Chem. Soc.* **2009**, *131*, 17303–17314.
(77) Dorsey, P.; Rubanov, M.; Wang, W.; Schulman, R. Digital Maskless Photolithographic Patterning of and Photo-Controlled Release of DNA Strands in Architectured Poly(Ethylene Glycol) Diacrylate Hydrogels. *Submitted* **2019**.
(78) SantaLucia, J. A Unified View of Polymer, Dumbbell, and Oligonucleotide DNA Nearest-Neighbor Thermodynamics. *Proc. Natl. Acad. Sci.* **1998**, *95* (4), 1460 LP – 1465.
(79) Chirieleison, S. M.; Allen, P. B.; Simpson, Z. B.; Ellington, A. D.; Chen, X. Pattern Transformation with DNA Circuits. *Nat. Chem.* **2013**, *5*, 1000.
(80) Fichte, M. A. H.; Weyel, X. M. M.; Junek, S.; Schäfer, F.; Herbivo, C.; Goeldner, M.; Specht, A.; Wachtveitl, J.; Heckel, A. Three-Dimensional Control of DNA Hybridization by Orthogonal Two-Color Two-Photon Uncaging. *Angew. Chemie Int. Ed.* **2016**, *55* (31), 8948–8952.
(81) Fern, J.; Schulman, R. Modular DNA Strand-Displacement Controllers for Directing Material Expansion. *Nat. Commun.* **2018**, *9* (1), 3766.
(82) English, M. A.; Soenksen, L. R.; Gayet, R. V; de Puig, H.; Angenent-Mari, N. M.; Mao, A. S.; Nguyen, P. Q.; Collins, J. J. Programmable CRISPR-Responsive Smart Materials. *Science (80-.).* **2019**, *365* (6455), 780 LP – 785.
(83) Badeau, B. A.; Comerford, M. P.; Arakawa, C. K.; Shadish, J. A.; DeForest, C. A. Engineered Modular Biomaterial Logic Gates for Environmentally Triggered Therapeutic Delivery. *Nat. Chem.* **2018**, *10* (3), 251–258.
(84) Dorsey, P. J.; Rubanov, M.; Wang, W.; Schulman, R. Digital Maskless Photolithographic Patterning of DNA-Functionalized Poly(Ethylene Glycol) Diacrylate Hydrogels with Visible Light Enabling Photodirected Release of Oligonucleotides. *ACS Macro Lett.* **2019**, *8* (9), 1133–1140.
(85) Shampine, L. F.; Reichelt, M. W. The MATLAB ODE Suite. *SIAM J. Sci. Comput.* **1997**, *18* (1), 1–22.
(86) Frank-Kamenetskii, M. D. Simplification of the Empirical Relationship between Melting Temperature of DNA, Its GC Content and Concentration of Sodium Ions in Solution. *Biopolymers* **1971**, *10* (12), 2623–2624.
(87) Erie, D.; Sinha, N.; Olson, W.; Jones, R.; Breslauer, K. A Dumbbell-Shaped, Double-Hairpin Structure of DNA: A Thermodynamic Investigation. *Biochemistry* **1987**, *26* (22), 7150–7159.
(88) Rentzeperis, D.; Ho, J.; Marky, L. A. Contribution of Loops and Nicks to the Formation of DNA Dumbbells: Melting Behavior and Ligand Binding. *Biochemistry* **1993**, *32* (10), 2564–2572.
(89) Zadeh, J. N.; Steenberg, C. D.; Bois, J. S.; Wolfe, B. R.; Pierce, M. B.; Khan, A. R.; Dirks, R. M.; Pierce, N. A. NUPACK: Analysis and Design of Nucleic Acid Systems. *J Comput Chem.* **2011**, *32* (1), 170–173.
(90) Kurylo, I.; Gines, G.; Rondelez, Y.; Coffinier, Y.; Vlandas, A. Spatiotemporal Control of DNA-Based Chemical Reaction Network via Electrochemical Activation in Microfluidics. *Sci. Rep.* **2018**, *8* (1), 6396.
(91) Lin, D. C.; Yurke, B.; Langrana, N. A. Mechanical Properties of a Reversible, DNA-Crosslinked Polyacrylamide Hydrogel. *J. Biomech. Eng.* **2004**, *126* (1), 104–110.

(92) Hu, Y.; Kahn, J. S.; Guo, W.; Huang, F.; Fadeev, M.; Harries, D.; Willner, I. Reversible Modulation of DNA-Based Hydrogel Shapes by Internal Stress Interactions. *J. Am. Chem. Soc.* **2016**, *138* (49), 16112–16119.
(93) Yin, B.-C.; Ye, B.-C.; Wang, H.; Zhu, Z.; Tan, W. Colorimetric Logic Gates Based on Aptamer-Crosslinked Hydrogels. *Chem. Commun.* **2012**, *48* (9), 1248–1250.
(94) Hahn, M. S.; Miller, J. S.; West, J. L. Three-Dimensional Biochemical and Biomechanical Patterning of Hydrogels for Guiding Cell Behavior. *Adv. Mater.* **2006**, *18* (20), 2679–2684.
(95) Hoffmann, J. C.; West, J. L. Three-Dimensional Photolithographic Micropatterning: A Novel Tool to Probe the Complexities of Cell Migration. *Integr. Biol. (Camb).* **2013**, *5* (5), 817–827.
(96) Hoffmann, J. C.; West, J. L. Three-Dimensional Photolithographic Patterning of Multiple Bioactive Ligands in Poly(Ethylene Glycol) Hydrogels. *Soft Matter* **2010**, *6* (20), 5056.
(97) Lu, Y.; Mapili, G.; Suhali, G.; Chen, S.; Roy, K. A Digital Micro-Mirror Device-Based System for the Microfabrication of Complex, Spatially Patterned Tissue Engineering Scaffolds. *J. Biomed. Mater. Res. - Part A* **2006**, *77* (2), 396–405.
(98) Lee, M. P.; Cooper, G. J. T.; Hinkley, T.; Gibson, G. M.; Padgett, M. J.; Cronin, L. Development of a 3D Printer Using Scanning Projection Stereolithography. *Sci. Rep.* **2015**, *5*, 9875.
(99) Ma, X.; Qu, X.; Zhu, W.; Li, Y.-S.; Yuan, S.; Zhang, H.; Liu, J.; Wang, P.; Lai, C. S. E.; Zanella, F.; Feng, G.-S.; Sheikh, F.; Chien, S.; Chen, S. Deterministically Patterned Biomimetic Human IPSC-Derived Hepatic Model via Rapid 3D Bioprinting. *Proc. Natl. Acad. Sci.* **2016**, *113* (8), 2206–2211.
(100) Na, J. H.; Evans, A. A.; Bae, J.; Chiappelli, M. C.; Santangelo, C. D.; Lang, R. J.; Hull, T. C.; Hayward, R. C. Programming Reversibly Self-Folding Origami with Micropatterned Photo-Crosslinkable Polymer Trilayers. *Adv. Mater.* **2015**, *27* (1), 79–85.
(101) Waldbaur, A.; Waterkotte, B.; Schmitz, K.; Rapp, B. E. Maskless Projection Lithography for the Fast and Flexible Generation of Grayscale Protein Patterns. *Small* **2012**, *8* (10), 1570–1578.
(102) Yin, H.; Ding, Y.; Zhai, Y.; Tan, W.; Yin, X. Orthogonal Programming of Heterogeneous Micro-Mechano-Environments and Geometries in Three-Dimensional Bio-Stereolithography. *Nat. Commun.* **2018**, *9* (1), 4096.
(103) Warner, J.; Soman, P.; Zhu, W.; Tom, M.; Chen, S. Design and 3D Printing of Hydrogel Scaffolds with Fractal Geometries. *ACS Biomater. Sci. Eng.* **2016**, *2* (10), 1763–1770.
(104) Zorlutuna, P.; Annabi, N.; Camci-Unal, G.; Nikkhah, M.; Cha, J. M.; Nichol, J. W.; Manbachi, A.; Bae, H.; Chen, S.; Khademhosseini, A. Microfabricated Biomaterials for Engineering 3D Tissues. *Adv. Mater.* **2012**, *24* (14), 1782–1804.
(105) Zhang, A. P.; Qu, X.; Soman, P.; Hribar, K. C.; Lee, J. W.; Chen, S.; He, S. Rapid Fabrication of Complex 3D Extracellular Microenvironments by Dynamic Optical Projection Stereolithography. *Adv. Mater.* **2012**, *24* (31), 4266–4270.
(106) K., M. A.; Daniel, N.; Luis, I.; Hossein, G. H.; Sushila, M.; U., R. G.; Parastoo, K.; Amir, M.; Remzi, D. M.; Shaochen, C.; Ryon, S. S.; Shrike, Z. Y.; Ali, K. Microfluidics-Enabled Multimaterial Maskless Stereolithographic Bioprinting. *Adv. Mater.* **2018**, *0* (0), 1800242.
(107) Brieke, C.; Rohrbach, F.; Gottschalk, A.; Mayer, G.; Heckel, A. Light-Controlled Tools. *Angew. Chemie Int. Ed.* **2012**, *51* (34), 8446–8476.
(108) Olejnik, J.; Krzymanska-Olejnik, E.; Rothschild, K. J. Photocleavable Aminotag

Phosphoramidites for 5′-Termini DNA/RNA Labeling. *Nucleic Acids Res.* **1998**, *26* (15), 3572–3576.
(109) Azagarsamy, M. A.; Anseth, K. S. Wavelength-Controlled Photocleavage for the Orthogonal and Sequential Release of Multiple Proteins. *Angew. Chemie Int. Ed.* **2013**, *52* (51), 13803–13807.
(110) Li, L.; Tong, R.; Chu, H.; Wang, W.; Langer, R.; Kohane, D. S. Aptamer Photoregulation in Vivo. *Proc. Natl. Acad. Sci.* **2014**, *111* (48), 17099 LP – 17103.
(111) DeForest, C. A.; Anseth, K. S. Cytocompatible Click-Based Hydrogels with Dynamically Tunable Properties through Orthogonal Photoconjugation and Photocleavage Reactions. *Nat. Chem.* **2011**, *3*, 925.
(112) Peng, L.; You, M.; Yuan, Q.; Wu, C.; Han, D.; Chen, Y.; Zhong, Z.; Xue, J.; Tan, W. Macroscopic Volume Change of Dynamic Hydrogels Induced by Reversible DNA Hybridization. *J. Am. Chem. Soc.* **2012**, *134* (29), 12302–12307.
(113) Spahl, W.; Budzikiewicz, H.; Geurtsen, W. Determination of Leachable Components from Four Commercial Dental Composites by Gas and Liquid Chromatography/Mass Spectrometry. *J. Dent.* **1998**, *26* (2), 137–145.
(114) Ouali, S.; Louis, Y.; Germain, P.; Gourdon, R.; Desjardin, V. Leaching and Biodegradation of Darocur 1173 Used as a Photo-Initiator in the Production of Photocrosslinked Silicone Acrylates. *J. Polym. Environ.* **2018**, *26* (1), 244–253.
(115) Bail, R.; Patel, A.; Yang, H.; Rogers, C. M.; Rose, F. R. A. J.; Segal, J. I.; Ratchev, S. M. The Effect of a Type I Photoinitiator on Cure Kinetics and Cell Toxicity in Projection-Microstereolithography. *Procedia CIRP* **2013**, *5*, 222–225.
(116) Wegener, M.; Hansen, M. J.; Driessen, A. J. M.; Szymanski, W.; Feringa, B. L. Photocontrol of Antibacterial Activity: Shifting from UV to Red Light Activation. *J. Am. Chem. Soc.* **2017**, *139* (49), 17979–17986.
(117) Polosukhina, A.; Litt, J.; Tochitsky, I.; Nemargut, J.; Sychev, Y.; De Kouchkovsky, I.; Huang, T.; Borges, K.; Trauner, D.; Van Gelder, R. N.; Kramer, R. H. Photochemical Restoration of Visual Responses in Blind Mice. *Neuron* **2012**, *75* (2), 271–282.
(118) Olejnik, J.; Lüdemann, H. C.; Krzymanska-Olejnik, E.; Berkenkamp, S.; Hillenkamp, F.; Rothschild, K. J. Photocleavable Peptide-DNA Conjugates: Synthesis and Applications to DNA Analysis Using MALDI-MS. *Nucleic Acids Res.* **1999**, *27* (23), 4626–4631.
(119) Huang, F.; Xu, H.; Tan, W.; Liang, H. Multicolor and Erasable DNA Photolithography. *ACS Nano* **2014**, *8* (7), 6849–6855.
(120) Menge, C.; Heckel, A. Coumarin-Caged DG for Improved Wavelength-Selective Uncaging of DNA. *Org. Lett.* **2011**, *13* (17), 4620–4623.
(121) Shan, W.; Liang, Y.; Zi-Yuan, L.; Junji, Z.; He, T.; Itamar, W. Light-Induced Reversible Reconfiguration of DNA-Based Constitutional Dynamic Networks: Application to Switchable Catalysis. *Angew. Chemie Int. Ed.* **2018**, *57* (27), 8105–8109.
(122) Jakubiak, J.; Wrzyszczyński, A.; Linden, L. Å.; Rabek, J. F. The Role of Amines in the Camphorquinone Photoinitiated Polymerization of Multifunctional Monomer. *J. Macromol. Sci. Part A* **2007**, *44* (2), 239–242.
(123) Cook, W. D. Photopolymerization Kinetics of Dimethacrylates Using the Camphorquinone/Amine Initiator System. *Polymer (Guildf).* **1992**, *33* (3), 600–609.
(124) De Oliveira, D. C. R. S.; Rocha, M. G.; Gatti, A.; Correr, A. B.; Ferracane, J. L.; Sinhoret, M. A. C. Effect of Different Photoinitiators and Reducing Agents on Cure Efficiency and Color Stability of Resin-Based Composites Using Different LED Wavelengths. *J. Dent.*

2015, *43* (12), 1565–1572.
(125) Lukacs, G. L.; Haggie, P.; Seksek, O.; Lechardeur, D.; Freedman, N.; Verkman, A. S. Size-Dependent DNA Mobility in Cytoplasm and Nucleus. *J. Biol. Chem.* **2000**, *275* (3), 1625–1629.
(126) Ibo, M.; Srivastava, V.; Robinson, D. N.; Gagnon, Z. R. Cell Blebbing in Confined Microfluidic Environments. *PLoS One* **2016**, *11* (10), e0163866.
(127) Paliwal, S.; Iglesias, P. A.; Campbell, K.; Hilioti, Z.; Groisman, A.; Levchenko, A. MAPK-Mediated Bimodal Gene Expression and Adaptive Gradient Sensing in Yeast. *Nature* **2007**, *446*, 46.
(128) Mavrogiannis, N.; Ibo, M.; Fu, X.; Crivellari, F.; Gagnon, Z. Microfluidics Made Easy: A Robust Low-Cost Constant Pressure Flow Controller for Engineers and Cell Biologists. *Biomicrofluidics* **2016**, *10* (3), 34107.
(129) Guo, J.; Zhou, M.; Yang, C. Fluorescent Hydrogel Waveguide for On-Site Detection of Heavy Metal Ions. *Sci. Rep.* **2017**, *7* (1), 7902.
(130) Choi, M.; Choi, J. W.; Kim, S.; Nizamoglu, S.; Hahn, S. K.; Yun, S. H. Light-Guiding Hydrogels for Cell-Based Sensing and Optogenetic Synthesis in Vivo. *Nat. Photonics* **2013**, *7*, 987.
(131) Matera, C.; Gomila, A. M. J.; Camarero, N.; Libergoli, M.; Soler, C.; Gorostiza, P. Photoswitchable Antimetabolite for Targeted Photoactivated Chemotherapy. *J. Am. Chem. Soc.* **2018**, *140* (46), 15764–15773.
(132) Cabré, G.; Garrido-Charles, A.; Moreno, M.; Bosch, M.; Porta-de-la-Riva, M.; Krieg, M.; Gascón-Moya, M.; Camarero, N.; Gelabert, R.; Lluch, J. M.; Busqué, F.; Hernando, J.; Gorostiza, P.; Alibés, R. Rationally Designed Azobenzene Photoswitches for Efficient Two-Photon Neuronal Excitation. *Nat. Commun.* **2019**, *10* (1), 907.
(133) Rustler, K.; Pockes, S.; König, B. Light-Switchable Antagonists for the Histamine H1 Receptor at the Isolated Guinea Pig Ileum. *ChemMedChem* **2019**, *14* (6), 636–644.
(134) Wang, L. L.; Chung, J. J.; Li, E. C.; Uman, S.; Atluri, P.; Burdick, J. A. Injectable and Protease-Degradable Hydrogel for SiRNA Sequestration and Triggered Delivery to the Heart. *J. Control. Release* **2018**, *285*, 152–161.
(135) Song, J.; Lee, M.; Kim, T.; Na, J.; Jung, Y.; Jung, G. Y.; Kim, S.; Park, N. A RNA Producing DNA Hydrogel as a Platform for a High Performance RNA Interference System. *Nat. Commun.* **2018**, *9* (1), 4331.
(136) Morales, D. P.; Morgan, E. N.; McAdams, M.; Chron, A. B.; Shin, J. E.; Zasadzinski, J. A.; Reich, N. O. Light-Triggered Genome Editing: Cre Recombinase Mediated Gene Editing with Near-Infrared Light. *Small* **2018**, *14* (30), 1800543.
(137) Canal, T.; Peppas, N. a. Correlation between Mesh Size and Equilibrium Degree of Swelling of Polymeric Networks. *J. Biomed. Mater. Res.* **1989**, *23* (10), 1183–1193.
(138) Amsden, B. Solute Diffusion within Hydrogels. Mechanisms and Models. *Macromolecules* **1998**, *31* (23), 8382–8395.
(139) Rawlings, J.; Ekerdt, J. *Chemical Reactor Analysis and Design Fundamentals*, 2.1.; Nob Hill: Madison, WI, 2012.
(140) Peppas, N. A.; Hilt, J. Z.; Khademhosseini, A.; Langer, R. Hydrogels in Biology and Medicine: From Molecular Principles to Bionanotechnology. *Adv. Mater.* **2006**, *18* (11), 1345–1360.
(141) Slaughter, B. V; Khurshid, S. S.; Fisher, O. Z.; Khademhosseini, A.; Peppas, N. A. Hydrogels in Regenerative Medicine. *Adv. Mater.* **2009**, *21* (32–33), 3307–3329.

(142) Peppas, N. A.; Reinhart, C. T. Solute Diffusion in Swollen Membranes. Part I. A New Theory. *J. Memb. Sci.* **1983**, *15* (3), 275–287.
(143) am Ende, M. T.; Peppas, N. A. Transport of Ionizable Drugs and Proteins in Crosslinked Poly(Acrylic Acid) and Poly(Acrylic Acid-Co-2-Hydroxyethyl Methacrylate) Hydrogels. II. Diffusion and Release Studies. *J. Control. Release* **1997**, *48* (1), 47–56.
(144) Wang, W. A Digital Maskless Photolithographic Patterning Method for DNA Based UV Photocleavable PEGDA Hydrogels with A Camphorquinone-Triethanolamine Photoinitiator, Johns Hopkins University, 2019.
(145) Ravi, N.; Mitra, A.; Hamilton, P.; Horkay, F. Characterization of the Network Properties of Poly(Ethylene Glycol)–Acrylate Hydrogels Prepared by Variations in the Ethanol–Water Solvent Composition during Crosslinking Copolymerization. *J. Polym. Sci. Part B Polym. Phys.* **2002**, *40* (23), 2677–2684.
(146) Qian, L.; Winfree, E. Scaling Up Digital Circuit Computation with DNA Strand Displacement Cascades. *Science (80-.).* **2011**, *332* (6034), 1196–1201.
(147) Gosnell, D. L.; Zimm, B. H. Measurement of Diffusion Coefficients of DNA in Agarose Gel. *Macromolecules* **1993**, *26* (6), 1304–1308.
(148) Tirado, M. M.; de la Torre, J. G. Translational Friction Coefficients of Rigid, Symmetric Top Macromolecules. Application to Circular Cylinders. *J. Chem. Phys.* **1979**, *71* (6), 2581–2587.
(149) de la Torre, J. G.; Bloomfield, V. A. Hydrodynamic Properties of Complex, Rigid, Biological Macromolecules: Theory and Applications. *Q. Rev. Biophys.* **1981**, *14* (1), 81–139.
(150) Stellwagen, E.; Lu, Y.; Stellwagen, N. C. Unified Description of Electrophoresis and Diffusion for DNA and Other Polyions. *Biochemistry* **2003**, *42* (40), 11745–11750.
(151) Sun, C.; Fang, N.; Wu, D. M.; Zhang, X. Projection Micro-Stereolithography Using Digital Micro-Mirror Dynamic Mask. *Sensors Actuators A Phys.* **2005**, *121* (1), 113–120.
(152) Han, L.-H.; Mapili, G.; Chen, S.; Roy, K. Projection Microfabrication of Three-Dimensional Scaffolds for Tissue Engineering. *J. Manuf. Sci. Eng.* **2008**, *130* (2), 21004–21005.
(153) Jakubiak, J.; Sionkowska, A.; Lindén, L. A.; Rabek, J. F. Isothermal Photo Differential Scanning Calorimetry. Crosslinking Polymerization of Muitifunctional Monomers in Presence of Visible Light Photoinitiators. *J. Therm. Anal. Calorim.* **2001**, *65* (2), 435–443.
(154) Neumann, M. G.; Miranda, W. G.; Schmitt, C. C.; Rueggeberg, F. A.; Correa, I. C. Molar Extinction Coefficients and the Photon Absorption Efficiency of Dental Photoinitiators and Light Curing Units. *J. Dent.* **2005**, *33* (6), 525–532.
(155) Tabata, T.; Takei, Y. Morphogens, Their Identification and Regulation. *Development* **2004**, *131* (4), 703 LP – 712.
(156) E., I. D. Mechanical Signaling and the Cellular Response to Extracellular Matrix in Angiogenesis and Cardiovascular Physiology. *Circ. Res.* **2002**, *91* (10), 877–887.
(157) Hollis 2nd, E. R.; Zou, Y. Expression of the Wnt Signaling System in Central Nervous System Axon Guidance and Regeneration. *Front. Mol. Neurosci.* **2012**, *5*, 5.
(158) Vempati, P.; Popel, A. S.; Mac Gabhann, F. Extracellular Regulation of VEGF: Isoforms, Proteolysis, and Vascular Patterning. *Cytokine Growth Factor Rev.* **2014**, *25* (1), 1–19.
(159) Kaminaga, A.; Vanag, V. K.; Epstein, I. R. A Reaction–Diffusion Memory Device. *Angew. Chemie Int. Ed.* **2006**, *45* (19), 3087–3089.
(160) Zadorin, A. S.; Rondelez, Y.; Gines, G.; Dilhas, V.; Urtel, G.; Zambrano, A.; Galas, J.;

Estevez-torres, A. Reaction – Diffusion French Fl Ag Pattern. *Nat. Chem.* **2017**, No. May, 1–7.
(161) Scalise, D.; Schulman, R. Designing Modular Reaction-Diffusion Programs for Complex Pattern Formation. *Technology* **2014**, *2* (1).
(162) Scalise, D.; Schulman, R. Emulating Cellular Automata in Chemical Reaction–Diffusion Networks. *Nat. Comput.* **2016**, *15* (2), 197–214.
(163) Zhang, D. Y.; Seelig, G. Dynamic DNA Nanotechnology Using Strand-Displacement Reactions. *Nat. Chem.* **2011**, *3* (2), 103–113.
(164) Smith, D. E.; Perkins, T. T.; Chu, S. Dynamical Scaling of DNA Diffusion Coefficients. *Macromolecules* **1996**, *29* (4), 1372–1373.
(165) Biehs, B.; François, V.; Bier, E. The Drosophila Short Gastrulation Gene Prevents Dpp from Autoactivating and Suppressing Neurogenesis in the Neuroectoderm. *Genes Dev.* **1996**, *10* (22), 2922–2934.
(166) Kwan, C. W.; Gavin-Smyth, J.; Ferguson, E. L.; Schmidt-Ott, U. Functional Evolution of a Morphogenetic Gradient. *Elife* **2016**, *5*, e20894.
(167) Ben-Zvi, D.; Barkai, N. Scaling of Morphogen Gradients by an Expansion-Repression Integral Feedback Control. *Proc. Natl. Acad. Sci.* **2010**, *107* (15), 6924 LP – 6929.
(168) Collavin, L.; Kirschner, M. W. The Secreted Frizzled-Related Protein Sizzled Functions as a Negative Feedback Regulator of Extreme Ventral Mesoderm. *Development* **2003**, *130* (4), 805 LP – 816.
(169) Barbieri, F.; Brunel, N. Can Attractor Network Models Account for the Statistics of Firing During Persistent Activity in Prefrontal Cortex? . *Frontiers in Neuroscience* . 2008, p 3.
(170) Krotov, D.; Hopfield, J. J. Dense Associative Memory for Pattern Recognition. In *Proceedings of the 30th International Conference on Neural Information Processing Systems*; NIPS'16; Curran Associates Inc.: USA, 2016; pp 1180–1188.
(171) You, Y.; Tataurov, A. V; Owczarzy, R. Measuring Thermodynamic Details of DNA Hybridization Using Fluorescence. *Biopolymers* **2011**, *95* (7), 472–486.
(172) Moreira, B. G.; You, Y.; Behlke, M. A.; Owczarzy, R. Effects of Fluorescent Dyes, Quenchers, and Dangling Ends on DNA Duplex Stability. *Biochem. Biophys. Res. Commun.* **2005**, *327* (2), 473–484.
(173) Tonnesen, M. G.; Feng, X.; Clark, R. A. F. Angiogenesis in Wound Healing. *J. Investig. Dermatology Symp. Proc.* **2000**, *5* (1), 40–46.
(174) Lee, P. C.; Salyapongse, A. N.; Bragdon, G. A.; Shears, L. L.; Watkins, S. C.; Edington, H. D. J.; Billiar, T. R. Impaired Wound Healing and Angiogenesis in ENOS-Deficient Mice. *Am. J. Physiol. Circ. Physiol.* **1999**, *277* (4), H1600–H1608.
(175) Chen, X.; Schauder, S.; Potier, N.; Van Dorsselaer, A.; Pelczer, I.; Bassler, B. L.; Hughson, F. M. Structural Identification of a Bacterial Quorum-Sensing Signal Containing Boron. *Nature* **2002**, *415* (6871), 545–549.
(176) Winfree, E.; Bekbolatov, R. Proofreading Tile Sets: Error Correction for Algorithmic Self-Assembly BT - DNA Computing; Chen, J., Reif, J., Eds.; Springer Berlin Heidelberg: Berlin, Heidelberg, 2004; pp 126–144.
(177) Chen, H.-L.; Goel, A. Error Free Self-Assembly Using Error Prone Tiles BT - DNA Computing; Ferretti, C., Mauri, G., Zandron, C., Eds.; Springer Berlin Heidelberg: Berlin, Heidelberg, 2005; pp 62–75.
(178) Chen Holin , Goel Ashish, Winfree Erik, L. C. Self-Assembling Tile Systems That Heal from Small Fragments. *Prelim. Proc. DNA Comput. 13* **2007**, 30–46.

(179) Kaminaga, A.; Vanag, V. K.; Epstein, I. R. A Reaction-Diffusion Memory Device. *Angew. Chemie - Int. Ed.* **2006**, *45* (19), 3087–3089.
(180) Chirieleison, S. M.; Allen, P. B.; Simpson, Z. B.; Ellington, A. D.; Chen, X. Pattern Transformation with DNA Circuits. *Nat. Chem.* **2013**, *5* (12), 1000–1005.
(181) Nomura, A.; Ichikawa, M.; Miike, H.; Ebihara, M.; Mahara, H.; Sakurai, T. Realizing Visual Functions with the Reaction–Diffusion Mechanism. *J. Phys. Soc. Japan* **2003**, *72* (9), 2385–2395.
(182) Nomura, A. Image Coding and Pooling with a Bio-Inspired Reaction-Diffusion Algorithm. *Procedia Comput. Sci.* **2015**, *71*, 125–130.
(183) Nomura, A.; Ichikawa, M.; Sianipar, R. H.; Miike, H. Edge Detection with Reaction-Diffusion Equations Having a Local Average Threshold. *Pattern Recognit. Image Anal.* **2008**, *18* (2), 289.
(184) Gillespie, D. T. Exact Stochastic Simulation of Coupled Chemical Reactions. *J. Phys. Chem.* **1977**, *81* (25), 2340–2361.
(185) Flajolet, P.; Gardy, D.; Thimonier, L. Birthday Paradox, Coupon Collectors, Caching Algorithms and Self-Organizing Search. *Discret. Appl. Math.* **1992**, *39* (3), 207–229.
(186) Walker, D. A.; Hedrick, J. L.; Mirkin, C. A. Rapid, Large-Volume, Thermally Controlled 3D Printing Using a Mobile Liquid Interface. *Science (80-.).* **2019**, *366* (6463), 360 LP – 364.
(187) Saha, S. K.; Wang, D.; Nguyen, V. H.; Chang, Y.; Oakdale, J. S.; Chen, S.-C. Scalable Submicrometer Additive Manufacturing. *Science (80-.).* **2019**, *366* (6461), 105 LP – 109.

Curriculum Vita

Phillip James Dorsey

Education

Johns Hopkins University, Baltimore, MD

- **Doctor of Philosophy, Chemical & Biomolecular Engineering** **Aug. 2015 – Jan. 2020**

Advisor: Prof. Rebecca Schulman, **Dynamic & Adaptive Biomolecular Materials Group**

Princeton University, Princeton, NJ **Graduation Date: June 2014**

- **Bachelor of Science in Engineering (BSE), Chemical & Biological Engineering**
- Certificate in **Engineering Biology,** Concentration in **Bioengineering & Biotechnology**

Skills:

Laboratory Techniques & Applications:

microfluidic process design & soft lithography, nucleic acid systems design, quantitative PCR, polymer chemistry, soft matter physics, fluorescence & atomic force microscopy, maskless photolithography, microscope automation

Computational Skills & Languages:

finite element analysis & continuum mechanics modeling, Java, Matlab, Python, Abaqus FEA, Comsol, ApsenPlus, AutoCAD, Rational DOORS, Synergis Adept

---

Research Experience and Projects

Johns Hopkins University, Baltimore, MD (Fall 2015-2020)

Advisor: Prof. Rebecca Schulman, Dynamic & Adaptive Biomolecular Materials Group

Design of Programmable Self-healing DNA-based Biomaterials

- Developed spatial DNA-based reaction-diffusion networks within soft materials as a means of developing programmable behaviors relevant to drug delivery applications including: controlled delivery of nucleic acids, molecular pattern sensing & chemical recognition
- Independently developed and managed projects using microfluidic assembly methods coupled with digital maskless photolithography to fabricate micron-scale multi-domain DNA-based hydrogels
- Utilized the above-mentioned microfluidic platform to store molecular patterns in biomaterials in the form of self-healing DNA-based reaction-diffusion gradients within polyethylene glycol hydrogels
- Expanded lab research portfolio by procuring and installing digital photolithographic patterning technologies to micro-fabricate multi-domain hydrogels in high-through-put to reduce raw material consumption and waste
- Currently constructing DNA-based circuitry for repairing and recognizing sets of molecular patterns in biomaterials to extend functions of neural computation to analog systems

---

Publications

1. P. Dorsey, M. Rubanov, W. Wang, & R. Schulman. *Digital maskless photolithographic patterning of DNA-functionalized poly(ethylene glycol) diacrylate hydrogels with visible light enabling photodirected release of oligonucleotides.* ***ACS Macro Lett.*** (2019-8)
2. P. Dorsey, D. Scalise, & R. Schulman. *DNA Reaction-Diffusion Attractor Patterns*. (In preparation)

3. J. Zenk, D. Scalise, K. Wang, P. Dorsey, J. Fern, A. Cruz, R. Schulman. *Stable DNA-based Reaction Diffusion Patterns*. ***RSC Advances***. (2017-7).

Post Baccalaureate Research Education Program (PREP) – Icahn School of Medicine at Mount Sinai (2014-2015)
Advisor: Dr. Kevin Costa, Cardiovascular Research Center

- Conducted a computational study of atomic force microscope (AFM)-type micro/nano-indentation response dependence on substrate mechanics
- Characterized the cytoskeletal properties of vascular smooth muscle cells (VSMC) in disease-associated states utilizing atomic force microscopy

Princeton University, Princeton, NJ (2013-2014)
Senior Thesis: ***Staphylococcus aureus biofilm formation and clogging dynamics within microfluidic environments***
Advisor: Prof. Howard Stone, Complex Fluids Group

- Investigated the physical and biochemical mechanisms governing bacterial biofouling processes in fluidic microenvironments in order to understand & mitigate biofouling mechanisms within implantable medical devices

---

Computational Skills: Java, Python, Abaqus FEA, Comsol, AspenPlus, GAMS, AutoCAD, MATLAB, Rational DOORS, Synergis Adept

---

Work Experience
Lockheed Martin – Electronic Systems: Mission Systems and Sensors, Moorestown, NJ
Combat System Interface Engineering Department (CSIE) College Tech Senior Intern **June-Aug. 2011/ 2012**

- Designed quick reference interface diagrams for helicopter data communication systems onboard US Navy cruisers and destroyers as a guide to help troubleshooting during Aegis Weapons System testing
- Created software diagrams of signal and message exchange choke points between MH 60 Romeo helicopters & SQQ-89 anti-submarine warfare systems
- Devised and consolidated interface diagrams highlighting possible data exchange choke points between MH 60 Romeo helicopters and shipboard receiving equipment

---

Funding Awards

- *2017 Johns Hopkins Catalyst Award*. **Award Amount: $75,000.** Submission Title: Biochemical waveguides as an 'information vasculature' for soft materials. Authors: Rebecca Schulman & Phillip Dorsey

---

Conferences and Presentations
2019 American Institute of Chemical Engineers Conference, Orlando, FL (November 2019) – Poster: *DNA Reaction-Diffusion Attractor Patterns* ***1st Place in Student NSEF Poster Session**
2019 International Conference on DNA Computing and Molecular Programming, Seattle, WA (August 2019) Presentation: *DNA Reaction-Diffusion Attractor Patterns*
2019 Materials Research Society Spring Conference, Phoenix, AZ (April 2019) – Presentation: *DNA-based Attractor Patterns* ***Winner of Best Oral Presentation Award**
2019 Biophysical Society Conference, Baltimore, MD (March 2019) – Poster: *Self-healing DNA-based reaction-diffusion patterns*
2018 NOBCChE National Conference, Orlando, FL (Sept. 2018) – Presentation: *Enabling self-healing DNA-based reaction-diffusion patterns with digital photolithography*

2017 Complex Active & Adaptive Materials Systems Gordon Research Conference, Ventura, CA (Jan. 2017) – Poster: *DNA-based Reaction-Diffusion Waveguides for Programming Soft Materials* ***Recipient of Carl Storm Underrepresented Minority Fellowship**

Leadership, Mentoring & Teaching Activities

Mentoring (Summer 2016-Present)

- Mentored and directly supervised two thesis-track masters students on projects focused on developing smart materials by embedding DNA-based biosensors and logic circuits into hydrogel substrates (2017-2019)
- Served as a graduate student guide & discussion panelist for the Penn State Millennium Scholars Program and UMBC Meyerhoff Bridge Summer Program visits at Johns Hopkins (Summer 2016-2019)

Schulman Laboratory Safety Officer

- Responsible for training of all lab members regarding lab protocols & operating procedures, chemical reagent storage, and proper disposal of hazardous waste materials

Laboratory Teaching Assistant, *EN.540.311/313 Chemical Engineering Laboratory* (Fall 2016)

- Instructed undergraduates on unit operations processes and techniques
- Performed equipment and maintenance repairs, and supply and inventory upkeep in teaching labs

Whiting School of Engineering Diversity Fellow (Fall 2015-Spring 2016)

- Copy editor and writer for *Flourish*, the Homewood Campus Minority Graduate Student Handbook

---

Honors, Fellowships, & Awards

Scientist Mentoring & Diversity Program MedTech Scholar 2018-2019, PhD GEM Associate Fellow (2015-Present)